

Development of the ATLAS High-Level Trigger Steering  
*and*  
Inclusive Searches for Supersymmetry

THÈSE

présentée à la Faculté des sciences de l'Université de Genève  
pour obtenir le grade de Docteur ès sciences, mention physique

par

Till Eifert  
*d'Allemagne*

Thèse N° 4100



**UNIVERSITÉ  
DE GENÈVE**

FACULTÉ DES SCIENCES

**Doctorat ès sciences  
mention physique**

Thèse de *Monsieur Till EIFERT*

intitulée :

**"Development of the ATLAS High-Level Trigger Steering  
and  
Inclusive Searches for Supersymmetry"**

La Faculté des sciences, sur le préavis de Messieurs A. G. CLARK, professeur ordinaire et directeur de thèse (Département de physique nucléaire et corpusculaire), M. POHL, professeur ordinaire (Département de physique nucléaire et corpusculaire), Ch. BEE, docteur (Centre de physique des particules de Marseille, Université d'Aix-Marseille II, Marseille, France), D. FROIDEVAUX, docteur (Département de physique, CERN, Genève), X. WU, docteur (Département de physique nucléaire et corpusculaire), autorise l'impression de la présente thèse, sans exprimer d'opinion sur les propositions qui y sont énoncées.

Genève, le 16 juin 2009

**Thèse - 4100 -**

**Le Doyen, Jean-Marc TRISCONE**

N.B.- La thèse doit porter la déclaration précédente et remplir les conditions énumérées dans les "Informations relatives aux thèses de doctorat à l'Université de Genève".

Nombre d'exemplaires à livrer par colis séparé à la Faculté : - 5 -

## Abstract

The presented thesis is divided into two distinct parts. The subject of the first part is the ATLAS high-level trigger (HLT), in particular the development of the HLT Steering, and the trigger user-interface. The second part presents a study of inclusive supersymmetry searches, including a novel background estimation method for the relevant Standard Model (SM) processes.

The trigger system of the ATLAS experiment at the Large Hadron Collider (LHC) performs the on-line physics selection in three stages: level-1 (LVL1), level-2 (LVL2), and the event filter (EF). LVL2 and EF together form the HLT. The HLT receives events containing detector data from high-energy proton (or heavy ion) collisions, which pass the LVL1 selection at a maximum rate of 75 kHz. It must reduce this rate to  $\sim 200$  Hz, while retaining the most interesting physics. The HLT is a software trigger and runs on a large computing farm. At the heart of the HLT is the Steering software.

The HLT Steering must reach a decision whether or not to accept an event within a time budget of less than 40 ms (LVL2) and under 4 s (EF), averaged over all events. Its decision is based on the results of customised trigger algorithms. These algorithms perform a specific data reconstruction task in a small geometrical detector region. The Steering controls the flow and execution of these algorithms, such that only interesting (typically high- $p_T$ ) detector regions are examined in several steps. The principles and design of this HLT selection strategy are discussed in detail. The final implementation of the Steering, including all required features such as pre-scaling, is presented. Furthermore, commissioning results from technical and cosmic ray runs are described. Finally, the common interface to all trigger results for off-line analysis and debugging is presented.

Supersymmetry (SUSY) is a theoretically attractive scenario for physics beyond the SM which may also provide a suitable dark matter candidate in models where R-parity (+1 for SM and  $-1$  for SUSY particles) is conserved. If SUSY is realised at a mass scale of  $\sim 1$  TeV, as favoured by several arguments, it will be accessible at the LHC at CERN within the first years of data-taking.

The second part of this thesis presents the inclusive one-lepton search strategy for generic SUSY models with R-parity conservation with the ATLAS detector at the LHC. The signature of this search mode is based on large missing transverse momentum from undetected neutralinos, multiple high- $p_T$  jets and one lepton. The corresponding discovery reach is shown for the first  $\text{fb}^{-1}$  of ATLAS data. Furthermore, background estimation techniques for inclusive SUSY searches are discussed. A novel background determination approach, denoted the *Tiles Method*, is proposed, which translates prior knowledge on the SM distributions of discriminating variables in a two or higher dimensional grid into an estimate of the abundances of SM and beyond-SM events. Depending on the grid granularity, the abundances are calculated by solving a system of linear equations or by minimising a log-likelihood function. The method does not rely on assumptions on background dominance for particular values of the variables, nor does it require iterations. Systematic effects due to uncertainties in the simulated prior distributions are investigated. Results for various mSUGRA scenarios are presented.

## Résumé

La thèse qui suit est divisée en deux parties distinctes. Le sujet de la première partie est le déclencheur de haut niveau (HLT), en particulier le développement du Steering et de l'interface utilisateur. La seconde partie présente une étude de recherche inclusive pour la supersymétrie, incluant une nouvelle méthode d'estimation pour les bruits de fond pertinents des processus du Modèle Standard (MS).

Le système de déclenchement de l'expérience ATLAS au Large Hadron Collider (LHC) effectue la sélection en ligne de physique en trois niveaux : niveau-1 (LVL1), niveau-2 (LVL2), et "Event Filter" (EF). LVL2 et EF forment ensemble le HLT. Le HLT reçoit des événements, contenant les données du détecteur des collision de protons (ou d'ions lourds) à haute énergie, qui passent la sélection LVL1 à un taux maximum de 75 kHz. Il faut réduire ce taux à  $\sim 200$  Hz, tout en gardant la physique la plus importante. Le HLT est un système de déclenchement logiciel et fonctionne sur une grande grappe de serveurs. Au coeur du HLT se trouve le logiciel du Steering.

Le Steering du HLT doit prendre la décision d'accepter un événement dans un temps de moins de 40 ms (LVL2) et en-dessous de 4 s (EF), en moyenne, pour tous les événements. Cette décision est basée sur les résultats des algorithmes spécialisés. Ces algorithmes effectuent une tâche spécifique de reconstruction des données dans une région géométrique restreinte du détecteur. Le Steering contrôle la direction du flux et l'exécution de ces algorithmes, de telle sorte que seulement des régions intéressantes (en général de haute énergie transversale) du détecteur sont examinées en plusieurs étapes. Les principes et la conception de cette stratégie de sélection du HLT sont traités en détails. La dernière version (mise en œuvre) du Steering, y compris toutes les caractéristiques exigées comme l'échelle du trigger (pre-scale), est présenté. En outre, les résultats de la mise en service technique et de la prise de données de rayons cosmiques sont décrits. Enfin, l'interface utilisateur commune pour tous les résultats du déclencheur, qui facilite l'analyse hors-ligne et le débogage, est présentée.

La Supersymétrie (SUSY) est un scénario attractif du point de vue théorique pour la physique au-delà du modèle standard qui, de plus, pourrait fournir un candidat approprié pour la matière sombre dans le cas où la parité de R serait conservée (+1 pour les particules MS et  $-1$  pour les particules supersymétriques). Si la SUSY est réalisée à une échelle de masse d'environ 1 TeV, comme privilégié par plusieurs arguments, la SUSY sera accessible au LHC du CERN dans les premières années de prise de données.

La deuxième partie de cette thèse présente la stratégie de recherche inclusive à un-lepton pour les modèles génériques de SUSY avec conservation de parité R à l'aide du détecteur ATLAS au LHC. La signature de ce mode de recherche est basée sur une grande quantité d'implusion transversale manquante, dus aux neutralinos non-observés, de multiples jets durs et un lepton. Le potentiel de découverte correspondant est montrée pour le premier  $\text{fb}^{-1}$  de données d'ATLAS. De plus, des techniques d'estimation de bruits de fond pour les recherches inclusives pour la SUSY sont examinées. Une nouvelle approche pour la détermination des bruits de fond, dénotée *Tiles Method*, est proposée ; elle traduit les connaissances préalables des distributions de certaines variables discriminatoires du MS, dans une grille de deux dimensions ou plus, en une estimation

de l'abondance d'événements du MS et d'au-delà de ce dernier. Dépendant de la granularité de la grille, les abondances sont calculées en résolvant des équations linéaires ou en minimisant des fonctions de probabilités logarithmiques. La méthode ne dépend pas des hypothèses sur la dominance du bruit de fond pour des valeurs particulières des variables, et ne requiert pas non plus d'itérations. Les effets systématiques dus aux incertitudes de la simulation des distributions initiales ("priors") sont examinés. Les résultats de différents scénarios mSUGRA sont présentés.

---



# Contents

<b>Nomenclature</b>	<b>x</b>
<b>1 Introduction</b>	<b>1</b>
<b>2 Motivation</b>	<b>3</b>
2.1 The Standard Model . . . . .	4
2.2 Phenomenology . . . . .	7
2.3 Beyond the Standard Model . . . . .	8
<b>I The High-Level Trigger System of the ATLAS Detector</b>	<b>13</b>
<b>3 The ATLAS Detector at the LHC</b>	<b>15</b>
3.1 The Large Hadron Collider at CERN . . . . .	15
3.1.1 Pile-Up . . . . .	18
3.1.2 Underlying Event . . . . .	19
3.2 The ATLAS Detector . . . . .	19
3.2.1 Magnet System . . . . .	21
3.2.2 Inner Detector . . . . .	22
3.2.3 Calorimetry . . . . .	23
3.2.4 Muon Spectrometer . . . . .	26
3.2.5 Trigger and Data Acquisition . . . . .	26
3.3 ATLAS Detector Commissioning . . . . .	28
<b>4 Development of the High-Level Trigger Steering</b>	<b>35</b>
4.1 ATLAS Trigger and Data Acquisition System . . . . .	36
4.1.1 LVL1 Trigger . . . . .	36
4.1.2 Data Acquisition . . . . .	39
4.1.3 High-Level Trigger . . . . .	41
4.2 HLT Steering Requirements . . . . .	42

---

4.2.1	On-Line triggering . . . . .	43
4.2.2	Data analysis . . . . .	43
4.2.3	Off-line studies . . . . .	43
4.3	Basic Steering Design and Concepts . . . . .	44
4.4	Trigger Configuration . . . . .	46
4.5	HLT Algorithms . . . . .	47
4.6	Inter-Algorithm Communication . . . . .	49
4.7	HLT Steering Logic . . . . .	51
4.8	Pre-scale and Pass-through of Triggers . . . . .	53
4.9	Monitoring . . . . .	55
4.10	Performance and Validation . . . . .	58
4.10.1	Timing performance . . . . .	59
4.10.2	Validation of the Pre-scale and Pass-through Implementation . . . . .	61
4.10.3	Cosmics Validation . . . . .	62
4.11	Conclusions . . . . .	66
<b>5</b>	<b>Trigger Menu</b>	<b>67</b>
5.1	Organisation and Conventions . . . . .	67
5.2	Trigger Menu for $L = 10^{31} \text{ cm}^{-2} \text{ s}^{-1}$ . . . . .	69
<b>6</b>	<b>Development of the Trigger User-Interface</b>	<b>75</b>
6.1	Trigger Data Flow . . . . .	75
6.2	Trigger Decision Result . . . . .	77
6.3	Trigger Decision Tool . . . . .	78
6.4	Trigger Access from ROOT . . . . .	79
6.5	Example: Trigger efficiencies . . . . .	80
<b>II</b>	<b>Inclusive Supersymmetry Searches</b>	<b>81</b>
<b>7</b>	<b>Supersymmetry</b>	<b>83</b>
7.1	Theoretical Framework . . . . .	83
7.1.1	Supersymmetric Lagrangian . . . . .	86
7.1.2	R-parity . . . . .	87
7.1.3	Soft supersymmetry breaking . . . . .	88
7.1.4	Mass spectrum . . . . .	91
7.2	Production and Decay Processes at the LHC . . . . .	93
7.3	Experimental Constraints . . . . .	96

---



---

7.4	ATLAS Search Strategy . . . . .	99
7.4.1	Measurements . . . . .	101
<b>8</b>	<b>Monte Carlo Simulations</b>	<b>103</b>
8.1	Monte Carlo Generators . . . . .	103
8.2	Detector Simulation . . . . .	105
8.3	Simulated Datasets . . . . .	106
8.3.1	SUSY Benchmark Points . . . . .	107
8.3.2	mSUGRA Signal Grid . . . . .	108
8.3.3	Standard Model Backgrounds . . . . .	110
<b>9</b>	<b>Reconstruction and Expected Performance</b>	<b>115</b>
9.1	Off-Line Reconstruction . . . . .	115
9.2	Electrons . . . . .	116
9.2.1	Pre-selection of electron candidates . . . . .	116
9.2.2	Electron identification with the cut-based method . . . . .	117
9.2.3	Performance . . . . .	120
9.3	Muons . . . . .	121
9.3.1	Reconstruction . . . . .	122
9.3.2	Performance . . . . .	124
9.4	Jets . . . . .	125
9.4.1	Reconstruction . . . . .	126
9.4.2	Jet calibration . . . . .	128
9.4.3	Performance . . . . .	129
9.5	Missing Transverse Energy . . . . .	129
9.5.1	Reconstruction . . . . .	130
9.5.2	Fake $E_T^{\text{miss}}$ . . . . .	131
9.5.3	Performance . . . . .	132
<b>10</b>	<b>Search for Supersymmetry in the Inclusive One-Lepton Channel</b>	<b>135</b>
10.1	Object and Variable Definition . . . . .	136
10.1.1	Electron-crack veto . . . . .	136
10.1.2	Overlap removal . . . . .	137
10.1.3	Global event variables . . . . .	137
10.2	Event Selection . . . . .	138
10.3	Trigger . . . . .	141
10.4	Systematic Uncertainties and Statistical Significance . . . . .	143
10.5	Expected Discovery Potential . . . . .	144

---

---

10.6 Comparison of a Multivariate Technique . . . . .	146
10.6.1 Pre-selection of events . . . . .	149
10.6.2 Input variables . . . . .	149
10.6.3 MVA results . . . . .	150
10.7 Conclusions . . . . .	154
<b>11 Background Estimation</b>	<b>159</b>
11.1 Introduction . . . . .	159
11.2 Two-Dimensional Sideband Background Estimation . . . . .	161
11.2.1 The $M_T$ Sideband Method . . . . .	161
11.2.2 Impact of Variable Correlations and SUSY Contamination . . . . .	162
11.2.3 Performance on the mSUGRA Grid . . . . .	163
11.2.4 The $M_T$ -Method with Decorrelated Variables . . . . .	165
11.3 The Tiles Method . . . . .	170
11.3.1 $2 \times 2$ Tiles Method . . . . .	171
11.3.2 $n \times n$ Tiles Method . . . . .	174
11.3.3 Signal Significance . . . . .	176
11.3.4 Uncertainties in the SM Tile Fractions . . . . .	176
11.3.5 Validation With Toy Experiments . . . . .	177
11.3.6 Signal Correlations . . . . .	179
11.3.7 Splitting SM Contributions . . . . .	179
11.3.8 Systematic Studies . . . . .	181
11.3.9 Stability Test . . . . .	187
11.4 Conclusions . . . . .	188
<b>12 Outlook</b>	<b>191</b>
12.1 Expected LHC start-up . . . . .	191
12.2 First SUSY data analysis . . . . .	193
12.3 Measuring SUSY with the LHC and ILC . . . . .	194
<b>Appendices</b>	
<b>A HLT Steering terminology</b>	<b>198</b>
<b>B Sample SUSY production and cascade decays</b>	<b>200</b>
<b>C StatTools - Calculation of Significances in Search Analyses</b>	<b>205</b>
C.1 Hypothesis testing . . . . .	205
C.1.1 Gauss approximation . . . . .	206

---

C.1.2	Poisson approximation . . . . .	207
C.1.3	Exact Poisson solution . . . . .	207
C.1.4	Monte Carlo sampling . . . . .	208
C.2	A numerical example . . . . .	209
<b>List of References</b>		<b>211</b>
<b>Acknowledgments</b>		<b>223</b>

---

# Nomenclature

The following coordinate system and nomenclature will be used throughout this thesis. The right-handed cartesian coordinates  $x$ ,  $y$ ,  $z$  are chosen such that the origin is the nominal interaction point within ATLAS,  $x$  points towards the centre of the LHC,  $y$  vertically upwards, and  $z$  along the beam axis ( $z > 0$  towards south-east).

Spherical coordinates are defined in the standard way: the radial distance  $r$  from the origin is

$$r = \sqrt{x^2 + y^2 + z^2},$$

the zenith angle  $\theta$  from the positive  $z$ -axis (beam axis) is

$$\theta = \arctan\left(\frac{\sqrt{x^2 + y^2}}{z}\right),$$

and the azimuth angle  $\phi$  from the positive  $x$ -axis (around the beam axis) is given by

$$\phi = \arctan\left(\frac{y}{x}\right).$$

The rapidity  $y$  and pseudorapidity  $\eta$  of an object are defined as

$$\begin{aligned} y &= -\frac{1}{2} \ln\left(\frac{E + p_z}{E - p_z}\right), \\ \eta &= -\frac{1}{2} \ln\left(\frac{p + p_z}{p - p_z}\right) = -\ln\left[\tan\left(\frac{\theta}{2}\right)\right], \end{aligned}$$

where  $p = |\vec{p}|$  is the magnitude of the momentum vector,  $p_z$  is the  $z$ -component, and  $E$  denotes the energy.

The transverse components, such as  $p_T$ ,  $E_T$ ,  $E_T^{\text{miss}}$ , are obtained by the projection onto the  $(x, y)$  plane, for example  $p_T = \sqrt{p_x^2 + p_y^2}$ .

The missing energy is defined in the transverse plane by  $E_T^{\text{miss}} = \sqrt{(\sum E_x)^2 + (\sum E_y)^2}$ .

The widely-used distance  $\Delta R$  in pseudorapidity and azimuthal space is given by

$$\Delta R = \sqrt{\Delta\eta^2 + \Delta\phi^2}.$$

---

Finally, the word “event” is defined as one proton bunch-crossing, rather than a proton–proton collision. At the LHC the nominal bunch-crossing rate is 40 MHz, while the expected proton–proton rate is  $\sim 1$  GHz. In principle both can be defined as an event. However, since the ATLAS detector records either all or no detector signals from a proton bunch-crossing, the above definition is more natural in this context.

---



# Chapter 1

## Introduction

With its unprecedented high energy and luminosity, the Large Hadron Collider (LHC) at CERN will mark the beginning of a new epoch in particle physics. The physics programme ranges from the precise measurement of the properties of known objects up to the exploration of the unknown high energy frontier. The presented thesis describes the author's work conducted at the ATLAS experiment during its construction, installation, and final phase of commissioning. It presents contributions to the ATLAS trigger software, and discusses prospects of searches for supersymmetry (SUSY) at the LHC.

Part I of this thesis presents the ATLAS trigger system, with emphasis on the high-level trigger (HLT). The challenging design and implementation of the HLT Steering component represents the author's main contribution to the trigger software. Most of the concepts and ideas behind the HLT were conceived by studying trigger systems of other major particle experiments, as well as the ATLAS/LHC specific requirements. After an introduction to the ATLAS detector in general, and the trigger system in particular, part I of this thesis concentrates on the HLT Steering. The architecture with the main design principles, the execution logic, and the interface to the HLT algorithms are described in detail. It is shown that the HLT performance meets the ATLAS requirements. Furthermore, the first successful HLT on-line event selection (using tracking algorithms in the second level trigger) of cosmic rays is presented. A recent trigger menu is then utilised as an illustration and realistic example of what the Steering must handle. Following the discussion of the trigger Steering, the trigger user-interface is introduced. The novel Steering together with the finalised trigger configuration necessitated a re-design of the trigger user-interface. This important layer between all trigger information and the physics analysis is described in Chapter 6.

In the second part of this thesis, an inclusive SUSY search study based on simulated data is described. The analysis inspired the development of several tools and techniques, covering aspects of particle physics, analysis techniques, and statistical procedures. Part II begins with a summary of the basic theoretical ideas behind SUSY. The features that are relevant for experimental studies at the LHC are highlighted, and the resulting general ATLAS search strategy is outlined. Next, the input Monte Carlo, and ATLAS reconstruction algorithms are described in detail. From these starting components a one-lepton analysis for generic R-parity conserving (RPC) SUSY models is presented and motivated. A multivariate analysis is considered and compared to the baseline analysis. Using a scan of minimal gravity-mediated SUSY breaking models (mSUGRA), the dis-

covery reach of both analyses are estimated for the first year(s) of LHC data. It is shown that ATLAS could discover (or exclude) RPC SUSY models at a mass scale below  $\mathcal{O}(1 \text{ TeV})$  using the one-lepton analysis with an integrated luminosity of  $1 \text{ fb}^{-1}$  of understood data.

Finally, Chapter 11 discusses background estimation techniques for inclusive SUSY searches. In the exciting time of first LHC collisions, the importance of understanding the Standard Model (SM) backgrounds using data cannot be overestimated. It is shown that the widely-used, so-called  $M_T$ -method to estimate SM background suffers from deficiencies that may lead to fake signal and false discovery claims. The method is improved by decorrelating the input variables, but an inherent sensitivity to the distribution of beyond-SM events remains, leading to incorrect background estimates. A novel background determination approach, denoted the *Tiles Method*, is proposed. The Tiles Method translates prior knowledge on the SM distributions of discriminating variables in a two or higher dimensional grid into an estimate of the abundances of SM and beyond-SM events. Depending on the grid granularity, the abundances are calculated by solving a system of linear equations or by minimising a log-likelihood function. The method does not rely on assumptions on background dominance for particular values of the variables, nor does it require iterations. Correlations between the variables are fully taken into account for SM events, while they are neglected or not for beyond-SM events. Systematic effects due to uncertainties in the simulated prior distributions are investigated. Results for various mSUGRA scenarios are presented.

---



## Chapter 2

# Motivation

The motivation that drives most scientific research originates from curiosity, and the field of particle physics is no exception. The desire to understand and describe nature, in the most fundamental way possible, has motivated natural scientists throughout the ages. The basic principles used in the attempts to capture nature are: *symmetry* (representing elegance and beauty in a mathematical/physical form) and *simplicity*. Most of today's physics is based on a few fundamental symmetries, which are believed to be deeply embedded in nature. The great number of observed phenomena is described by only four basic forces, the *gravitational force* (responsible for the movement of planets), the *electromagnetic force* (describing electrical and magnetic phenomena, i.e. most of the effects in daily life), the *weak nuclear force* (that powers the burning of the Sun), and the *strong nuclear force* (which holds the nucleus of an atom together).

The best known description of gravity is given by Einstein's General Relativity theory [1], which closely links the spacetime geometry of our Universe to the gravitational force. Gravity is the weakest of the four forces, but dominates on cosmological scales. This is because the basic quantity it couples to, the mass of matter, is always positive and thus cannot cancel (in contrast to for example the total electric charge of the Earth which is close to zero).

The other three fundamental forces are described in a different theoretical framework, called quantum field theory (QFT), which unifies quantum mechanics, classical field theory, and special relativity. The three forces are collectively described by what is known as the *Standard Model* of particle physics [2]. So far, all attempts to also incorporate gravity into this model have failed. It seems the geometrical description of gravity is incompatible with basic principles of quantum mechanics. Nonetheless, some extreme situations in nature, such as the big bang or black holes or neutron stars, can only be correctly described by a unified theory. In fact, this is a very active field in modern theoretical physics, where the two most prominent frameworks are string theory and quantum loop gravity.

Both General Relativity and the Standard Model are highly predictive. Amazingly, the two theories have survived all confrontations with precision measurements so far. Yet, there is one piece in the Standard Model that has eluded discovery. This missing piece is the Higgs boson, which is required in order to give mass to the electroweak gauge bosons and to the fundamental fermionic particles.

## 2.1 The Standard Model

The formulation of the Standard Model (SM) of particle physics represents one of the great achievements of the twentieth century. A complete description of the SM is far beyond the scope of this thesis. However, a few of the most salient features are summarised.

The SM describes all fundamental matter particles (fermions) and the electromagnetic, weak, and strong interactions involving the exchange of gauge bosons, using the QFT formalism. It thereby combines the two QFT descriptions of the electroweak and strong interactions. The former description already unifies the relativistic electromagnetic theory, called quantum electrodynamics (QED), with the theory for weak interactions, as initially proposed by Glashow, Weinberg, and Salam [3, 4, 5]. The theory of strong interactions is called quantum chromodynamics (QCD), with an allusion to the charge of the strong force, named *colour*.

The most common approach to formulate a QFT uses the Lagrangian ( $\mathcal{L}$ ), which is a (scalar) function that represents the dynamics of a given system. The equations of motion can then be derived using the least action principle. Feynman generalised the least action principle to the path integral formulation and the so-called Feynman diagrams [6, 7]. They provide a deep physical insight into the interactions of particles: particles interact in all possible (allowed) ways; the probability for each final state is the sum over all such possibilities. A Feynman diagram represents a class of particle paths, which join and split as described by the diagram.

Both the unified electroweak theory and QCD are formulated as Yang-Mills theories [8]. This means they are gauge QFTs based on certain symmetry groups. Astonishingly, symmetry gauging gives rise to the force fields in a natural way. In the simple example of classical electrodynamics, many electromagnetic potentials describe the same electromagnetic field. This freedom of choice is called *gauge invariance* because the physics observables are invariant in the chosen gauge (here the electromagnetic potential). The invariance is caused by a continuous symmetry, which always implies a conservation law (Noether's theorem [9]). The idea of (local) gauge invariance as a dynamical principle to construct interacting field theories was first elaborated by Weyl [10].

In QED for instance, the requirement of local gauge invariance under the  $U(1)_{\text{em}}$  symmetry group leads to the introduction of a new gauge field. This field transforms just as Maxwell's equations. Indeed, it describes the massless spin-1 photon field. In much the same way, local invariance requirements in the electroweak theory bring in the gauge bosons of the two forces: massive  $W^+$ ,  $W^-$ , and  $Z$  bosons which mediate the weak force, and the massless  $\gamma$  boson of electromagnetism. The underlying symmetry group of the electroweak theory is  $SU(2)_L \otimes U(1)_Y$ , representing the weak isospin or chiral symmetry (L) and the weak hypercharge (Y) symmetry. The two neutral gauge bosons  $B^0$ ,  $W^0$  of  $SU(2)_L \otimes U(1)_Y$  mix (described by the Weinberg angle) and thereby form the  $Z$  and  $\gamma$  bosons. Finally, the requirement of local gauge invariance in QCD results in the eight massless spin-1 gluons of the strong force. The gauge symmetry group of QCD is  $SU(3)_C$  and describes three colour degrees of freedom.

The combined  $SU(3)_C \otimes SU(2)_L \otimes U(1)_Y$  symmetry group, together with the dynamical symmetry gauging principle is often seen as the basis of the SM.

An important issue is related to the massive gauge bosons ( $W^\pm$  and  $Z$ ). The presence of any (fermionic or gauge) mass term violates the chiral symmetry  $SU(2)_L$ . A solution to this severe

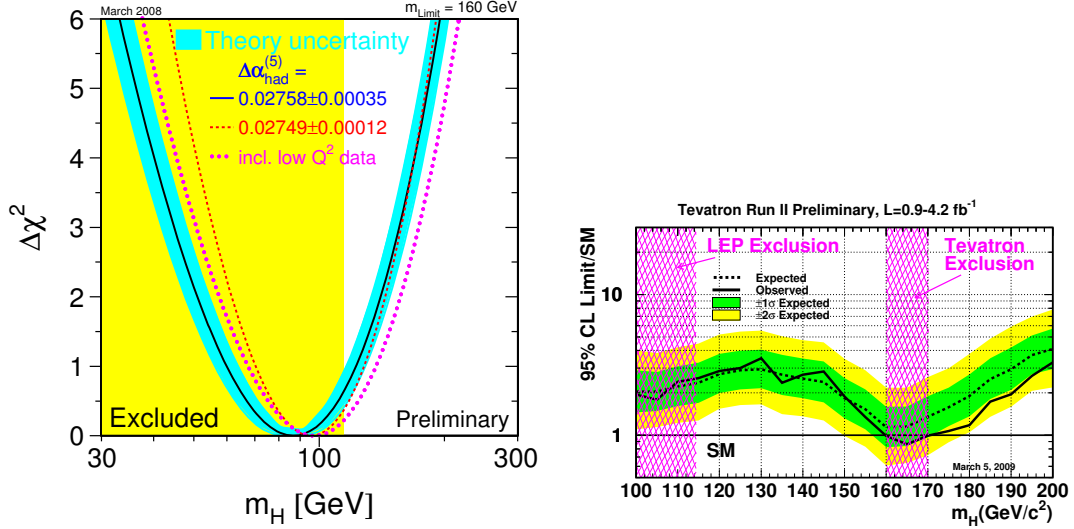


**Figure 2.1:** Global fit to electroweak precision data (left) [17], and Higgs boson mass exclusions from LEP and Tevatron (right) [16].

problem was suggested by Higgs [11, 12]: the gauge invariance could be *spontaneously broken* with the addition of (at least) one doublet  $\phi$  of complex scalar fields, with Lagrangian

$$\mathcal{L}_{\text{Higgs}} = (\partial^\mu \phi)^\dagger (\partial_\mu \phi) - V(\phi),$$

where the potential  $V(\phi) = \mu^2(\phi^\dagger \phi) + \lambda(\phi^\dagger \phi)^2$  is the key to spontaneous symmetry breaking.<sup>1</sup> This Higgs mechanism renders massive  $W^\pm$ ,  $Z$ , and fermions possible, while retaining a massless photon. Additionally, a massive Higgs boson ( $h$ ) is predicted, where the only free parameter is the Higgs mass. The Higgs boson is the only SM particle which has not yet been discovered. Further strong arguments for a scalar Higgs boson arise from the amplitude of (longitudinal)  $W^+ W^-$  scattering. If only the  $Z$  and  $\gamma$  bosons are exchanged, then the amplitude violates unitarity. The Higgs contributions, however, can cancel the divergence. Major searches for the Higgs boson have been conducted at the Large Electron-Positron Collider (LEP) at CERN and at the Tevatron collider at FNAC. The LEP lower limit for the Higgs boson mass is  $m_h > 114.4$  GeV [15], while the Tevatron has recently excluded a Higgs boson mass between 160 and 170 GeV [16], both at 95% confidence level. The exclusion results together with a global fit to precision electroweak measurements are shown in Fig. 2.1.

In the formulation of the SM, it is also noteworthy that the  $SU(2)$  and  $SU(3)$  symmetry groups are non-abelian. As an important consequence, the  $W^\pm$  and gluon gauge bosons carry weak and colour charge respectively. They can therefore self-couple, contributing to their self-energy and thus to the running of the coupling constants. This is one illustrative example of the deep relation between the underlying symmetries and the effective theory.

<sup>1</sup>Other physicists, Brout and Englert [13], as well as Guralnik *et al.* [14], had reached the same conclusion independently about the same time.

**Table 2.1:** Fundamental fermionic particles in the SM grouped according to family. No right-handed neutrinos are included. Braces indicate weak isospin doublets. The subscripts  $L$  and  $R$  denote the left and right handed components respectively.

Family		I	II	III
leptons	$L_{\text{lep}}$	$(e, \nu_e)_L$	$(\mu, \nu_\mu)_L$	$(\tau, \nu_\tau)_L$
	$R_{\text{lep}}$	$e_R$	$\mu_R$	$\tau_R$
quarks ( $\times 3$ colours)	$L_q$	$(u, d)_L$	$(c, s)_L$	$(t, b)_L$
	$R_q$	$u_R, d_R$	$c_R, s_R$	$t_R, b_R$

QCD enjoys two special properties:

- *Confinement*, which describes the rapid increase of the strong force when trying to separate two coloured particles (in contrast to all other forces which diminish with increasing distance) [18].
- *Asymptotic freedom*, which means that at very small distances (or equivalently very high-energy reactions) coloured particles interact very weakly [19, 20].

The very important consequences of QCD confinement and asymptotic freedom are: we can use perturbation theory for high-energy processes, but not in the low energy regime; coloured particles (gluons and quarks) will undergo so-called hadronisation, before we could possibly “observe” them. In the process of hadronisation, the coloured objects fragment (group themselves) into colour singlet (neutral) objects. The resulting colour singlet objects are hadrons and mesons. A collimated “jet” of such hadrons and mesons is what we detect experimentally, if the initial parton was generated with high momentum, i.e. it originates from a hard-scattering process.

The fundamental particles of the SM are fermions. There are three generations (or families) of coloured up- and down-type quarks, and three families of charged and neutral leptons. The quarks come in three colours, as described in the quark model developed by Gell-Mann [21]. Table 2.1 summarises the fermionic particles of the SM. The question why the fundamental fermionic particles come in three generations cannot be answered by the SM (already the discovery of the muon led to the famous quote by Rabi: “Who ordered that?”). Theorists hope to address this question with more fundamental theories (with extended symmetries).

The quark mass eigenstates as given in Table 2.1 are not the weak eigenstates. The latter are mixed states where a unitary  $3 \times 3$  matrix, called *Cabibbo-Kobayashi-Maskawa (CKM) matrix* [22, 23], governs the transformation. The implications of this quark mixing are very important for CP-violation, see for instance Ref. [24].

For completeness, the SM Lagrangian (before electroweak symmetry breaking and without Fadeev-

Popov ghost terms) reads [2]

$$\begin{aligned}
\mathcal{L}_{\text{SM}} = & \underbrace{-\frac{1}{4}W_a^{\mu\nu}W_{\mu\nu}^a - \frac{1}{4}B^{\mu\nu}B_{\mu\nu} - \frac{1}{4}G_a^{\mu\nu}G_{\mu\nu}^a}_{\text{kinetic energies and self-interactions of the gauge bosons}} \\
& + \underbrace{\bar{L}\gamma^\mu \left( i\partial_\mu - \frac{1}{2}g\tau_a W_\mu^a - \frac{1}{2}g'Y B_\mu \right) L + \bar{R}\gamma^\mu \left( i\partial_\mu - \frac{1}{2}g'Y B_\mu \right) R}_{\text{kinetic energies and electroweak interactions of the fermions}} \\
& + \underbrace{\left| \left( i\partial_\mu - \frac{1}{2}g\tau_a W_\mu^a - \frac{1}{2}g'Y B_\mu \right) \phi \right|^2 - \mu^2 \phi^\dagger \phi - \lambda(\phi^\dagger \phi)^2}_{\text{Higgs doublet field } \phi \text{ with electroweak couplings}} \\
& + \underbrace{g_s G_\mu^a \bar{q}_i \gamma^\mu \mathbf{T}_{ij}^a q_j}_{\text{quark gluon interactions}} + \underbrace{(M_1 \bar{L} \phi R + M_2 \bar{L} \phi_c R + h.c.)}_{\text{Yukawa fermion masses and Higgs couplings}},
\end{aligned}$$

where  $L$  denotes quark and lepton isospin doublets,  $R$  stands for isospin singlets (quark or lepton),  $q$  is a quark field,  $(W, B, G)$  and  $(g, g', g_s)$  are the three gauge fields and the three coupling constants of the (weak isospin, hypercharge, gluon) fields,  $\phi$  is the scalar Higgs field with  $\mu$  and  $\lambda$  describing its potential,  $(\tau, Y, \mathbf{T})$  are the symmetry group generators (in the same order as before), and  $M_1, M_2$  contain the Higgs-Yukawa couplings to the fermions.

In its simplest version, the SM requires a total of 19 a priori unknown parameters: 9 fermion masses (quarks and charged leptons), 4 quark-mixing matrix (CKM) quantities, 2 gauge boson masses (for example the  $Z$  and Higgs boson masses), 3 coupling constants, and 1 strong CP parameter.

## 2.2 Phenomenology

The SM theory completely describes the basic interactions of the known fundamental particles. In experimental particle physics, the quantities of interest are observables such as the cross section, or kinematic variables. At hadron colliders, the calculation of these observables, however, requires in addition to the theoretical framework two major phenomenological additions. This is because of the QCD confinement which causes perturbation theory to be inapplicable at low energies. The two additions are:

1. *Parton density functions* (PDFs) that describe (or parameterise) the probability of a given parton inside a proton, as a function of momentum transfer ( $Q^2$ ) and the Bjorken  $x$ .
2. *Fragmentation and Hadronisation* of the coloured particles. These non-perturbative processes are described by phenomenological shower models which have been tuned to agree with measured properties.

The SM augmented with PDFs and shower generators allows for example to predict the production cross sections as a function of centre-of-mass (CM) energy, as shown in Fig. 2.2 for various physics processes.

The total proton–proton (p–p) cross section at a CM energy of 14 TeV is predicted to be 102 mb [26]. This is split into elastic (23 mb) and inelastic (79 mb) parts.

The inelastic cross section is strongly dominated by QCD processes, while the expected Higgs cross section is many orders of magnitude smaller. Similarly (but not shown in Fig. 2.2), the possible production of new physics would proceed in most scenarios with very small cross sections compared to QCD processes or also with respect to electroweak  $W^\pm$ ,  $Z$  boson production.

Despite ever faster hardware and software, the rate with which events can be stored to disk is limited. In fact, the sustainable rate is many orders of magnitude below the total interaction rate.<sup>2</sup> A powerful on-line selection mechanism, called *trigger*, is therefore needed. One of the big challenges is to retain the rare physics processes of interest (such as the Higgs production), while rejecting nearly all events in real time. The trigger system of the ATLAS experiment is the subject of the first part of this thesis.

## 2.3 Beyond the Standard Model

The SM is a remarkably successful theory. With the addition of neutrino masses, it describes (almost) all presently known phenomena. No unambiguous experimental hints of beyond-SM physics have been found yet. Nevertheless, it seems evident that the SM will have to be extended to describe physics at higher energy scales. Certainly, a new model will be required at (or near) the energy scale where quantum gravitational effects become important. This energy scale is the so-called Planck scale  $M_P = \sqrt{\hbar c / G_{\text{Newton}}} = 1.22 \cdot 10^{19}$  GeV. Looking at nuclear and particle physics, we find phenomena everywhere in the range from a few meV (atomic binding energies) to a few hundred GeV (electroweak gauge bosons, top quark). Why should there not be new physics in the next 16 orders of magnitude in energy between the electroweak and Planck scale ? [27]

In addition to this “no physics desert” argument, there are several other reasons suggesting beyond-SM physics (maybe in the few TeV energy regime). Some of the apparent empirical and theoretical limitations of the SM can be summarised as:

- *Gauge hierarchy problem* describes the enormous quantum corrections which the squared bare Higgs mass receives from virtual effects of every particle that couples directly or indirectly to the Higgs field [28]:

$$m_H^2 = m_0^2 + \Delta m_H^2,$$

where

$$\Delta m_H^2 \propto \int_0^\infty d^4k \frac{k^2 + m_f^2}{(k^2 + m_f^2)^2} + \dots \propto \Lambda_{\text{UV}}^2 + \dots$$

---

<sup>2</sup>Anticipating some numbers of Chapter 3, the LHC total p–p interaction rate is expected to be approximately 1 GHz, while the ATLAS experiment can afford to store events at a continuous rate of  $\sim 200$  Hz.

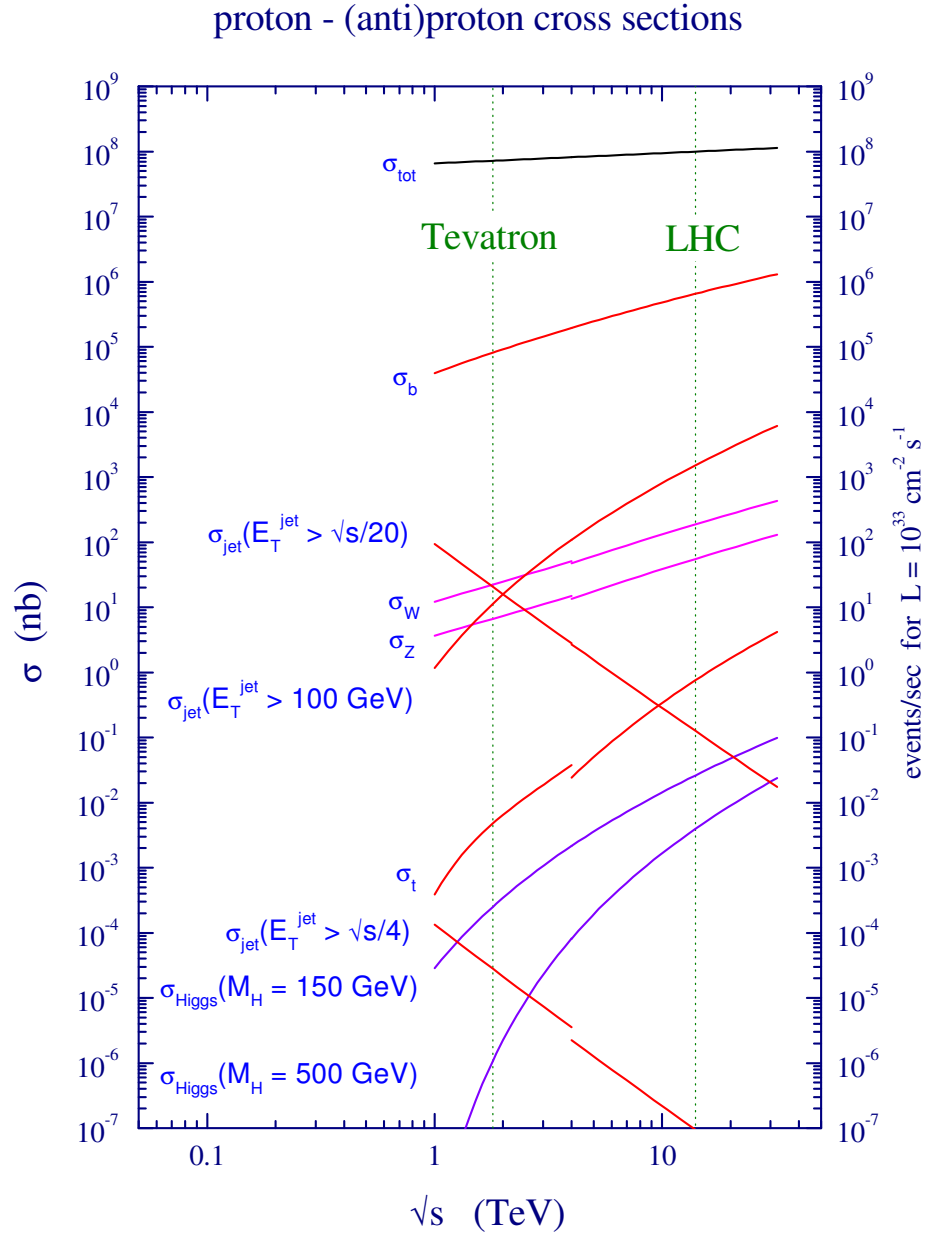


**Figure 2.2:** Expected production cross sections (at next-to-leading order) and event rates (for  $L = 10^{33} \text{ cm}^{-2} \text{ s}^{-1}$ ) for several SM physics processes at p-(anti)p colliders, as a function of the centre-of-mass energy [25]. For  $\sqrt{s} < 4 \text{ TeV}$   $p\text{-}\bar{p}$  collisions (as in the Tevatron) are considered. The discontinuity at  $\sqrt{s} \approx 4 \text{ TeV}$  indicates the position where a transition to p-p (as in the LHC) is made.



The integral is quadratically divergent, and the cut-off  $\Lambda_{UV}$  sets the scale for new physics. Each of the SM leptons and quarks can play the role of the fermion  $f$  above, while the largest contribution comes from the top quark. Typically, the cut-off  $\Lambda_{UV}$  is believed to be at the GUT scale ( $\sim 10^{16}$  GeV) or Planck scale ( $\sim 10^{19}$  GeV) with the immediate problem of the huge discrepancy to the Higgs mass scale, which requires what is known as *fine tuning* to keep a light and stable Higgs mass.

Theoretical bounds on the mass of the Higgs boson can be inferred from: unitarity (longitudinal  $W^+ W^-$  scattering)  $m_h \lesssim 780$  GeV [29]; as well as vacuum stability and triviality put lower and upper limits on  $m_h$  depending on  $\Lambda_{UV}$ , for example  $m_h < 180$  GeV if  $\Lambda_{UV} = 10^{19}$  GeV [30]. Additionally, the Higgs boson mass can be indirectly limited from a global electroweak fit, which strongly favours a light Higgs mass [17], cf. Fig. 2.1.

- *Grand unification* of the gauge couplings. As mentioned earlier, the electromagnetic and weak nuclear forces have been merged into the electroweak force, and the corresponding couplings unify at  $\sim 100$  GeV. Estimates of the three SM gauge couplings  $g$ ,  $g'$ , and  $g_s$  at very high energies (through the use of the renormalisation group equations (RGEs)) indicate that they almost, but not quite merge at about  $10^{15}$  GeV [31]. From a theoretical viewpoint, this is not appealing as it is contrary to the idea of a grand unified theory (GUT) with one all-embracing symmetry group (usually  $SU(5)$  or  $SO(10)$ ). This is mainly an aesthetic argument about the beauty (symmetry) of the theory, but it also concerns the (large) number of independent parameters in the SM.
- *Baryogenesis and leptogenesis* are the (hypothetical) processes that created the asymmetry between baryons and the asymmetry between leptons, respectively, in the early universe. As a result, we would obtain the observed dominance of matter over antimatter. Sakharov proposed three conditions that are necessary for the baryogenesis [32]: Baryon number violation, C- and CP-violation, as well as the departure from thermodynamic equilibrium. The first, and to a lesser extent the second condition are difficult to realise in the SM (with the required rates) and suggest beyond-SM physics [33].
- *Dark matter* (and maybe *dark energy*). Evidence for the existence of dark matter follows from many observations, the most popular being galaxy clusters with an excess of gravitational force [34], the rotational speed of spiral galaxies [35], and anisotropy measurements of the cosmic microwave background [36]. In the past, many dark matter candidates have been discussed, but most were discarded [37]. Black holes and brown dwarfs were examined, as well as neutrinos. However, all of them can — at most — only account for a small fraction of dark matter. The most likely scenario is that a new unknown fundamental particle is responsible for dark matter. Particles that would have been produced in the big bang and would have survived until today, generically called weakly interacting massive particles (WIMPs) are the most favoured type.

The gauge hierarchy problem can be seen as a disturbing sensitivity of the Higgs potential to new physics in almost any imaginable way, rather than a real problem of the SM itself. Possible solutions include [38]: new physics enters not much above the electroweak energy scale and regularises the quadratic divergences; the cut-off  $\Lambda_{UV}$  is much closer to the electroweak scale than we think (because of new physics that alter the gauge coupling running or because gravity is ac-



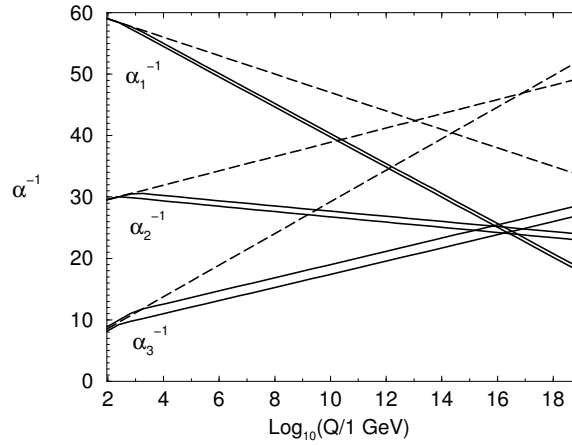


**Figure 2.3:** Extrapolation of the inverse gauge coupling constants  $\alpha^{-1}(Q)$  in the Standard Model (dashed lines) and in supersymmetry (solid lines), taken from Ref. [39]. The calculation is based on the renormalisation group equations, including two-loop corrections. The three gauge couplings correspond to the  $U(1)_Y \otimes SU(2)_L \otimes SU(3)_C$  symmetries:  $\alpha_1$  (electromagnetic/hypercharge),  $\alpha_2$  (weak),  $\alpha_3$  (strong).

tually stronger and only diluted in our 4 dimensions); the SM is simply fine tuned (cf. anthropic principle).

Supersymmetry is an attractive scenario for physics beyond the SM. It solves the hierarchy problem by a striking cancellation between the various contributions (regularisation by new physics). All fermion correction terms are accompanied by corresponding scalar terms (with opposite sign). Given that the SM fermion and supersymmetry scalar masses are different, the quadratic divergences are turned into logarithmic divergences [39]. In order not to enter too much the regime of fine tuning again, the supersymmetry masses should be less than a few TeV or so [40].

Furthermore, the lightest supersymmetric particle would in many supersymmetry models provide a suitable WIMP candidate for dark matter [41, 42]. In order to generate roughly the observed relic dark matter density, the mass of such a WIMP should not exceed  $\mathcal{O}(1 \text{ TeV})$  [43, 44].

Finally, the additional supersymmetric particles alter the RGEs in such a way that the three gauge couplings neatly merge at around  $10^{16} \text{ GeV}$ . Fig. 2.3 compares the SM (dashed lines) with the supersymmetry (solid lines) predictions for the running of the gauge couplings. The supersymmetry modifications to the RGEs are rather generic and parameter independent, as long as the new particles are not too heavy (below a few tens of TeV) [45].

The ATLAS and CMS experiments at LHC at CERN will hopefully find some of the anticipated new physics (not necessarily supersymmetry) in the TeV energy range!

Search strategies for various beyond-SM scenarios have been prepared and exercised at the LHC experiments. One inclusive supersymmetry search mode at the ATLAS experiment is presented in the second part of this thesis.



## **Part I**

# **The High-Level Trigger System of the ATLAS Detector**



## Chapter 3

# The ATLAS Detector at the LHC

The construction of the Large Hadron Collider (LHC) and its detectors has been completed and both machine and detectors are in the final phase of commissioning.

This chapter gives a brief overview of the LHC machine in Section 3.1. Described are the main machine parameters, the effects of minimum bias, pile-up, and the underlying event. Section 3.2 introduces the ATLAS detector, motivates the chosen detector design, and lists the key performance goals. Subsequently, all main ATLAS detectors/components are presented: the solenoid and toroidal magnet systems, the inner detector, the electromagnetic and hadronic calorimeters, the muon spectrometer, and the trigger and data acquisition system. Finally, Section 3.3 briefly summarises the ATLAS commissioning using cosmic ray data.

### 3.1 The Large Hadron Collider at CERN

The Large Hadron Collider (LHC) at CERN, Geneva, is the world's newest and most powerful particle collider. It is designed to provide proton–proton (p–p) collisions at a centre-of-mass energy of 14 TeV, a design luminosity of  $10^{34} \text{ cm}^{-2} \text{ s}^{-1}$  and a proton bunch-crossing rate of 40 MHz.<sup>1</sup> The LHC can also collide heavy ions (lead nuclei), with an energy of 2.8 TeV per nucleon at a peak luminosity of  $10^{27} \text{ cm}^{-2} \text{ s}^{-1}$ .

A comprehensive description of the technical design of the LHC machine can be found in Ref. [46], as well as in the Design Reports [47, 48, 49]. A brief overview is given in the following.

Four main detectors are situated at the interaction points (IPs) of the LHC:

- *ATLAS* (A Toroidal LHC Apparatus) is a general-purpose detector [50], see also Section 3.2;
- *CMS* (Compact Muon Solenoid) is a general-purpose detector [51];

---

<sup>1</sup>Due to the radio frequency accelerator mechanism, protons are grouped in several bunches inside the accelerator tunnel. Therefore, p–p collisions occur at discrete time intervals, rather than in a continuous manner.

- *LHCb* is a dedicated detector for precision measurements of CP violation and rare decays of B hadrons [52];
- *ALICE* (A Large Ion Collider Experiment) is a general-purpose, heavy-ion detector which focuses on QCD and the strong-interaction sector of the SM at very high energy densities [53].

Furthermore, the LHC accommodates the following experiments, located at some hundred meters distance to IPs:

- *LHCf* is an experiment dedicated to the measurement of neutral particles emitted in the very forward region of LHC collisions [54];
- *TOTEM* is an experiment to measure the total p–p cross section with a luminosity independent method and study elastic and diffractive scattering at the LHC [55].

The accelerator complex has been deployed making full use of existing civil engineering infrastructure at CERN, but modifications and additions were also needed. In order to save costs, the LHC ring has been installed in the 26.7 km long and 3.7 m wide (in the arcs) tunnel that was constructed earlier for the CERN Large Electron–Positron (LEP) machine. The tunnel comprises eight straight sections and eight arcs. It lies between 45 m and 170 m below the surface on a plane inclined at 1.4% sloping towards the Lake Léman. Underground and surface structures for the ATLAS and CMS detectors (at points 1 and 5 respectively) are new, while those for the ALICE and LHCb detectors (at points 2 and 8 respectively) were originally built for LEP. Figure 3.1 details the LEP and LHC underground structures, also indicating the positions of the four detectors.

The LHC machine is a two-ring-superconducting-hadron accelerator and collider. Its main technical design is driven by physics aims, namely the discovery of rare processes. The rate of generated physics processes is given by  $R = L\sigma$ , where  $L$  is the machine luminosity and  $\sigma$  is the cross section of the physics process under study. The luminosity depends only on machine parameters whereas the cross section is a pure physics quantity which generically increases with the collision energy. The study of rare processes, hence, requires high beam energies and high beam intensities. To bend the 7 TeV protons, the LHC accommodates 1232 superconducting dipole magnets that provide the required magnetic field strength of 8.33 T. The luminosity can be approximated by

$$L = \frac{N_B f_{rev} N_p^2}{4\pi\sigma_t^2}$$

where  $N_B$  denotes the number of bunches,  $f_{rev}$  is the revolution frequency,  $N_p$  is the number of particles per bunch, and  $\sigma_t$  is the transverse beam size at the IP. The high peak luminosity of  $10^{34} \text{ cm}^{-2} \text{ s}^{-1}$  is thus achieved by a large number of bunches ( $N_B = 2808$ ), a small bunch spacing ( $1/f_{rev} = 25 \text{ ns}$ ), a high number of protons per bunch ( $N_p = 1.15 \cdot 10^{11}$ ), and a good beam focus ( $\sigma_t = 16.7 \mu\text{m}$ ). Running at the design luminosity, LHC will provide an integrated luminosity of around  $100 \text{ fb}^{-1}$  per year.

The full crossing angle  $\theta_C$  at the IP reduces the luminosity by a geometric factor which reads

$$F \approx 1/\sqrt{1 + \left(\frac{\theta_C \sigma_z}{2\sigma_t}\right)^2}$$

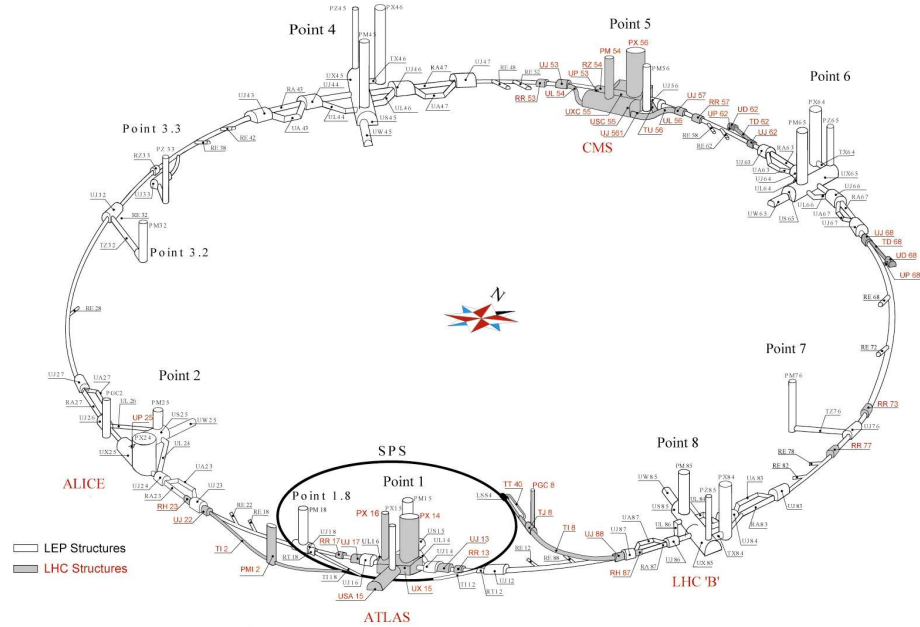


**Figure 3.1:** Civil engineering structure of the LHC tunnel, the access shafts, and underground structures housing the detectors [46]. New structures that were built for the LHC are represented in grey while re-used LEP structures are shown in white.

**Table 3.1:** Summary of the key LHC parameters [47]. Note that the parameters  $\theta_C$ ,  $\sigma_z$ ,  $\sigma_t$ ,  $F$ , and  $L$  are specific for the ATLAS/CMS interaction points.

Beam parameters	
Main collision type	proton–proton
Centre-of-mass energy	14 TeV
Bunch-crossing rate	40.08 MHz
Number of bunches ( $N_B$ )	2808
Number of particles per bunch ( $N_p$ )	$1.15 \cdot 10^{11}$
Stored energy per beam	362 MJ
Full crossing angle ( $\theta_C$ )	$285 \mu\text{rad}$
Luminosity related parameters	
RMS bunch length ( $\sigma_z$ )	7.55 cm
RMS beam size ( $\sigma_t$ )	$16.7 \mu\text{m}$
Geometric luminosity reduction factor ( $F$ )	0.836
Nominal peak luminosity $L$	$10^{34} \text{ cm}^{-2} \text{ s}^{-1}$
p–p collisions per bunch-crossing (at nominal peak luminosity)	$\mathcal{O}(20)$

where  $\sigma_z$  is the longitudinal beam size at the IP. Table 3.1 lists the key parameters of the LHC accelerator.

The LHC machine is supplied with protons or heavy ions from the existing accelerator complex at CERN. This comprises both linear and ring accelerators, which have all been upgraded to meet the demanding requirements of the LHC to provide a proton injection energy of 450 GeV.

### 3.1.1 Pile-Up

The total inelastic p–p cross section at the nominal LHC energy ( $\sqrt{s} = 14 \text{ TeV}$ ) is expected to be approximately 79 mb [26]. It includes contributions from single and double-diffractive scattering which are estimated to be 14 and 10 mb, respectively. The total inelastic cross section together with  $L = 10^{34} \text{ cm}^{-2} \text{ s}^{-1}$  yields a p–p interaction rate of nearly 1 GHz which translates to an average of 25 interactions per bunch-crossing [56]. The vast majority of these interactions, however, generate only little transverse momentum ( $p_T$ ) as they stem from long-range p–p interactions. The (experimental) definition of minimum-bias events depends on the experiment’s trigger. It is usually associated to non-single-diffractive events, given by  $\sigma_{\text{NSD}} = \sigma_{\text{inel.}} - \sigma_{\text{SD}} = 65 \text{ mb}$ . Minimum-bias events are dominated by the soft interactions mentioned above (due to their huge abundance) but hard interactions contribute as well.

The soft interactions, found in every event, can be seen as a superposed noise. Further, most detectors have readout latencies that exceed the small bunch spacing of 25 ns, thus detector signals can arise from previous bunch-crossings. Both effects together form what is called pile-up. It has had a strong impact on the technical design of all LHC detectors and also influences physics analyses.



### 3.1.2 Underlying Event

The underlying event is the “soft” part associated with a hard scattering. Unlike minimum-bias interactions, the underlying event arises from the same  $p$ - $p$  interaction as the hard scattering of interest. In the typical definition, the underlying event is everything except the two outgoing hard scattered jets. This includes: beam–beam remnants, additional (multiple) parton–parton interactions, as well as initial and final state radiation.

The underlying event has been studied and compared to MC simulation in detail at the Tevatron [57]. A study on predictions for minimum bias and the underlying event at the LHC can be found in Ref. [58].

## 3.2 The ATLAS Detector

ATLAS and CMS are two general-purpose detectors. Both have a detector design that was driven by the main physics goals: the search for the origin of electroweak symmetry breaking and the search for new physics beyond the SM. Yet the design chosen by the two detector collaborations differs strongly in dimensions, density and material of the hardware and electronics. In both cases the design was strongly influenced by the priorities set on the performance of the various sub-detectors.

In the following, the ATLAS detector is introduced and its main sub-detectors are briefly described. A comprehensive description can be found in Ref. [50] as well as in the Technical Design Reports (TDRs) for the overall technical design [59] and the expected performance [56]. Specific references describing the main components of the ATLAS detector are given in the corresponding sections.

As mentioned above, the main goals of the LHC physics programme are the search for the Higgs boson and searches for new physics phenomena. These benchmark physics studies together with the harsh conditions at the LHC set the requirements for the ATLAS performance. The detector challenges can be outlined as follows [59, 56]:

---

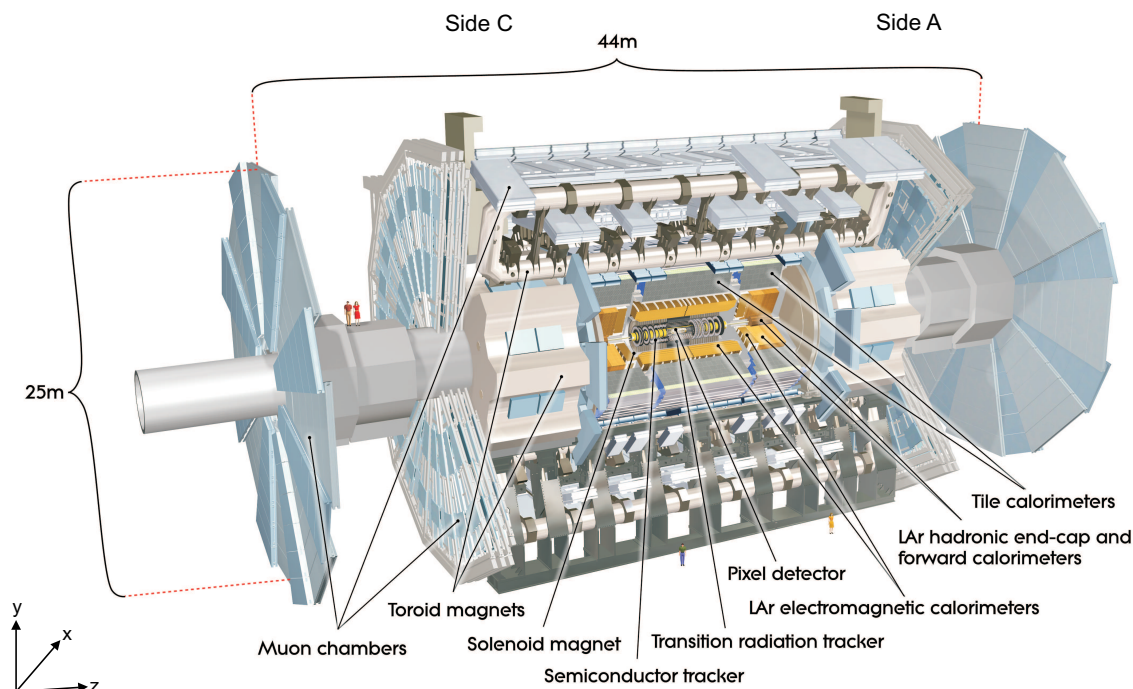


**Figure 3.2:** Cut-away view of the ATLAS detector [50]. The standard ATLAS Cartesian coordinates, and the detector sides A and C are indicated (side A is towards the Alps and side C towards Charlie’s (pub in St Genis)).

Experimental environment	Design challenges
Bunch-crossing rate of 40 MHz (25 ns = 7.5 m bunch spacing)	Fast trigger, precise timing, “pipeline” electronics: Trigger Level-1 latency is $< 2.5 \mu\text{s}$
$\sim 1 \text{ GHz}$ interaction rate at $L = 10^{34} \text{ cm}^{-2} \text{ s}^{-1}$ ( $\sim 25$ interactions per bunch crossing)	Efficient pattern recognition to reduce $\text{GHz} \rightarrow \text{trigger level-1} \rightarrow 75 \text{ kHz} \rightarrow$ high-level trigger $\rightarrow 200 \text{ Hz} \rightarrow \text{disk storage}$
$\sim 300 \text{ MB/s}$ data rate ( $200 \text{ Hz} \times \mathcal{O}(1.5 \text{ MB/event})$ )	Powerful data processing farms, distributed data analysis (computing grid)
Irradiation rate / 10 LHC years: $5 \times 10^{14} \text{ n}_{\text{eq}}/\text{cm}^2$	Radiation hard detector technologies and radiation tolerant electronics throughout the experiment
High charged multiplicities ( $\mathcal{O}(1000)$ tracks per event, $10^{10} / \text{sec}$ )	Highly granular pixel/silicon detectors
High background rates (beam halo muons, neutrons, beam-gas collisions)	Precise muon timing, redundant pattern recognition, radiation hardness

The overall ATLAS detector layout is shown in Fig. 3.2 and Table 3.2 summarises its key performance goals [50]. The detector dimensions are 25 m in diameter and 44 m in length. The total weight is approximately 7000 tonnes. In the following sections, the main detectors and components of the ATLAS experiment are introduced.

**Table 3.2:** Summary of the key ATLAS performance goals [50]. Note that for high- $p_T$  muons, the muon spectrometer performance is independent of the inner detector system. The units for  $E$  and  $p_T$  are in GeV.

Detector component	Required resolution	$\eta$ coverage	
		Measurement	Trigger
Tracking	$\sigma_{p_T}/p_T = 0.05\% \oplus 1\%$	$\pm 2.5$	
EM calorimeter	$\sigma_E/E = 10\%/\sqrt{E} \oplus 0.7\%$	$\pm 3.2$	$\pm 2.5$
Hadronic calorimeter (jets)			
barrel and end-cap	$\sigma_E/E = 50\%/\sqrt{E} \oplus 3\%$	$\pm 3.2$	$\pm 3.2$
forward	$\sigma_E/E = 100\%/\sqrt{E} \oplus 10\%$	$3.1 <  \eta  < 4.9$	$3.1 <  \eta  < 4.9$
Muon spectrometer	$\sigma_{p_T}/p_T = 10\%$ at $p_T = 1$ TeV	$\pm 2.7$	$\pm 2.4$

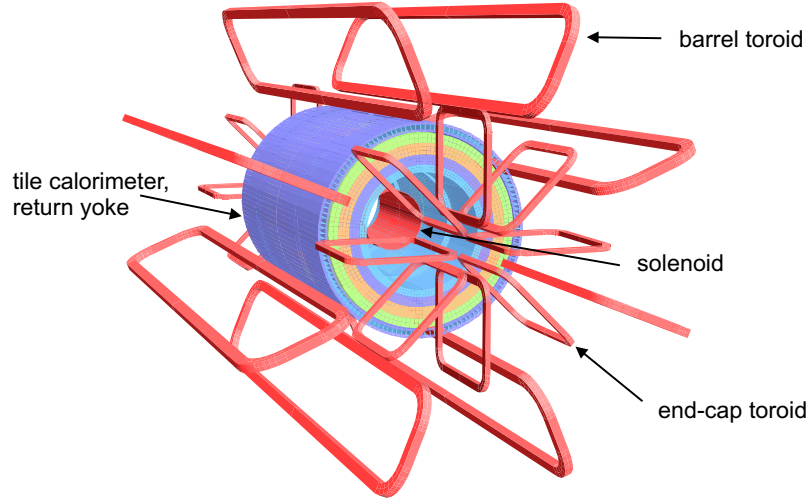


**Figure 3.3:** Arrangement of the ATLAS magnet windings and the tile calorimeter steel [50]. The solenoid windings are situated inside the calorimeter volume. The tile calorimeter is modelled by four layers with different magnetic properties, plus an outside return yoke.

### 3.2.1 Magnet System

The ATLAS magnet system, shown in Fig. 3.3, consists of three large air-core toroids (two end-caps and one barrel) as well as a solenoid. This composite system of four superconducting magnets has been one of ATLAS most challenging engineering accomplishments due to its unusual configuration and large size [60].

The central solenoid is designed to provide a 2 T axial magnetic field for the inner detector and is powered by an approximately 8 kA power supply [61]. The solenoid is located in the barrel cryostat between the electromagnetic calorimeter and the inner detector. To minimise the upstream material, which degrades the performance of the electromagnetic calorimeter, the layout has been carefully optimised. This requires, in particular, that the solenoid windings and the electromagnetic calorimeter share a common vacuum vessel. The magnetic flux is returned in the steel of

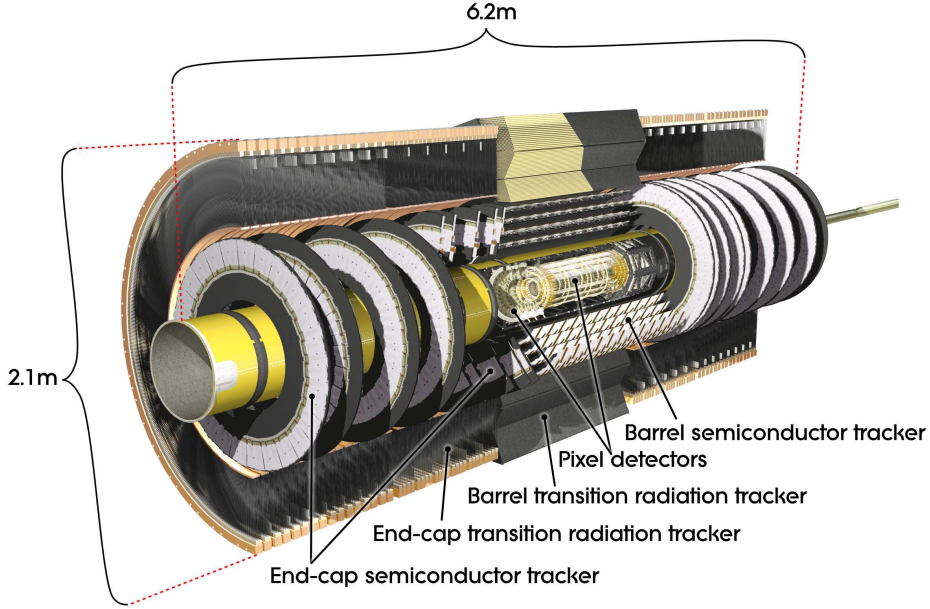


**Figure 3.4:** Cut-away view of the ATLAS inner detector [50].

the hadronic calorimeter and its support structure. The inner (outer) diameter of the solenoid is 2.46 m (2.56 m) and the axial length is 5.8 m. The coil weight is 5.4 tonnes and the stored energy is 40 MJ.

The barrel toroid and two end-cap toroids are designed to provide the magnetic field for the muon spectrometer. Each toroid consists of eight superconducting coils powered by a 20.5 kA power supply [62, 63]. The barrel toroid coils are housed in eight individual cryostats, while the end-cap coils are housed in one large cryostat (one such per side). The performance in terms of bending power  $\int Bdl$  is 1.5 to 5.5 Tm in the range  $|\eta| < 1.4$  (barrel toroid) and approximately 1 to 7.5 Tm in the region  $1.6 < |\eta| < 2.7$  (end-cap toroids). The bending power is lower in the transition region where the magnets overlap. The overall size of the barrel toroid system is 25.3 m in length and the inner and outer diameters are 9.4 m and 20.1 m. The total weight is 830 tonnes. The two end-cap toroids, each have a size of 5 m in length and an inner (outer) diameter of 1.65 m (10.7 m) and a total weight of 240 tonnes.

### 3.2.2 Inner Detector

The ATLAS inner detector (ID), shown in Fig. 3.4, is designed to provide hermetic and robust pattern recognition, excellent momentum resolution and both primary and secondary vertex measurements, for charged particles above a nominal  $p_T$  threshold of 0.5 GeV. Precision measurements are provided over a range of  $|\eta| < 2.5$  which is matched by the precision measurements of the electromagnetic calorimeter. The ID is immersed in the 2 T magnetic field generated by the central solenoid. It consists of a pixel detector, a semiconductor tracker (SCT), and a transition radiation tracker (TRT).

The high radiation environment of the LHC imposes strong requirements on ID sensors, on-

detector electronics, mechanical structure and services. Unlike most of the ATLAS experiment, which is designed for a lifetime of ten years, the innermost pixel layer (B-layer) has to be replaced after several years of operation at the nominal luminosity [50, 64].

A comprehensive description of the ATLAS ID can be found in Ref. [50], in the TDRs of the ID [65, 66] and pixel detector [67], as well as in Refs. [64, 68, 69]. A brief summary of the ID sub-detectors is given in the following.

The *pixel detector* measures charged particles using silicon sensors (pixels), which have a minimum size of  $50 \times 400 \mu\text{m}^2$ . In the barrel region, the pixels are arranged on three concentric cylinders around the beam axis ( $45.5 \text{ mm} < R < 242 \text{ mm}$ ), while in the end-cap regions they are located on five disks (on each side) perpendicular to the beam axis ( $88.8 \text{ mm} < R < 149.6 \text{ mm}$ ). Typically, three pixel layers are crossed by each track. The intrinsic accuracy is:  $10 \mu\text{m}$ ,  $115 \mu\text{m}$  in  $(R - \phi)$ ,  $z$  coordinates, respectively, in the barrel; and  $10 \mu\text{m}$ ,  $115 \mu\text{m}$  in  $(R - \phi)$ ,  $R$  coordinates, respectively, in the two disks. The pixel detector has a total number of approximately 80.4 million readout channels. The B-layer defines essentially the secondary vertex measurement accuracy since it permits measurements at the smallest radius of  $\sim 5 \text{ cm}$ .

The *SCT* is a silicon microstrip detector. Its geometry is similar to the pixel detector: Four cylindrical layers are located at  $299 \text{ mm} < R < 514 \text{ mm}$  and nine disks (on each side) at  $275 \text{ mm} < R < 560 \text{ mm}$ . Each track crosses eight SCT strip layers (four space points). In the barrel region, the SCT uses small-angle (40 mrad) stereo strips to measure both coordinates, with one set of strips in each layer parallel to the beam axis. They consist of 6.4 m long daisy-chained sensors with a strip pitch of  $80 \mu\text{m}$ . In the end-cap region, the detectors have a set of strips running radially and a set of stereo strips at an angle of 40 mrad. The mean pitch of the strips is also approximately  $80 \mu\text{m}$ . The intrinsic accuracy is:  $17 \mu\text{m}$ ,  $580 \mu\text{m}$  in  $(R - \phi)$ ,  $z$  coordinates, respectively, in the barrel; and  $17 \mu\text{m}$ ,  $580 \mu\text{m}$  in  $(R - \phi)$ ,  $R$  coordinates, respectively, in the disks. The total number of readout channels in the SCT is approximately 6.3 million.

The *TRT* consists of straw tubes, 4 mm in diameter, that cover a range up to  $|\eta| < 2$ . On average, 36 hits are provided by the TRT. It measures precisely only  $R - \phi$  coordinates with an intrinsic accuracy of  $130 \mu\text{m}$  per straw. In the barrel region, the 144 cm long straws are parallel to the beam axis. Their wires are divided into two halves at approximately  $\eta = 0$ . In the end-cap region, the 37 cm long straws are arranged radially in wheels. The total number of TRT readout channels is approximately 351 thousand. The TRT's capability to detect transition-radiation photons enhances the overall ATLAS electron identification performance.

The three independent sub-detectors of the ID are complementary: the combination of precision trackers at small radii together with the TRT at larger radius gives robust pattern recognition and high precision in both  $R - \phi$  and  $z$  coordinates. The TRT straw hits contribute significantly to the momentum measurement, since the lower precision per point is compensated by the larger number and longer measured track length.

### 3.2.3 Calorimetry

The ATLAS calorimeter system, shown in Fig. 3.5, covers a range of  $|\eta| < 4.9$  using different techniques suited to the widely varying requirements of the physics processes of interest and of



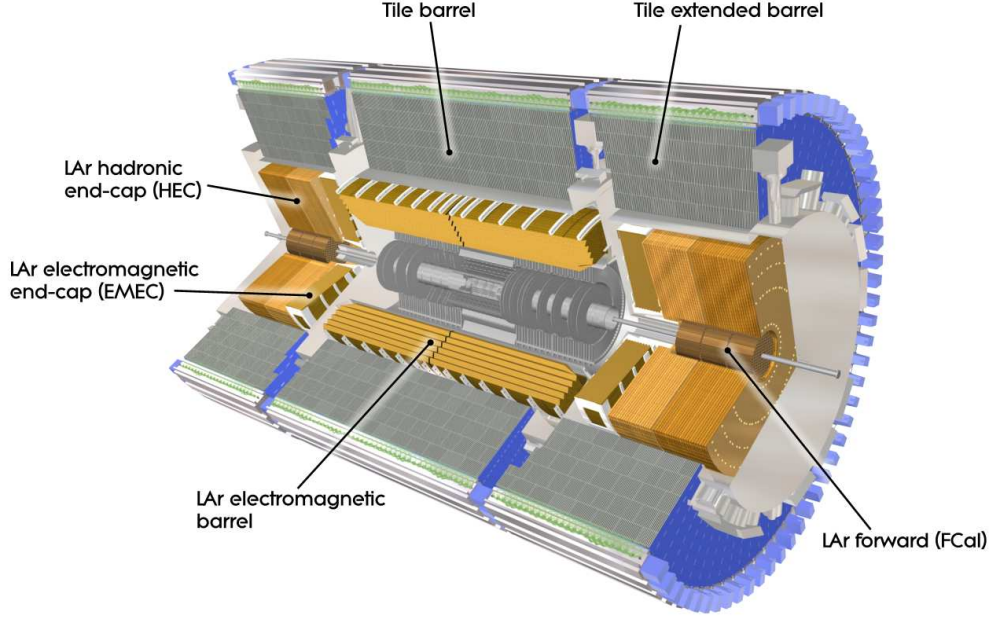


**Figure 3.5:** Cut-away view of the ATLAS calorimeter system [50].

the radiation environment over this large  $\eta$ -range. It accommodates an electromagnetic (EM) calorimeter, a hadronic calorimeter, and forward calorimeters (FCal).

A full description can be found in Ref. [50] and in the ATLAS calorimeter TDRs [70, 71, 72]. In the following, the sub-detectors are briefly described.

The *EM calorimeter* is composed of a barrel covering the region  $|\eta| < 1.475$  and two end-caps (EMEC) covering the region  $1.375 < |\eta| < 3.2$ . It is a liquid-argon (LAr) sampling detector with accordion-shaped kapton electrodes and lead absorber plates. The novel accordion geometry provides complete  $\phi$  symmetry without azimuthal cracks. The barrel and two EMECs are each housed in their own cryostat. The barrel is further divided into two identical half-barrels, separated by a small gap (4 mm) at  $z = 0$ . Each EMEC is mechanically divided into two coaxial wheels. The total thickness of the EM calorimeter in terms of radiation lengths ( $X_0$ ) is  $> 22$  in the barrel and  $> 24$  in the end-caps.

The segmentation of the EM calorimeter is as follows: For precision measurements within  $|\eta| < 2.5$ , matched to the ATLAS ID  $\eta$ -coverage, the EM calorimeter is segmented into three longitudinal sections with varying granularities depending on  $\eta$ . The middle section, for instance, consists of square towers of  $\Delta\eta \times \Delta\phi = 0.025 \times 0.025$  for  $|\eta| < 2.5$ , see Fig. 3.6. The EMEC inner wheel ( $|\eta| > 2.5$ ) is segmented into two longitudinal sections and has a coarser lateral granularity. A presampler detector (active LAr layer) is used to correct for energy losses due to up-stream material.<sup>2</sup> It covers the region  $|\eta| < 1.8$ .

In total there are more than 170 thousand readout channels in the EM calorimeter.

<sup>2</sup>There is approximately  $2 X_0$  ( $2.5 X_0$ ) material in front of the presampler (first layer) at  $\eta = 0$  [50].

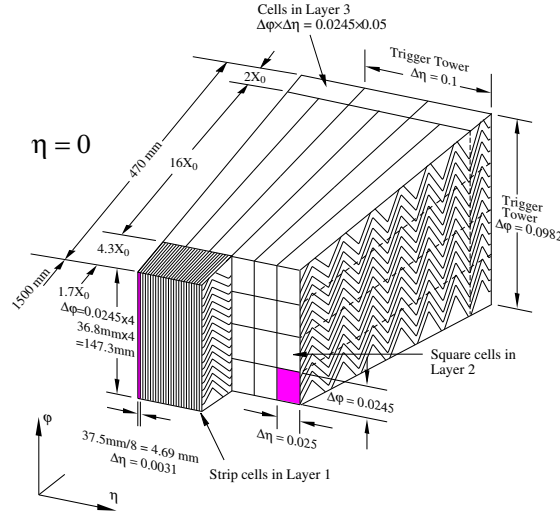


**Figure 3.6:** Sketch of an EM calorimeter barrel module. The granularity in eta and phi of the cells of each of the three layers and of the trigger towers is indicated.

The *hadronic calorimeter* consists of a barrel covering the region  $|\eta| < 1.0$ , two extended barrels covering the region  $0.8 < |\eta| < 1.7$ , and two hadronic end-caps (HEC) covering the region  $1.5 < |\eta| < 3.2$ . The barrel and extended barrels are sampling tile detectors, using steel as the absorber and scintillating tiles as the active material. They are hence named Tile barrel and Tile extended barrels. The HEC is a sampling LAr detector.

The Tile barrel and extended barrels are placed directly outside the EM calorimeter envelope. All Tile calorimeters are divided azimuthally into 64 modules and longitudinally into three layers, with approximately  $1.5$ ,  $4.1$ , and  $1.8$  interaction lengths ( $\lambda$ ) thick for the barrel and  $1.5$ ,  $2.6$ , and  $3.3 \lambda$  for the extended barrels. The scintillating tile is read out by wavelength shifting fibres into two separate photomultiplier tubes. The granularity is  $\Delta\eta \times \Delta\phi = 0.1 \times 0.1$  ( $0.2 \times 0.1$ ) for the barrel and extended barrels in the first two layers (last layer).

The HEC calorimeter consists of two independent wheels per end-cap, located directly behind the EMEC and sharing the same LAr cryostat. Each wheel is built from 32 identical wedge-shaped modules, and is divided into two longitudinal segments. The granularity is  $\Delta\eta \times \Delta\phi = 0.1 \times 0.1$  ( $0.2 \times 0.2$ ) in the region  $1.5 < |\eta| < 2.5$  ( $2.5 < |\eta| < 3.2$ ).

The FCal is a LAr copper or tungsten detector and is integrated into the end-cap cryostats. It is approximately  $10 \lambda$  deep, and consists of three modules in each end-cap: the first, made of copper, is optimised for EM measurements, while the other two, made of tungsten, measure predominantly the energy of hadronic interactions.

The ATLAS calorimeters, with  $22 - 24 X_0$  and about  $10 \lambda$  for the EM and hadronic detectors respectively, provide good containment for EM and hadronic showers<sup>3</sup>, as well as limited punch-through into the muon system. Including the  $1.3 \lambda$  from the outer support, the total thickness is approximately  $11 \lambda$  at  $\eta = 0$ . Together with the large  $\eta$ -coverage, this thickness ensures good missing energy measurements, which is important in particular for Supersymmetry searches.

<sup>3</sup>Important to provide good energy resolution, also for high-energy jets.

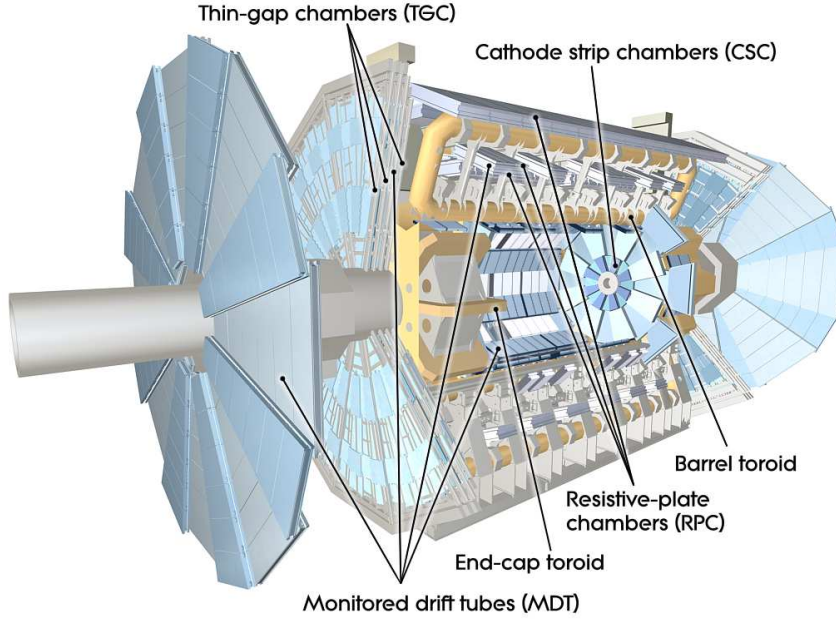


**Figure 3.7:** Cut-away view of the ATLAS muon spectrometer [50].

### 3.2.4 Muon Spectrometer

The ATLAS muon spectrometer, shown in Fig. 3.7, is designed to provide precision muon momentum measurements and a stand-alone trigger subsystem [73]. It is based on the magnetic deflection of muon tracks in the large superconducting air-core toroid magnets, instrumented with separate trigger and high-precision tracking chambers. In the barrel region, tracks are measured in chambers arranged in three cylindrical layers around the beam axis; in the end-cap regions, the chambers are installed in planes perpendicular to the beam, also in three layers.

In the region  $|\eta| < 2.7$ , a precision measurement of the track coordinates in the principal bending direction of the magnetic field is provided by the Monitored Drift Tubes (MDTs) and by Cathode Strip Chambers (CSCs). The latter are multiwire proportional chambers with cathodes segmented into strips. The stringent requirements on the relative alignment of the muon chambers are met by a combination of precision mechanical-assembly techniques and optical alignment systems.

The muon trigger subsystem consists of Resistive Plate Chambers (RPCs) in the barrel and Thin Gap Chambers (TGCs) in the end-cap regions. In addition to well-defined  $p_T$  thresholds, these trigger chambers provide bunch-crossing identification<sup>4</sup>, and measure the muon coordinate in the direction orthogonal to that determined by the precision-tracking chambers.

### 3.2.5 Trigger and Data Acquisition

The ATLAS trigger and data acquisition system (TDAQ), schematically shown in Fig. 3.8, is based on three distinct levels of on-line event selection: level-1 (LVL1), level-2 (LVL2), and event

<sup>4</sup>The timing of the trigger chambers must be better than the bunch spacing of 25 ns.



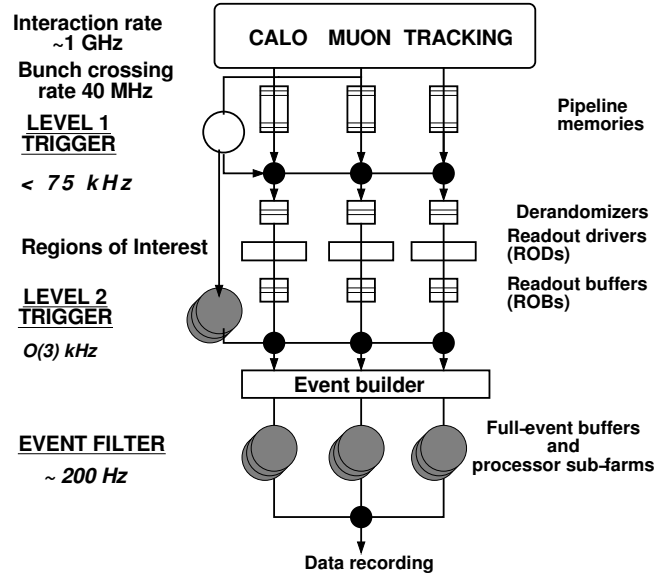


Figure 3.8: Schematic view of the ATLAS TDAQ system.

filter (EF) [74, 75]. LVL2 and EF together form the high-level trigger (HLT). Each trigger level refines the decision made at the previous level, and reduces the data rate gradually by adding additional selection criteria.<sup>5</sup> A detailed description of the ATLAS trigger system, with emphasis put on HLT, is given in Chapter 4. In the following, a brief overview is presented, also introducing the data acquisition system (DAQ).

The LVL1 trigger is based on custom-made electronics and is designed to search for high- $p_T$  muons, electrons, photons, jets, and  $\tau$ -leptons decaying into hadrons, as well as large missing and total transverse energy. Its selection is based on information from a subset of detectors: muons are identified using the muon trigger chambers (RPCs and TGCs), the remaining objects are identified using reduced-granularity information<sup>6</sup> from all the calorimeters. Note that the ATLAS ID is not used in the LVL1 trigger. The LVL1 decision is made in less than  $2.5 \mu\text{s}$ , reducing the rate to a maximum of 75 kHz.

Unlike the LVL1 trigger, HLT is a software based system running on computing farms. The LVL2 trigger refines the LVL1 trigger objects (muons, electrons etc.). The available detector data (including the ATLAS ID) is read out at full granularity and precision. However, only detector data around the given LVL1 trigger objects is actually read out, thus limiting the required data transfers to an average of approximately 2% of all available data.<sup>7</sup> The LVL2 trigger is designed to reduce the rate to an order of 3 kHz, with an event processing time of the order of 40 ms, averaged over all events.

<sup>5</sup>The ATLAS trigger system follows the early rejection approach: as soon as an event fails all trigger criteria of a given processing step/level, it is rejected and cannot be resurrected subsequently. Conversely, accepted events have passed through all processing steps. Since nearly all initial events must be rejected, this approach saves valuable processing time, see Chapter 4 for more details.

<sup>6</sup>The calorimeter is divided into relatively coarse trigger towers, cf. Fig. 3.6.

<sup>7</sup>The LVL1 trigger identifies regions of interest (ROIs) holding the LVL1 trigger object's  $\eta$ ,  $\phi$ , and type. These ROIs are propagated to LVL2. A more detailed description is given in Chapter 4.

The final trigger level, the EF, further reduces the trigger rate to approximately 200 Hz, with an average processing time of order of four seconds. Its selection mechanisms are derived from off-line analysis procedures. All detector data is available at full granularity and precision.

The DAQ controls all data movements down the trigger selection chain, see Fig. 3.8. It receives and buffers the event data from the detector-specific readout electronics after a LVL1 trigger accept. Subsequently, the requested event data fragments are transferred to the LVL2 trigger. In case of a LVL2 accept, all parts of the event data are assembled in the event builder nodes. The full event data are then moved by the DAQ to the EF trigger. In case of an EF accept, the full event data are moved to permanent storage.

In addition, the DAQ provides configuration, control, and monitoring of the TDAQ and ATLAS detector during data-taking. Supervision of the detector hardware (gas systems, power supply voltages, etc.) is provided separately by the detector control system [76].

### 3.3 ATLAS Detector Commissioning

The commissioning of the ATLAS detector started in 2005 together with the detector installation. After installation, the detector components were connected to the electronics readout channels and to the services (gas, cooling, etc.), and integrated into the ATLAS TDAQ system. All components were extensively tested, including test-beams, prior to the in-situ commissioning.

Some of the main aspects of the in-situ commissioning have been:

- test channel mapping and timing,
- spot hot and noisy cells/channels,
- verify hardware stability during operation,
- exercise the detector operation, global TDAQ, and off-line analysis chain,
- understand the detector performance, including alignment and calibration using cosmic rays.

The ATLAS detector was largely operational and ready for the LHC start-up, in September 2008. It had been collecting cosmic ray events in combined mode and was kept fully operational since end of August 2008. The official LHC start-up was September 10th 2008. Protons were injected into the LHC from the pre-accelerator complex, at an energy of 450 GeV. The LHC machine was operated with a single proton beam, both directions were operated successively, with and without RF capturing. Furthermore, collimators  $\pm 140$  m away from the detectors were used to stop the beam and thus generate “splash events”.

ATLAS recorded about 70 of a total of 100 generated “splash events”, see Fig. 3.9 for the first beam event seen by ATLAS. These spectacular events have been used: for initial timing adjustments of detector components (including the trigger) with respect to the bunch crossing signal; and to correlate the position and energy response of various detector systems.

---

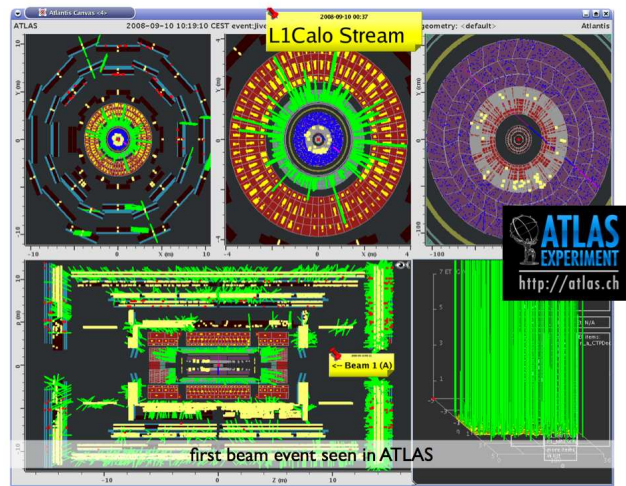


**Figure 3.9:** First collimator “splash event” seen by ATLAS. The collimator position is 140 m in front of the ATLAS interaction point.

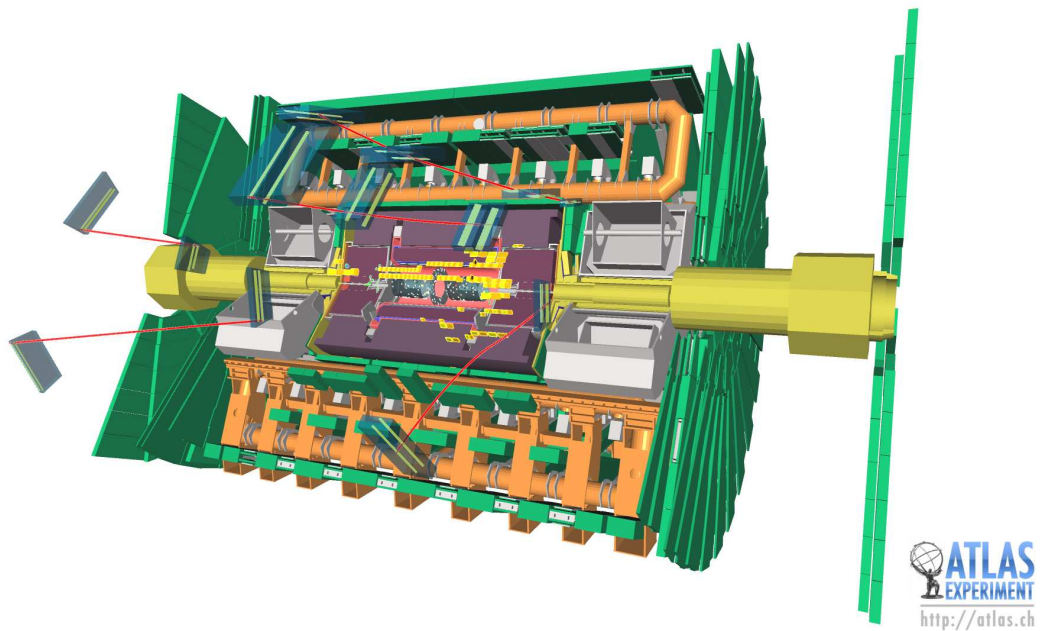


**Figure 3.10:** Beam-halo event from single LHC beam operation on 10th September 2008.



**Figure 3.11:** Oscilloscope traces of discriminated beam pick-up (BPTX) signal (C1, yellow) and minimum bias trigger scintillator (MBTS) analogue signals (C2, C3, C4) during an injection of 1 bunch without RF capture. The bunch manages to circulate a few times. After 7 turns its intensity falls below the threshold of the BPTX discriminator.

The single beam runs (with the collimators off) have also been used to record “beam-halo events”, see Fig. 3.10, which originate from protons leaving the beam pipe and creating secondary muons. The beam pick-up signal along with the minimum bias trigger of a single proton beam without RF capturing is shown in Fig. 3.11.

Due to an LHC incident on September 19th [77] further beam commissioning has been stopped (expected to resume around winter 2009). The full ATLAS detector performed a large campaign to collect cosmic ray events until the end of October 2008. More than 200 million events were recorded with various magnet and detector configurations, as shown in Fig. 3.12. Profiting from the LVL2 tracking algorithms (described in Section 4.10), approximately 100 thousand muons were recorded going through the pixel detector, which has the smallest effective area for cosmic rays. The cosmic events are very important for improving data quality and monitoring procedures, as well as for initial detector alignment and calibration. Fig. 3.13 shows ATLAS event displays of a few cosmic ray tracks observed in the ATLAS inner detector.

Preliminary results of the inner detector alignment with cosmic ray tracks are shown in Fig. 3.14 for the pixel barrel (the end-caps have limited statistics). The achieved precision is indicated by the track residuals. It can be seen that after the detector alignment, the residuals are greatly improved and not too far from those which are expected from a perfect Monte Carlo geometry. Similarly, the SCT and TRT barrels were aligned using cosmic tracks. The overall scale and ultimate precision of the inner detector poses a challenging problem in terms of understanding the detector. The track-based alignment using cosmic rays has been successfully tested and will continue to provide a good starting point for the whole alignment process.

The alignment of the muon spectrometer with cosmic tracks is shown in Fig. 3.15. Neglecting multiple scattering, the straight tracks from cosmic rays result in a sagitta centred around zero, if the toroidal field is switched off. This is exploited for the geometrical alignment. The three plots show the improvements obtained from the optical and the track-based alignment.

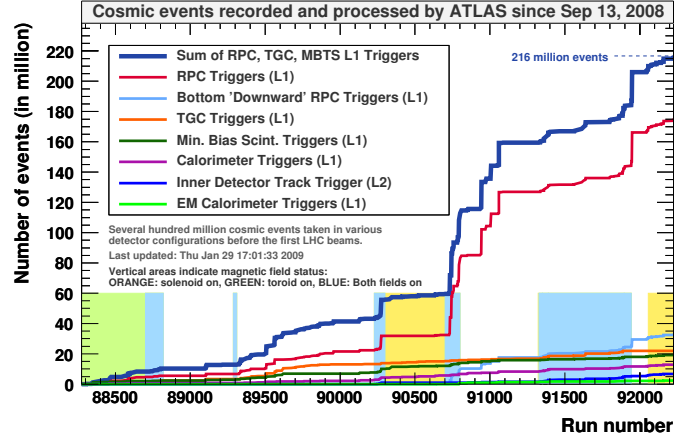


**Figure 3.12:** Integrated cosmic data rate for ATLAS versus the run number (after the single-beam runs). For most of the runs the full ATLAS detector was operational. In some high-rate runs, the LAr calorimeter was taken out, allowing trigger accept rates of approximately 500 Hz. The magnetic field status is indicated by vertical areas as follows. Yellow colour: only solenoid on, green colour: only toroid on (including barrel and end-caps), blue colour: all magnet systems on.

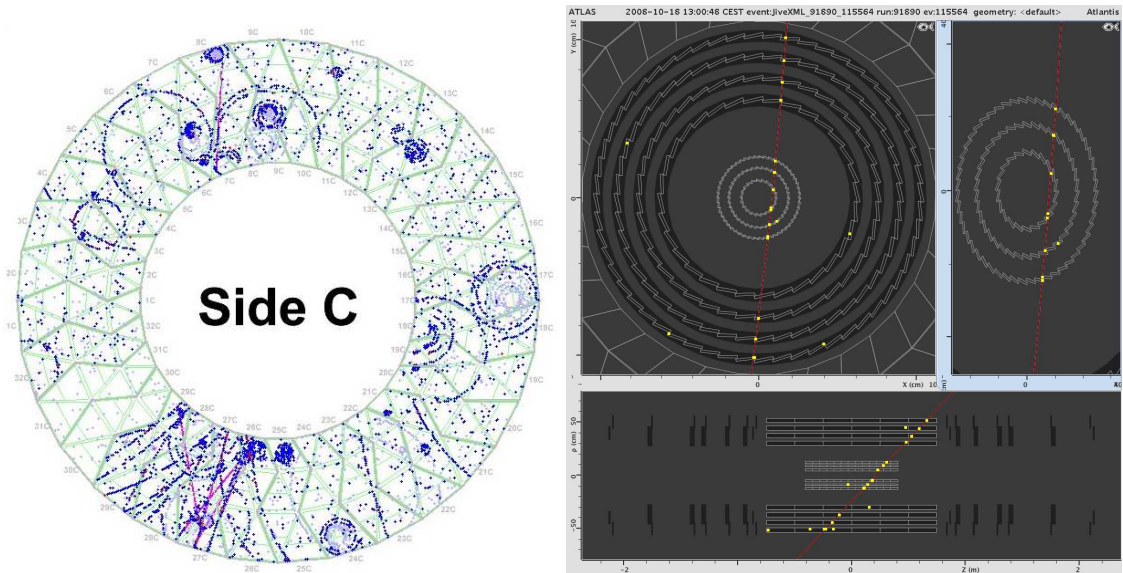


**Figure 3.13:** Left: one of the first events with cosmic tracks observed in the ATLAS TRT barrel, with the solenoid switched on. Right: cosmic ray event going through the pixel and SCT detectors.



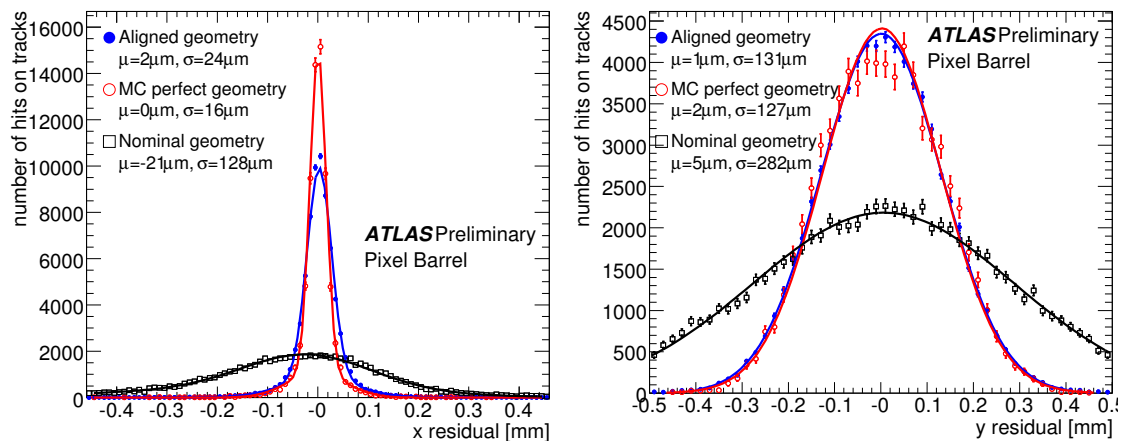


**Figure 3.14:** Residual distribution in  $x$  (left) and  $y$  (right), integrated over all hits-on-tracks in the pixel barrel for the nominal geometry and the preliminary aligned geometry. The residual is defined as the measured hit position minus the expected hit position from the track extrapolation. Shown is the projection onto the local  $x$  ( $y$ ) coordinate, which is the precision (non-precision) coordinate.

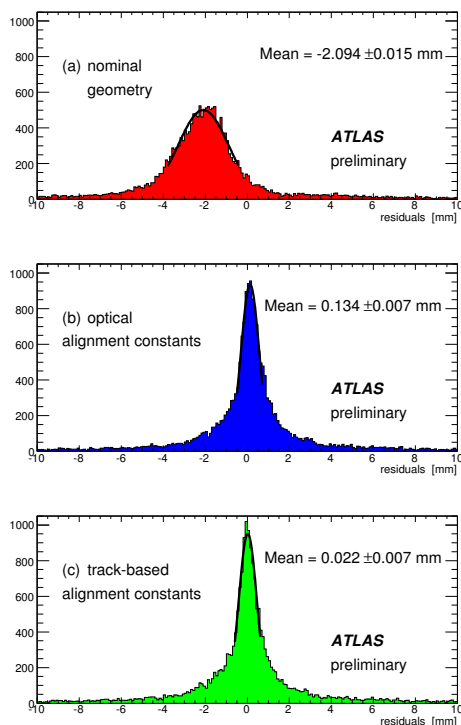


**Figure 3.15:** Measured muon track sagitta, in the precision plane, for cosmic ray data taken without magnetic field in the middle barrel of the muon spectrometer. The three plots show the sagitta distribution for three different geometries: (top) as obtained from the nominal geometry, (middle) using the optical alignment system based geometry, (bottom) after alignment with straight tracks.

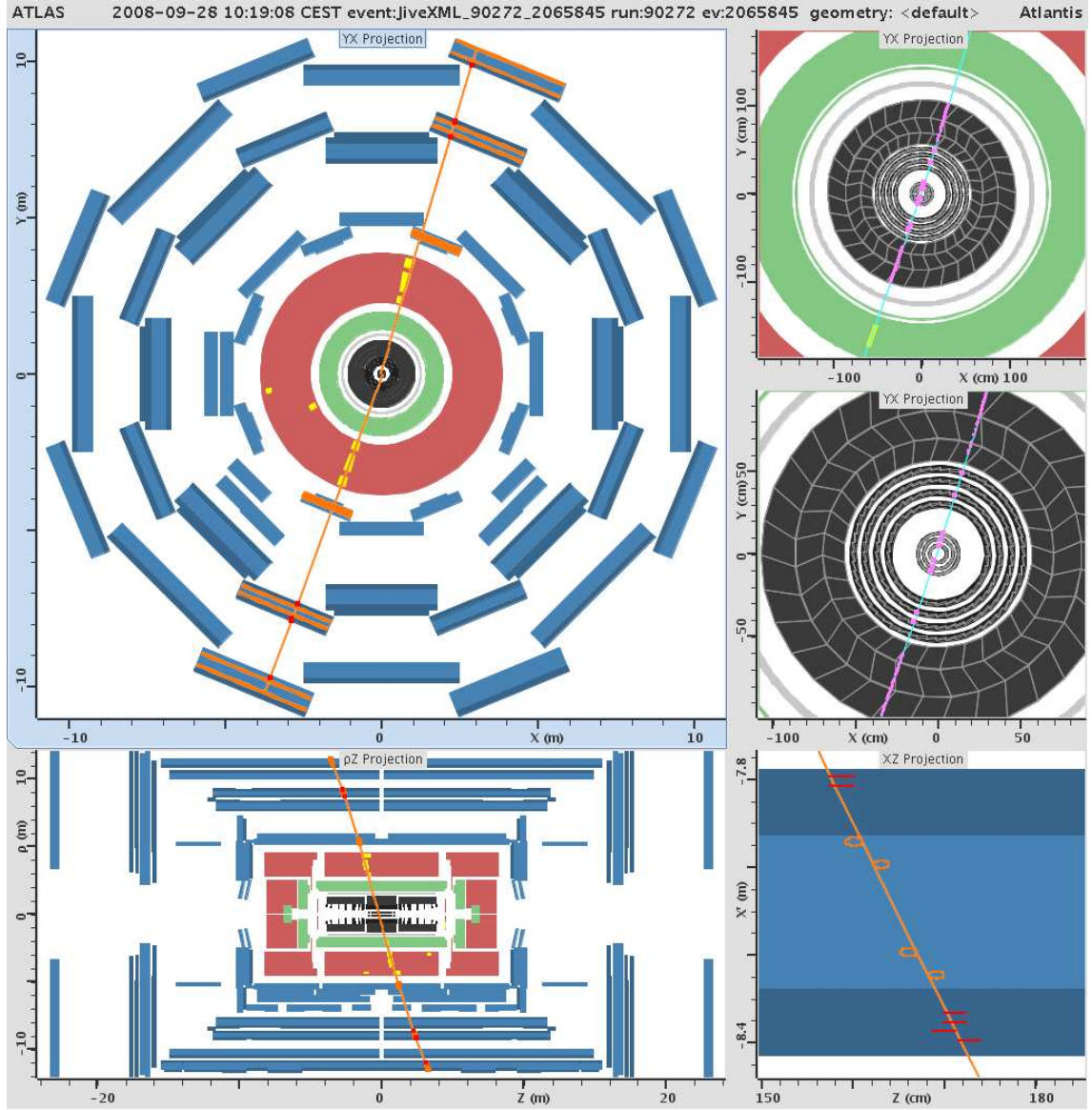


**Figure 3.16:** ATLAS event display of a cosmic ray with hits in all barrel detectors. Both solenoid and toroid magnets were on during this run. Muon station hits and energy deposits in the hadronic calorimeter can be seen in the top/left ( $x,y$  projection) and bottom/left ( $R,z$  projection) displays; inner detector hits (pixel, SCT, and TRT) are indicated in the middle/right ( $x,y$  projection) and together with the EM calorimeter in the top/right ( $x,y$  projection) display. The bottom/right display shows a  $x,z$  projection of the event.

Further cosmic ray measurements that have been performed and compared to special cosmic Monte Carlo simulation include: electronic noise, signal shape, energy response (linearity), energy loss ( $dE/dx$ ), resolution, as well as correlations between various detector components.

Fig. 3.16 shows an ATLAS event display of a cosmic ray interacting with the muon stations, calorimeters, and the inner detector.

The preliminary schedule is to re-start combined ATLAS operation in cosmic ray mode between June and July 2009, and commence the continuous running mode one month before the LHC start-up (expected in winter 2009). More detailed information on the ATLAS commissioning status can be found in Ref. [78, 79].



## Chapter 4

# Development of the High-Level Trigger Steering

The high-level trigger (HLT) of the ATLAS experiment at the Large Hadron Collider receives events which pass the LVL1 trigger at a maximum rate of 75 kHz and has to reduce the rate to  $\sim 200$  Hz while retaining the most interesting physics. It is a software trigger and performs the reduction in two stages: the LVL2 trigger and the event filter (EF). At the heart of the HLT is the Steering software. The Steering controls the flow and execution of the physics selection algorithms, depending on the configured triggers, and in such a way that the execution time is kept minimal. Ultimately, it must decide whether or not the event has fulfilled the criteria for acceptance. This chapter is dedicated to the detailed description of the HLT Steering. The author contributed significantly to its design and implementation.

This chapter is organised as follows. Section 4.1 expands on the brief introductory ATLAS trigger description, which was given in Section 3.2.5. All three trigger levels and the data acquisition are discussed. The basic design, trigger parameters relevant for physics analyses, and important concepts and interfaces for the HLT Steering are described.

The subsequent Sections 4.2–4.3 present details of the final HLT Steering design and its implementation, the principles behind it, and the requirements and constraints it is subject to. In Section 4.4 the design of the trigger configuration and menu is described. The HLT algorithm interface is introduced in Section 4.5. Supported algorithm types are compared and the built-in caching mechanism is explained.

The trigger data management and inter-algorithm communication is discussed in Section 4.6, and the HLT Steering execution logic along with error handling, result building, and streaming tags is described in Section 4.7.

Section 4.8 describes the important Steering logic to pre-scale or conversely unconditionally accept (pass-through) a trigger. The HLT monitoring is introduced in Section 4.9. Sample plots are given for simulated as well as cosmic data. Finally, Section 4.10 summarises the experience gained from technical and cosmic runs with commissioning trigger menus. The system performance is shown to meet the requirements, the mechanism of pre-scales and pass-throughs is validated, and

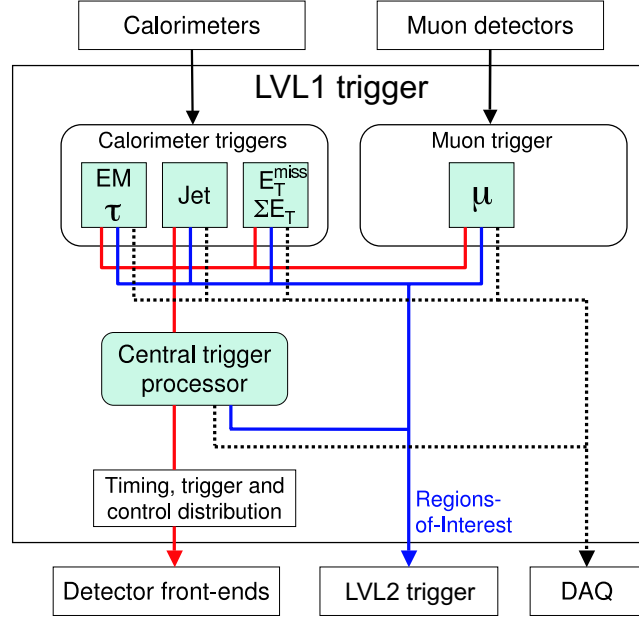


**Figure 4.1:** Block diagram of the LVL1 trigger. The overall LVL1 accept decision is made by the central trigger processor, taking input from calorimeter and muon trigger results. The paths to the detector front-ends, LVL2 trigger, and data acquisition system are shown in red, blue and black/dashed, respectively.

the first HLT on-line event selection of muon tracks reconstructed in the inner detector is presented.

## 4.1 ATLAS Trigger and Data Acquisition System

The trigger and data acquisition (TDAQ) system must work in the challenging environment of  $\sim 10^9$  p-p interactions per second and the large number ( $\sim 10^8$ ) of electronics channels of the ATLAS detector. The resulting total data rate of approximately  $1 \text{ GHz} \times 1.5 \text{ MB} \simeq 1.5 \text{ PB/s}$  must be reduced to the approximately 300 MB/s which can be sustained to mass storage, while efficiently retaining rare physics signatures for off-line analysis. To achieve this, ATLAS has designed a three-level trigger system (see Fig. 3.8 in Section 3.2.5) [74, 75].

### 4.1.1 LVL1 Trigger

The first level trigger (LVL1) is implemented in custom electronics (mainly ASICs and FPGAs).<sup>1</sup> Its decision is based on relatively coarse data from two subsystems, the calorimeters and dedicated muon trigger stations, see Fig. 4.1. Note that no tracking information from the inner detector is available at LVL1.

Both subsystems search for inclusive high- $E_T$  objects (muons, electromagnetic/tau/hadronic clusters, jet clusters, missing and scalar transverse energy sums) with programmable trigger thresholds.

<sup>1</sup>ASIC and FPGA stand for application-specific integrated circuit and field-programmable gate array.

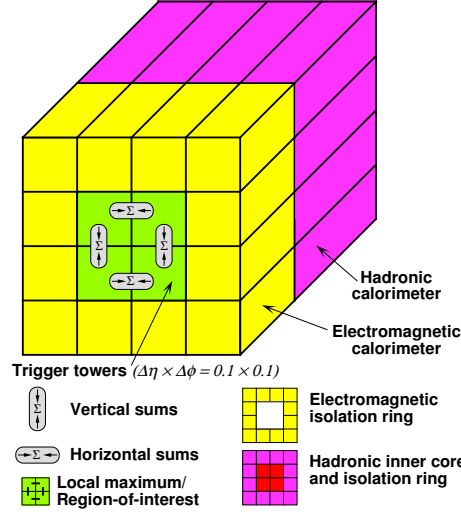


**Figure 4.2:** Schematic view of the LVL1 electron/photon and tau trigger algorithms.

Threshold multiplicities (mostly 3-bit) of detected high- $E_T$  objects are reported to the central trigger processor (CTP). The LVL1 decision (accept or reject) is made by the CTP which compares the threshold multiplicities to a configurable trigger selection table, or “trigger menu”. It is not based on the object’s geometrical information ( $\eta$  and  $\phi$ ). For accepted events, this geometrical information is sent to the second level trigger (LVL2). Together with the passed trigger thresholds, the  $\eta$  and  $\phi$  information form a so-called Region of Interest (ROI). The full set of ROIs seeds event selection in LVL2: objects are reconstructed around the ROIs.

During the LVL1 latency of  $2.5 \mu\text{s}$  the data of all sub-detectors are kept in pipeline memories. For accepted events, the data are then transferred from the pipeline memories to the readout buffers (ROBs). LVL1 reduces the event rate from the initial 40 MHz to a maximum of 75 kHz.

The LVL1 system also provides the important functionality of bunch-crossing identification: each trigger signal has to be correctly mapped to one bunch-crossing. The pure dimensions of the muon spectrometer makes this a challenging task, while for the calorimeters, the long signal width complicates the identification.

### Calorimeter Triggers

The LVL1 calorimeter triggers [80] obtain information from all the calorimeters: EM and hadronic in the barrel, end-cap, and forward regions. The granularity, however, is reduced by the use of trigger towers which merge several calorimeter cells yielding  $0.1 \times 0.1$  in  $\Delta\eta \times \Delta\phi$  (in most parts, but larger at higher  $|\eta|$ ) separately for the EM and hadronic calorimeters.<sup>2</sup>

Within the calorimeter triggers, the cluster processor aims at identifying high- $E_T$  electrons/photons and  $\tau$ -leptons. The algorithm searches for electrons/photons ( $\tau$ -leptons) in  $2 \times 2$  EM (combined EM and hadronic) trigger tower clusters in which at least one out of the four possible two-tower sums exceeds a pre-defined threshold. In addition, isolation thresholds are programmed for the

<sup>2</sup>Fig. 3.6 shows a trigger tower in the EM barrel.

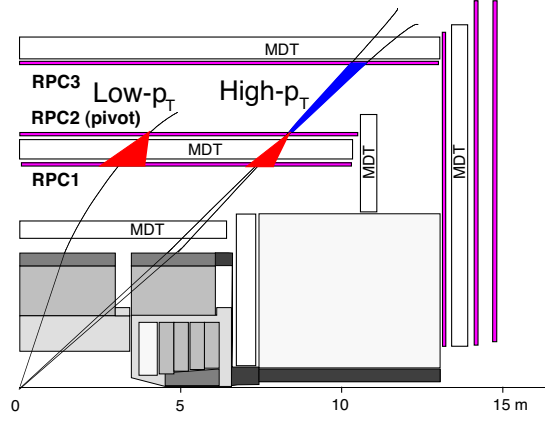


**Figure 4.3:** Schematic view of the LVL1 muon barrel trigger. Also shown are the low- $p_T$  (red) and high- $p_T$  (blue) roads.

twelve-tower ring in the EM calorimeter, as well as for the  $2 \times 2$  hadronic-tower core sum behind the cluster (not for  $\tau$ -leptons) and the twelve-tower hadronic ring around it. Fig. 4.2 depicts the LVL1 EM and tau trigger towers. Also shown are the EM and hadronic isolation rings. The electron/photon and  $\tau$  triggers extend to  $|\eta| < 2.5$ . In total eight threshold sets (cluster threshold plus isolation criteria) can be set for the electron/photon triggers and another eight are shared with the  $\tau$  triggers.

The jet/energy processor identifies jets and also produces energy sums ( $E_T$ ,  $E_x$ ,  $E_y$ ) on the basis of  $2 \times 2$  combined (EM and hadronic) trigger towers. In total eight threshold sets, which consist of the minimum  $E_T$  and the window size ( $0.4 \times 0.4$ ,  $0.6 \times 0.6$ ,  $0.8 \times 0.8$ ), are available for the jets as well as four and eight threshold sets for the total- $E_T$  (scalar sum) and  $E_T^{\text{miss}}$  (vector sum from  $E_x$ ,  $E_y$ ), respectively. The scalar and vector energy sums are obtained using all (coarsely granulated) trigger towers, including those from the forward calorimeters. Finally, four threshold sets can be set for an approximative total- $E_T$  in jets, based on the number of jets passing each of the eight jet thresholds. Jet triggers cover up to  $|\eta| < 3.2$ , while the total- $E_T$  and  $E_T^{\text{miss}}$  triggers extend to  $|\eta| < 4.9$ .

ROIs of the calorimeter triggers are positioned at the (trigger tower) window's centre. Passed thresholds are flagged in all ROIs. In addition, for the energy sum ROIs, values of  $E_x$  and  $E_y$  are provided.

### Muon Triggers

The LVL1 muon triggers [81, 82] are based on signals from the muon chambers, RPCs in the barrel and TGCs in the end-caps (see Fig. 3.7 in Section 3.2.4). Both chambers provide a sufficiently good timing resolution for bunch-crossing identification. A successful muon is a coincidence of two (low  $p_T$ ) or three (high- $p_T$ ) muon station hits within a road to the interaction point, as shown in Fig. 4.3. The road's width is given by the pre-defined  $p_T$ -threshold. The logic provides six programmable  $p_T$ -thresholds and the triggers cover a range of up to  $|\eta| < 2.4$ .

Muon ROIs have a granularity of about  $0.1 \times 0.1$  in  $\Delta\eta \times \Delta\phi$  in the barrel. Unlike calorimeter

ROIs, that flag every passed threshold, only the highest passed  $p_T$ -threshold is flagged for muons. This is possible because no additional isolation criteria are used in the muon triggers.

### Central Trigger Processor

The overall LVL1 decision (accept or reject) is made by the central trigger processor (CTP) [83]. It receives trigger information from the calorimeter and muon triggers: all threshold multiplicities ( $\eta$  and  $\phi$  are ignored) of the electrons/photons,  $\tau$ -leptons, jets, and muons; as well as flags indicating which thresholds were passed for total and missing transverse energy, and for total jet transverse energy. Additional input comes from special triggers: filled-bunch triggers based on beam-pickup monitors, and minimum bias triggers based on scintillation counters. All CTP input flags are compared to a programmable LVL1 trigger menu which consists of trigger conditions and trigger items:

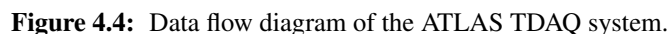
- A *trigger condition* sets a multiplicity requirement for a given threshold (e.g. multiplicity for a muon threshold ' $p_T > 15 \text{ GeV}$ '  $> 1$ ). Further trigger conditions are derived from CTP internally generated signals: two random triggers, two pre-scaled clocks, and eight triggers for bunch-crossing groups. The maximum number of programmable trigger conditions is 256.
- *Trigger items* are formed from a logical combination of the trigger conditions. Every trigger condition may contribute to every trigger item. Each trigger item also has a mask/veto, a priority (CTP dead time), and a pre-scaling factor. In total 256 distinct trigger items can be set. The overall LVL1 decision is the logical OR combination of all trigger items.

A LVL1 accept is propagated, together with the 40.08 MHz LHC clock and some other signals, to the detector front-end and readout systems. The geometrical information (ROI) of the trigger objects is retained in the LVL1 subsystems. Upon a LVL1 accept, the ROI is sent together with the corresponding passed thresholds to LVL2 where it seeds the HLT selection process. Furthermore, the full 256 trigger item acceptance bitmap is sent to LVL2 and the data acquisition. It comprises the raw trigger decision, the decision after veto, and after veto and pre-scaling:  $3 \times 256$ -bits. A comprehensive description of the LVL1 to LVL2 interface is given in Ref. [84, 85].

### 4.1.2 Data Acquisition

The data acquisition (DAQ) system moves and buffers data from the various detectors to the HLT and subsequently to mass storage. Fig. 4.4 illustrates the DAQ data flow. Starting from LVL1, the various components are explained in the following.

During the LVL1 event selection latency ( $< 2.5 \mu\text{s}$ ) all event data are buffered in memories located within the detector-specific front-end electronics. Upon a LVL1 accept, the corresponding event data are transferred to the DAQ. These data transfers are passed through detector-specific readout drivers (RODs) before all event fragments are temporarily stored in readout buffers (ROBs) which are part of the readout systems (ROSS). The ROSS run on standard computing nodes.



Once a L2PU has finished processing an event, the LVL2 result is sent to a dedicated ROS for later inclusion in the event data, and a result summary is transferred back to the LVL2 supervisor. At this stage, the data-flow manager (DFM) takes over control from the LVL2 supervisor. The DFM runs on standard computing nodes. A detailed study of the DFM performance (in terms of DAQ and network) can be found in Ref. [86].

If LVL2 rejects an event, then the DFM informs all ROSs to expunge the event fragments. Otherwise, the DFM assigns the event to one event building node (standard computer), also called sub-farm input (SFI). The SFI node collects all event data fragments from the ROSs and builds a single event data-structure. The event filter (EF) computing nodes pull the events from the

SFIs. Subsequently, the SFI notifies the DFM which in turn informs all ROSs to expunge the corresponding event fragments. On the EF nodes the HLT Steering runs the final event selection algorithms. Additionally, the Steering classifies the selected events according to a pre-configured set of data streams. Upon an EF accept, the event data is transferred to one of the output computer nodes, also called sub-farm output (SFO). The SFOs store the full event data in local files (one for each data stream) until they have been successfully transferred to CERN's central data-recording facility [87, 88].

The overall control of the experiment is covered by two independent systems: the DAQ control system and the detector control system (DCS). The former system is responsible for controlling the hardware and software components of the detector as well as of the TDAQ which are required for data-taking. The DCS system, on the other hand, is charged with the supervision of detector equipment (voltage, temperature, gas, etc.). Both systems are implemented in a distributed manner, following the division of the sub-detectors and components of ATLAS.

### 4.1.3 High-Level Trigger

The high-level trigger (HLT) is a software-based trigger, running on farms built from commodity computing and network technology. It is an asynchronous, distributed system. The HLT is subdivided into LVL2 and the Event Filter (EF). LVL2 reduces the output rate to around 3 kHz. The EF should further reduce the rate to  $\sim 200$  Hz. Both levels have access to the full granularity of all the detector data and follow the principle of further refining the signatures identified at LVL1. LVL2 must retrieve event fragments from the ROBs, while EF has the full event data in memory. The use of ROIs, alleviates the time consuming data transfers between LVL2 and the ROSs. LVL2 algorithms are highly optimised for speed. If LVL2 accepts an event, all the fragments from the ROBs are combined and sent to one EF processor for further consideration. The EF further refines the classification of LVL2, using its longer time budget to run more complex algorithms, often based on the same tool-set as off-line reconstruction. It also benefits from more detailed calibration and alignment constants than LVL2.

Each trigger level must reach a decision quickly enough to handle the output rate of the previous level. Given the input rates and the number of processing slots (computers times processors in each computer) available at each level in the nominal configuration for start-up, the average decision times must be less than 40 ms for LVL2 and under 4 s in the EF. This is just an example as the relative allocation of processors between LVL2 and EF is flexible to some extent. The majority of this time is available for event processing but at LVL2 it also includes data access from the ROSs via the network. The architecture and present status of the ATLAS TDAQ system is described further in [89, 90].

The three-level architecture and the use of LVL1 ROIs for guidance keeps the event-building bandwidth minimal. In order to minimise the HLT decision time, and hence maximise the event rate the HLT can handle, the software is designed to reject events as early as possible. The HLT Steering software is at the heart of the HLT and implements these novel features of the ATLAS HLT selection strategy, as described in the following sections.

Initial implementations of the HLT Steering were presented before in [91, 92, 93, 94]. In the au-



turn of 2005 the implementation was reviewed. Several new concepts were introduced as a result of new work on the trigger configuration [95, 96]. Use-cases, such as *re-running of the trigger* for optimisation studies, were better understood. New functional requirements were identified, for example extended support for error handling and monitoring. The new implementation [97] was completed in the spring of 2007 and has been extensively tested since then. It will be used for ATLAS data-taking during the first LHC collisions, and is presented in the following sections since the author significantly contributed to its realisation.

The HLT Steering terminology, which is introduced in due course and used throughout this part of the thesis, is summarised in Appendix A.

## 4.2 HLT Steering Requirements

The HLT Steering must work on the LVL2 and EF processing nodes in the ATLAS TDAQ environment, as described in Section 4.1. Thus, its design and implementation has been governed by several requirements. These, together with other important boundary conditions, can be summarised as:

- *ROI mechanism*: initial seeding of LVL2 by the LVL1 ROIs, and more generally each trigger level or step starts from the result of the previous one.
- *Early-rejection*: minimise the processing time by rejecting events as soon as it becomes clear that the event can no longer pass the trigger.
- *Time critical*: the time overhead of the HLT Steering should be small compared to the overall time budget of the trigger, to leave most of the time for the event selection algorithms.
- Allow for *operational flexibility* to enable and disable triggers, adjust pre-scale and pass-through factors.
- Flexible trigger configuration that allows the construction of *complex menus* from simple building blocks.
- Work in both *on-line* and *off-line* software environments.
- Steer the *trigger event selection algorithms*, support *inter-algorithm communication*.
- Build the HLT result and assign data streaming tags.
- Facilitate a configurable and extensive *error-handling* and *monitoring system* of the HLT software.

Apart from the obvious case of on-line data-taking, there are several other scenarios in which the HLT Steering will be run. These use-cases, summarised below, put some additional constraints on the implementation of the HLT Steering. Clearly the on-line requirements are the highest priority, but the ability to use identical software off-line to emulate, study and tune the on-line performance is also of great importance to the experiment.

---



### 4.2.1 On-Line triggering

On-line triggering is the primary use-case. The Steering runs on-line on the HLT farm nodes. It operates in between the ATLAS DAQ system and the HLT algorithms. Once the DAQ system assigns an event for examination to a LVL2 or EF processing unit, the Steering takes over control for the given event, and schedules the execution of a set of pre-defined HLT algorithms. The most stringent requirement in on-line running is to reach a decision whether or not to accept an event within very tight time constraints.

The data returned by the HLT Steering contains the accept/reject decision, error flags, the status of the different triggers (electrons, muons, taus, jets, etc.), and various other data from intermediate processing. Certain data objects produced by trigger algorithms may be included too. From LVL2, all this information is appended to the raw event data and sent to the EF, which uses some of the intermediate information and data objects to set up seeded reconstruction to pick up where LVL2 left off. The EF itself produces similar data which, along with LVL2, are included in the raw event data that is ultimately stored off-line if the event is accepted. The amount of detail in these data can be increased for debugging.

The Steering supports pre-scale and unconditional-accept (pass-through) of triggers, both are explained in detail in Section 4.8. Pre-scales will be used by the shift crew to control the rates of triggers which will vary with the luminosity and beam conditions. LVL1 pre-scales can be changed during a run at a luminosity block boundary<sup>3</sup>, while LVL2 and EF pre-scales must be configured before the run begins. The pre-scale and pass-through capabilities are also used to: collect data from low-threshold triggers (reduce rate by pre-scale); and to obtain information from rejected events (force the acceptance of a few events using pass-through). This is essential for commissioning, monitoring, debugging, and efficiency calculations. Statistical data are also available for both accepted and rejected events through the monitoring system, as described in Section 4.9.

### 4.2.2 Data analysis

The information produced by the Steering, either from on-line data taking or re-running the trigger off-line, can be accessed for subsequent analysis. Basic information about which triggers were passed is easily available in all levels of off-line data, along with the more detailed information described above. The trigger user-interface is described in more detail in Chapter 6.

### 4.2.3 Off-line studies

The trigger can be run as part of the off-line reconstruction on simulated or real data. In the latter case, the results can be compared to those obtained on-line. It is also possible to take the output data from reconstruction, and re-run the decision part of the trigger with different selection criteria. This functionality is aimed at optimisation studies to tune selection cuts.

---

<sup>3</sup>A luminosity block is defined as the shortest time interval for which the integrated luminosity, corrected for dead-time and pre-scales, can be determined. It is expected to be of the order of one minute for ATLAS.

The ability to run the HLT in both on-line and off-line software environments is especially important in the startup phase of the experiment, at low luminosity. During this phase, the HLT will be run in full pass-through mode to accept all events. The HLT can then be re-run off-line to tune and optimise the algorithms on real data.

### 4.3 Basic Steering Design and Concepts

The HLT Steering runs in the off-line software framework, to which it adds the functionality necessary for triggering. An interface layer based on the off-line framework makes it possible to run the Steering in both off-line and on-line environments. The Steering is called from the on-line software application that runs on HLT farm nodes. It in turn calls, on demand, the HLT algorithms which have also been written utilising the off-line software framework. The Steering is written in C++ with an object-oriented and modular design. Several components of the Steering are re-used for example in the trigger user-interface.

The HLT selection consists — in LVL2 and EF — of a number of triggers, called *trigger chains*. The fulfilment of at least one of these chains is the requirement for events to be accepted. Chains at a given trigger level are normally run only if the preceding chain (or LVL1 trigger item) of the previous trigger level has fired.

Since data read-out is time-consuming, the HLT is run in a seeded manner, with the ROIs identified at LVL1 acting as seeds. Each chain is thus run once on each ROI (or combinations thereof) in the event. Also the ROI type (EM, tau/hadronic, jet, total- $E_T$ ,  $E_T^{\text{miss}}$ , total- $E_T$  in jets, and muon) and ROI threshold is used, e.g. a LVL2 60 GeV electron trigger chain runs on all ROIs of type EM which passed the LVL1 55 GeV threshold. Data readout and processing occurs mainly in a limited region around the ROI position.

In order to minimise the processing time, each chain is processed in a step-wise manner. At each chain step, the selection is refined by the readout of increasing amounts of data from the detector, and increasingly complex processing. At the end of each step a requirement, called a *trigger signature*, is applied. Following the early-rejection principle, the first signature that fails causes the whole chain to fail for the event.

Signatures at each step consist of a requirement on the multiplicity of objects, called *trigger elements* (TEs), of a given type. This type describes the initial ROI type and the processing state, briefly characterised by a label such as “L2\_e60cl” which stands for a LVL2, 60 GeV electron candidate TE after the calorimetry reconstruction.<sup>4</sup> TEs are produced by HLT algorithms, which may take one or more TE types as input to produce a single output type. The initial TEs for LVL2 are formed from the LVL1 ROIs and correspondingly the LVL2 TEs seed the EF algorithms.

HLT algorithms are separated into two classes: feature extraction algorithms (FEX) which perform more time-consuming operations such as data unpacking and the calculation of physics quantities in trigger data objects, referred to as *features*; and hypothesis algorithms (HYPO) which typically perform quick selection cuts (energy, isolation etc.) based on existing features.

---

<sup>4</sup>String-labels are used in the trigger configuration. At run-time, however, hash-IDs (integers) of the strings are employed in order to increase the processing speed.

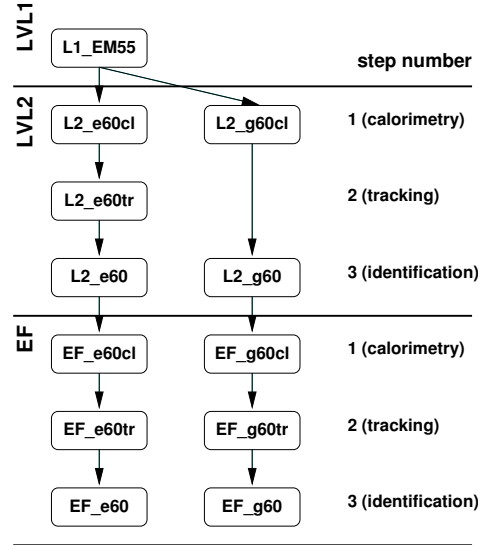


**Figure 4.5:** Diagram of trigger chains in the HLT selection for electrons and photons of at least 60 GeV transverse momentum. Horizontal lines separate trigger levels (LVL1/LVL2/EF). Boxes represent signatures of chains, which must be satisfied. In this example, `L2_e60cl` represents the presence of at least one trigger element passing calorimetry cuts for 60 GeV electrons. The `tr` postfix represents tracking-related cuts and the chain name without a postfix is reserved (by convention) for the final step of a trigger chain.

Typically, one chain step leads to the execution of a FEX and a HYPO algorithm. This algorithm pair is run, on demand by the trigger chain, over all input TEs (all ROIs). Whenever the selection cuts of a HYPO algorithm fail for a given input TE, the output TE must not be considered in the signature. This is achieved with a TE *active state*, so the HYPO can flag an output TE as inactive. Once more, following the early-rejection principle, TEs that fail (flagged as inactive) at a given step are not further processed by any HLT algorithm.

A schematic view of the selection in the HLT is given in Fig. 4.5, where the concept of trigger chains, trigger signatures, and chain steps is illustrated.

At the end or beginning of each trigger level, pre-scale factors can be applied to the various chains in order to reduce the input rate to the next trigger level (EF) or to permanent storage. Conversely, pass-through factors can also be applied to chains in order to accept a given fraction of the events that would normally be rejected. In this case the chain is run normally (including pre-scaling) but is finally accepted regardless of its actual result. For simplicity there are no pre-scale or pass-through factors at the intermediate steps of LVL2 and EF. The pass-through chains are intended to occupy a minimal fraction of the trigger output bandwidth and are designed for trigger efficiency studies, commissioning, and debugging.

The full description of LVL1 and HLT (i.e. definition of trigger chains (HLT), trigger items (LVL1), trigger signatures, TEs, algorithm parameters, etc.) is called a *trigger configuration* and is stored in a relational database (TriggerDB) or in XML files. For on-line running of the HLT the TriggerDB provides and archives the configurations. The XML files, holding equivalent information, are used for local tests not relying on the availability of the database [96].

**Table 4.1:** Simplified trigger menu table. PS indicates “pre-scale” and PT means “pass-through”.

Generic name	LVL1 item	LVL2 chain	EF chain
e5	L1_EM3 (PS)	L2_e5	EF_e5
e5_PT	L1_EM3 (PS)	L2_e5_PT	EF_e5_PT
e10	L1_EM8	L2_e10	EF_e10
g10	L1_EM8	L2_g10	EF_g10
2e10	L1_2EM8	L2_2e10	EF_2e10
e20_XE12	L1_EM18_XE12	L2_e20_xe12	EF_e20_xe12
XE12	L1_XE12 (PS)	L2_xe12_PT	EF_xe12_PT

## 4.4 Trigger Configuration

The trigger configuration holds all information necessary to set up LVL1, LVL2, and the EF. Table 4.1 shows a simplified trigger menu table (only LVL1 items and HLT chains are listed). It is a small selection from a draft trigger menu designed for start-up of the LHC. The full menu contains electron (e), photon (g), muon (mu), tau (tau), jet (j), b-jet (b), missing energy (xe), total energy (te), jet energy (je) and B-physics triggers, in single, multiple and combined triggers, with various thresholds each. It has low threshold, pre-scaled (PS) and pass-through (PT) items to help understand and cross-check the trigger. The numbers in the trigger names represent nominal thresholds in GeV. At LVL1, EM refers to electromagnetic clusters; electrons and photons cannot be separated at this level because there is no inner tracker data available. The latest ATLAS draft trigger menu for running at  $L = 10^{31} \text{ cm}^{-2} \text{ s}^{-1}$  and 10 TeV centre-of-mass energy is presented in Chapter 5. This section describes the concepts and principles of the trigger configuration.

Each trigger has a generic name, with a corresponding LVL1 item, LVL2 chain and EF chain. These HLT chains are central to the design of the HLT Steering. A chain is composed of several steps. These are the steps needed to confirm or reject this particular trigger in an event.

Fig. 4.6 illustrates the trigger configuration concepts using the example of the 10 GeV electron trigger. The left most diagram shows the break down of the trigger into the LVL1 item L1\_EM8, the LVL2 chain L2\_e10, and the EF chain EF\_e10. For a given event, the L2 (EF) chain will only be followed up if the preceding trigger L1\_EM8 (L2\_e10) fires.

Zooming into the L2\_e10 chain, we see it consists of three chain steps (second diagram from left). Each step leads to the execution of one or more trigger algorithms whose results are compared to a requirement. This requirement, of a given chain step, is fully specified by a list of TEs that are required to satisfy this step. The list of required TEs is called *trigger signature*. In our example, the three steps require each one TE with the labels (types): L2\_e10cl, L2\_e10tr, and L2\_e10.

As described in Section 4.3, TEs are abstract objects which represent the state of the reconstruction. By convention, cl means cluster, tr stands for tracking, and the chain name alone (here L2\_e10) is reserved for TEs of the final chain step. At the beginning of LVL2 processing, the initial TEs are formed from the LVL1 ROIs. All subsequent TEs are produced by HLT algorithms. This process is prescribed by so-called *trigger sequences* which define how one or several input TE

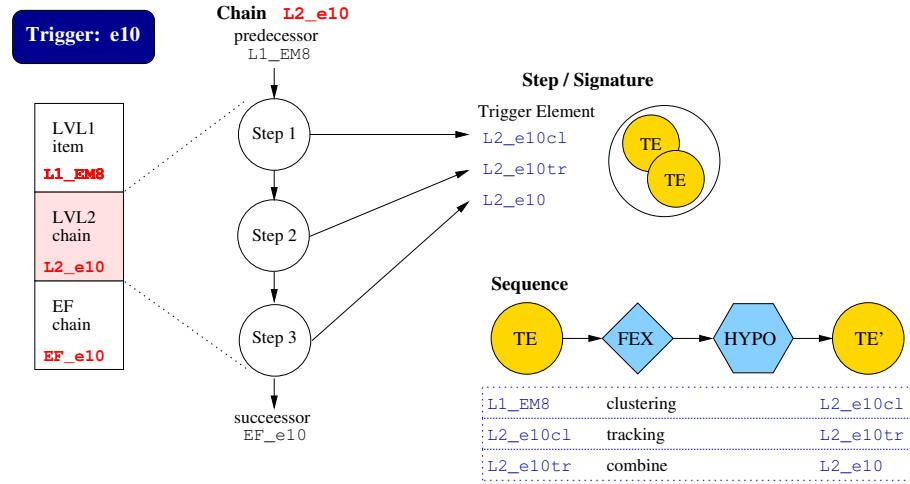


**Figure 4.6:** Illustration of the main configuration concepts using the example of the 10 GeV electron trigger. The diagrams are described in the text.

types are transformed to exactly one output TE type via one or more HLT algorithms. In Fig. 4.6 (bottom right), three sequences are shown which configure the generation of the required TEs for the L2\_e20 chain. For example, a calorimeter-clustering algorithm is configured to transform a LVL1 EM cluster ROI-TE (L1\_EM8) to a LVL2 EM cluster TE (L2\_e10c1).

A typical sequence consists of a single input TE type, one FEX and one HYPO algorithm and (necessarily) a single output TE type. Other algorithm types and more complex logic (multiple inputs) are also possible, as will be explained in the next section.

These simple building blocks (HLT chains, their steps defined by the TE requirements (signatures), and the complete list of sequences) form the core of the HLT trigger configuration. They fully define what HLT algorithms to run on a given event, as further described in Section 4.7.

## 4.5 HLT Algorithms

HLT algorithms are broadly divided into two classes: feature extraction (FEX) and hypothesis (HYPO) algorithms. FEX algorithms are normally seeded by one TE (ROI), either from LVL1 or refined by a previous step. They retrieve detector data from within this ROI, and try to find a feature in these data, such as a track or calorimeter cluster. At the end they update the ROI position if it has been more accurately determined. Hypothesis algorithms follow FEX algorithms. Their job is to compare the trigger data objects (features) produced by the FEX algorithm against some hypothesis and mark the output TE of the sequence as valid (active) or invalid (inactive) according to the success or failure of the hypothesis. Examples of hypotheses are: cut on the shape parameters of a calorimeter cluster; cut on the cluster-track matching variables of an electron candidate; apply an  $E_T$  threshold.

More details on the concrete implementation of the ATLAS electron/photon, jet, muon, etc. HLT algorithms can be found in Ref. [98, 99, 100]. In the following, the abstract design and general functionality of HLT algorithms is described.

HLT algorithms are bundled in so-called sequences (cf. Section 4.4). The first algorithm of a sequence is responsible for creating the output TE instance(s), which are then further updated by subsequent algorithms.

FEX algorithms may create TEs and append new data to existing TEs, whereas HYPO algorithms may only change the active state of TEs. Accordingly, common functionality for all algorithms is provided by the base class, from which two additional classes, one realising generic FEX functionality and the other generic HYPO functionality, are derived. A typical algorithm sequence consists of one FEX followed by one HYPO algorithm.

HYPO algorithms operate on a single TE type. They run once for every available TE of this type, have read-only access to the features and can change the output-TE's active state. FEX algorithms may take an arbitrary number of TE types as input, and produce a single output type. Moreover, they can access data from the input TEs or their predecessors, and produce output data (features) which are then attached to the output TE. The algorithm in the first position of a sequence is responsible for creating the output TE instances and can thus only be a FEX algorithm.

More targeted functionality is provided by classes further derived from the FEX base class as follows.

- **Single ROI FEX** (`HLT::FexAlgo`): This class of algorithms is designed to run several times per event and in each cycle operate on one input/output TE pair. Algorithms derived from the `FexAlgo` class are responsible for performing the reconstruction of atomic objects like energy clusters or tracks. The base class internally loops over all active TEs of the input type, and creates an output TE instance.
- **Multiple ROI FEX** (`HLT::ComboAlgo`): This is designed for the case where TEs (ROIs) must be combined, in particular to reconstruct decays. Use-cases include triggers for  $Z \rightarrow e^+e^-$ ,  $D_s^+ \rightarrow \phi\pi^+$  and  $B^0 \rightarrow \mu^+\mu^-$ . The base class performs the combinatorics on the available input TEs, applies a preselection on the combinations, and creates output TEs in the passing cases. Algorithms run on a single input TE combination and one output TE instance.
- **Event-wide FEX** (`HLT::AllTEAlgo`): This class of algorithms also takes a configurable number of input TE types. However, in this case the base class simply provides the algorithm with the list of all active TE instances for the specified input types. The algorithm has therefore access to all the instances of each input TE type, and may create an arbitrary number of output TEs (of one type). It is thus run only once per event. This is useful for the case of algorithms that require a global view of the event: for instance, at LVL2 the missing transverse energy ( $E_T^{\text{miss}}$ ) is refined by accounting for the muon energy. This is naturally done in an `AllTEAlgo`, with the input types being muon TEs, in addition to the original  $E_T^{\text{miss}}$  from LVL1.

It is noteworthy to point out that an `AllTEAlgo` will also be executed if no active input TE instances are found in an event. It thereby provides means to have unseeded algorithms (no input ROIs required).

A caching mechanism is included to avoid unnecessary execution of sequences and algorithms. When configuring chains, it is often the case that the same sequence may be invoked in more

than one chain, especially in similar chains which differ only by a pre-scale factor, or that share a common starting point but differ in later steps. In this case, the sequence will be run on each ROI only the first time it is needed, and the results taken from the cache after that. It is also common that several sequences will be defined with the same FEX algorithm but different hypothesis algorithms, for example in order to apply different thresholds to the same calorimeter cluster. In this case, the FEX algorithm will only be run once for a given ROI, after which the cached results are used. The different hypothesis algorithms are run in every sequence of course. This caching is implicit and allows a complex configuration to be built up from a common set of sequences and algorithms.

The division of HLT algorithms into FEX and HYPO and the caching mechanisms allow the longest part of the processing to be done once for an ROI by a common FEX algorithm, while the quick application of selection cuts by different HYPO algorithms can be done as many times as necessary.

## 4.6 Inter-Algorithm Communication

As aforementioned, the execution of HLT algorithms is (normally) seeded by TEs produced by previous algorithms. Thus, TEs provide a natural medium for inter-algorithm communication. Trigger data objects (features) are therefore attached to TEs and can be accessed by subsequent algorithms. A Steering tool, called *Trigger Navigation*, holds and manages the full HLT data structure consisting of all TEs, their interconnections, and the attached features. An example Navigation data structure (for one event) is shown in Fig. 4.7. The Navigation is implemented as an independent tool to facilitate its use outside the scope of the HLT Steering (cf. Section 4.2).

The primary Navigation structure is a directed graph where nodes are the TEs. Edges denote “seeded by” relationships from an output TE to input TE(s). The graph is bi-coloured, where the two ‘colours’ describe the active state of TEs. In addition to the TE state, the Navigation also holds the links between TEs and features. For each event the HLT Navigation starts from one single “initial” TE (top node in Fig. 4.7). It represents the event as a whole and thus facilitates attaching event-wise features that are shared between various triggers. All TEs in the second layer represent LVL1 ROIs, one node for each geometrical region and type (EM, muon, jet, etc.). Each ROI-TE node then develops into a number of TEs, one for each passed LVL1 threshold (third layer). From here on, all further TE nodes of the HLT Navigation are created by HLT algorithms.

Apart from on-line running, the Navigation also plays an important role in trigger optimisation studies. In these studies, the selection is first run with loose trigger selection cuts (or no cuts) in order to execute all possible trigger algorithms and hence extract all possible features. In the second stage, the HLT selection is run in a special mode on the same events: to save time, all FEX algorithms are disabled and the HYPOs obtain information from the Navigation structure generated in the first run. Running in this special mode is very fast because HYPO algorithms are much quicker than running the full trigger. Thus, many different selection cuts can be evaluated.



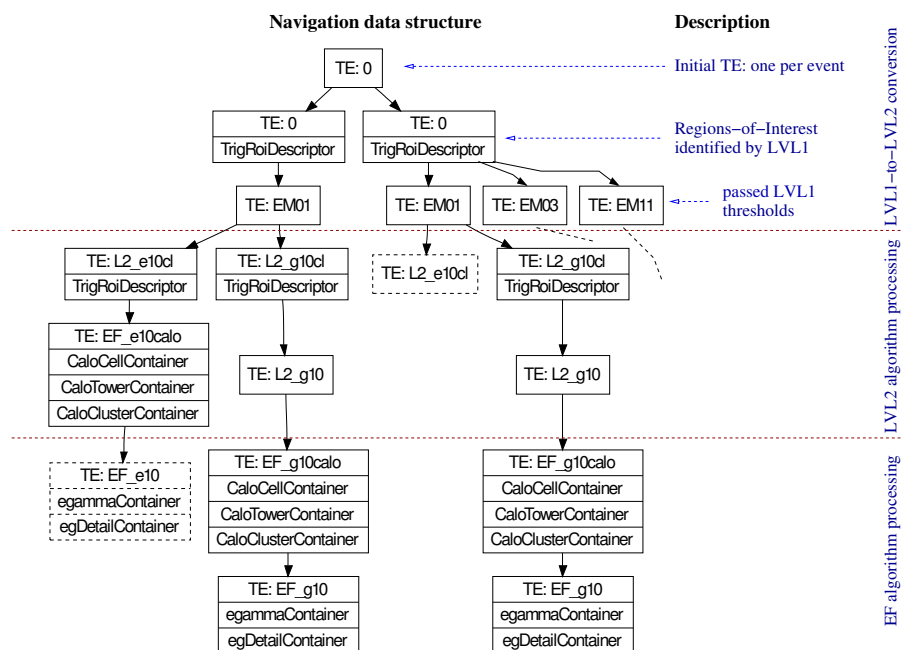


**Figure 4.7:** Subset of the HLT Navigation data structure of one simulated ttbar event. Only algorithms for electron and photon triggers are enabled. Each box corresponds to one TE with its label in the heading. Features attached to the TEs (here: ROI descriptor, collections of calorimeter cells, towers and clusters) are represented by additional rows below the label in each TE box. Inactive TEs are depicted by dashed boxes. The Navigation fragments initiated by the LVL1 ROI thresholds EM03 and EM11 are not drawn for space reasons.



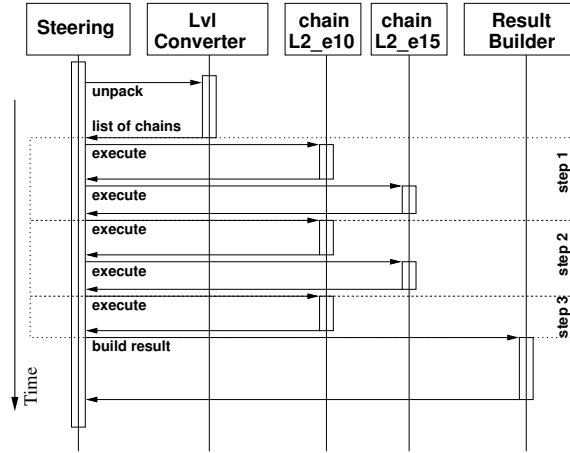


**Figure 4.8:** Simplified logic sequence diagram showing the HLT Steering for 2 chains. In this example, the chain L2\_e15 is rejected at the second step, and thus not executed in the third step.

## 4.7 HLT Steering Logic

The HLT Steering controls the execution of the selection algorithms, based on the configured triggers as well as the event state (which ROIs are active). The flow and logic of a full HLT Steering execution cycle is described in this section. Fig. 4.8 shows a simple HLT Steering logic sequence diagram.

The first task is creation of the initial TEs needed as input to the first sequences. This is known as the *LvlConverter*. At LVL2, this is done from LVL1 ROIs, cf. top part of Fig. 4.7. In the EF, the initial TEs are created from the LVL2 output instead. One TE is created for each threshold of each ROI, since LVL1 ROIs can pass multiple LVL1 thresholds. Following this, all relevant chains are activated. Relevant chains are those whose predecessor (in the previous level) was successful. Only active chains will be processed by the HLT Steering. Since the configuration may contain hundreds of chains, but only a few (order 10) will typically be relevant for an event, this saves time.

The Steering then proceeds with the execution of all active chains. It continues until all chains have become inactive either because they successfully reached their last step or because they failed at some step.

Each chain is a self-consistent object. It is aware of its internal status (active/inactive, current step, pre-scale flag, pass-through flag, etc.), and its trigger signatures (one per step). The execution of algorithms is fully handled through the use of sequences: In each step, the trigger signature provides a list of required TE(s). In other words, each step requires certain multiplicities of one or more active TE type(s). In order to find out which algorithms to run, each required TE type is matched to one sequence, whose output TE type is identical to the required TE type.<sup>5</sup> The so found sequence(s) then reveal the HLT algorithm(s) to be run. Thus, when a chain's execute method is called it performs the following processing steps:

<sup>5</sup>To speed-up event processing, this matching is performed during the Steering's initialisation since it only changes with a new trigger configuration. Thus, when a chain object runs on an event, it has the valid sequences already.

1. Abort if chain is already inactive, otherwise read signature of current step.
2. For each required TE type in the signature, execute the associated sequence. The sequence is responsible for handling the algorithms.
3. Check result(s) of sequence(s) against requirement(s).
4. Deactivate chain if the check fails or if a too severe error occurred during step (2).
5. Otherwise, increase internal step counter by one.
6. Set chain passed-status to true and deactivate chain if there are no more steps.

The sequence, again a self-contained object, calls the HLT algorithms. Looping over the input TEs (ROIs) is performed in the HLT algorithm base class (unless it is an `AllTEAlgo`). The same sequence object can be used from within many chains. Subsequent calls to the sequence's `execute`, however, will return the cached results.

The result check of step (3) compares the number of active TEs, which were produced by the algorithms bundled in the sequence, against the required number of the chain step.<sup>6</sup>

As a consequence of the Steering execution design described above, HLT algorithms are only executed on-demand by a trigger chain. For example, the existence of two muon ROIs does not automatically lead to the execution of the corresponding muon algorithms. Only if a muon trigger chain demands muon TEs, will the muon algorithms run on all muon ROIs.

Once all chains have been executed, the event is either successful, or not because all chains broke prematurely. Either way, pre-scale and pass-through factors are applied as this could change the decision.<sup>7</sup> The original outcome together with the pre-scale and pass-through results are stored for each chain so the reason the event passed (or failed) can be understood later. This along with other data are compiled to make the HLT results (one for each LVL2, EF) which are appended to the raw event data for use off-line. This procedure is known as *result building*. It runs regardless of whether the event was accepted or rejected. The HLT result contains a header summarising the overall trigger decision, plus more detailed intermediate information from the event processing. It includes the chain state (raw success, after pre-scale, after pass-through) of all chains which were activated in the beginning of event processing. Also the last active step and the most severe error code of the chains are saved. Furthermore, the HLT result contains the Navigation data structure and some of the features which are useful for debugging, trigger efficiency studies, and seeding the next trigger level: for example, ROI-like objects are recorded at LVL2 and used to seed algorithms in the EF. Other data representing physics properties of trigger objects (clusters, tracks) can be added to the payload and the actual content is subject to the configuration.

Based on the successful trigger chains, one or several data streaming tags are assigned to the event during the result building. This information is also stored in the HLT result. Streaming tags are

---

<sup>6</sup>Signatures consisting of different TE types need a more thorough comparison: In addition to the straightforward requirement on each TE type, the TEs of a successful combination must originate from different detector regions (ROIs). The Steering has a simple built-in mechanism, based solely on the LVL1 ROI objects, to reject obvious cases. More customised overlap checks, for instance based on  $\eta$  and  $\phi$ , can be added in form of HLT algorithms.

<sup>7</sup>In order to save time, the Steering can be configured to apply pre-scale factors before executing the chains.

---

used by the DAQ to classify events and thus write events into different data streams. Physics streams (such as electron/gamma, muon, jets, etc.) are designed for off-line physics analyses. Calibration streams provide partial or full event data for specialised detector alignment and calibration tasks. Furthermore, a debug stream contains all events which caused errors during on-line processing. Finally, an express stream is designed to collect a subset of the physics data (order of 10%). It is foreseen that this data will be reconstructed within 24 hours. The purpose of the express stream is to quickly check data quality, monitor the detector status, and thus provide a rapid alert for on-line detector and TDAQ problems.

Errors and exceptions from HLT algorithms and all of the Steering components are caught, before they can cause problems upstream. To facilitate reporting and debugging of problems, an HLT error object is employed. It provides pre-defined as well as configurable values for the error's *action* and *reason*:

Action	Reason	Steering internal reason
continue	unknown	no_lv11_items
abort_chain	missing_feature	no_lv12_chains
abort_event	bad_job_setup	no_lv11_result
abort_job	std_exception	wrong_hlt_result
unspecified	missing_rod	no_hlt_result
	...	...

The *action* value is immediately applied by the Steering. The reason is reported to the on-line monitoring system and is also stored as part of the HLT result.

## 4.8 Pre-scale and Pass-through of Triggers

HLT trigger chains can be configured with pre-scale (PS) and pass-through (PT) factors. PS factors allow to reduce the rate of a given chain while PT factors increase it, both with respect to the nominal chain acceptance rate. Both PS and PT scaling of chains is handled by the HLT Steering which provides two scaling engines for this purpose: one based on random numbers (default) and one based on a periodic scaler. Both engines can handle integer and float PS/PT scaling factors. The implemented logic is as follows:

PS factor ( $F_{PS}$ )	
$F_{PS} < 0$	reject chain in all cases,
$0 \leq F_{PS} \leq 1$	do nothing (default),
$F_{PS} > 1$	reject chain in $(F_{PS} - 1)$ out of $F_{PS}$ cases,
PT factor ( $F_{PT}$ )	
$F_{PT} < 1$	do nothing (default),
$F_{PT} \geq 1$	accept (pass-through) chain in 1 out of $F_{PT}$ cases independently of the chain decision,

where an active PT flag dominates over an active PS flag. The special case of always accepting a chain is covered by a PT factor of 1.

Following the PS and PT logic, the expected number of events for a given LVL2 chain are

$$\begin{aligned}
 N^{\text{active\_L2}} &= N^{\text{passed\_L1}} \\
 N_{\text{raw}}^{\text{passed\_L2}} &= N^{\text{active\_L2}} \cdot \varepsilon^{\text{L2}} \\
 N_{\text{PS}}^{\text{passed\_L2}} &= \begin{cases} 0 & \text{if } F_{\text{PS}}^{\text{L2}} < 0, \\ N_{\text{raw}}^{\text{passed\_L2}} & \text{if } 0 \leq F_{\text{PS}}^{\text{L2}} \leq 1, \\ N_{\text{raw}}^{\text{passed\_L2}} \cdot 1/F_{\text{PS}}^{\text{L2}} & \text{if } F_{\text{PS}}^{\text{L2}} > 1 \end{cases} \\
 N_{\text{PT}}^{\text{passed\_L2}} &= \begin{cases} N_{\text{PS}}^{\text{passed\_L2}} & \text{if } F_{\text{PT}}^{\text{L2}} < 1, \\ N_{\text{PS}}^{\text{passed\_L2}} + \frac{N^{\text{active\_L2}} - N_{\text{PS}}^{\text{passed\_L2}}}{F_{\text{PT}}^{\text{L2}}} & \text{else,} \end{cases}
 \end{aligned} \tag{4.1}$$

where  $N^{\text{active\_L2}}$  is the number of events for which the chain was run (equal to the number for which the corresponding LVL1 trigger fired  $N^{\text{passed\_L1}}$ ),  $N_{\text{raw}}^{\text{passed\_L2}}$  denotes the number of events that passed the chain (before PS or PT),  $\varepsilon^{\text{L2}}$  is the selection efficiency of the given LVL2 chain,  $N_{\text{PS}}^{\text{passed\_L2}}$  is the number of events that passed the chain after applying PS, and  $N_{\text{PT}}^{\text{passed\_L2}}$  is the number of events that passed the chain after applying PS and PT. The scaling factors are denoted by  $F_{\text{PS}}^{\text{L2}}$  and  $F_{\text{PT}}^{\text{L2}}$ . Note that all quantities are for one given trigger chain.

By default, EF chains inherit an active PT flag from their preceding LVL2 chain. This is controlled by a global Steering option.<sup>8</sup> If it is off, then the expected event numbers of an EF chain are given by Eq. (4.1) after replacing the labels L1 and L2 by L2 and EF respectively. In the other case, an active EF PT flag can arise from the EF itself or from LVL2 (it is the logical OR). Thus, the expected number of events after PS and PT is higher. It is given by

$$N_{\text{PT}}^{\text{passed\_EF}} = N_{\text{PT}}^{\text{flagged\_L2}} + N_{\text{PT}}^{\text{flagged\_EF}} + N_{\text{raw}}^{\text{accept\_EF}}, \tag{4.2}$$

where the first term ( $N_{\text{PT}}^{\text{flagged\_L2}}$ ) denotes all events with an active PT flag from LVL2, the second term ( $N_{\text{PT}}^{\text{flagged\_EF}}$ ) comprises all events with an active PT flag from EF and a non-active LVL2 PT flag, and the third term ( $N_{\text{raw}}^{\text{accept\_EF}}$ ) contains all events which: were not PT flagged in LVL2 or EF, not PS flagged in EF, but accepted by the EF trigger chain. The three terms can be decomposed into

$$\begin{aligned}
 N_{\text{PT}}^{\text{flagged\_L2}} &= \begin{cases} 0 & \text{if } F_{\text{PT}}^{\text{L2}} < 1, \\ \frac{N^{\text{active\_L2}}}{F_{\text{PT}}^{\text{L2}}} & \text{else,} \end{cases} \\
 N_{\text{PT}}^{\text{flagged\_EF}} &= \begin{cases} 0 & \text{if } F_{\text{PT}}^{\text{EF}} < 1, \\ \frac{N_{\text{PT}}^{\text{passed\_L2}} - N_{\text{PT}}^{\text{flagged\_L2}}}{F_{\text{PT}}^{\text{EF}}} & \text{else,} \end{cases} \\
 N_{\text{raw}}^{\text{accept\_EF}} &= \begin{cases} 0 & \text{if } F_{\text{PS}}^{\text{EF}} < 0, \\ (N_{\text{PT}}^{\text{passed\_L2}} - N_{\text{PT}}^{\text{flagged\_L2}} - N_{\text{PT}}^{\text{flagged\_EF}}) \cdot \varepsilon^{\text{EF}} & \text{if } 0 \leq F_{\text{PS}}^{\text{EF}} \leq 1, \\ (N_{\text{PT}}^{\text{passed\_L2}} - N_{\text{PT}}^{\text{flagged\_L2}} - N_{\text{PT}}^{\text{flagged\_EF}}) \cdot \frac{\varepsilon^{\text{EF}}}{F_{\text{PS}}^{\text{EF}}} & \text{if } F_{\text{PS}}^{\text{EF}} > 1 \end{cases}
 \end{aligned} \tag{4.3}$$

---

<sup>8</sup>This option is most likely going to be removed, leaving the current default as the only option.

In the current HLT Steering and TriggerDB implementation, PS and PT factors can be changed in every new run. LVL1 PS factors, however, can be adapted on a luminosity block basis (order of 1 min). It provides the trigger operator with the flexibility needed to quickly react to changes in beam and detector conditions.

Upcoming extensions of the ATLAS trigger PS mechanism are:

1. Change the HLT PS factors on a luminosity block basis. The technical challenge is to keep all HLT farm nodes synchronised, and also assure that all events are treated with the correct set of PS factors.<sup>9</sup> This new HLT feature is foreseen to be tested in the next major software release.
2. Dynamic change of PS factors to compensate for the falling accelerator luminosity and thus make full use of the available data processing bandwidth. An automatic feedback system is in development to monitor the total output rate and adapt LVL1 PS factors accordingly. This has been successfully realised for instance in the CDF experiment [101].

## 4.9 Monitoring

For successful data-taking a continuous monitoring of the trigger and its performance is essential. The shift crew must be able to react immediately to malfunctions of the system in order to minimise the loss of data. Periods with bad trigger conditions or detector performance have to be identified to allow their exclusion from the off-line data analysis.

Different aspects of the monitoring of the HLT can be considered: the monitoring of the HLT Steering decision and trigger rates, a persistent data quality check of the events processed by the HLT and the operational monitoring of the HLT Steering. Data quality checks are more important for the off-line quality assessment. Rate measurements, on the other hand, are sensitive to the stability of the HLT on-line operation, the accelerator and beam conditions, and the performance of the sub-detectors that are used in the trigger.

The HLT Steering provides a monitoring framework which is based on ROOT [102] histograms. The individual trigger algorithms running in the HLT use this framework in order to fill histograms with variables that are sensitive to the trigger behaviour and the algorithms' performance. The Steering code itself is independent of the monitoring code, and the monitoring histograms are configurable within the TriggerDB. All histograms can be filled continuously. They can also be individually reset for convenient data-taking intervals like runs and luminosity blocks.

In the on-line environment the monitoring histograms from the individual HLT farm nodes are combined (summed up or averaged) by the on-line histogramming service (OH) [103] and made available for further processing. The histograms serve as a basis for the on-line and off-line assessment of data quality and the trigger performance monitoring, as well as for software validation of the HLT Steering and algorithm code.

---

<sup>9</sup>Due to the asynchronous and distributed nature of the HLT system, two events processed in parallel by two nodes do not necessarily belong to the same luminosity block. Therefore, HLT nodes have to hold a list of PS sets where each set is associated to one luminosity block number.

---

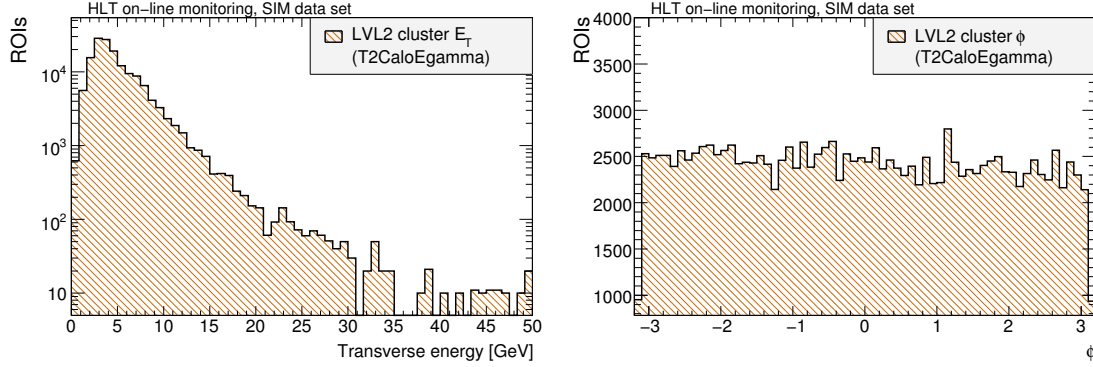


**Figure 4.9:** HLT on-line monitoring examples, based on the Sim data, see text in Section 4.9. Distribution of the LVL2 cluster algorithm's transverse energy (left) and  $\phi$  (right).

In the following, two datasets are used to illustrate the HLT on-line monitoring of trigger algorithms and the Steering, as well as to show the Steering performance and validation tests (next Section 4.10). The two datasets are:

*SIM data:* Simulation of the ATLAS LVL2 and EF, using athenaMT and athenaPT respectively. The employed raw event data file has been obtained from an official ATLAS enhanced minimum bias sample ( $\sqrt{s} = 14$  TeV). In the enhanced minimum bias sample, the following lowest unprescaled LVL1 trigger selections are applied: EM3, MU4, J18, FJ18, XE25, TE250. This provides a higher statistics sample with little bias.

*COSMIC data:* Cosmic ray data-taken with the ATLAS detector in the autumn of 2008. The detector and trigger configuration varied over the runs, since many different aspects were studied. It is noteworthy, however, that the trigger system was configured with a special cosmic commissioning setup. Details of the trigger menu will be discussed where needed.

In the example of the LVL2 cluster algorithm (T2CaloEgamma), the list of monitored variables includes:  $E_T$  and  $\eta$ ,  $\phi$  of the electromagnetic clusters; ratio of the core-cell energy to the total energy, as well as the number of electron candidates as a function of the pseudorapidity  $\eta$ . Furthermore, the algorithms' execution time is monitored. Fig. 4.9 shows the T2CaloEgamma on-line monitoring distributions of  $E_T$  (left) and  $\phi$  (right), obtained from running on the Sim dataset. Note that it peaks around 5 GeV, the point where the EM3 trigger is fully efficient.

In addition to the monitoring of variables inside the algorithms, the monitoring of the HLT Steering itself is performed after each trigger level (after the result building). At this stage, access to the full trigger information is available for accepted and also rejected events.

Examples of the Steering on-line monitoring are given in Fig. 4.10 which shows the number of LVL1 ROIs per event for the SIM dataset (left) and COSMIC data (right).

Further HLT on-line monitoring examples are shown in Fig. 4.11: The left-hand plot shows the LVL2 muon (muFast)  $\phi$  distribution, obtained from COSMIC data. As expected, a peak can be seen at  $\phi \simeq 1.6$  corresponding to the muons originating from cosmic rays (mainly protons) which enter the ATLAS cavern primarily through the access shafts. No peak is present around  $\phi \simeq -1.6$  because the muon spectrometer was inactive in that region at that time.

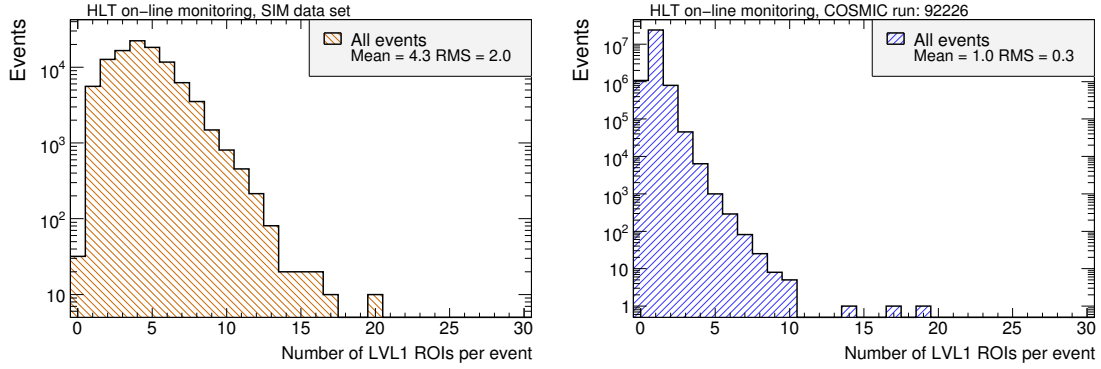


**Figure 4.10:** The number of LVL1 ROIs per event from SIM data (top left) and COSMIC data (top right) as obtained from the Steering on-line monitoring.

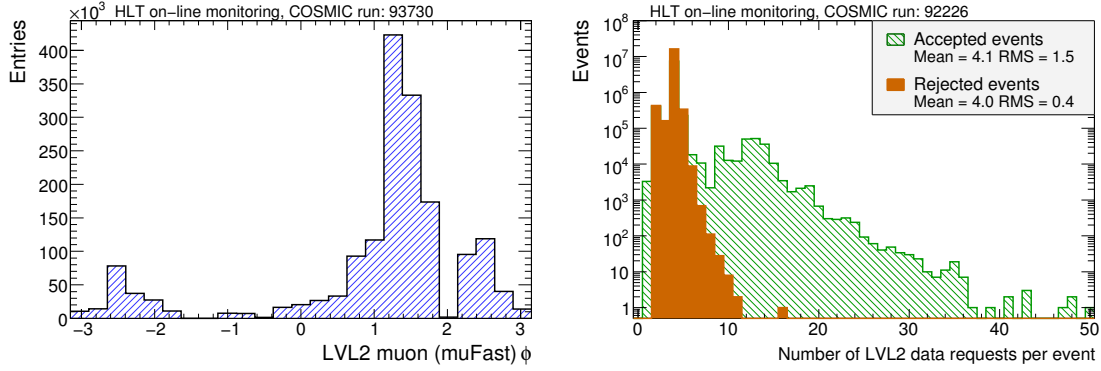


**Figure 4.11:** Left plot: Distribution of LVL2 muons in  $\phi$  from COSMIC data. Note that the muon spectrometer around  $\phi \simeq -1.6$  was inactive in this run. Right plot: Number of data requests to the ROSs per event during LVL2 processing for accepted (green/striped) and rejected (orange/filled) events.

The right-hand plot of Fig. 4.11 shows the number of data requests during LVL2 processing, also obtained from COSMIC data, for accepted (green/dashed histogram) and rejected (orange/filled histogram) events. Following the early-rejection principle, rejected events cause less data requests than the accepted events. A certain fraction of the accepted events, however, generates no or only few data requests. These events have no or only few ROIs, and are passed-through at LVL2 (COSMIC HLT menu).

All LVL2 and EF chain results are monitored separately, before and after pre-scale and pass-through factors have been applied. Furthermore, all chain results are monitored on a per step level. This allows to assess the trigger's step-wise event reduction. The information can also be monitored for groups of chains.

One important client of the chain result monitoring is the HLT on-line rate calculation. Since the HLT is an asynchronous and distributed system, overall trigger rates cannot be calculated at each node separately. Instead, the combined information from all nodes is used. The HLT trigger rates comprise the total-acceptance rate as well as rates of all individual chains at each step. The LVL2 (EF) rates are determined by multiplying the LVL1 (LVL2) input rate with the ratio of accepted to total input events. LVL1 information is available via the CTP.

An extensive timing monitoring has been implemented. It comprises, for both trigger levels, the following timers:

- overall HLT Steering execution time, including all sub-systems; (also the data retrieval time);
- overall HLT Steering execution time broken down into rejected and accepted events;
- total execution time of the combined trigger chains as well as the individual chains, including all executed algorithms;
- total execution time of each trigger sequence, including all executed algorithms;
- total execution time of each algorithm;
- execution time of the Steering components: result builder, level converter, and the monitoring itself.

Further quantities which are monitored include: HLT errors that occur during event processing (cf. Section 4.7). The TE numbers are counted and monitored for every type. This includes TEs which represent the LVL1 ROIs (and LVL1 thresholds). The TE monitoring information allows for an additional monitoring of the trigger sequences' performance and selectivity. Additionally, the LVL1 and HLT ROIs'  $\eta$  and  $\phi$  are monitored in order to spot malfunctioning sub-detectors or triggers. Differences between two trigger steps or levels provides a good handle to evaluate the refined reconstruction in the step-wise event processing.

## 4.10 Performance and Validation

The full HLT system, including the Steering and the various HLT algorithms, has been tested, and their performance been measured, in a series of technical runs, in off-line production, as well as in a long period of cosmic data-taking [89, 104, 105]. It has been run for many hours in a stable manner, which indicates that a reasonable level of robustness (in terms of software code, memory leaks etc. in the Steering) has been achieved. These tests will continue in preparation for the start of p-p collisions in 2009.

In technical runs the TDAQ system runs on simulated data which is pre-loaded into the ROS computer nodes. After each major software release, a series of technical runs are performed in order to spot and fix software issues, and more generally integrate the HLT software into the DAQ on-line environment. The resulting software releases are subsequently used for cosmic ray data-taking.

The trigger system has been commissioned with increasingly complex menus (up to about 500 triggers) reading data from all detectors. Initially in autumn 2008, the HLT system was configured in a transparent mode in which the HLT selection is run but every incoming event is accepted (i.e. full pass-through mode). Running in this mode, HLT results of both event types, those which would have been accepted and rejected, have been validated by thorough comparison to off-line

---



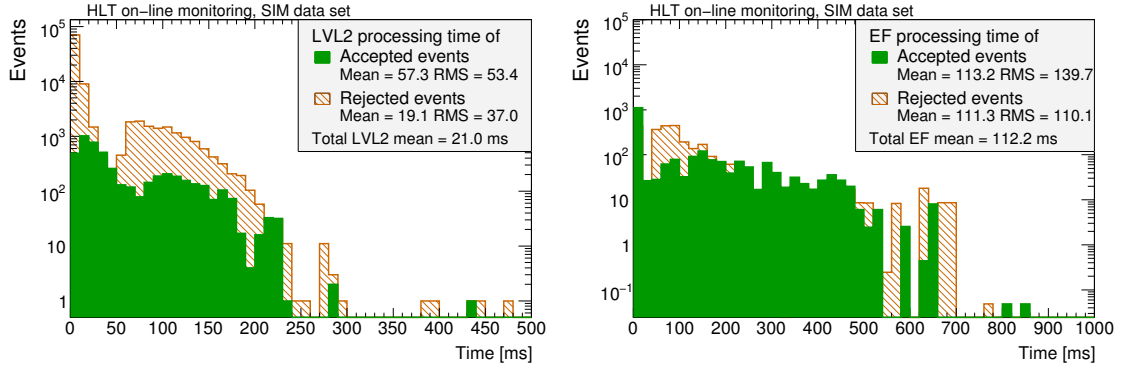


**Figure 4.12:** LVL2 (left) and EF (right) processing time for accepted (green/filled histogram) and rejected events (orange/dashed histogram). The data are obtained from the Sim dataset, see text.

reconstruction. A further test has been to re-run the full HLT system off-line and compare all results in detail with their on-line counterparts.

In later cosmic data-taking periods, the HLT system participated in the on-line event selection: standard LVL2 tracking algorithms were employed to perform a full inner detector scan and thus preserve the full dataset of muons passing through the inner detector independently of the total rate of the LVL1 trigger.

#### 4.10.1 Timing performance

The timing performance of the HLT Steering has been measured on simulated as well as cosmic data. Timing measurements on the simulated data used the latest draft trigger menu for  $10^{31} \text{ cm}^{-2} \text{ s}^{-1}$  (see Chapter 5), including all pre-scale factors, while various commissioning menus were employed during the cosmic data-taking. The main purpose of the commissioning menus was to study all aspects of the whole trigger system. Consequently, most trigger components were run in full debug mode, several similar algorithms were used to cross-check results, many instances of the same algorithms were run with slightly different configurations, and – particularly important for the time measurements – the tracking algorithms performed a full inner detector scan opposed to reading detector data only around the given ROI(s). Hence, absolute time measurements from the cosmic data have to be seen as upper limits.

The time measurements with the SIM dataset were conducted as follows: Standard ATLAS raw event data files, similar to the TDAQ output after an EF accept, were generated from the SIM dataset. Subsequently, the LVL2 and EF processing-unit simulations (athenaMT and athenaPT) processed the raw event data files. A computer with an Intel(R) Xeon(R) CPU E5420 at 2.33 GHz with 4 cores was used to run a recent release of the ATLAS software (14.5.0.5 AtlasProduction). This computer configuration is close to the final setup which is used for the HLT on-line farm nodes.

Fig. 4.12 shows the measured overall processing time of LVL2 (left) and EF (right) for accepted (green/filled histogram) and rejected events (orange/stripped histogram). It should be pointed out that the LVL2 data retrieval time contribution is missing since this simulation was not run in the

full TDAQ system (no ROB and network readout delays). Therefore, approximately 0.5 to 1.0 ms have to be added to the total LVL2 time consumption for every (not cached) data request per event. Nonetheless, with an average of 4 to 5 ROIs per event and around 3 data requests per ROI in LVL2, the measured mean LVL2 time of 21 ms is still consistent with the available processing power that allows for 40 ms. For the EF timing, the average 112 ms are well within the planned time budget of the order of 4 s.

The effect of early-rejection can be seen in Fig. 4.12: the mean time spent on rejecting LVL2 events is 19.1 ms whereas an average of nearly 60 ms are dedicated to accepted LVL2 events. In the EF, however, the mean time difference for rejecting and accepting an event is not very pronounced. There are mainly two effects: one concerning the long processing time to reject EF events, and another effect that causes many EF events to be accepted after very little execution time.

The first effect is because the EF resembles more the off-line reconstruction software than the fast LVL2 algorithms: hypothesis cuts are mostly applied only after all reconstruction tools have finished. In the trigger configuration of EF, many triggers use long sequences of FEX algorithms with no intermediate hypothesis testing, or similarly trigger chains where all processing is done in a single chain step. In such cases, all relatively slow FEX algorithms need to be executed on each input TE (ROI) as there is no intermediate step to test the candidate and potentially stop further processing. One such example is the EF trigger algorithm sequence of electron tracking (generation of the TE `EF_e20_mediumlid`) which consists of 14 FEX algorithms prior to a single hypothesis testing algorithm. This suboptimal trigger configuration causes a higher time consumption for rejected events: no clear peak of rejected EF events in the lower time bins. It also indicates potential for improvements in the EF trigger menu: small and simple hypothesis testing algorithms can be added in-between the long sequences of FEX algorithms.

The other feature of the EF timing shown in Fig. 4.12 is the peak of accepted EF events in the lowest processing time bin. Events falling into this bin can be characterised as: almost no processing is performed in EF, and accepted by HLT. It is due to events which normally failed LVL2 but have an active LVL2 pass-through flag. No EF trigger algorithms can run in such an event because all TEs (ROIs) have been deactivated already. Since the active LVL2 pass-through flag is propagated by default to EF, these events are immediately accepted by EF.

The time contribution of the HLT Steering has been assessed by running an empty trigger menu. The mean processing times are 3.2 ms (LVL2) and 3.9 ms (EF) which correspond to about 15% (LVL2) and 3.5% (EF) of the total processing times. The time contributions of the built-in monitoring tools are estimated to be 13% (LVL2) and < 1% (EF). This meets the aim that the Steering overhead should be small compared to the algorithm time.

To see the effect of algorithm caching, the trigger was run with the mechanism disabled. It was shown that caching provides roughly a factor five reduction in time [106]. The benefit will vary depending on the configuration and the event data.

Fig. 4.13 lists the mean, mean + RMS, and maximum execution time of the different LVL2 algorithms for the SIM dataset (left) and a COSMIC run (right). The entries are order by the mean time and only the first 21 are shown. One can see that most time is spent on full detector scan algorithms (`TrigIDSCAN_FullScan`, `TrigTRTSegFinder`) and on the minimum bias algorithm (`TrigL2MinBiasSPC_Fex`) which essentially also performs a full inner detector scan.

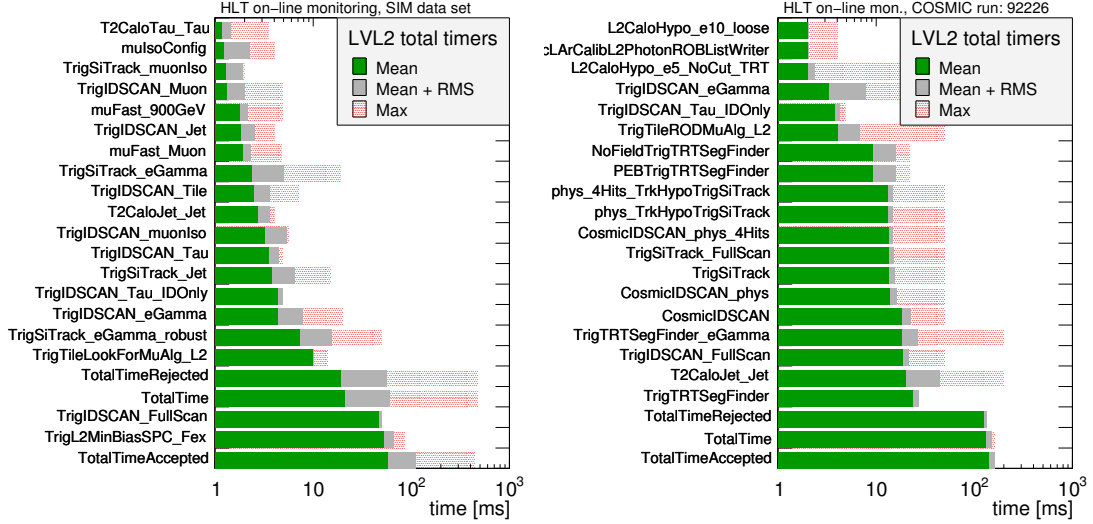


**Figure 4.13:** Selection of the most time consuming (on average) LVL2 algorithms and the total LVL2 times shown for the SIM (left) and COSMIC (right) datasets, see text in Section 4.9. Mean (filled/green histogram), mean + RMS (dotted/blue bars), and maximum time (striped/red) are given for each algorithm/total timer. Note that different trigger menus were employed for the SIM and COSMIC datasets, see text.

For the COSMIC run 92226, Fig. 4.13 unfolds the contributions to the high mean LVL2 processing time of 130 ms. All three tracking algorithms (`TrigIDSCAN`, `TrigTRTSegFinder`, `TrigSiTrack`) run in full scan mode, with varying hypothesis configuration, each consuming between 10 and 20 ms. Algorithm caching should reduce the number of executions to three. Due to the special commissioning conditions, however, caching was not in place for the full scan algorithms. Also the little time difference between accepted events (140 ms) and rejected events (125 ms) is caused by the dominating time of the full scan algorithms which were run on every LVL1 event. It is noteworthy that the mean processing time of `TrigIDSCAN_FullScan` is 45.9 ms in the SIM data and 18.5 ms in the COSMIC run. This is mainly caused by the higher hit occupancy and number of tracks in the SIM data compared to the COSMIC run.

#### 4.10.2 Validation of the Pre-scale and Pass-through Implementation

The Steering implementation of the PS and PT mechanisms can be tested by comparing the expected to the observed event numbers. Fig. 4.14 shows, for a selection of LVL2 (left) and EF (right) trigger chains, the number of events each trigger chain was run (black/cross-lines bars), passed its selection criteria (blue/striped bars), passed after PS (red/dotted bars), and passed after PS and PT (green/filled bars). All data are from the SIM data set. It can be seen that the LVL2 `e10` and `e12` triggers are active for the same number of events. This is expected because both start from the same LVL1 trigger item `L1_EM7`.

The LVL2 trigger chain `L2_em20_passHLT` is configured with a PS factor of 750 yielding an expected reduction of  $1/750 \simeq 0.0013$  which is in agreement with the observed reduction of  $0.0017 \pm 0.0008$  (the error is due to statistics). The LVL2 trigger chain `L2_e25i_loose` is

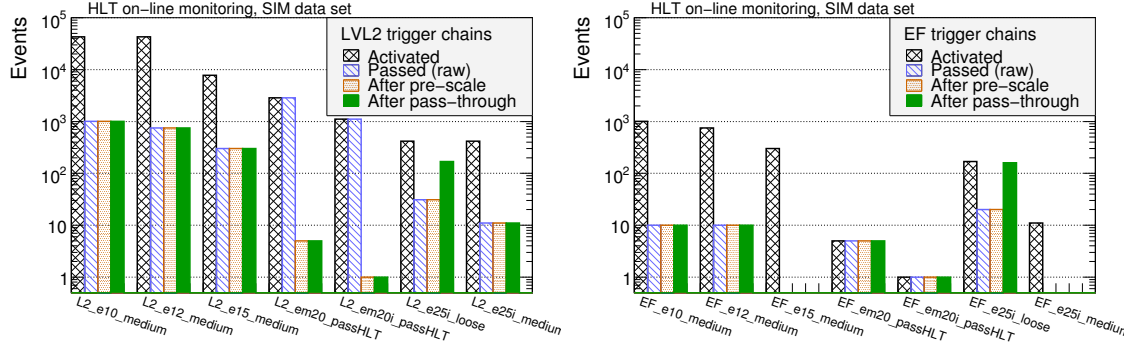


**Figure 4.14:** A selected subset of LVL2 (left) and EF (right) trigger chain results. For each chain, the following event numbers are given: chain was run (black/cross-lines), chain passed before PS, PT (blue/striped), chain passed after PS (red/dotted), and chain passed after PS and PT (green/filled). Both plots are obtained from the SIM data, see text.

configured with PS and PT factors of 1 and 3, respectively. Again, the expected factor of  $1/3 \simeq 0.33$  is in agreement with the observed value which is found to be  $0.36 \pm 0.04$ .<sup>10</sup>

As the names suggest, the EF trigger chains `EF_em20_passHLT` and `EF_em20i_passHLT` pass-through all events. This is not the case for the EF chain `EF_e25i_loose`, which refines the cluster, the track, and the matching in three steps. It is configured with the default PS of 0 and PT of 1 and hence cannot assign the PS or PT flag to events. It does, however, inherit events with an active PT flag from LVL2. From Eqs. (4.2) and (4.3), we obtain  $N_{PT}^{\text{flagged\_L2}} = 138.3$ ,  $N_{PT}^{\text{flagged\_EF}} = 0$ , and  $N_{\text{raw}}^{\text{accept\_EF}} = 20.4$  yielding a total number of expected events of 158.7 which agrees with the observed value of  $161 \pm 13$ .

Using toy experiments, Eqs. (4.1) to (4.3) have also been validated for complex trigger setups where PS and PT factors were set for both LVL2 and EF, and with the option to switch LVL2 PT inheritance on and off (cf. Section 4.8).

### 4.10.3 Cosmics Validation

In the beginning of the ATLAS cosmic data-taking, the HLT was run in a transparent mode, i.e. no events were rejected in the HLT, although algorithms were running. This has been used to intensively study and debug the full HLT system.

Starting in September 2008, the HLT actively joined the on-line cosmic event selection: LVL2 algorithms scanned the inner detector (ID) to enrich a physics data stream with ID muon tracks. Fig. 4.15 shows an ATLAS event display of a cosmic ray with hits in the barrel ID, seen and triggered by LVL2 (run 90127). The solenoid magnetic field was off in this run.

The use of LVL2 cosmic trackers has been rendered possible by the validation work of an ATLAS task-force which studied and optimised the LVL2 trackers' efficiencies and fake rates with respect to off-line reconstructed tracks. In the following a brief overview is given.

<sup>10</sup>From Eq. (4.1), we get  $1/F_{PT}^{\text{L2}} = (N_{PT}^{\text{passed\_L2}} - N_{PS}^{\text{passed\_L2}})/(N^{\text{active\_L2}} - N_{PS}^{\text{passed\_L2}})$ .

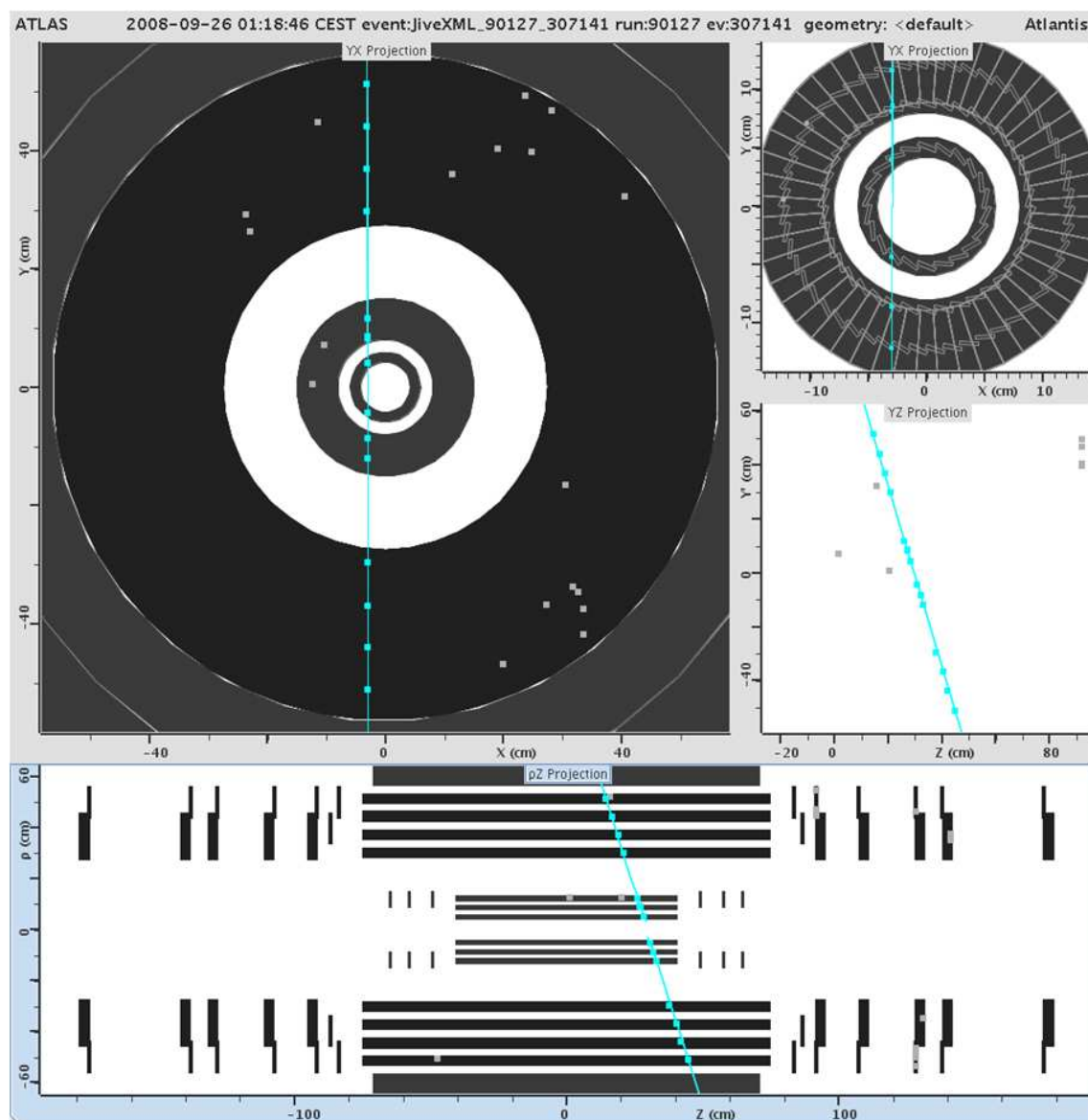


**Figure 4.15:** ATLAS event display of a cosmic ray with hits in the barrel inner detector, seen and triggered by LVL2 (run 90127). The solenoid magnetic field was off.

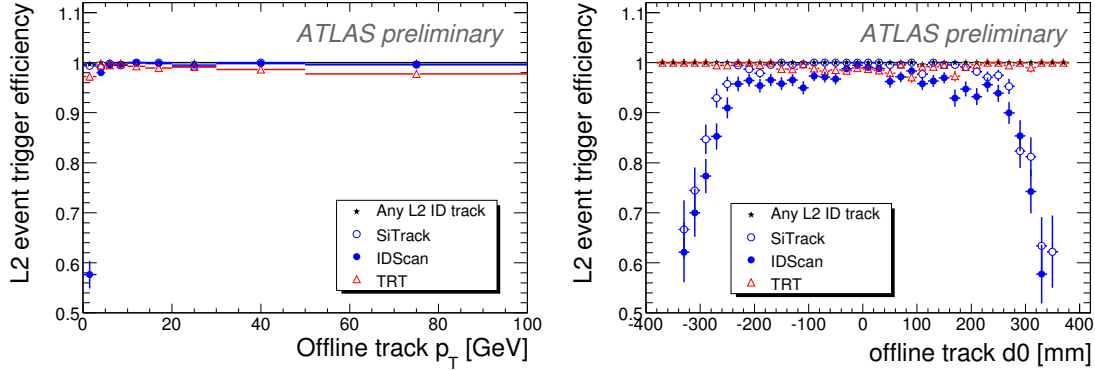


**Figure 4.16:** LVL2 reconstruction efficiency for cosmic ray tracks with respect to off-line reconstruction, as a function of the track transverse momentum  $p_T$  (left) and of the track impact parameter  $d_0$  (right). Different symbols indicate different LVL2 algorithms as shown in the legend.

LVL1 muon triggers in the barrel and end-caps have a high rate for cosmic muons. The fraction that contains an ID track, however, is low.<sup>11</sup> HLT (LVL2) tracking was introduced to exercise the HLT system with the goal of increasing the rate of ID tracks.

Three tracking algorithms are available at LVL2: TrigTRTSegFinder, SiTrack, and IDSCAN. As the names suggest, the first one searches for tracks in the TRT, and the latter two scan the Pixel and SCT detectors respectively for tracks. All three algorithms have been studied in cosmic runs with and without the solenoid magnetic field.

The main aspects covered are:

- *Efficiencies:* The efficiencies of the three LVL2 tracking algorithms were studied stand-alone as well as in combined mode (running all algorithms, and trigger on the logical-OR). The efficiency was defined with respect to off-line reconstructed tracks and for various track selections (standard off-line definitions).
- *Fake rate:* The rate of fake tracks was estimated for the tracking algorithms from a random trigger stream.
- *Monte Carlo comparison:* preliminary studies compared the data distribution of track parameters with the MC expectations.
- *Correlations* between the LVL2 ID tracks and LVL2 stand-alone muons were tested and quantified.

As part of these studies, the HLT algorithms' parameters have been tuned for cosmic data (including timing, thresholds etc.).

Fig. 4.16 shows the obtained LVL2 efficiencies for golden silicon tracks<sup>12</sup> as a function of the off-line track transverse momentum and depending on the track impact parameter. Errors were

<sup>11</sup>Simulations of cosmic data predict a rate of approximately 0.5 Hz of tracks going through the Pixel detector. The LVL1 muon triggers provided a rate of about 0.03 Hz due to a relatively low efficiency for tracks going through the ID.

<sup>12</sup>Golden silicon tracks are defined to contain at least 3 silicon space points in the upper and 3 in the lower ID.

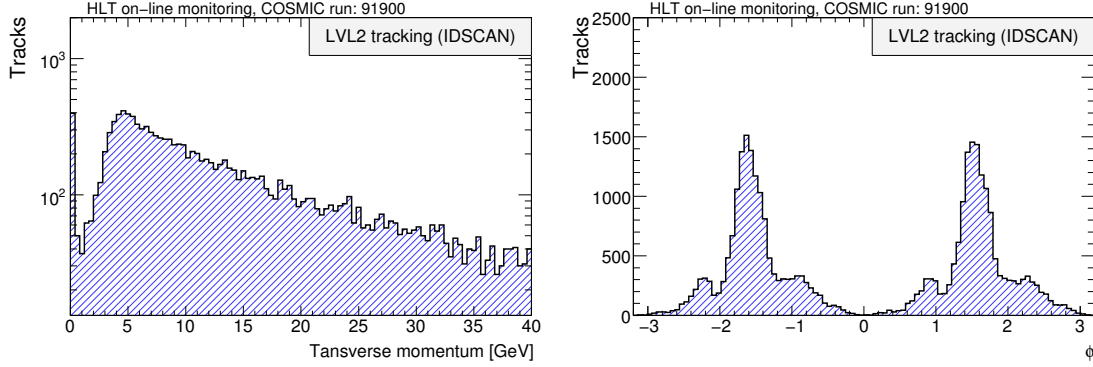


**Figure 4.17:** LVL2 IDSCAN track distribution of  $p_T$  (left) and  $\phi$  (right), obtained from cosmic run 91900. Note that the peak at  $p_T \simeq 0$  is due to tracks for which the track-fitter failed (either because of very small or very high momentum).

estimated using the binomial error formulae ( $\sqrt{\varepsilon(1-\varepsilon)/N}$ ) and are therefore zero at  $\varepsilon = 1$ . It was also shown that the LVL2 tracks are well correlated with LVL2 stand-alone muons in  $\eta$  and  $\phi$ .

Following these findings, ATLAS activated LVL2 tracking in the cosmic runs and started to successfully select large statistics samples of ID muon tracks. Fig. 4.17 shows the  $p_T$  (left) and  $\phi$  distribution of tracks found by IDSCAN. Both plots are obtained from HLT on-line monitoring of the cosmic run 91900.

The Steering, at the heart of the HLT system, contributed to this first effective HLT on-line event selection of cosmic data. Its design and implementation were found to be satisfactory: no substantial design flaws have been spotted, no major changes were requested.

Together with the full HLT system, the Steering's flexibility enabled the employment of the LVL2 cosmic track finder algorithms whose setup differs in some ways from the nominal HLT design. It is noteworthy to point out these differences, in particular because it indicates which parts of the HLT and Steering were used and hence validated, and which were not.

In terms of the Steering design, the main characteristics of the LVL2 cosmic tracking setup are as follows.

*No trigger chain seeding:* the cosmic tracking LVL2 trigger chains start from any LVL1 accepted event.<sup>13</sup> By default, one LVL2 (EF) trigger chain is only activated if the single preceding LVL1 (LVL2) trigger chain (item) fired.

*No ROI mechanism:* the LVL2 cosmic tracking algorithms do not start from any LVL1 ROI. In other words, the full ID scan is performed no matter what ROIs are present.<sup>14</sup>

This shows that the Steering is compliant with the demanding requirements of commissioning and cosmic running. Concurrently, however, it also shows that the LVL1–LVL2 interface, i.e. trigger chain seeding and algorithm seeding through ROIs, is not fully validated yet with real data.

HLT validation studies with cosmic ray data continue. A full validation of the ATLAS trigger

<sup>13</sup>an HLT chain can be configured without a preceding trigger (lower chain).

<sup>14</sup>the AllTEAlgo (cf. Section 4.5) runs once per event no matter how many input ROIs (TEs) are present.



system, however, will only be possible with LHC collision data.

## **4.11 Conclusions**

The HLT Steering implements the key features of the ATLAS HLT event selection strategy: seeded data access and reconstruction through the ROI mechanism, and step-wise reconstruction for early-rejection. It supports and facilitates the building of complex menus from the simple building blocks of chains, sequences and algorithms. The built-in caching mechanism saves valuable processing time and simplifies the configuration. The time overhead of the Steering is modest. It is well instrumented for monitoring which is vital for running on-line. It has already been used successfully in technical and cosmic runs.



## Chapter 5

# Trigger Menu

The ATLAS trigger menu is a configurable trigger selection table. It describes all triggers of the three levels: LVL1, LVL2, and EF. The latest draft trigger menu for running at  $L = 10^{31} \text{ cm}^{-2} \text{ s}^{-1}$  at 10 TeV centre-of-mass (CM) energy is used to exemplify its variety and complexity, which is constructed from simple building blocks, and must be handled by the HLT Steering. By definition, all proposed trigger menus (for various luminosities) are preliminary and represent work in progress. A comprehensive description of the trigger menu can be found in Ref. [26].<sup>1</sup>

Section 5.1 explains how the trigger menu is organised, and divided into so-called slices, as well as certain naming conventions. In Section 5.2 the ATLAS draft trigger menu for  $10^{31} \text{ cm}^{-2} \text{ s}^{-1}$  is presented. The primary physics triggers are given along with the expected trigger rates.

### 5.1 Organisation and Conventions

The trigger menu consists of a multitude of triggers: LVL1 is limited to 256, whereas HLT is basically unlimited. At the time of writing, the ATLAS  $10^{31} \text{ cm}^{-2} \text{ s}^{-1}$  menu — which is a subset of the full trigger menu — bundles 174 LVL1 trigger items, 146 LVL2 trigger chains, and 149 EF chains.<sup>2</sup> It is therefore important to sub-divide the menu into smaller organisational units.

Triggers can be classified according to the required physics object type(s) (electron, photon, jet, electron + jet, etc.), the multiplicity (e.g. single electron, multi electrons), and category/purpose (physics, performance, calibration, etc.). The trigger menu is primarily organised in so-called *slices*, i.e. depending on the physics object type: Minimum bias, electron/photon (EGamma), tau, muon, B-physics, jet, b-jets, missing energy/total energy, and calibration.

Combined (or multi-object) triggers, e.g. electron+jet, are either contained in the slice of the main (first) object, or inserted into a so-called *combined slice*. All slices are further sub-divided into: primary triggers, supporting triggers, backup triggers, and calibration triggers. Primary triggers

---

<sup>1</sup>The latest up-to-date ATLAS trigger menus can be found on the web-page <https://twiki.cern.ch/twiki/bin/view/Atlas/TriggerPhysicsMenu>.

<sup>2</sup>Several LVL1 trigger items are not yet followed up at LVL2.

are used to accumulate the data sample for a physics or performance study. A supporting trigger is used to measure some property of a primary trigger. Typical examples are: efficiency triggers, monitoring triggers, tracking study triggers, isolation study triggers, and multi-object triggers (will be needed at higher luminosities). Backup triggers may be used if the rate is higher or lower than we expect. Finally, calibration triggers are used explicitly to collect data for detector calibration.

The naming convention for LVL1 trigger items and HLT trigger chains follows from the LVL1 ROI threshold types:

LVL1 ROI Type	LVL1 name	HLT name
Electromagnetic	EM	e (electron)
		g (gamma)
		em (electromagnetic) - not yet classified as e or g
Muon	MU	mu
Tau	TAU	tau
Jet	J	j
Forward jets (+z)	FJ	fj
Backward jets (-z)	BJ	
Total transverse energy	TE	te
Total energy from jets	JE	je
Missing energy	XE	xe

These LVL1 (HLT) names, together with a number indicating the threshold value (should be within 10% of the value obtained off-line) and the optional “I” (“i”) for isolation criteria, build the ROI threshold (Trigger element (TE)) names and thus serve as the basic constituent of trigger names: LVL1 trigger items (HLT trigger chains) are formed from logical combinations of ROI thresholds (trigger elements (TEs)), cf. Sections 4.1.1 and 4.3.

Trigger item/chain names are, by convention, the concatenation of all required objects (ROIs/TEs) separated by a “-” symbol, and prefixed by a trigger level specifier (L1, L2, or EF). Multiple objects of the same type are combined and prefixed with the multiplicity number. The logical NOT condition is specified with a “v” prefix.

Some instructive examples illustrate this naming convention:

Sample trigger name	Description
L1_EM20I	LVL1 trigger item that requires: at least one ROI of type EM which has passed the 20 GeV threshold and the isolation requirements.
L2_2e20i	LVL2 trigger chain that requires: at least two active TEs named e20i (passed through all LVL2 algorithms)
L1_J70_XE30	LVL1 trigger item that requires: at least one ROI of type J which has passed the 70 GeV threshold, and a LVL1 XE trigger which has passed the 30 GeV threshold.
L1_J70_vFJ20	LVL1 trigger item that requires: at least one ROI of type J which has passed the 70 GeV threshold, and not any ROI of type FJ which has passed the 20 GeV threshold.
EF_tau20i_xe30	EF trigger chain that requires: at least one active TE named tau20i, and at least one active TE named xe30.

These generic trigger names can be extended with labels to indicate additional selection criteria, e.g. `_loose`, and `_medium` for the electron selection (track quality, cluster shape, track-cluster matching), or `_noMu` for missing energy triggers not including the muon correction.

## 5.2 Trigger Menu for $L = 10^{31} \text{ cm}^{-2} \text{ s}^{-1}$

The scheduled LHC running in 2009/2010 foresees an initial machine luminosity of up to  $\sim 10^{31} \text{ cm}^{-2} \text{ s}^{-1}$ , and 10 TeV CM energy. The latest ATLAS draft trigger menu for these LHC conditions is outlined in the following.

The bulk of this trigger menu is composed of commissioning, monitoring, and calibration triggers. A small fraction of the triggers are for physics studies, mainly concerning Standard Model processes. Therefore, most triggers will be combinations of low thresholds, loose selections, and operation in pass-through mode wherever possible.

Grouped by physics slice, all primary physics triggers with the expected rates are introduced. Additionally, as an example, the electron/photon trigger slice is presented in more detail, including triggers from all categories.

Trigger rates are determined off-line from a sample of enhanced minimum bias MC data. A full description can be found in Ref. [26]. All rates presented in the following are for  $L = 10^{31} \text{ cm}^{-2} \text{ s}^{-1}$ , 10 TeV CM energy, and the errors are only due to statistics of the dataset.

Primary physics triggers of the *Minimum bias slice*:

LVL1 item	PS (LVL1, LVL2)	LVL2 chain	EF chain	EF Rate [Hz]
L1_RDO_FILLED	40955, 163	L2_MbSpTrk	EF_MbSpTrk	$\sim 4$
L1_MBTS	184000, 1	L2_Mbts	EF_Mbts	$\sim 4$

The L1\_RDO\_FILLED is a CTP internal trigger which selects random filled bunch crossings. Its

effective LVL1 pre-scale factor of 40955 results from the random trigger settings and the actual LVL1 pre-scale factor. The L2\_MbSpTrk trigger requires at least 40 spacepoint hits in Pixel and SCT. Its pre-scale factor of 163 will be adjusted to retain a rate of approximately 4 Hz. The EF\_MbSpTrk trigger is configured to pass-through all events.

The L1\_MBTS trigger is based on the minimum bias trigger scintillators (MBTS) which are designed to function only during initial data-taking at low luminosities. After 3-4 months of higher luminosity operation the scintillators will become inefficient due to radiation damage. Both HLT chains are configured to run in full pass-through mode.

Primary physics triggers of the *electron/photon slice*, which are all expected to run in a non pre-scaled mode (PS factor 1):

LVL1			LVL2		EF	
Item	Rate [Hz]	chain	Rate [Hz]	chain	Rate [Hz]	
L1_2EM3	$3270 \pm 30$	L2_2e5_medium	$10.5 \pm 0.2$	EF_2e5_medium	$1.5 \pm 0.6$	
L1_EM7	$2610 \pm 20$	L2_e10_medium	$79 \pm 4$	EF_e10_medium	$13 \pm 2$	
L1_EM18	$145 \pm 6$	L2_e20_loose	$8 \pm 1$	EF_e20_loose	$4 \pm 1$	
L1_EM100	$\sim 0$	L2_em105_passHLT	$\sim 0$	EF_em105_passHLT	$\sim 0$	
L1_EM18	$145 \pm 6$	L2_g20_loose	$15 \pm 2$	EF_g20_loose	$10 \pm 2$	

The `_passHLT` label means that no selection is performed (all events pass-through). All electron/photon triggers (primary, backup, supporting, and calibration) are listed in Table 5.1, where also the motivation/description is given.

Primary physics triggers of the *muon slice*, which are all expected to run in a non pre-scaled mode:

LVL1		LVL2		EF	
Item	Rate [Hz]	chain	Rate [Hz]	chain	Rate [Hz]
L1_MU10	$605 \pm 12$	L2_mu10	$14 \pm 2$	EF_mu10	$13 \pm 2$
L1_2MU4	$89 \pm 4$	L2_2mu4	$1.8 \pm 0.6$	EF_2mu4	$1.5 \pm 0.6$

The L2\_mu10 and L2\_2mu4 triggers are configured with pass-through factors of 100 and 50, respectively, in order to retain a small fraction of unbiased events for monitoring and validation. The physics motivation for the two triggers is: B-physics,  $W$  and  $Z$  bosons,  $t\bar{t}$ , Drell-Yan (mu10), and B-physics, Drell-Yan,  $J/\Psi$ ,  $\Upsilon$ ,  $Z$  boson (2mu4).

Primary physics triggers of the *tau slice*:

LVL1		EF	
Item	Rate [Hz]	chain	Rate [Hz]
L1_TAU9I	$457 \pm 5$	EF_tau16i_loose_EF_xe30	$4 \pm 1$
L1_TAU40	$28 \pm 3$	EF_tau50_loose	$1.1 \pm 0.5$
L1_2TAU9I	$170 \pm 6$	EF_2tau20i_loose	$1.5 \pm 0.6$

The intermediate LVL2 triggers are omitted for space reasons in the listing. The physics motivation for these primary tau triggers is: SM  $W \rightarrow \tau\nu$  (tau16i\_loose\_EF\_xe30); heavy Higgs,  $Z'$ , exotics ( tau50\_loose); and SM  $Z \rightarrow \tau\tau$ ,  $h \rightarrow \tau\tau$ , heavy Higgs,  $Z'$  (2tau20i\_loose).

Primary triggers of the *missing energy/total energy slice*:

Item	LVL1	PS	chain	LVL2	chain	EF
	Rate [Hz]			Rate [Hz]		Rate [Hz]
L1_XE70	$\sim 0$	-	L2_xe70	$\sim 0$	EF_xe70	$\sim 0$
L1_XE40	$\sim 0.4$	20	L2_xe40	$\sim 0.4$	EF_xe40	$\sim 0.05$

The possibility of removing the PS factor from the xe40 (and or a xe35) trigger is being considered. The motivation is to have a backup trigger for SM processes such as  $W \rightarrow e\nu$  and  $W \rightarrow \tau\nu$ . The missing energy/total energy slice further comprises several backup and supporting triggers with thresholds ranging from 15 GeV up to 80 GeV in steps of 5 GeV where the muon correction is included or not.

Primary triggers of the *jet slice*:

	LVL1		LVL2		EF	
Item	Rate [Hz]	PS	chain	PT	chain	PT
L1_J5	$\sim 0.07$	$3 \cdot 10^5$	L2_J5	1	EF_J10	1
L1_J10	$\sim 0.25$	$4.2 \cdot 10^4$	L2_J23	1	EF_J50	1
L1_J18	$\sim 0.4$	$6 \cdot 10^3$	L2_J50	1	EF_J80	1
L1_J23	$\sim 0.6$	$2 \cdot 10^3$	L2_J60	1	EF_J115	1
L1_J35	$\sim 0.5$	500	L2_J80	1	EF_J140	1
L1_J42	$\sim 1.4$	100	L2_J110	1	EF_J180	1
L1_J70	$\sim 1.6$	15	L2_J150	1	EF_J265	1
L1_J120	$3.1 \pm 0.8$	-	L2_J205	1	EF_J350	1
L1_3J10	$\sim 0.02$	$2 \cdot 10^4$	L2_3J15	1	EF_3J25	1
L1_3J18	$\sim 0.5$	100	L2_3J35	1	EF_3J60	1
L1_3J70	$\sim 0.4$	-	L2_3J120	1	EF_3J180	1
L1_4J10	$\sim 0.02$	$4 \cdot 10^3$	L2_4J15	1	EF_4J45	1
L1_4J18	$\sim 0.09$	100	L2_4J35	1	EF_4J80	1
L1_4J23	$3.1 \pm 0.8$	-	L2_4J50	1	EF_4J95	1
L1_4J35	$1.1 \pm 0.5$	-	L2_4J80	1	EF_4J125	1

Note that most single and multijet triggers are pre-scaled at LVL1 and all are fully passed-through (PT factor 1) at LVL2 and EF. Therefore, the LVL2 and EF rates are equivalent to the LVL1 rates. Single jet triggers with and without PS factors are needed for cross section studies. The jet triggers which are not pre-scaled (L1\_J120, L1\_3J70, L1\_4J23, L1\_4J35) are expected to be used in search studies for new physics.

Triggers for forward jets and total energy from jets are configured in a similar manner: high PT factors at LVL1 which gradually decrease as the threshold rises. Not pre-scaled forward jet

trigger are FJ120, 2FJ35, and 2FJ70 with expected rates of approximately 0.0, 0.2, and 0.0 Hz, respectively. Out of the four total-energy-in-jet triggers, JE340 is not pre-scaled with an expected rate of about 0.9 Hz.

Triggers in the *B-physics slice* are targeted for specific decay channels, e.g.  $B \rightarrow J/\Psi + X$ ,  $D_S \rightarrow \phi(KK)\pi$ ,  $J/\Psi \rightarrow ee$ . They start from LVL1 muon and electromagnetic ROIs and then apply cuts on the invariant mass during HLT processing.

Multi-object triggers will become important with higher luminosities. Therefore, they are studied as part of supporting triggers but are not considered primary triggers in the  $10^{31}$  trigger menu.

---

**Table 5.1:** Summary of the electron/photon triggers for  $L = 10^{31} \text{ cm}^{-2} \text{ s}^{-1}$ . The expected trigger rates were obtained from a sample of minimum bias MC data, with 10 TeV CM energy.

Trigger name	EF rate [Hz]	PS	Motivation/Description
<b>Primary physics triggers</b>			
2e5_medium	$1.5 \pm 0.6$	-	$J/\Psi$ , $\Upsilon$ , Drell-Yan
e10_medium	$13 \pm 2$	-	b/c, Drell-Yan, $Z \rightarrow \tau\tau$
e20_loose	$4 \pm 1$	-	$W$ and $Z$ bosons, $t\bar{t}$
em105_passHLT	$\sim 0$	-	exotics
g20_loose	$10 \pm 2$	-	direct photons
<b>Supporting triggers: calculate efficiency of primary triggers</b>			
e5_medium	$4.6 \pm 0.1$	60	Efficiency for 2e5_medium, e10_medium
g10_loose	$\sim 0.6$	100	Efficiency for g20_loose
<b>Supporting triggers: monitor, debug HLT</b>			
e20_loose_passHLT	$\sim 0.5$	750	no cuts in HLT
e20_loose_passL2	$\sim 0.2$	200	no cuts in L2
e20_loose_passEF	$\sim 0.1$	125	no cuts in EF
g20_loose_passHLT	$\sim 0.5$	750	no cuts in HLT
g20_loose_passL2	not yet in menu		no cuts in L2
g20_loose_passEF	not yet in menu		no cuts in EF
<b>Supporting triggers: tracking</b>			
e10_medium_SiTrk	$14 \pm 2$	-	study SiTrk LVL2 tracking algorithm
e10_medium_IDSCAN	not yet in menu		study IDSCAN LVL2 tracking algorithm
e10_medium_TRT	not yet in menu		study TRTSegFinder LVL2 tracking algorithm
<b>Supporting triggers: isolation</b>			
e20i_loose	$2 \pm 0.7$	-	study isolation of e20_loose
g20i_loose	$3 \pm 0.8$	-	study isolation of g20_loose
<b>Special triggers: Multi objects</b>			
2e10_medium	not yet in menu		
2g20_loose	$<< 1$	-	
<b>Backup triggers:</b>			
2e5_medium1	$\sim 0.5$	-	can replace 2e5_medium
2e6_medium	$\sim 0.5$	-	can replace 2e5_medium
2e6_medium1	$\sim 0.5$	-	can replace 2e5_medium
e12_medium	$9 \pm 2$	-	can replace e10_medium
g25	$\sim 1.5$	-	can replace g20_loose
<b>Calibration triggers: detector studies</b>			
g3_larcalib	$<< 1$	$6 \cdot 10^8$	
g10_larcalib	$\sim 0.5$	100	
g20_larcalib	$4 \pm 1$	-	
g20i_larcalib	$3 \pm 1$	-	





## Chapter 6

# Development of the Trigger User-Interface

The ATLAS trigger user-interface is designed to provide easy access to all on-line trigger results as well as the associated trigger menu. It is contained in the ATLAS off-line software to facilitate trigger-aware analyses ranging from standard physics studies to off-line debugging of the trigger system. A comprehensive description can be found in Ref. [107, 108]. An overview is given in the following, since the author significantly contributed to the concepts behind the trigger user-interface and the HLT event data model, as well as their implementation.

Section 6.1 presents the trigger data flow. Described are the on-line and off-line side of the data stream, consisting of the trigger decision, further HLT results, and the trigger configuration data. Section 6.2 details the content and structure of the LVL1 and HLT decision result object. The user-interface to the trigger data is introduced in Section 6.3 for standard off-line analyses, and in Section 6.4 for lightweight ROOT-based analyses. Section 6.5 presents an example trigger electron efficiency study.

### 6.1 Trigger Data Flow

ATLAS trigger data can be divided into event-wise and run-wise data. All trigger results created during event processing are part of the event-wise data stream. The trigger menu and all other trigger configuration information, on the other hand, are valid over a full run (or at least a luminosity block). Consequently, this data is managed separately. Fig. 6.1 shows the event-wise trigger data flow (red/dotted lines) and run-wise configuration data flow (red/solid lines) in the on-line (left side) as well as in the off-line (right side) environment [109].

The three trigger levels obtain all of their configuration information from a special trigger configuration database (TriggerDB). The TriggerDB provides all information that is needed to run the full on-line trigger. It includes the complete trigger menu with all pre-scaling and pass-through factors, all LVL1 hardware settings, and all HLT algorithm properties. Once a trigger configuration is put into the TriggerDB, it will be saved forever. This enables for example re-running the

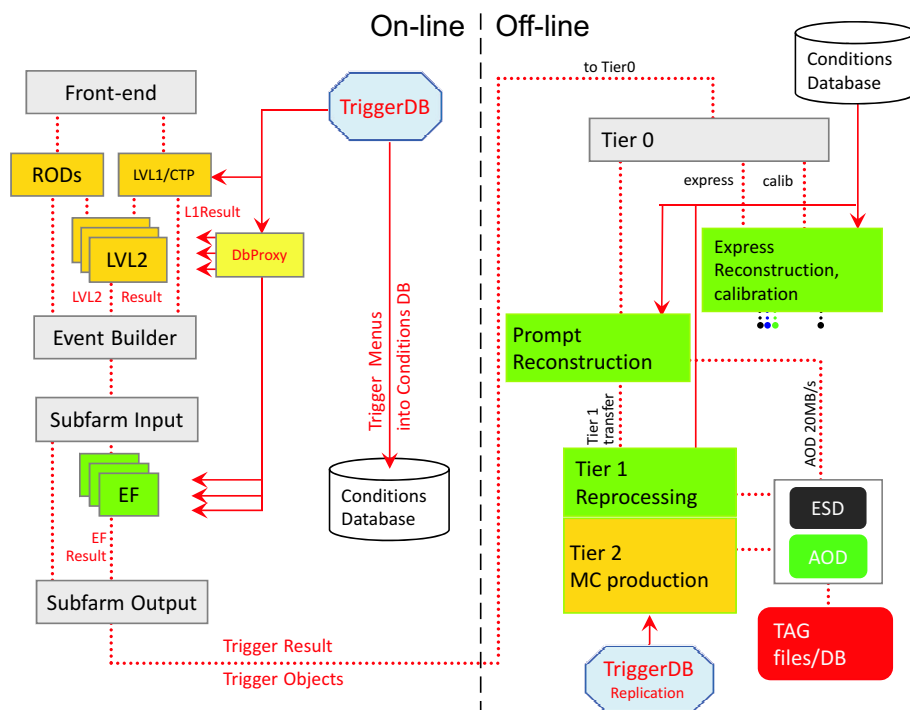


**Figure 6.1:** ATLAS event and trigger data flow diagram. Shown on the left side are the on-line event and trigger data flow from the front-end electronics, through the trigger system, to the output nodes (Subfarm Output); and on the right side the off-line data flow and event processing. Event-wise data flow is indicated by red/dotted lines, whereas the run-wise trigger configuration data flow is shown by red/solid lines. The labels are described in the text.

trigger off-line using the same trigger setup as at the time of data-taking. Special database proxies (labeled DbProxy in Fig. 6.1) enable fast concurrent data retrievals, as required by the large number of HLT nodes (several thousands).

A subset of the trigger configuration is also saved into the ATLAS conditions database. In contrast to the TriggerDB, the conditions database is accessible from outside the ATLAS on-line computer nodes: all ATLAS computing sites have access to the main conditions database or a local replication. The trigger configuration data in the conditions database is sufficient to fully interpret all trigger results in the raw event data stream. Monte Carlo production, however, requires the full TriggerDB in order to run the trigger simulation. Hence, the TriggerDB is replicated to the production sites.

The primary computing site at CERN is called Tier 0, while the terms Tier 1, 2, and 3 are used to describe secondary, tertiary etc. computing sites which are distributed around the world [110]. During the ATLAS off-line reconstruction, raw event data files are processed resulting in either event summary data (ESD) or analysis data object (AOD) files. As a part of this ESD or AOD reconstruction, all raw event-wise trigger data is merged and stored in one trigger result object per event. As is common in the ATLAS event data model, the trigger result class is transient/persistent separated.<sup>1</sup> The TAG files (or database) contain a few characteristic event quantities in order to quickly select interesting ESD or AOD files.

The run-wise trigger configuration data is read from the conditions database and saved into the analysis file header. This facilitates subsequent trigger usage: all trigger information, including the configuration, is available in the analysis files. Configuration information can also contain data with an interval of validity smaller than one full run, for example LVL1 pre-scales can be changed with every luminosity block (order of 1 min).

## 6.2 Trigger Decision Result

The trigger decision object holds all of the event-wise trigger information. Its content together with the size is listed in Table 6.1. In order to save disk space, the information is encoded. In particular, Steering and TriggerDB internal integers are used to identify trigger items and chains.

To decode the event-wise trigger decision, i.e. make it human-readable, the trigger configuration is required. In particular, it allows to:

- Map trigger names to the corresponding chain counter (HLT) or bit position (LVL1);
- Retrieve the full trigger definitions: LVL1 and HLT requirements (at each chain step);
- Obtain pre-scale (LVL1 and HLT), pass-through (HLT) factors, and the LVL1 trigger veto mask.

---

<sup>1</sup>Transient/persistent separation implies that the class is divided into one which is used for disk storage (persistent) and one for the actual use in the analysis software (transient). The main benefits are: Schema evolution (allows reading of old data from disk); and minimisation of used disk space (through the use of data compression).

---

**Table 6.1:** Content of the event-wise trigger decision object. *Active chains* are those which were run in the given event.

Trigger level	Description	Size
LVL1	Acceptance flags for all 256 LVL1 trigger items before and after the application of pre-scales and veto	$3 \times 256$ bits
HLT	Active chains: Acceptance flags before and after pre-scales and pass-throughs; Index of last successful chain step; Error codes which occurred within given chain; Chain identifier (chain counter).	3 bits per chain 7 bits per chain 6 bits per chain 16 bits per chain
HLT	Navigation data structure: Trigger Elements and their cross-linking User-defined list of trigger data objects (features), e.g. reconstructed EM clusters, tracks, etc.	Variable
HLT	Streaming tags, Steering internal errors, unique key of employed trigger menu	Variable

### 6.3 Trigger Decision Tool

The trigger decision tool (TDT) is the common trigger-user interface. It facilitates the use of trigger data in analysis files. The TDT is implemented in the ATLAS off-line framework. It was developed in 2007 and has been used in many physics and trigger studies since then.

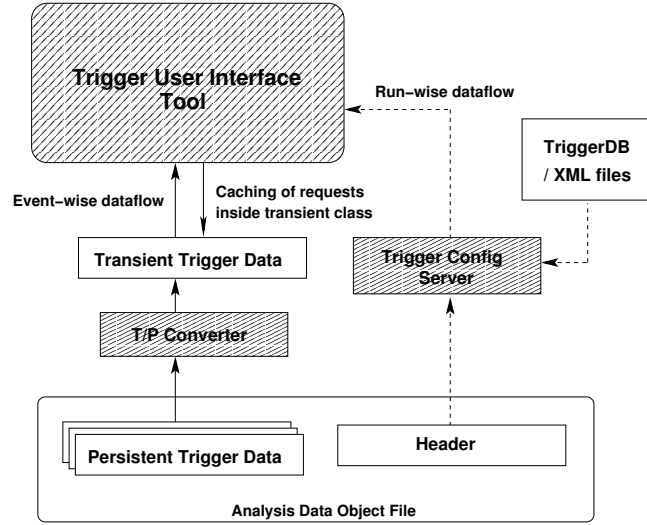
The main concept behind the TDT is to combine the encoded trigger event results with the trigger configuration data to provide the full trigger information in one common and user-friendly tool.

Fig. 6.2 illustrates the TDT design. For every event, the TDT requests the encoded trigger result object. The corresponding trigger configuration information is obtained from a trigger configuration service (TrigConfigSvc). Several complementary implementations of the TrigConfigSvc, all sharing the same abstract interface, support different configuration sources: TriggerDB, XML files, ATLAS conditions database, and the analysis file header. The TrigConfigSvc is also used in on-line trigger software.

The process of mapping event-wise trigger results to the configuration data is performed by the TDT only on demand. Once the mapping has been built for a given event, it is cached into the transient trigger result object to speed-up further queries.

The main use-cases covered by the TDT functionality can be summarised as:

- *Trigger aware analysis:* the TDT can be used to query (by name), whether a given event has passed a LVL1, LVL2, or EF trigger. It further provides the triggers' pre-scale, and pass-through factors as well as the corresponding flags.
- *Trigger studies:* The TDT can be used to retrieve any stored trigger objects, e.g. tracks,



**Figure 6.2:** Design of the trigger user-interface tool (trigger decision tool). Shown are the event-wise data retrieval of the encoded trigger result object, and the flow of trigger configuration data.

clusters, etc. Using the Navigation structure, it can distinguish between objects that failed and passed a given trigger. The TDT can map LVL1 to LVL2 to EF triggers and TEs (ROIs).

## 6.4 Trigger Access from ROOT

Recent developments, known as *AthenaROOTAccess* (ARA), made it possible to access ATLAS pool files (i.e. standard analysis files, e.g. AODs) directly from ROOT, without using the (entire) ATLAS off-line software framework (Athena).<sup>2</sup> However ARA makes use of the transient/persistent system of the off-line software framework. It is important to point out that analyses based on the ARA approach cannot:

- Make use of conditions data or the detector description;
- Utilise tools or services from the off-line software.

These limitations cause the TDT to be unusable in ARA-based analyses. The TDT itself is an Athena tool which relies on several other tools and services (e.g. TrigDecisionSvc) to access conditions data (trigger menu).

Developments to extend and improve the TDT, with the goal to remedy these issues, are in progress. A new TDT version is foreseen for later in 2009. For the time being, an alternative approach has been provided for ARA analyses. It is based on providing access to all basic trigger objects, including the trigger menu. Combining the trigger configuration with the event-wise trigger decision information, however, is left to the user. It has been shown (see next Section 6.5) that this ARA workaround is equivalently capable of providing access to trigger data as the TDT, at the expense of requiring more user code.

<sup>2</sup>More details can be found in: <https://twiki.cern.ch/twiki/bin/view/AtlasProtected/AthenaROOTAccess>

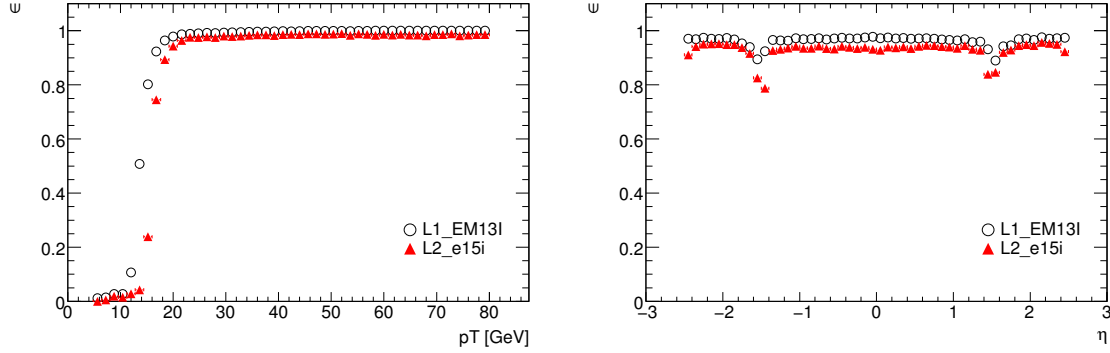


**Figure 6.3:** Trigger electron efficiencies of the LVL1 item `L1_EM13I` (open/circles) and the LVL2 chain `L2_e15i` (red-filled/triangles) as a function of the off-line electron variables transverse momentum (left) and pseudorapidity (right).

## 6.5 Example: Trigger efficiencies

The trigger data access has been exercised and validated using a trigger electron efficiency study. In this study, all trigger related data have been thoroughly tested: data from the TDT and the ARA based approach were compared, and results were cross-checked with the trigger log files.

The trigger electron efficiency was studied with respect to off-line reconstructed electrons. Therefore, a  $\Delta R = \sqrt{(\Delta\eta)^2 + (\Delta\phi)^2}$  matching between off-line and trigger electrons was performed. This requires, in particular, the following processing steps for every event:

1. Retrieve list of all off-line electrons (optionally, passing certain criteria).
2. Retrieve complete list of trigger electrons which satisfied the trigger item/chain of interest (e.g. `L2_e25i`). One important cross-check: the list must contain at least one electron if the (single) trigger fired.
3. Match trigger to off-line electrons by imposing a maximum  $\Delta R$ . Off-Line electron properties ( $\eta$ ,  $\phi$ ,  $p_T$ , etc.) can directly be accessed from the electron objects, whereas LVL1 ROIs and trigger LVL2/EF features (cluster, track) are needed for the trigger LVL1 and HLT electrons, respectively.

Fig. 6.3 shows the resulting trigger efficiencies of the LVL1 item `L1_EM13I` and the successive LVL2 chain `L2_e15i` as a function of the off-line electron variables  $p_T$  (left) and  $\eta$  (right). All efficiencies are with respect to off-line electrons which were reconstructed with the  $e/\gamma$  algorithm and have passed the tight electron requirements [50]. The `I/i` in the two trigger names denote isolation requirements. The employed dataset is a PYTHIA [111]  $Z \rightarrow ee$  simulation sample which passed through the full detector simulation. The obtained results are in agreement with those of standard ATLAS studies [26]. They show a few distinctive and expected features:

- turn-on not perfect at 15 GeV given thresholds set at LVL1 and LVL2,
- transition region between barrel and end-cap EM calorimeter visible at  $|\eta| \sim 1.4 - 1.5$ .

## **Part II**

# **Inclusive Supersymmetry Searches**





## Chapter 7

# Supersymmetry

Supersymmetry is one of the theoretically favoured theories for physics beyond the Standard Model (SM). This chapter introduces supersymmetry and gives an overview of the general ATLAS search strategy.

Section 7.1 briefly summarises the theoretical framework of supersymmetry. Following the common phenomenological approach, the Minimal Supersymmetric Standard Model (MSSM) is assumed. Its particle content is described, the important concept of R-parity is introduced, and the necessary soft symmetry breaking mechanism is outlined.

In Section 7.2 the leading order production modes and the typical decay chains of supersymmetry particles at the LHC are described. Section 7.3 presents current experimental limits on supersymmetry. Finally, Section 7.4 explains the inclusive ATLAS strategy to find supersymmetric signatures, and the basic ideas to measure the properties of supersymmetric particles and the fundamental parameters of the underlying theory after a possible discovery.

### 7.1 Theoretical Framework

Comprehensive descriptions of supersymmetry can be found in Ref. [39, 112, 113, 114]. A detailed discussion of its relevance for dark matter can be found for instance in Ref. [37]. This section summarises the basic concepts and outlines a few important features which are relevant for experimental searches at hadron colliders.

As discussed in Chapter 2, the main theoretical motivation for supersymmetry is that it offers an elegant solution to the infamous “hierarchy problem” [115]. By assuming a symmetry relating fermions and bosons, the potentially dangerous quantum correction contributions to scalar masses (the Higgs boson mass!) arising from the SM fermions are cancelled by similar loop correction terms that arise from the related scalars. This symmetry between fermions and bosons is called supersymmetry. The required relative minus signs in the loop contributions are naturally provided by the spin-statistics theorem for fermions and bosons.

The supersymmetry transformation that turns bosonic states into fermionic states, and vice versa,

is generated by the operator  $Q$

$$Q|\text{Boson}\rangle = |\text{Fermion}\rangle, \quad Q|\text{Fermion}\rangle = |\text{Boson}\rangle.$$

The possible forms of such a supersymmetry are constrained in order to provide an interacting quantum field theory that also holds chiral fermions. The generators  $Q$  and  $Q^\dagger$  (the hermitian conjugate of  $Q$ ) must therefore satisfy an algebra of anticommutation and commutation relations with the schematic form

$$\begin{aligned} \{Q, Q^\dagger\} &= P^\mu, \\ \{Q, Q\} &= \{Q^\dagger, Q^\dagger\} = 0, \\ [P^\mu, Q] &= [P^\mu, Q^\dagger] = 0, \end{aligned}$$

where  $P^\mu$  is the four-momentum generator of space-time translations.

The single-particle states of a supersymmetry theory are grouped in irreducible representations of the algebra, called *supermultiplets*. Two states belong to the same supermultiplet if one can be generated from the other by some combination of  $Q$  and  $Q^\dagger$  (plus some space-time translation and or rotation). A supermultiplet contains both boson and fermion states, which are called *superpartners*, such that the number of boson and fermion degrees of freedom are equal.<sup>1</sup> Furthermore, all members of a supermultiplet must have equal masses because the squared-mass operator  $P^2$  commutes with the generators  $Q$  and  $Q^\dagger$ . Finally, particles of the same supermultiplet must also be in the same representation of the gauge group, and hence have the same electric charge, weak isospin, and colour degrees of freedom. This is because the supersymmetry generators  $Q$  and  $Q^\dagger$  also commute with the generators of gauge transformations.

The simplest possible supermultiplet that is consistent with the above properties has a single Weyl fermion (two spin helicity states) and two real scalars (each with one degree of freedom). The two scalars are typically assembled into a complex scalar field. This type of particle assignment is called a *chiral* or *matter* supermultiplet.

The next-simplest arrangement contains a spin-1 vector boson. This boson must be a massless gauge boson (at least before spontaneous gauge symmetry breaking), if the theory is to be renormalizable. The two bosonic degrees of freedom (two helicity states) are balanced by a massless spin-1/2 Weyl fermion. Such fermion superpartners of the gauge bosons are called *gauginos*. This next-simplest combination is named a *gauge* or *vector* supermultiplet.

The chiral and gauge supermultiplets suffice to accommodate all fundamental SM particles.<sup>2</sup> Their superpartners all differ in spin by 1/2. The used naming conventions and the particle arrangements are as follows. SM fermions (quarks and leptons) must all be members of chiral supermultiplets.<sup>3</sup> The corresponding scalar partners are constructed by prepending an “s” (for scalar) to the name, as in: squarks, sleptons, sfermions, and so on. The left-handed and right-handed parts of the SM fermions belong to different supermultiplets since they transform differently under the gauge transformations. Therefore, each fermion has two complex scalar superpartners, one for each

<sup>1</sup>This can be shown from the basic commutation relations.

<sup>2</sup>The spin-2 graviton, however, would require a spin-3/2 superpartner, called *gravitino*.

<sup>3</sup>The reason being that only chiral supermultiplets can contain fermions whose left-handed parts transform differently under the gauge group than their right-handed parts.

**Table 7.1:** Chiral (top) and gauge (bottom) supermultiplets in the MSSM. Also given are their transformation properties under the SM gauge group  $SU(3)_C \times SU(2)_L \times U(1)_Y$ . The spin-0 fields are complex scalars, and the spin-1/2 fields are left-handed two-component Weyl fermions. Note that all these fields are the gauge eigenstates, as opposed to the mass eigenstates which can mix.

Chiral supermultiplets		spin-0	spin-1/2	spin-1	$SU(3)_C, SU(2)_L, U(1)_Y$
squarks, quarks ( $\times 3$ families)	$Q$	$(\tilde{u}_L, \tilde{d}_L)$	$(u, d)_L$	-	$(\mathbf{3}, \mathbf{2}, \frac{1}{6})$
	$\bar{u}$	$\tilde{u}_R^*$	$u_R^\dagger$	-	$(\bar{\mathbf{3}}, \mathbf{1}, -\frac{2}{3})$
	$\bar{d}$	$\tilde{d}_R^*$	$d_R^\dagger$	-	$(\bar{\mathbf{3}}, \mathbf{1}, \frac{1}{3})$
sleptons, leptons ( $\times 3$ families)	$L$	$(\tilde{\nu}, \tilde{e}_L)$	$(\nu, e)_L$	-	$(\mathbf{1}, \mathbf{2}, -\frac{1}{2})$
	$\bar{e}$	$\tilde{e}_R^*$	$e_R^\dagger$	-	$(\mathbf{1}, \mathbf{1}, 1)$
Higgs, higgsinos	$H_u$	$(H_u^+, H_u^0)$	$(\tilde{H}_u^+, \tilde{H}_u^0)$		$(\mathbf{1}, \mathbf{2}, +\frac{1}{2})$
	$H_d$	$(H_d^0, H_d^-)$	$(\tilde{H}_d^0, \tilde{H}_d^-)$		$(\mathbf{1}, \mathbf{2}, -\frac{1}{2})$
Gauge supermultiplets		spin-0	spin-1/2	spin-1	$SU(3)_C, SU(2)_L, U(1)_Y$
gluino, gluon		-	$\tilde{g}$	$g$	$(\mathbf{8}, \mathbf{1}, 0)$
winos, W bosons		-	$\tilde{W}^\pm, \tilde{W}^0$	$W^\pm, W^0$	$(\mathbf{1}, \mathbf{3}, 0)$
bino, B boson		-	$\tilde{B}^0$	$B^0$	$(\mathbf{1}, \mathbf{1}, 0)$

handedness. For example, the two superpartners of the electron are  $\tilde{e}_L$  and  $\tilde{e}_R$ , where the tilde ( $\sim$ ) symbol is used to indicate superpartners of SM particles. Note that the handedness here refers to the helicity of the SM electron (and not to the helicity of the spin-0 selectron). Similarly to the two selectrons, we have  $\tilde{\mu}_L, \tilde{\mu}_R$ , and  $\tilde{\tau}_L, \tilde{\tau}_R$ . The SM neutrinos come only left-handed, neglecting their very small masses, their supersymmetric partners are thus denoted by  $\tilde{\nu}_e, \tilde{\nu}_\mu$ , and  $\tilde{\nu}_\tau$ . Finally, the squarks are named  $\tilde{q}_L$  and  $\tilde{q}_R$  with  $q = u, d, s, c, b, t$ .

The spin-0 Higgs boson naturally fits into a chiral supermultiplet. However, at least two Higgs chiral supermultiplets are required in order to avoid gauge anomalies, and give mass to the up-type quarks, down-type quarks, and the leptons. Following the MSSM, two Higgs supermultiplets are assumed. The two (SM) Higgs  $SU(2)_L$ -doublet complex scalar fields come with weak hypercharge  $Y = 1/2$  and  $Y = -1/2$  and are called  $H_u$  and  $H_d$  respectively (the names indicate which one gives mass to the up-type/down-type quarks). The Higgs superpartners are called higgsinos, and are again denoted by adding the tilde symbol.

These chiral supermultiplets are listed in Table 7.1 (top part). They describe all of the required chiral supermultiplets for a minimal and viable supersymmetric extension of the SM.

The vector bosons of the SM are placed in gauge supermultiplets. Their fermionic superpartners are generally referred to as *gauginos*. The eight SM gluons of the  $SU(3)_C$  gauge group are accompanied by eight spin-1/2 *gluinos*, which also form a colour-octet. Again, the tilde symbol is used to denote the superpartners:  $g$  and  $\tilde{g}$ . In the electroweak gauge symmetry  $SU(2)_L \times U(1)_Y$  sector, the vector gauge bosons  $W^\pm, W^0$ , and  $B^0$  are associated with spin-1/2 superpartners  $\tilde{W}^\pm, \tilde{W}^0$ , and  $\tilde{B}^0$ , called *winos* and *bino*. The mixed mass eigenstates  $Z$  and  $\gamma$  have correspondingly mixed gaugino superpartners called *zino* and *photino*. The gauge supermultiplets are summarised

in the bottom part of Table 7.1.

Together, the chiral and gauge supermultiplets as discussed above and shown in Table 7.1, make up the particle content of the MSSM.

However, not a single supersymmetric particle has yet been found. If all particles of a given supermultiplet were to have equal masses, as required by the supersymmetry, then many of the superpartners would have been extremely easy to detect at previous colliders. Therefore, if supersymmetry indeed does exist, it can only be a broken symmetry in the vacuum state chosen by nature.

In order to keep the supersymmetry solution to the hierarchy problem, “soft” breaking mechanisms are considered. The effective Lagrangian of the broken MSSM then reads

$$\mathcal{L} = \mathcal{L}_{\text{SUSY}} + \mathcal{L}_{\text{soft}},$$

where  $\mathcal{L}_{\text{SUSY}}$  contains all of the gauge and Yukawa interactions and preserves supersymmetry invariance, and  $\mathcal{L}_{\text{soft}}$  violates supersymmetry but contains only mass terms and coupling parameters with *positive* mass dimension. The soft supersymmetry breaking term results in corrections to the Higgs scalar masses that are logarithmic in the ultraviolet momentum cutoff  $\Lambda_{\text{UV}}$  (and not quadratic as in the SM).

The masses of all supersymmetric particles are determined by the parameters of  $\mathcal{L}_{\text{soft}}$ . Their contributions to the Higgs boson mass can be used to place a theoretical upper limit on the expected sparticle masses. Assuming  $\Lambda_{\text{UV}} \sim M_{\text{P}}$  (Planck scale) and the coupling constants  $\lambda \sim 1$ , one finds that the lightest superpartners should have masses of less than about 1 TeV [39].

### 7.1.1 Supersymmetric Lagrangian

The basic principles of constructing a supersymmetric Lagrangian are similar to those used for the SM: the corresponding action  $S = \int \mathcal{L} d^4x$  is required to be invariant under certain symmetry transformations. In the SM this invariance requirement under local symmetry transformations leads to the well known gauge fields and thus ultimately provides the basis for the strong and electroweak forces. In supersymmetry the action  $S$  is in addition required to be invariant under the global supersymmetry transformation which turns bosons into fermions and vice versa.

For the sake of completeness, the full Lagrangian density for a renormalizable supersymmetric theory that describes chiral and gauge supermultiplets (as needed for the MSSM) reads as follows:

$$\begin{aligned} \mathcal{L}_{\text{SUSY}} &= \mathcal{L}_{\text{chiral}} + \mathcal{L}_{\text{gauge}} \\ &\quad - \sqrt{2}g(\phi^* T^a \psi)\lambda^a - \sqrt{2}g\lambda^{\dagger a}(\psi^\dagger T^a \phi) + g(\phi^* T^a \phi)D^a, \end{aligned}$$

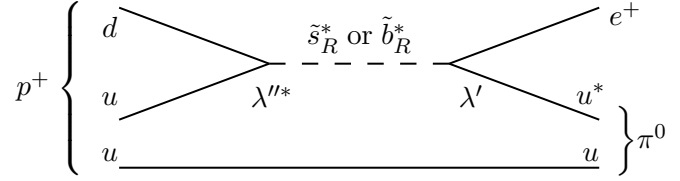
with

$$\mathcal{L}_{\text{chiral}} = -D^\mu \phi^{*i} D_\mu \phi_i + i\psi^{\dagger i} \bar{\sigma}^\mu D_\mu \psi_i - \frac{1}{2} \left( W^{ij} \psi_i \psi_j + W_{ij}^* \psi^{\dagger i} \psi^{\dagger j} \right) - W^i W_i^*,$$

and

$$\mathcal{L}_{\text{gauge}} = -\frac{1}{4} F_{\mu\nu}^a F^{\mu\nu a} + i\lambda^{\dagger a} \bar{\sigma}^\mu D_\mu \lambda^a + \frac{1}{2} D^a D^a,$$

**Figure 7.1:** Proton decay  $p \rightarrow e^+ \pi^0$  with both  $\Delta B = 1$  and  $\Delta L = 1$ , mediated by a supersymmetric strange or bottom squark (taken from Ref. [39]).



where  $\phi_i, \psi_i$  denote scalar, fermionic fields respectively with the index  $i$  running over all gauge and flavour degrees of freedom;  $D_\mu$  is the gauge-covariant derivative;  $\bar{\sigma}^\mu$  describes the Pauli matrices (in the Weyl spinor notation);  $\lambda^a$  denotes a fermion gaugino with the index  $a$  running over the representation of the gauge group ( $a = 1, \dots, 8$  for  $SU(3)_C$  colour gluons and gluinos;  $a = 1, 2, 3$  for  $SU(2)_L$  weak isospin;  $a = 1$  for  $U(1)_Y$  weak hypercharge);  $g$  is the gauge coupling;  $T^a$  is the gauge group transformation operator;  $D^a$  is a necessary bosonic auxiliary field;  $F_{\mu\nu}^a$  is the usual Yang-Mills field strength  $F_{\mu\nu}^a = \partial_\mu A_\nu^a - \partial_\nu A_\mu^a + g f^{abc} A_\mu^b A_\nu^c$ ; and  $W^i, W^{ij}$  are both derived from the superpotential  $W$  (defined below) by  $W^{ij} = \frac{\delta^2}{\delta\phi_i \delta\phi_j} W$  and  $W^i = \frac{\delta W}{\delta\phi_i}$  respectively.

In a renormalizable supersymmetric field theory, the interactions and masses (before symmetry breaking) of all particles are determined just by their gauge transformation properties and by the superpotential  $W$ , given by

$$W = L^i \phi_i + \frac{1}{2} M^{ij} \phi_i \phi_j + \frac{1}{6} y^{ijk} \phi_i \phi_j \phi_k,$$

where  $L^i$  are parameters with dimensions of  $[\text{mass}]^2$ ,  $M^{ij}$  is a symmetric mass matrix for the fermion fields, and  $y^{ijk}$  is a Yukawa coupling of a scalar  $\phi_k$  and two fermions  $\psi_i \psi_j$  that must be totally symmetric under interchange of  $i, j, k$ .

It is noteworthy that the structure and parameters of the supersymmetric Lagrangian are highly limited. Given the supermultiplet particle content, the form of the superpotential is restricted by the requirement of gauge invariance. For the MSSM, all of the dimensionless couplings and all but one mass term correspond directly to parameters in the SM that have been measured already. For example, the coupling constant of a gluino to a squark and a quark is the QCD constant  $\alpha_S$ . A large number of unknown parameters enter, however, through  $\mathcal{L}_{\text{soft}}$ , as will be further discussed later.

Furthermore, by imposing a local supersymmetry invariance, an additional field which describes gravity has to be introduced. The resulting locally supersymmetric theory is called *supergravity* [116]. It necessarily unifies the space-time symmetries of ordinary general relativity with local supersymmetry transformations. In supergravity, the spin-2 graviton has a spin-3/2 fermion superpartner called the gravitino.

### 7.1.2 R-parity

The general superpotential  $W$  (as shown above) contains terms that introduce baryon number (B) and total lepton number (L) violating processes. These terms are excluded in the MSSM.

The most obvious experimental constraint comes from the non-observation of proton decay, which is both B- and L-violating (see Fig. 7.1). Many other processes also give strong constraints on the

violation of lepton and baryon numbers, see for instance Ref. [117, 118]. In order to avoid such processes, at least one of the couplings must be extremely small, or the involved supersymmetric particles must be very heavy.

In the MSSM B- and L-violating processes are eliminated by adding a new symmetry. This new symmetry is called *R-parity*, defined for each particle as

$$P_R = (-1)^{3(B-L)+2s} \quad (7.1)$$

where  $s$  is the spin of the particle. All SM particles (including the Higgs bosons) have even R-parity ( $P_R = +1$ ), while all supersymmetric particles (squarks, sleptons, gauginos, and higgsinos) have odd R-parity ( $P_R = -1$ ).

R-parity is a multiplicative quantum number. If it is exactly conserved, then there can be no mixing between the sparticles and the SM particles. Furthermore, every interaction vertex in the theory contains an even number of  $P_R = -1$  sparticles. This has three extremely important phenomenological consequences:

1. Sparticles can only be produced in even numbers (usually pairs).
2. The *lightest supersymmetric particle* (LSP) must be absolutely stable. Since no exotic strong or EM bound states (isotopes) have been observed, the LSP should be neutral and colourless. This would make the LSP a suitable candidate for the non-baryonic dark matter that seems to be required by cosmology [37, 41, 42, 43].
3. Each sparticle gradually decays into a state that contains an odd number of LSPs (usually just one).

These characteristics of R-parity conserving (RPC) supersymmetry have been of great importance for the design of inclusive search channels in collider experiments. The detector signature of an LSP is similar to that of a heavy neutrino. The LSP would escape direct detection resulting in the characteristic feature expected for supersymmetric events: an imbalance of the energy measured in the detector. Hadron colliders can only measure the transverse component of the missing energy. This is because the longitudinal component (along the beam pipe) of the initial energy is unknown in the parton–parton scattering (see Chapter 9).

### 7.1.3 Soft supersymmetry breaking

As mentioned earlier, if supersymmetry exists at all, it must be broken. The theoretical expectation is a spontaneous symmetry breaking mechanism, which works in a manner analogous to the electroweak symmetry breaking in the ordinary SM: the Lagrangian of the underlying model is invariant under supersymmetry, but the vacuum state is not.

Many models of spontaneous symmetry breaking have been studied. In fact, the question of how supersymmetry is exactly broken is one of the most intriguing topics within theoretical supersymmetry. In the MSSM, however, our ignorance of the exact mechanism is simply parameterised by introducing extra terms that break supersymmetry explicitly in the effective MSSM Lagrangian.

It has been shown that a softly broken supersymmetric theory (symmetry-breaking couplings of positive mass dimension) is free of quadratic divergences in quantum corrections to scalar masses, to all orders in perturbation theory [119].

The soft symmetry breaking terms in the MSSM read

$$\begin{aligned}\mathcal{L}_{\text{soft}}^{\text{MSSM}} = & -\frac{1}{2} \left( M_3 \widetilde{g} \widetilde{g} + M_2 \widetilde{W} \widetilde{W} + M_1 \widetilde{B} \widetilde{B} + \text{c.c.} \right) \\ & - \left( \widetilde{u} \mathbf{a}_u \widetilde{Q} H_u - \widetilde{d} \mathbf{a}_d \widetilde{Q} H_d - \widetilde{e} \mathbf{a}_e \widetilde{L} H_d + \text{c.c.} \right) \\ & - \widetilde{Q}^\dagger \mathbf{m}_Q^2 \widetilde{Q} - \widetilde{L}^\dagger \mathbf{m}_L^2 \widetilde{L} - \widetilde{u} \mathbf{m}_u^2 \widetilde{u}^\dagger - \widetilde{d} \mathbf{m}_d^2 \widetilde{d}^\dagger - \widetilde{e} \mathbf{m}_e^2 \widetilde{e}^\dagger \\ & - m_{H_u}^2 H_u^* H_u - m_{H_d}^2 H_d^* H_d - (b H_u H_d + \text{c.c.}),\end{aligned}$$

where,  $M_3$ ,  $M_2$ , and  $M_1$  are the gluino, wino, and bino mass terms. The second line contains the (scalar)<sup>3</sup> couplings, each of  $\mathbf{a}_u$ ,  $\mathbf{a}_d$ ,  $\mathbf{a}_e$  is a complex  $3 \times 3$  matrix in family space, with dimensions of [mass]. The third line consists of squark and slepton mass terms. Again, each shown  $\mathbf{m}_X^2$  is a  $3 \times 3$  matrix in family space. Finally, the last line displays supersymmetry-breaking contributions to the Higgs potential.

Unlike the supersymmetry preserving Lagrangian ( $\mathcal{L}_{\text{SUSY}}$ ), the soft-symmetry-breaking Lagrangian terms ( $\mathcal{L}_{\text{soft}}^{\text{MSSM}}$ ) introduce a large number of unknown parameters. A careful count reveals 105 independent parameters (masses, mixing angles, and phases) in the MSSM which cannot be removed or associated to measured SM parameters [120].

Many of these 105 MSSM parameters imply flavour mixing or CP-violating processes, which are severely restricted by experiment:

- Slepton mixing, implying the individual lepton numbers are not conserved, is strongly limited by experimental bounds, for instance from the process  $\mu \rightarrow e\gamma$  ( $Br(\mu \rightarrow e\gamma) < 1.2 \cdot 10^{-11}$  [121]). This sets tight limits on the off-diagonal entries of  $\mathbf{m}_e^2$  and  $\mathbf{m}_L^2$ .
- The squark (flavour) mixing has strong experimental constraints from flavour changing neutral current (FCNC) measurements, such as the neutral kaon system. More constraints come from the neutral  $D$  system and the process  $b \rightarrow s\gamma$  ( $Br(b \rightarrow s\gamma) = (3.55 \pm 0.26) \cdot 10^{-4}$  [122]), and other beauty or strange quark decays to lighter quarks. All of these processes would be allowed (enhanced) by flavour mixing soft-symmetry-breaking terms.
- Strict constraints on CP-violating phases follow from limits on the electric dipole moments of the neutron and electron [123].
- Further constraints can arise through virtual sparticles, as for instance in the anomalous magnetic moment of the muon ( $a_\mu = (11659208 \pm 6) \cdot 10^{-10}$  [124]).

All of these CP-violating and flavour-changing effects of the MSSM can be avoided by assuming a more universal symmetry breaking. The resulting constrained MSSM has far fewer parameters. In order to understand such simplification patterns in  $\mathcal{L}_{\text{SUSY}}$ , it is necessary to consider models in which supersymmetry is spontaneously broken.

The common approach in supersymmetry breaking models is to assume that the MSSM soft terms arise indirectly or radiatively. The origin of the symmetry breaking is some “hidden sector” of particles that have no direct couplings to the chiral supermultiplets in the “visible sector” of the MSSM. The two sectors share some interaction which mediates the supersymmetry breaking from the hidden to the visible sector and thus results in the MSSM soft terms.

There are mainly two competing models that aim at describing this mediating interaction. The first model proposes gravitational interactions, which are associated to new physics that enters near the Planck scale. The energy scale of the hidden sector should be of the order of  $10^{11}$  GeV in such gravity-mediated scenarios. This model is further described below.

The second model assumes that the flavour-blind mediating interactions are the SM electroweak and QCD gauge interactions. In this *gauge-mediated supersymmetry breaking* (GMSB) scenario, the MSSM soft terms come from loop diagrams involving some messenger particles. These messengers are new chiral supermultiplets that couple to supersymmetry-breaking terms and also have the SM gauge interactions. The scale of supersymmetry breaking in the GMSB is only of the order of  $\sim 10^4$  GeV.

### Gravity mediated breaking

This is the supersymmetry breaking model that has been employed for the studies of this thesis. In the minimal form, called *minimal supergravity* (mSUGRA), the soft terms in  $\mathcal{L}_{\text{soft}}^{\text{MSSM}}$  are all determined by just four parameters  $m_{1/2}$ ,  $m_0$ ,  $A_0$ , and  $B_0$ :

$$\begin{aligned} M_3 &= M_2 = M_1 = m_{1/2}, \\ \mathbf{m}_Q^2 &= \mathbf{m}_u^2 = \mathbf{m}_d^2 = \mathbf{m}_L^2 = \mathbf{m}_e^2 = m_0^2 \mathbf{1}, & m_{H_u}^2 &= m_{H_d}^2 = m_0^2, \\ \mathbf{a}_u &= A_0 \mathbf{y}_u, & \mathbf{a}_d &= A_0 \mathbf{y}_d, & \mathbf{a}_e &= A_0 \mathbf{y}_e, \\ b &= B_0 \mu, \end{aligned}$$

at a renormalisation scale  $Q \approx M_P$ . This framework avoids the soft terms that imply flavour-changing and CP-violating processes. It is further highly predictive, the entire MSSM particle spectrum can be calculated from these four soft parameters plus one MSSM parameter  $\mu$ . The  $\mu$  term  $\mu H_u H_d$  is part of the MSSM superpotential  $W$ .

By demanding that the soft terms generate a scalar potential that gives the correct electroweak symmetry breaking,  $\mu$  and  $B_0$  can be traded for  $\text{sgn}(\mu)$  and  $\tan\beta$ . The  $\tan\beta$  parameter is defined as the ratio of the Higgs vacuum expectation values,

$$\tan\beta = \langle H_u^0 \rangle / \langle H_d^0 \rangle.$$

It is easy to imagine that the essential physics of supersymmetry breaking is not captured by these five parameters of mSUGRA (or by the minimal GMSB with six parameters), but rather described by the general MSSM (which includes all theoretically viable couplings). However, the high number of parameters in the general soft-symmetry-breaking terms of the MSSM also introduces a tremendous arbitrariness. This can result in many processes, e.g. strong FCNC, that are already ruled out by experiment. Furthermore, in phenomenological studies it is highly impractical if not



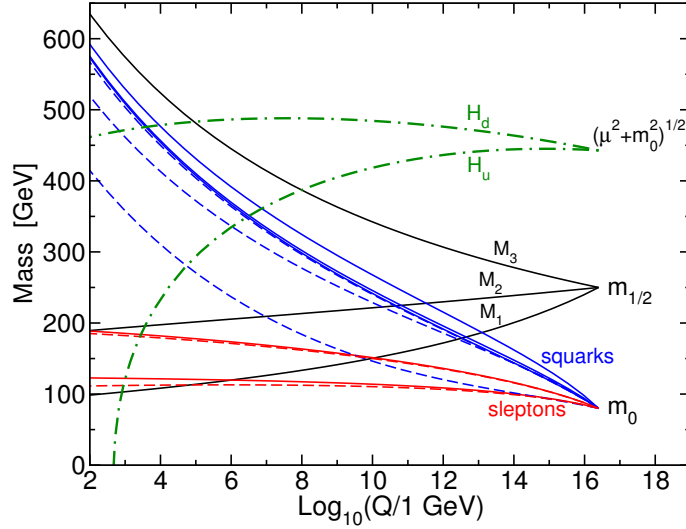


**Figure 7.2:** RGE evolution of scalar and gaugino mass parameters in the MSSM, taken from Ref. [39]. The calculation is based on mSUGRA boundary conditions ( $m_0 = 80$  GeV,  $m_{1/2} = 250$  GeV,  $A_0 = -500$  GeV, and  $\tan\beta = 10$ ) imposed at  $2.5 \cdot 10^{16}$  GeV. The parameter  $\mu^2 + m_{H_u}^2$  runs negative in order to provoke electroweak symmetry breaking.

impossible to scan the 105 dimensional parameter space of the general MSSM. We are therefore obliged to explore the also rich phenomenology predicted by constrained models.

A comprehensive description of mSUGRA can be found in Ref. [125, 126, 127, 128, 129].

### 7.1.4 Mass spectrum

The particle mass spectrum is obtained from evolving the mass parameters (32 in the general MSSM), defined in the soft symmetry breaking Lagrangian at some very high energy scale  $Q_0$ , down to the electroweak scale. This process is governed by the renormalisation group equations (RGE). Fig. 7.2 shows the RGE running of scalar and gaugino masses for one specific mSUGRA model. The parameter values at the electroweak scale can be used to extract physical masses, cross sections, and other observables. Several publicly available programs perform the RGE running (for various models) and the extraction of physical observables. The tool mostly used within ATLAS, called *ISAJET*, is described in Ref. [130].

The electroweak symmetry breaking in the MSSM is complicated by the fact that there are two complex Higgs doublets, with eight real scalar degrees of freedom. After the spontaneous symmetry breaking, three degrees of freedom become the longitudinal modes of the  $Z$  and  $W^\pm$  massive bosons. The remaining five real scalar fields are the Higgs bosons of the MSSM: two CP-even neutral scalars  $h^0$  and  $H^0$ , one CP-odd neutral scalar  $A^0$ , and a charge +1 scalar  $H^+$  and its conjugate charge -1 scalar  $H^-$ . By convention,  $h^0$  is lighter than  $H^0$ . An interesting feature in the MSSM is that the mass of the lightest Higgs boson ( $h^0$ ) is predicted to be below  $\sim 135$  GeV, where important mass corrections are considered [131, 132, 133]. This however assumes that all

**Table 7.2:** Supersymmetric and Higgs particles in the MSSM, with spin, R-parity, the gauge and mass eigenstates. The sfermion mixing for the first two families was assumed to be negligible.

Names	Spin	$P_R$	Gauge Eigenstates	Mass Eigenstates
Higgs bosons	0	+1	$H_u^0$ $H_d^0$ $H_u^+$ $H_d^-$	$h^0$ $H^0$ $A^0$ $H^\pm$
squarks	0	-1	$\tilde{u}_L$ $\tilde{u}_R$ $\tilde{d}_L$ $\tilde{d}_R$ $\tilde{s}_L$ $\tilde{s}_R$ $\tilde{c}_L$ $\tilde{c}_R$ $\tilde{t}_L$ $\tilde{t}_R$ $\tilde{b}_L$ $\tilde{b}_R$	(same) (same) $\tilde{t}_1$ $\tilde{t}_2$ $\tilde{b}_1$ $\tilde{b}_2$
sleptons	0	-1	$\tilde{e}_L$ $\tilde{e}_R$ $\tilde{\nu}_e$ $\tilde{\mu}_L$ $\tilde{\mu}_R$ $\tilde{\nu}_\mu$ $\tilde{\tau}_L$ $\tilde{\tau}_R$ $\tilde{\nu}_\tau$	(same) (same) $\tilde{\tau}_1$ $\tilde{\tau}_2$ $\tilde{\nu}_\tau$
neutralinos	1/2	-1	$\tilde{B}^0$ $\tilde{W}^0$ $\tilde{H}_u^0$ $\tilde{H}_d^0$	$\tilde{\chi}_1^0$ $\tilde{\chi}_2^0$ $\tilde{\chi}_3^0$ $\tilde{\chi}_4^0$
charginos	1/2	-1	$\tilde{W}^\pm$ $\tilde{H}_u^\pm$ $\tilde{H}_d^\pm$	$\tilde{\chi}_1^\pm$ $\tilde{\chi}_2^\pm$
gluino	1/2	-1	$\tilde{g}$	(same)

sparticles that can contribute to  $m_{h^0}^2$  in loops have masses not exceeding 1 TeV.

The higgsinos and electroweak gauginos mix with each other because of the effects of electroweak symmetry breaking. The electrically neutral states ( $\tilde{H}_u^0$ ,  $\tilde{H}_d^0$ , and  $\tilde{B}$ ,  $\tilde{W}^0$ ) form four mass eigenstates that are called *neutralinos* ( $\tilde{\chi}_1^0$ ,  $\tilde{\chi}_2^0$ ,  $\tilde{\chi}_3^0$ , and  $\tilde{\chi}_4^0$ ). The charged states ( $\tilde{H}_u^\pm$ ,  $\tilde{H}_d^\pm$ , and  $\tilde{W}^\pm$ ,  $\tilde{W}^\pm$ ) combine to form two mass eigenstates with charge  $\pm 1$  called *charginos* ( $\tilde{\chi}_1^\pm$ ,  $\tilde{\chi}_2^\pm$ ). By convention, the lowest index denotes the lightest sparticle. Typically, the LSP is the lightest neutralino ( $\tilde{\chi}_1^0$ ), unless the gravitino is lighter or R-parity is not conserved.

The gluino cannot mix with other sparticle states because it is a colour-octet. In most models the gluino mass is considerably heavier than the lighter neutralinos and charginos.

The scalar squark and slepton gauge eigenstates can mix among each other if they have the same electrical charge, R-parity, and colour quantum numbers. Most of these mixing angles, however, are very small for the flavour-blind soft symmetry breaking parameters of the MSSM. Therefore, mixing of the sfermions in the first two families is generally neglected. Conversely, the third family squarks and sleptons can have substantial mixing between the left-handed and right-handed states. These pair mixings are taken into account in the MSSM. The mixed states are denoted by a 1 or 2 subscript, as in  $\tilde{t}_1$ ,  $\tilde{t}_2$  (where again the 1 subscript denotes the lightest particle). It turns out that in most models the squarks of the first and second families are nearly degenerate and much heavier than the sleptons. This is because each squark mass gets large radiative corrections from loops involving the gluino. The lightest squarks are in many models the  $\tilde{t}_1$  and  $\tilde{b}_1$ , and the lightest slepton is predicted to be the  $\tilde{\tau}_1$ . A very light  $\tilde{\tau}_1$  compared to the other sleptons (modelled by a high  $\tan\beta$  in mSUGRA/GMSB) enhances the  $\tau$ -lepton rate in supersymmetric decay chains.

Following the common approach to neglect the mixing between the first and second family, we find the mass eigenstates listed in Table 7.2.

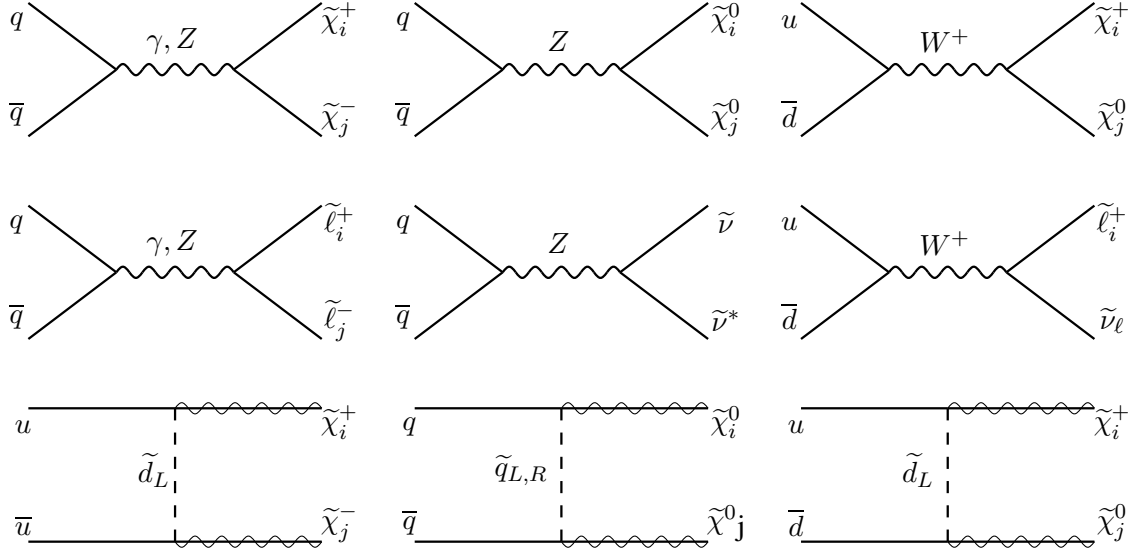


**Figure 7.3:** Feynman diagrams (leading-order) for electroweak production of supersymmetric particles from quark-antiquark annihilation, taken from Ref. [39].

## 7.2 Production and Decay Processes at the LHC

This section gives a brief overview of the expected patterns of supersymmetric production and the subsequent decay chains, at the LHC. Here and in the following, exact R-parity conservation is assumed. As discussed, supersymmetric particles are therefore produced in pairs. The coupling of two particles to SM partons can either be of electroweak or QCD strength.

The supersymmetric particles interact similarly to their SM superpartners (since they belong to the same supermultiplet). The mass eigenstates, however, can mix and thus receive couplings belonging to several sparticles. For example, the charginos and neutralinos couple to light squarks primarily due to their gaugino content (the coupling due to the Higgs component is negligible for nearly massless initial-state quarks).

The second important rule is that every interaction vertex must have an even number of sparticles.

With these concepts in mind, it is straightforward to find the leading-order Feynman diagrams that constitute the sparticle production at hadron colliders. Fig. 7.3 shows the processes that involve an electroweak interaction. All reactions obtain contributions from electroweak vector bosons in the  $s$ -channel. Additionally, the processes leading to  $\tilde{\chi}_i^+ \tilde{\chi}_j^-$ ,  $\tilde{\chi}_i^0 \tilde{\chi}_j^0$ , and  $\tilde{\chi}_i^- \tilde{\chi}_j^0$  sparticles also have  $t$ -channel squark-exchange contributions (bottom three diagrams).

Fig. 7.4 shows the leading-order Feynman diagrams for strong gluino and squark production at hadron colliders from gluon-gluon and gluon-quark fusion. The remaining diagrams for strong gluino and squark production from quark-antiquark annihilation and quark-quark scattering are shown in Fig. 7.5. All processes (leading to  $\tilde{g}\tilde{g}$ ,  $\tilde{q}\tilde{q}^*$ , and  $\tilde{q}\tilde{q}$  sparticle pairs) get contributions from

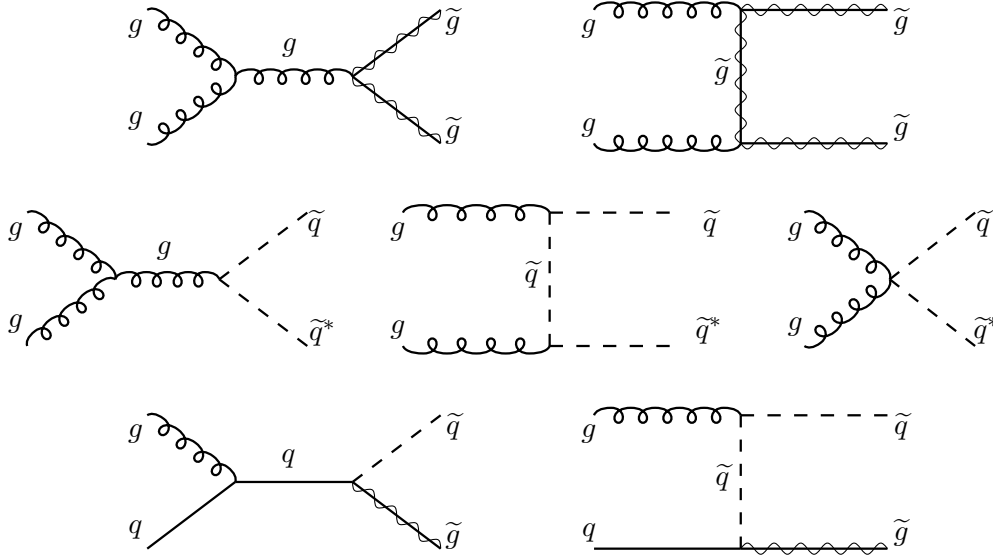


**Figure 7.4:** Feynman diagrams (leading-order) for gluino and squark production from gluon-gluon and gluon-quark fusion, taken from Ref. [39].

the  $t$ -channel exchange of an appropriate squark or gluino, and all but the quark-quark scattering also have  $s$ -channel contributions.

Note that in Figs. 7.3–7.5 the charged conjugated and crossed diagrams are omitted in favour of clearness.

The production cross sections of the various channels shown above depend on the parton density functions (PDFs) evolved to the appropriate  $Q^2$ -scale at the hadron collider, and on the supersymmetric particle spectrum. To a first approximation, the Tevatron is a quark-antiquark collider, while the LHC is a gluon-gluon and gluon-quark collider (due to the higher center-of-mass energy at the LHC).

At the Tevatron, the electroweak production of neutralinos and charginos is expected to have the largest cross section. This is because in typical supersymmetry models the sleptons are considerably lighter than squarks and the gluino. At the LHC, the situation is expected to be reversed: the strong production of squarks and gluinos from gluon-gluon and gluon-quark fusion dominates, unless the gluino and squarks are heavier than about 1 TeV.

The decay of a sparticle is expected to typically proceed through numerous chains of decays into gradually lighter sparticles and SM particles. This is called a cascade decay. For the following discussion of possible sparticle decays, the usual assumption is made that the lightest neutralino ( $\tilde{\chi}_1^0$ ) is the LSP. Consequently, every sparticle decay eventually ends with one  $\tilde{\chi}_1^0$ , and several SM particles. Another possibility for the LSP is the gravitino. This, however, is not discussed here.

Neutralinos and charginos can decay into lepton+slepton or quark+squark, through their electroweak gaugino admixture ( $\tilde{B}^0$ ,  $\tilde{W}^0$ ,  $\tilde{W}^\pm$ ). Secondly, a neutralino or chargino may also decay

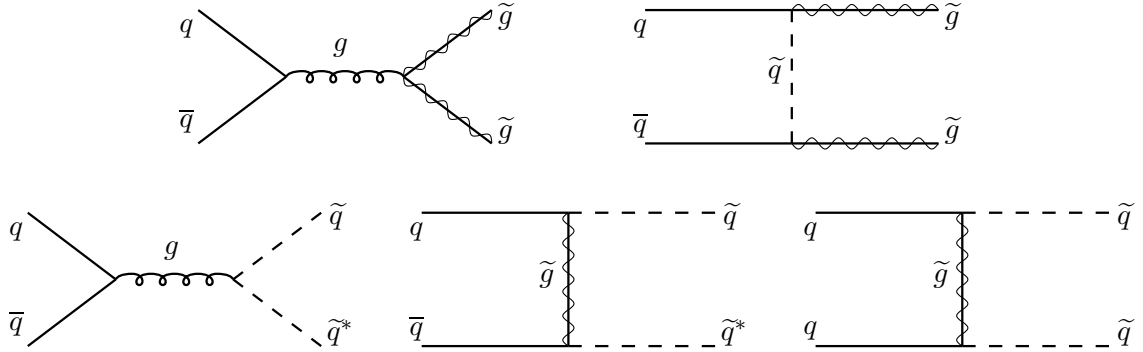


**Figure 7.5:** Feynman diagrams for strong gluino and squark production from quark-antiquark annihilation and quark-quark scattering, taken from Ref. [39].

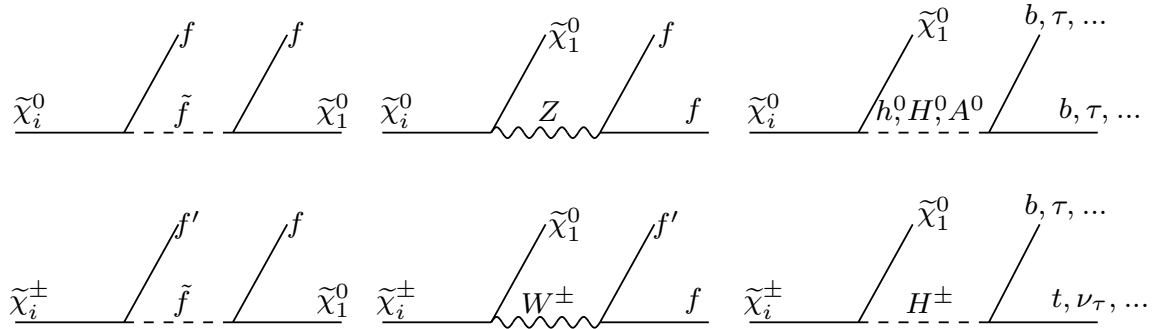


**Figure 7.6:** Neutralino and chargino decays with  $\tilde{\chi}_1^0$  in the final state, taken from Ref. [39]. The intermediate scalar or vector boson in each case can be either on-shell (so that actually there is a sequence of two-body decays) or off-shell, depending on the sparticle mass spectrum.

into any lighter neutralino or chargino plus a Higgs scalar or an electroweak gauge boson. This is because of the inherited gaugino-higgsino-Higgs and  $SU(2)_L$  gaugino-gaugino-vector boson couplings. If all two-body decays for a given chargino or neutralino are kinematically forbidden, then the decay can proceed through a three-body process with an off-shell gauge boson or gaugino.

The Feynman diagrams for the neutralino and chargino decays with  $\tilde{\chi}_1^0$  in the final state that seem most likely to be important are shown in Fig. 7.6, where  $f$  denotes a fermion, and  $f$  and  $f'$  are distinct members of one  $SU(2)_L$  multiplet (and one of the  $f$  or  $f'$  is an antifermion in each decay). To the extent that sleptons are probably lighter than squarks, the lepton+slepton decays can dominate. The  $\tilde{\tau}_1$  is often the lightest slepton, because of the commonly found enhanced mixing of staus. This results in larger branching fractions into final states with taus, rather than electrons or muons.

Sleptons can decay into a SM lepton and a neutralino or chargino, because of the gaugino content of the latter two. These weak two-body decays are:

$$\tilde{\ell}^\pm \rightarrow \ell^\pm \tilde{\chi}_i^0, \quad \tilde{\ell}^\pm \rightarrow \nu \tilde{\chi}_i^\pm, \quad \tilde{\nu} \rightarrow \nu \tilde{\chi}_i^0, \quad \tilde{\nu} \rightarrow \ell^\pm \tilde{\chi}_i^\mp.$$

In particular the decays with a  $\tilde{\chi}_1^0$  in the final state are kinematically allowed, if the  $\tilde{\chi}_1^0$  is the LSP.

The right-handed sleptons do not couple to the  $SU(2)_L$  gauginos (winos) but only to the bino. Thereby, they prefer the decay to the bino-like  $\tilde{\chi}_1^0$ .

Squarks inherit the strong and electroweak interaction couplings of their superpartners. If kinematically allowed, then the dominating squark decay is into a gluino+quark (of QCD strength). Otherwise, a squark will decay weakly into a quark + neutralino or chargino. In the neutralino and chargino final states, left-handed and right-handed squarks have different preferences: in an analogous way to sleptons right-handed squarks are expected to decay into the bino-like  $\tilde{\chi}_1^0$ , while the left-handed squarks decay preferentially into heavier and more wino-like neutralinos and charginos.

An interesting feature might be the decay of the lightest stop ( $\tilde{t}_1$ ). If both decays  $\tilde{t}_1 \rightarrow t\tilde{g}$  and  $\tilde{t}_1 \rightarrow t\tilde{\chi}_1^0$  are kinematically forbidden, then the decay into a chargino  $\tilde{t}_1 \rightarrow b\tilde{\chi}_1^\pm$  dominates. If this decay is also closed due to kinematics, then the lightest stop can only decay to a charm quark  $\tilde{t}_1 \rightarrow c\tilde{\chi}_1^0$  (which is flavour-suppressed) or through a four-body process. These decays might be very slow resulting in a quasi-stable  $\tilde{t}_1$ .

The decay of coloured gluinos can only proceed through squarks, either on-shell or virtual. In typical models, the gluino is heavier than the squarks, thus the two-body decay  $\tilde{g} \rightarrow q\bar{q}$  is open and dominates.

The production of supersymmetric particles and the subsequent cascade decays are illustrated using two examples in Appendix B.

### 7.3 Experimental Constraints

So far, no signal consistent with supersymmetry has been found. Experiments have set a number of direct and indirect limits, which are briefly summarised in the following.

As already mentioned in Section 7.1.3, indirect limits arise from processes that are either very rare or forbidden in the SM but have contributions from sparticle loops. These include  $\mu \rightarrow e\gamma$ ,  $b \rightarrow s\gamma$ , neutral meson mixing, electric dipole moments for the neutron and the electron, etc. There are also virtual sparticle effects on SM predictions like the anomalous magnetic moment of the muon.<sup>4</sup> The measurements of such processes already exclude some otherwise viable supersymmetry models.

The WMAP total cold dark matter limit,  $\Omega h^2 < 0.14$  [134], can be taken as an indirect constraint from experimental cosmology. In supersymmetry with exact  $R$ -parity conservation, the LSP might be this cold dark matter. The best supersymmetric dark matter candidate (for detection) is the lightest neutralino [43]. The sneutrino has been largely ruled out: the mass range 550 to 2300 GeV gives a cosmologically interesting relic density, but the scattering cross section of a sneutrino in this range with nucleons is much larger than the limits found by direct dark matter detection experiments [135]. A gravitino LSP, as is commonly found in GMSB models, might be the cold dark matter but would be impossible to directly detect because it interacts too weakly. In order

---

<sup>4</sup>The latest BNL measurements of  $a_\mu$  deviate by  $3.4\sigma$  from the SM predictions [2]. This could be interpreted as a hint for new physics, in particular supersymmetry.

to get the observed dark matter density today, the thermal-averaged effective annihilation cross section times the relative speed  $v$  of the LSPs should be about  $\langle\sigma v\rangle \sim 1\text{pb} \sim \alpha^2/(150\text{GeV})^2$  [43].

To first approximation, a neutralino LSP has the correct electroweak interaction strength and mass. More detailed and precise calculations reveal that an efficient neutralino LSP pair annihilation is required in order to not exceed the observed cold dark matter density. This can be turned into a limit for the MSSM (or mSUGRA) parameter space. Fig. 7.7 shows the mSUGRA parameter space taking into account a cold dark matter density consistent with WMAP data [136].

However, it is important to point out that simple extensions can completely change the predicted relic dark matter density in supersymmetry models, without changing much the predictions for collider experiments. Thus, the dark matter limit must be taken with care.

The most significant direct constraints on supersymmetric particles have been obtained at LEP and at the Tevatron collider. All following limits are at 95% confidence level and assume the MSSM, in particular with exact  $R$ -parity conservation. Further constraints in less canonical modes can be found in Ref. [2].

The lower mass limits for charged sparticles from the LEP experiments are nearly half of the beam energy, which reached a centre-of-mass energy of 209 GeV. Fig. 7.8 shows in the left plot the combined LEP constraints for sleptons, depending on the lightest neutralino mass. These constraints are very robust, as few model assumptions have been made. Smuon masses below 95 to 99 GeV, depending on the  $\tilde{\chi}_1^0$  mass, are excluded as long as the  $\tilde{\mu}_R - \tilde{\chi}_1^0$  mass difference is larger than 5 GeV [2, 137].

In the case of staus, the subsequent decays of  $\tau$ -leptons lead to reduced selection efficiencies. Furthermore, the enhanced mixing of left and right-handed components has to be considered, since it influences the coupling to the  $Z$  boson. In the worst case of no coupling between the stau and  $Z$  boson, stau masses smaller than 86 to 95 GeV are excluded, depending again on the  $\tilde{\chi}_1^0$  mass, and assuming a stau- $\tilde{\chi}_1^0$  mass difference of at least 7 GeV [2, 137].

Selectrons are excluded with masses below 100 GeV, for  $\tilde{\chi}_1^0$  masses  $< 85$  GeV, and for  $\mu = -200$  GeV and  $\tan\beta = 1.5$  [2, 137]. Additionally, a lower limit of 73 GeV can be set independently of the  $\tilde{\chi}_1^0$  mass.

The LEP chargino mass bound is 92 GeV, assuming gaugino and sfermion mass unification [2, 137]. Lower mass limits for the lightest neutralino can be derived indirectly at LEP from: chargino pair production, slepton, and Higgs boson searches. The absolute lower limit is  $m_{\tilde{\chi}_1^0} > 47$  GeV.

The most constraining squark and gluino mass limits come in general from Tevatron Run II. The canonical supersymmetry searches performed at the Tevatron experiments CDF and DØ select multiple jets plus missing transverse energy or three isolated leptons in the final state. Results from DØ, based on an integrated luminosity of  $\sim 2.1\text{fb}^{-1}$ , exclude squark masses below 379 GeV and gluino masses smaller than 308 GeV, within the framework of mSUGRA with  $\tan\beta = 3$ ,  $A_0 = 0$ , and  $\mu < 0$  [138]. This exclusion together with previous results from other experiments is shown in the right plot of Fig. 7.8.

Comparable exclusion results have been obtained by the CDF experiment, based on an integrated luminosity of  $2.0\text{fb}^{-1}$ : in a mSUGRA scenario with  $A_0 = 0$ ,  $\mu < 0$  and  $\tan\beta = 5$ , squark and

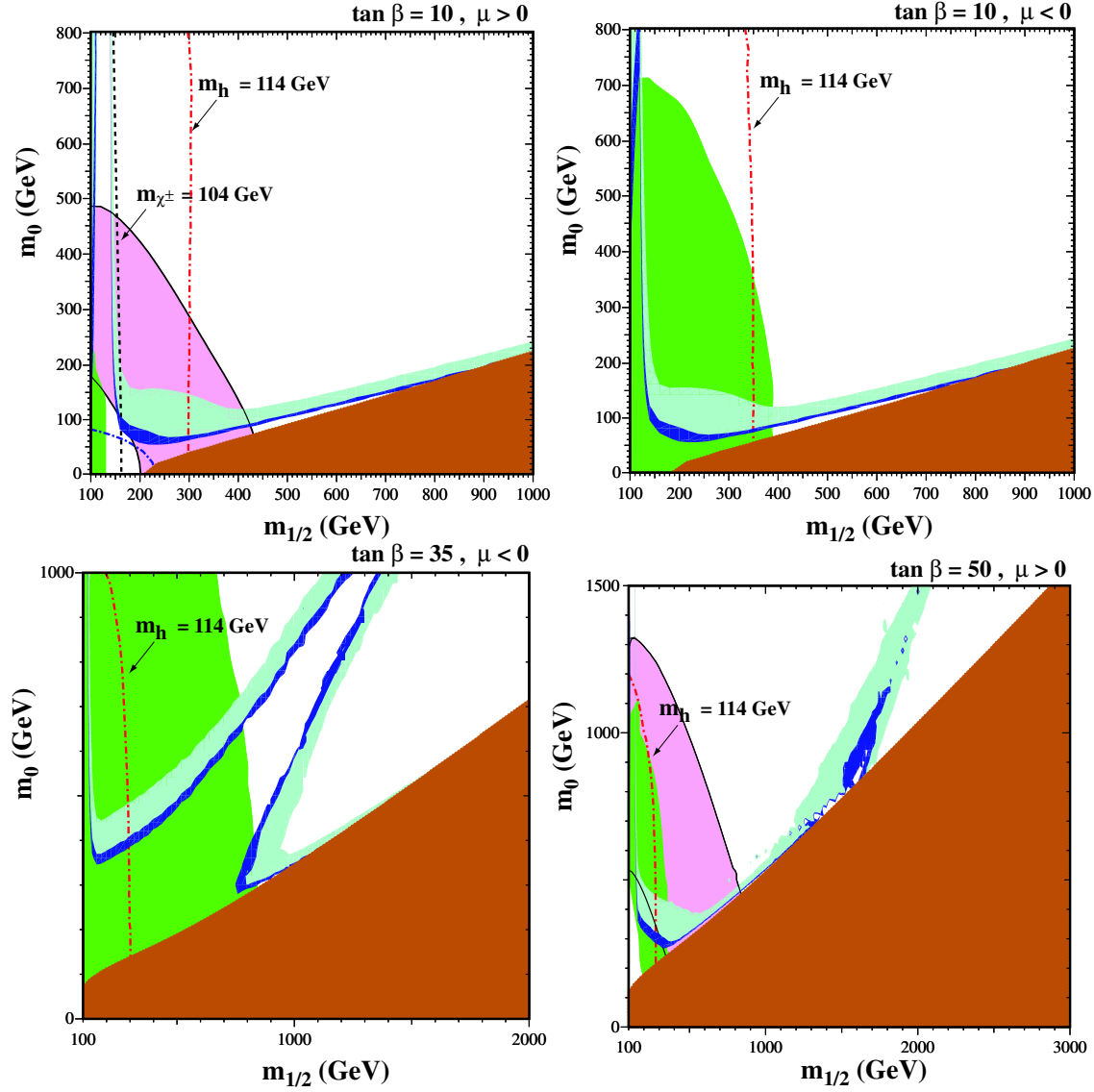


**Figure 7.7:** The  $(m_{1/2}, m_0)$  mSUGRA parameter space planes for a)  $\tan \beta = 10, \mu > 0$ , b)  $\tan \beta = 10, \mu < 0$ , c)  $\tan \beta = 35, \mu < 0$ , and d)  $\tan \beta = 50, \mu > 0$ , taken from Ref. [136]. In each plot, the region allowed by the older cosmological constraint  $0.1 < \Omega h^2 < 0.3$  has medium blue shading, and the region allowed by the newer cosmological constraint  $0.094 < \Omega h^2 < 0.129$  has very dark blue shading. The disallowed region where  $m_{\tilde{\tau}_1} < m_{\tilde{\chi}^0}$  has dark red shading. The regions excluded by  $b \rightarrow s\gamma$  have medium green shading, and those in plots a) and d) that are favoured by  $g_\mu - 2$  at the  $2\text{-}\sigma$  level have medium pink shading. A dot-dashed line in plot a) delineates the LEP constraint on the selectron mass and the contours  $m_{\tilde{\chi}^\pm} = 104$  GeV ( $m_h = 114$  GeV) are shown as near-vertical black dashed (red dot-dashed) lines in plot a) (each panel).



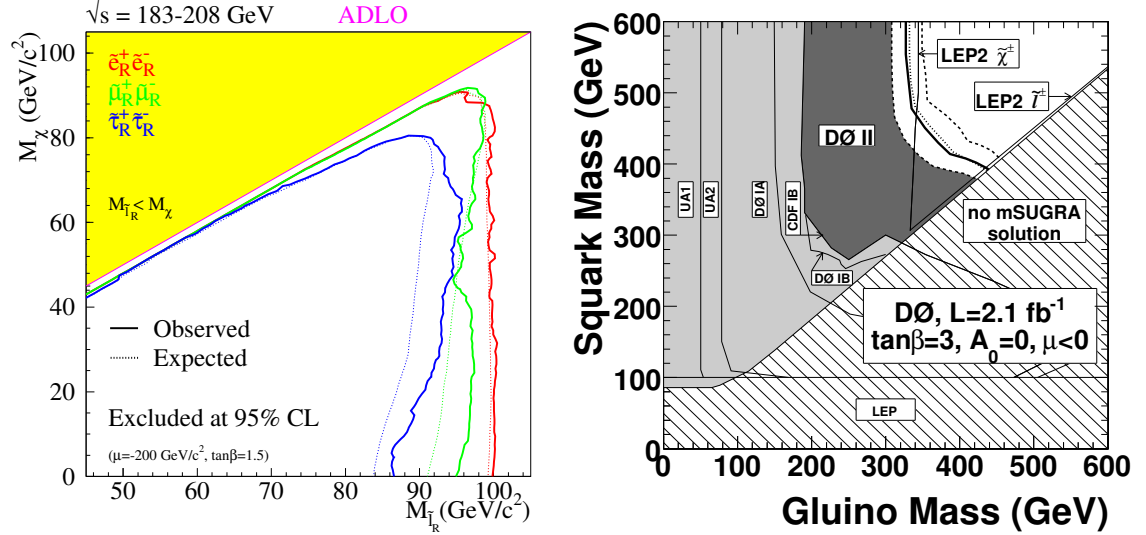


**Figure 7.8:** SUSY exclusion at the 95% confidence level from LEP and DØ. Left plot: LEP exclusion in the (slepton mass, lightest neutralino mass) plane [137]. Right plot: DØ exclusion in the (squark mass, gluino mass) plane [138].

gluino masses are excluded up to about 392 GeV in the region where gluino and squark masses are similar (see left plot in Fig. 7.9) [139]. These results can be translated into an exclusion region in the mSUGRA parameter space, as shown in the right plot of Fig. 7.9.

## 7.4 ATLAS Search Strategy

The ATLAS inclusive supersymmetry (SUSY) search strategy was developed using a twofold approach. Detailed studies have been used to define inclusive search channels using specific SUSY benchmark points: SU3, SU4 etc. (defined in Section 8.3.1). Final states from these benchmark points and all relevant SM background processes have been studied using a detailed simulation of the detector. The various search channels are exclusive with respect to each other, simplifying the procedure of combining the results.

The insight gained from these detailed studies has been applied to several scans over subsets of SUSY parameter space. By design these scans consist of a large number of signal points. Hence fast, parameterised simulations have been used. The goal is to verify that the inclusive search channels provide sensitivity to a wide range of SUSY models.

All inclusive search channels are based on the generic SUSY detector signature: missing energy ( $E_T^{\text{miss}}$ ) + several high transverse momentum ( $p_T$ ) jets + a certain number of leptons. The word 'lepton' is used to denote isolated electrons and muons. The main ATLAS inclusive SUSY search modes are classified by the lepton requirement as follows (see Ref. [26] for details):

- **Zero-lepton mode:** The presence of multiple jets together with large  $E_T^{\text{miss}}$  forms the least

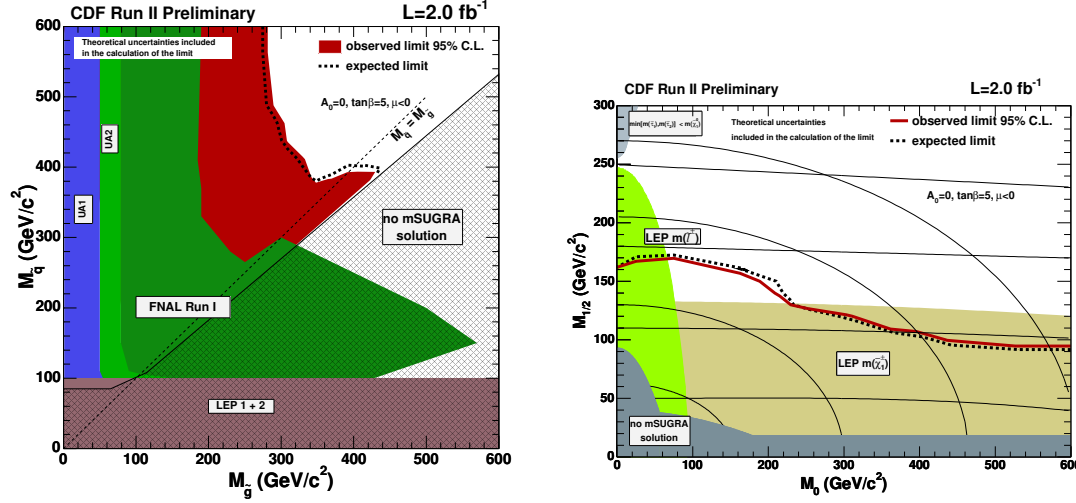


**Figure 7.9:** SUSY exclusion at the 95% confidence level from CDF [139]. Left plot: exclusion in the (squark mass, gluino mass) plane, assuming mSUGRA with the indicated parameters. Right plot: excluded parameter space region in the  $(m_0, m_{1/2})$  mSUGRA plane. The nearly horizontal and vertical lines represent iso-mass curves for the gluinos and squarks respectively, each set corresponds to masses of 150, 300, 450, and 600 GeV.

model-dependent SUSY signature. Typically, at least four jets are required to reduce the background from QCD and (W/Z+jets) processes.

- **One-lepton mode:** Requiring one lepton in addition to multiple jets and  $E_T^{\text{miss}}$  greatly reduces the QCD multijet background and also gives better control over the remaining backgrounds ( $t\bar{t}$  and W+jets productions). In SUSY models where  $\tau$  decays of gauginos are dominant, the fraction of leptonic  $\tau$  decays is expected to still provide a considerable 1-lepton rate. This search mode will be described in more detail in the following chapters.
- **Two-lepton mode:** Requiring two leptons in addition to multiple jets and  $E_T^{\text{miss}}$ . Opposite-sign leptons can arise from neutralino decays ( $\tilde{\chi}_2^0 \rightarrow \ell^+ \ell^- \tilde{\chi}_1^0$ ). They should be of the same flavour in order not to induce significant rates of  $\mu \rightarrow e\gamma$  and other lepton-flavour-violating interactions. Same-sign dileptons can be common in SUSY because the gluino is a self-conjugate Majorana fermion. In SM processes, however, the rate for same-sign dileptons is very small.
- **Three-lepton mode:** In SUSY, the trilepton signal can arise from direct gaugino production or from squark and gluino decays. Two approaches have been studied: 3-leptons + 1 very-high  $p_T$  jet and 3-leptons +  $E_T^{\text{miss}}$ .
- **Tau mode:** SUSY models generically violate lepton universality. In some models  $\tau$  decays can dominate. This search mode selects hadronic  $\tau$  decays since leptonic decays are indistinguishable from prompt leptons and therefore included in the previous search modes. In addition to the hadronic  $\tau$  decay, four jets and  $E_T^{\text{miss}}$  are required.

- **b-jet mode:** Light  $\tilde{b}$  and  $\tilde{t}$  together with enhanced heavy flavour production (due to Higgsino couplings) lead to many b quarks in SUSY decay chains. This feature can be exploited to suppress QCD background. This search mode requires four jets, out of which at least two are b-tagged, and  $E_T^{\text{miss}}$ .

### 7.4.1 Measurements

Once a signature consistent with SUSY has been established, the experimental focus will be to reconstruct the sparticle mass spectrum, to constrain the model parameters, and to measure the spin of the new (s)particles. In RPC models, sparticle decay chains cannot be fully resolved since the LSPs escape detection. As a consequence, edge positions rather than mass peaks in invariant mass distributions are measured and fitted.

One suitable sparticle decay chain is

$$\tilde{q}_L \rightarrow \tilde{\chi}_2^0 q (\rightarrow \tilde{\ell}^\pm \ell^\mp q) \rightarrow \tilde{\chi}_1^0 \ell^+ \ell^- q \quad (7.2)$$

leading to final states containing two opposite-sign electrons or muons, hard jets and missing energy. These characteristics ensure a large signal to background ratio. The kinematic endpoint in the dilepton invariant mass distribution is a function of the sparticle masses involved. If the sleptons are heavier than the  $\tilde{\chi}_2^0$  then the decay proceeds through the three body channel  $\tilde{\chi}_2^0 \rightarrow \tilde{\chi}_1^0 \ell^+ \ell^-$ . In this case the invariant mass distribution is non-triangular in shape with an endpoint equal to the difference of the mass of the two neutralinos  $m_{\ell\ell}^{\text{edge}} = m_{\tilde{\chi}_2^0} - m_{\tilde{\chi}_1^0}$  [140, 141]. If at least one of the sleptons is lighter than the  $\tilde{\chi}_2^0$  then the two-body decay channel  $\tilde{\chi}_2^0 \rightarrow \tilde{\ell}^\pm \ell^\mp \rightarrow \tilde{\chi}_1^0 \ell^+ \ell^-$  dominates. The dilepton invariant mass distribution is triangular with a sharp edge at the endpoint:

$$m_{\ell\ell}^{\text{edge}} = m_{\tilde{\chi}_2^0} \sqrt{1 - \left(\frac{m_{\tilde{\ell}}}{m_{\tilde{\chi}_2^0}}\right)^2} \sqrt{1 - \left(\frac{m_{\tilde{\chi}_1^0}}{m_{\tilde{\ell}}}\right)^2}. \quad (7.3)$$

A measurement of the dilepton endpoint thus gives a handle on the masses of the two lightest neutralinos and any sleptons that are lighter than  $\tilde{\chi}_2^0$ . Figure 7.10 shows the dilepton invariant mass distribution for two SUSY benchmark models. The SM background has been reduced by subtracting opposite flavour lepton pairs. The fitting function is a triangular distribution (7.3), smeared with a resolution function. To determine the masses of all sparticles involved in the decay chain (7.2), further invariant mass distributions involving a jet are used. In addition, several other sparticle decay chains give further kinematic endpoints. As an indication of the precision with which the LSP mass can be reconstructed, the  $\tilde{\chi}_1^0$  mass, as obtained from endpoints of the lepton+jets edges and the dilepton edges, is found to be  $88 \pm 60$  GeV (SU3) and  $62 \pm 126$  GeV (SU4) for an integrated luminosity of  $1 \text{ fb}^{-1}$  and  $0.5 \text{ fb}^{-1}$ , respectively [26]. The true  $\tilde{\chi}_1^0$  masses are 118 GeV (SU3) and 60 GeV (SU4).

Once enough edge positions have been measured, model parameters can be constrained. In the initial phase a limited number of measurements with rather large uncertainties would only allow to fit SUSY models with few parameters. In an optimistic scenario in which SUSY has been discovered and first endpoints have been measured with early data, i.e. an integrated luminosity of

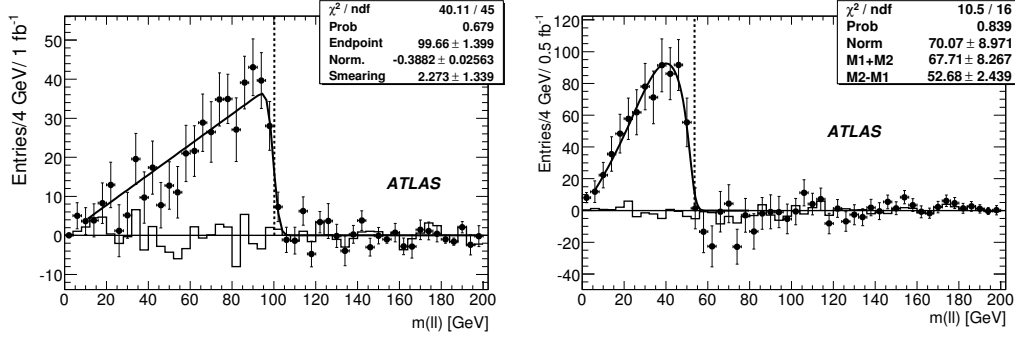


**Figure 7.10:** Left: Distribution of invariant mass after background subtraction for the SU3 benchmark point with an integrated luminosity of  $1 \text{ fb}^{-1}$ . Right: the same distribution is shown for the SU4 benchmark point and an integrated luminosity of  $0.5 \text{ fb}^{-1}$ . The line histogram is the SM contribution, while the points are the sum of SM and SUSY contributions. The fitting function is superimposed and the expected position of the endpoint is indicated by a dashed line. (Taken from Ref. [26])

$1 \text{ fb}^{-1}$ , it is shown in Ref. [26] that most of the 5 mSUGRA parameters can already be constrained (for the two studied benchmark points).

Assuming mSUGRA, the achievable precision in cosmological parameters derived from LHC data for  $300 \text{ fb}^{-1}$  was evaluated in Ref. [142]. The neutralino relic density  $\Omega_\chi h^2$ , calculated using *MICROMEGAS* [143], is obtained with a precision of  $\sim 3\%$ . A more general approach was considered in Ref. [144] where dark matter properties are estimated assuming the MSSM. The error on  $\Omega_\chi h^2$  is found to be  $\sim 9\%$ , again for  $300 \text{ fb}^{-1}$  of data.

A method to measure the spin of SUSY particles at the LHC has been proposed in Ref. [145]. This method exploits the fact that angular distributions in sparticle decays lead to charge asymmetry in lepton-jet invariant mass distributions. It was shown with simulation studies that the asymmetry distributions are sufficient to determine the correct spin of some SUSY particles, and reject other possibilities.

## Chapter 8

# Monte Carlo Simulations

The generation of specific physics processes along with the detailed simulation of the detector response is a crucial part of modern high-energy physics. It is important for the design of detectors, to estimate the physics reach, for a detailed understanding of the data, and for precision measurements.

The first LHC physics runs, at a reduced luminosity (initially  $10^{31} \text{ cm}^{-2} \text{ s}^{-1}$ ) and 10 TeV centre-of-mass (CM) energy, are foreseen for winter of 2009. The SUSY studies presented in this thesis are therefore solely based on simulated data. In this chapter the employed simulated datasets are introduced. They were generated as part of the so-called ATLAS computing system commissioning (CSC) programme [26]. The author's contribution was the production of the  $25 \times 25$  mSUGRA signal grid (described in Section 8.3.2), including the generation of the SUSY spectra, and the whole production chain (generation, simulation) making full use of the computing grid.

Section 8.1 briefly describes the Monte Carlo event generators. Section 8.2 gives an overview of the ATLAS detector simulation. Finally, all simulated signal and background samples, which are relevant for the following SUSY analysis, are detailed in Section 8.3.

### 8.1 Monte Carlo Generators

The ATLAS software framework provides interfaces<sup>1</sup> to most general-purpose Monte Carlo (MC) event generators, including: PYTHIA [111], HERWIG [146], Sherpa [147], AcerMC [148], ALPGEN [149], MadGraph/MadEvent [150], and MC@NLO [151, 152]. In addition to these, further generators are available for the generation of more specific processes.

Parton-level MC generators are configured to use HERWIG/JIMMY or PYTHIA for the hadronisation and the underlying event modelling. In the former case, HERWIG is employed for the hadronisation and the JIMMY program [153] (versions 4.2 and 4.31) to simulate the underlying

---

<sup>1</sup>The event generator interfaces provide mechanisms to feed the generated particle-level events into the ATLAS simulation software package.

ing event. The model parameters of the underlying event were tuned to published data from the Tevatron and other experiments, as described in Ref. [58] and references therein.

The specialised TAUOLA package [154] (version 2.7) is utilised for the simulation of  $\tau$ -lepton decays. The radiation of photons from charged leptons is also treated separately, using the PHOTOS QED radiation package [155] (version 2.15).

Wherever available, MC generators and tools are taken from the LHC computing grid generator-services sub-project. Furthermore, a common definition of particle masses is used among all generators, e.g. all simulated datasets employed in the present work were generated with a top quark mass of 175 GeV.

Parton distribution functions (PDFs) are linked into all MC generators using the Les Houches accord PDF interface library (LHAPDF) [156]. All datasets employed in the present work used the PDF sets [157, 158, 159] CTEQ6L for leading order (LO) MC event generators, and CTEQ6M for the next-to-leading order (NLO) MC event generator MC@NLO.

A brief description of the employed MC generators is given in the following, details about the datasets (generator filter settings, production cross sections etc.) are further described in Section 8.3.

The *PYTHIA* MC event generator [111] is used for the simulation of QCD jets. The new implementation of parton showering, commonly known as  $p_T$ -ordered showering, is used, as well as the new underlying event model where the phase-space is interleaved/shared between initial-state radiation (ISR) and the underlying event.

The *HERWIG* MC event generator [146, 160] is employed for the simulation of SUSY processes. The pre-generated input tables (SUSY particle masses, and branching ratios) for these processes are provided by ISAJET and ISAWIG [130]. *HERWIG* is also used to generate electroweak boson pair samples ( $WW$ ,  $ZZ$ ,  $WZ$ ). The simulation of the underlying event is performed with JIMMY [153].

The *ALPGEN* MC event generator [149] (version 2.05) is used for several processes:  $W$  and  $Z$  boson production in association with up to five jets, and  $t\bar{t}$  production with up to three additional jets. *ALPGEN* calculates the exact matrix elements of multiparton hard processes in hadronic collisions, at leading order in QCD and electroweak interactions. The parton multiplicity in the matrix element ( $N = 1$  to 6) has to be specified before running *ALPGEN*, i.e. the simulation of the physics process is sliced in  $N$ -partons samples. *HERWIG* and *JIMMY* are inserted for the hadronisation and simulation of the underlying event, respectively. In order to perform the parton-showering and matrix element matching *ALPGEN* implements the MLM [161] technique.<sup>2</sup> Since exclusive matching is applied, the matched samples (each with  $N$ -partons) can be added, and the inclusive sample is obtained after summing up all  $N$ -partons samples. Also the total (inclusive) cross section is given by the sum over all cross sections, each multiplied by its MLM matching efficiency.

The *MC@NLO* event generator [151, 152] (version 3.3) was employed for the production of the

---

<sup>2</sup>The MLM matching technique prevents double counting of parton emission either through the matrix element or the parton shower. The procedure vetoes events where the parton shower generates jets that have already been generated by the *ALPGEN* matrix elements.

---

primary  $t\bar{t}$  sample. It is one of the few MC tools incorporating full NLO QCD corrections to a selected set of processes in a consistent way. Thereby, MC@NLO affords a quite stable absolute cross section prediction and a good description of the final state kinematics for events with up to one additional QCD jet. The generated events can come with positive or negative weight, where the negatively weighted events are due to loop correction terms. This MC@NLO specific effect has to be carefully considered in the analysis. QCD showering and fragmentation are performed using the HERWIG [146, 160] program, while JIMMY is utilised for the simulation of the underlying event.

## 8.2 Detector Simulation

The detector simulation is an essential ingredient for a successful physics programme. It is indispensable for the design, validation, and understanding of the various detector components and their responses. The ATLAS collaboration utilises both a fast and a full detector simulation. Both are briefly introduced in the following.

The ATLAS fast simulation package (ATLFAST) [162, 163] is designed to provide a fast ATLAS detector response simulation, and thereby facilitate the production of large signal and background event samples. The interaction of particles in the detector material is not simulated. Instead, a parametrised detector response is adopted. First, MC generated four-vectors, corresponding to electrons, photons, etc., are subject to a perfectly homogeneous magnetic field in the tracker. Next, energies of the MC particles are deposited in a simplified calorimeter cell map. The ATLFAST output particles are then “reconstructed” from this calorimeter cell map in conjunction with the MC truth information. Simple isolation criteria and appropriate smearing functions are applied to these pseudo “reconstructed” particles as a function of the particle type. Comprehensive studies and validation efforts have shown good agreement between full and fast simulation, providing an adequate fast simulation for many physics studies [163]. Nonetheless, it is clear that several specific studies, such as the identification of non-isolated electrons or the treatment of converted photons, will always have to be addressed with the full detector simulation.

Note that the standard ATLAS off-line reconstruction algorithms are not used as ATLFAST provides pseudo reconstructed physics objects. Consequently, no reconstruction efficiencies are applied within ATLFAST.

Two new on-going developments improve the ATLFAST realism at the expense of an increased CPU time consumption:

- *ATLFAST II* provides a fast simulation of the ATLAS calorimeter with full granularity, and dead channels. It can be used to run all ATLAS off-line reconstruction algorithms.
- *FATRAS*, a fast ATLAS track simulation that implements material effects for particles that traverse detector material in a stochastic way. It also exploits ATLAS off-line software.

These new fast simulation packages are in the process of validation and have not been used in this thesis.

---



**Table 8.1:** Simulated SUSY benchmark samples, ATLAS MC sample ID, production cross section (LO and NLO), the available number of MC events, and the corresponding integrated luminosity  $L = \int \mathcal{L} dt$ .

Signal	sample ID	$\sigma^{\text{LO}}$ [pb]	$\sigma^{\text{NLO}}$ [pb]	$N_{\text{MC}}$	$L$ [fb <sup>-1</sup> ]
SU1	5401	7.43	10.86	$200 \cdot 10^3$	18.4
SU2	5402	4.86	7.18	$50 \cdot 10^3$	7.0
SU3	5403	18.59	27.68	$500 \cdot 10^3$	18.1
SU4	6400	262.00	402.19	$200 \cdot 10^3$	0.5
SU6	5404	4.48	6.07	$30 \cdot 10^3$	4.9
SU8	5406	6.44	8.70	$50 \cdot 10^3$	5.7

The ATLAS full detector simulation is based on GEANT4 [164] which is interfaced to the common ATLAS software environment [165]. An extensive physics validation programme has shown that the GEANT4 simulation meets the expected precision. The comparison with experimental data from stand-alone and combined test-beam gives very good agreement, normally at the level of a few percent or better [110]. In addition to the ideal ATLAS detector geometry description, which corresponds to the experimental setup as designed, a realistic (or distorted) description includes alignment and placement shifts, as well as material distortions similar to those anticipated in the installed detector. During the commissioning, this realistic detector description underwent continuous updates to better match the real ATLAS detector geometry, including more detailed descriptions of the magnetic field and material.

The average detector simulation time for  $t\bar{t}$  events is approximately 1990 kSI2K seconds (full GEANT4-based) and 0.1 kSI2K seconds (ATLFAST) [166], where 2 to 3 kSI2K seconds corresponds to one second on a modern computer.

### 8.3 Simulated Datasets

The same simulated datasets as in the SUSY CSC notes (part of the so-called CSC book [26]) have been used for the studies presented in this work. All samples were produced by MC simulation inside the official ATLAS software (version 12.0.6) and production frameworks, and passed through the detailed GEANT4 detector simulation (unless stated otherwise) using the realistic detector geometry description.

The discovery reach plots differ slightly from those in the SUSY CSC chapter “Prospects for Supersymmetry Discovery Based on Inclusive Searches”, because the high statistics Alpgen  $t\bar{t}$  samples are used here, whereas the CSC plots have been obtained with the MC@NLO top samples.

All results given in this work correspond to an integrated luminosity of  $L = 1 \text{ fb}^{-1}$ , and all used datasets were generated for 14 TeV CM energy.



### 8.3.1 SUSY Benchmark Points

For detailed SUSY studies a set of SUSY benchmark points in the mSUGRA framework was chosen by ATLAS.<sup>3</sup>

As a guiding principle for the benchmark points, the predicted cosmological relic density of neutralinos was required to be roughly consistent with the observed cold dark matter density ( $\Omega h^2 < 0.14$  [134]). This translates into SUSY model parameters that result in a particle spectrum which ensures an efficient annihilation of neutralinos in the early universe. In the mSUGRA scenario, this can only be realised in a reduced parameter region where the annihilation is enhanced either by a significant higgsino component in the lightest neutralino or through mass relationships. The following SUSY benchmark points are defined in terms of the mSUGRA parameters at the unification scale:

- SU1:  $m_0 = 70 \text{ GeV}$ ,  $m_{1/2} = 350 \text{ GeV}$ ,  $A_0 = 0$ ,  $\tan\beta = 10$ ,  $\mu > 0$ . Coannihilation region where  $\tilde{\chi}_1^0$  annihilate with near-degenerate  $\tilde{\ell}$ .
- SU2:  $m_0 = 3550 \text{ GeV}$ ,  $m_{1/2} = 300 \text{ GeV}$ ,  $A_0 = 0$ ,  $\tan\beta = 10$ ,  $\mu > 0$ . Focus point region near the boundary where  $\mu^2 < 0$ . This is the only region in mSUGRA where the  $\tilde{\chi}_1^0$  has a high higgsino component, thereby enhancing the annihilation cross section for processes such as  $\tilde{\chi}_1^0 \tilde{\chi}_1^0 \rightarrow WW$ .
- SU3:  $m_0 = 100 \text{ GeV}$ ,  $m_{1/2} = 300 \text{ GeV}$ ,  $A_0 = -300 \text{ GeV}$ ,  $\tan\beta = 6$ ,  $\mu > 0$ . It corresponds to the “bulk” region where LSP annihilation occurs primarily through light slepton exchange.
- SU4:  $m_0 = 200 \text{ GeV}$ ,  $m_{1/2} = 160 \text{ GeV}$ ,  $A_0 = -400 \text{ GeV}$ ,  $\tan\beta = 10$ ,  $\mu > 0$ . Low mass point close to Tevatron bound.
- SU6:  $m_0 = 320 \text{ GeV}$ ,  $m_{1/2} = 375 \text{ GeV}$ ,  $A_0 = 0$ ,  $\tan\beta = 50$ ,  $\mu > 0$ . The funnel region where  $2m_{\tilde{\chi}_1^0} \approx m_A$ . Since  $\tan\beta \gg 1$ , the width of the pseudoscalar Higgs boson  $A$  is large and  $\tau$  decays dominate.
- SU8.1:  $m_0 = 210 \text{ GeV}$ ,  $m_{1/2} = 360 \text{ GeV}$ ,  $A_0 = 0$ ,  $\tan\beta = 40$ ,  $\mu > 0$ . Variant of the coannihilation region with  $\tan\beta \gg 1$ , so that only  $m_{\tilde{\tau}_1} - m_{\tilde{\chi}_1^0}$  is small. We will refer to this point as SU8.

Table 8.1 lists the LO and NLO cross sections of the benchmark points at 14 TeV CM energy, as obtained from the PROSPINO program [167, 168] (version 2.0.6), using the default settings, and the CTEQ6M PDF set [157].

All SUSY particle masses and branching ratios were generated with the ISASUGRA program, which belongs to the ISAJET package [130], using a top quark mass of 175 GeV. These spectra were then input to the HERWIG MC event generator. No event filter at the generator level was used in the production. Note that these SUSY samples are inclusive in the sense that they include all decay channels which are possible in the given SUSY model. Table 8.2 details the SUSY

---

<sup>3</sup>Another set of SUSY benchmark points was chosen in the GMSB framework. These GMSB benchmark points were used for detailed studies within the CSC SUSY efforts, but are not presented here because they are not used in the following analysis.

---

**Table 8.2:** SUSY particle masses in GeV for the benchmark points. The spectra were generated with ISAJET, using a top quark mass of 175 GeV. The benchmark points are defined in the text.

Particle	SU1	SU2	SU3	SU4	SU6	SU8
$\tilde{d}_L$	764.90	3564.13	636.27	419.84	870.79	801.16
$\tilde{u}_L$	760.42	3563.24	631.51	412.25	866.84	797.09
$\tilde{b}_1$	697.90	2924.80	575.23	358.49	716.83	690.31
$\tilde{t}_1$	572.96	2131.11	424.12	206.04	641.61	603.65
$\tilde{d}_R$	733.53	3576.13	610.69	406.22	840.21	771.91
$\tilde{u}_R$	735.41	3574.18	611.81	404.92	842.16	773.69
$\tilde{b}_2$	722.87	3500.55	610.73	399.18	779.42	743.09
$\tilde{t}_2$	749.46	2935.36	650.50	445.00	797.99	766.21
$\tilde{e}_L$	255.13	3547.50	230.45	231.94	411.89	325.44
$\tilde{\nu}_e$	238.31	3546.32	216.96	217.92	401.89	315.29
$\tilde{\tau}_1$	146.50	3519.62	149.99	200.50	181.31	151.90
$\tilde{\nu}_\tau$	237.56	3532.27	216.29	215.53	358.26	296.98
$\tilde{e}_R$	154.06	3547.46	155.45	212.88	351.10	253.35
$\tilde{\tau}_2$	256.98	3533.69	232.17	236.04	392.58	331.34
$\tilde{g}$	832.33	856.59	717.46	413.37	894.70	856.45
$\tilde{\chi}_1^0$	136.98	103.35	117.91	59.84	149.57	142.45
$\tilde{\chi}_2^0$	263.64	160.37	218.60	113.48	287.97	273.95
$\tilde{\chi}_3^0$	466.44	179.76	463.99	308.94	477.23	463.55
$\tilde{\chi}_4^0$	483.30	294.90	480.59	327.76	492.23	479.01
$\tilde{\chi}_1^+$	262.06	149.42	218.33	113.22	288.29	274.30
$\tilde{\chi}_2^+$	483.62	286.81	480.16	326.59	492.42	479.22
$h^0$	115.81	119.01	114.83	113.98	116.85	116.69
$H^0$	515.99	3529.74	512.86	370.47	388.92	430.49
$A^0$	512.39	3506.62	511.53	368.18	386.47	427.74
$H^+$	521.90	3530.61	518.15	378.90	401.15	440.23

particle mass spectra for each benchmark point.

Albeit the SUSY samples are all generated with mSUGRA, they provide a rather wide range of possible decay topologies. For all these points, the gluino mass is less than 1 TeV, and the ratio  $M(\tilde{g})/M(\tilde{\chi}_1^0) = 6\text{--}8$ . For all points except SU2, the squark and gluino masses are comparable. Hence gluinos and squarks are strongly produced and decay giving relatively hard jets, possible leptons, and missing transverse energy. These features are relatively general among different SUSY models.

### 8.3.2 mSUGRA Signal Grid

A scan over the mSUGRA parameter space has been used to sample a wider range of possible signal signatures and to estimate the discovery reach.

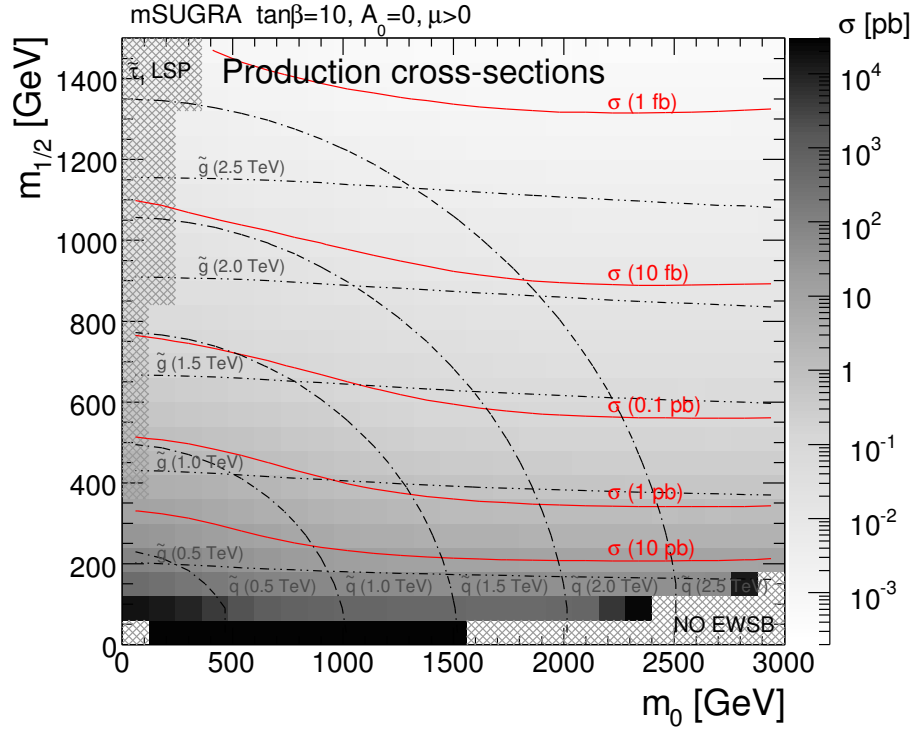


**Figure 8.1:** Production cross sections (LO) for the mSUGRA grid, as obtained from HERWIG [146] (version 6.510). The dashed region is theoretically not viable in the models due to lack of electroweak symmetry breaking. Also shown are contour lines of equal gluino and squark masses in steps of 500 GeV.

By design such a scan consists of a large number of signal points. Hence the ATLFast detector simulation was used instead of the GEANT4 based full simulation.

Dark matter and other existing constraints were ignored in the scan, in order to provide a wide range of possible SUSY patterns. In any case, as already stated in Chapter 7, most constraints can be satisfied by modifying the SUSY breaking model while leaving the basic phenomenology untouched.

The employed  $25 \times 25$  mSUGRA grid uses fixed  $\tan\beta = 10$ ,  $A_0 = 0$ , and  $\mu > 0$ . It varies  $m_0$  from 60 GeV to 2940 GeV in 25 steps of 120 GeV, and  $m_{1/2}$  from 30 GeV to 1470 GeV in 25 steps of 60 GeV. SUSY spectra were generated using ISAJET [130] (version 7.75) with a top quark mass of 175 GeV. Out of the 625 possible grid points, a spectrum could be successfully generated for 600; the other 25 failed for theoretical reasons (no electroweak symmetry breaking, or tachyonic particles). For each good point 20 thousand events were produced using HERWIG/JIMMY [146, 153] and ATLFast [162]. No event filter at the generator level was used in the production.

The LO cross sections of the mSUGRA grid were obtained from HERWIG [146] (version 6.510). They are indicated in Fig. 8.1 by the grey background level as well as the red contour lines. As expected, the cross sections reflect the squark and gluino masses.

### 8.3.3 Standard Model Backgrounds

The SM background processes most relevant to SUSY searches are  $t\bar{t}$ ,  $W + \text{jets}$ ,  $Z + \text{jets}$ , QCD jet production, and diboson production. All these processes are discussed below.

Different MC generators were used for the different processes, in an attempt to optimise the reliability of the estimate for the SM backgrounds. Pile-up and cavern background simulations were not included in the signal and background samples.

For all the samples except QCD jet production a sample corresponding to at least  $1 \text{ fb}^{-1}$  of integrated luminosity was simulated.

#### QCD jet production

Multijet production via QCD processes is the dominant high- $p_T$  process at the LHC and is an important background in many of the physics studies. Even if NLO corrections are partially known, the remaining uncertainties from missing higher-order corrections remain large. Therefore, LO estimates were used and large errors were assigned to cover the uncertainty.

For QCD multijets with  $p_T^{\text{jet}} > 25 \text{ GeV}$ , PYTHIA [111] predicts a total production cross section of  $367 \mu\text{b}$  at LO, while it is estimated to be  $477 \mu\text{b}$  at NLO, as obtained from NLOJET++ [169, 170].

For the simulation of QCD multijet samples, ALPGEN is an appropriate choice. For practical reasons, however, it was impossible to generate ALPGEN samples with sufficiently large MC statistics. As a backup solution the shower MC generator PYTHIA was used, for which adequate statistics could be generated by producing samples in  $p_T$ -slices (denoted as J1, J2, etc.) of the hard scattering.

An event filter at generation level was applied, requiring:

- at least one jet with transverse momentum above 80 GeV,
- at least one other jet with transverse momentum above 40 GeV,
- and missing transverse energy above 100 GeV.

Details of the PYTHIA production of QCD multijets are given in Table 8.3.

These event filter selection requirements, as well as the following ones, are below the analysis cuts (see Chapter 10).

#### Vector boson production ( $W/Z + \text{jets}$ )

Vector boson production constitutes an important background to SUSY searches, in particular  $W$  and  $Z$  boson production in association with several hard jets, and with significant missing transverse energy. The missing transverse energy can arise from leptonic  $W$  decays ( $W \rightarrow l\nu$ ),  $Z$

**Table 8.3:** PYTHIA production of QCD jets,  $p_T$ -range of the hard scattering, ATLAS MC sample ID, production cross section, event filter efficiency, effective cross section, the available number of MC events, and the corresponding integrated luminosity.

Sample	$p_T$ -range [GeV]	ID	$\sigma$ [pb]	$\varepsilon_{\text{EF}}$	$\sigma_{\text{eff}}$ [pb]	$N_{\text{MC}}$	$L$ [fb $^{-1}$ ]
J4	140 – 280	8090	$3.16 \cdot 10^5$	0.0029	916.4	$70 \cdot 10^3$	0.08
J5	280 – 560	8091	$1.25 \cdot 10^4$	0.0524	655	$85 \cdot 10^3$	0.13
J6	560 – 1120	8092	344	0.196	67.4	$35 \cdot 10^3$	0.52
J7	1120 – 2240	8093	5.3	1.0	5.3	$4 \cdot 10^3$	0.75
J8	> 2240	8094	$2.2 \cdot 10^{-2}$	1.0	$2.2 \cdot 10^{-2}$	$4 \cdot 10^3$	180

decays into neutrinos ( $Z \rightarrow \nu\nu$ ), but also leptonic  $Z$  decays ( $Z \rightarrow ll$ ) where at least one lepton is not identified.

The total  $W$  production cross section multiplied with the branching ratio for a subsequent leptonic decay ( $W \rightarrow l\nu$ ) accounts for 20.5 nb at NNLO, while the  $Z$  production cross section including the branching ratio for a leptonic decay ( $Z \rightarrow ll$ ) with  $m_{ll} > 60$  GeV is 2.02 nb at NNLO [171].

It is important to simulate the kinematics of the additional jets as accurately as possible. The  $W$  + jets and  $Z$  + jets samples were therefore simulated with the ALPGEN [149] generator.

In the AlpGen matrix element calculation, partons were required to have transverse momentum above 40 GeV, and be separated from each other by  $\Delta R > 0.7$ . Showering and hadronisation are provided through the HERWIG program and multi-parton interactions are modelled by the JIMMY program. In order to achieve a correct description of the jet multiplicities, it is necessary to match the jets produced by the matrix element generator and the ones produced by parton showering (MLM matching [161]).

An event filter at generation level was applied, requiring:

- at least four jets, each with transverse momentum above 40 GeV,
- out of which at least one jet has a transverse momentum above 80 GeV,
- and missing transverse energy above 80 GeV.

The LO cross sections were normalised to the results from the NNLO calculations [171] by applying a  $k$  factor of 1.15 (1.27) for the  $W$  ( $Z$ ) samples.

Table 8.4 details the ALPGEN production of SM  $W$  and  $Z$  bosons in association with jets. The N-partons samples have to be summed to produce the multijet samples. Also the total cross section is given by the sum over all parton multiplicities.

### Top quark production

The production of  $t\bar{t}$  quark pairs is the dominant SM background for most SUSY searches. It has been simulated with the MC event generators MC@NLO [151, 152] and ALPGEN [149]. Note

**Table 8.4:** ALPGEN production of  $W$  and  $Z$  bosons + jets, additional matrix element parton multiplicity (N), ATLAS MC sample ID, production cross section, parton - jet MLM matching efficiency, event filter efficiency,  $k$  factor, recalculated effective cross section, the available MC number of events, and the corresponding integrated luminosity  $L$ .

Sample	N	ID	$\sigma$ [pb]	$\varepsilon_{\text{MLM}}$	$\varepsilon_{\text{EF}}$	$k$ factor	$\sigma_{\text{eff}}^{\text{NLO}}$ [pb]	$N_{\text{MC}}$	$L$ [fb $^{-1}$ ]
$W_{e\nu}$	2	5223	504	0.5430	0.00244	1.15	0.77	$4 \cdot 10^3$	5.2
	3	5224	122	0.4305	0.06460	1.15	3.90	$16 \cdot 10^3$	4.1
	4	5225	28.4	0.3490	0.20330	1.15	2.32	$10 \cdot 10^3$	4.3
	5	5226	6.1	0.3433	0.28452	1.15	0.69	$3 \cdot 10^3$	4.3
$W_{\mu\nu}$	3	8203	122	0.4309	0.01322	1.15	0.79	$4 \cdot 10^3$	5.1
	4	8204	28.4	0.3490	0.18681	1.15	2.13	$10 \cdot 10^3$	4.7
	5	8205	6.1	0.3503	0.28520	1.15	0.70	$4 \cdot 10^3$	5.7
$W_{\tau\nu}$	2	8208	504	0.5415	0.00196	1.15	0.61	$3 \cdot 10^3$	4.9
	3	8209	122	0.4277	0.05449	1.15	3.27	$14 \cdot 10^3$	4.3
	4	8210	28.4	0.3525	0.26725	1.15	3.08	$14 \cdot 10^3$	4.5
	5	8211	6.1	0.3474	0.38370	1.15	0.94	$5 \cdot 10^3$	5.3
$Z\nu\nu$	3	5124	79.8	0.4213	0.02501	1.27	1.07	$40 \cdot 10^3$	37.4
	4	5125	18.5	0.3417	0.38164	1.27	3.06	$48 \cdot 10^3$	15.7
	5	5126	3.96	0.3424	0.55204	1.27	0.95	$14 \cdot 10^3$	14.7
$Zee$	1	5161	179.8	0.6755	0.00260	1.27	0.41	$1.5 \cdot 10^3$	3.7
	2	5162	56.4	0.5407	0.10710	1.27	4.15	$49 \cdot 10^3$	11.8
	3	5163	14.1	0.4204	0.36650	1.27	2.76	$22 \cdot 10^3$	8.0
	4	5164	3.26	0.3482	0.48173	1.27	0.70	$6 \cdot 10^3$	8.6
	5	5165	0.7	0.3522	0.56220	1.27	0.18	$2 \cdot 10^3$	11.1
$Z\mu\mu$	3	8109	14.1	0.4213	0.03187	1.27	0.24	$11 \cdot 10^3$	45.8
	4	8110	3.26	0.3431	0.37120	1.27	0.53	$5 \cdot 10^3$	9.4
	5	8111	0.7	0.3522	0.54226	1.27	0.17	$2 \cdot 10^3$	11.8
$Z\tau\tau$	2	8114	56.4	0.5321	0.00565	1.27	0.22	$4 \cdot 10^3$	18.2
	3	8115	14.1	0.4215	0.05448	1.27	0.41	$7 \cdot 10^3$	17.1
	4	8116	3.26	0.3458	0.14466	1.27	0.20	$4 \cdot 10^3$	20.0
	5	8117	0.7	0.3435	0.20196	1.27	0.06	$1 \cdot 10^3$	16.7

**Table 8.5:** MC@NLO production of  $t\bar{t}$  processes, ATLAS MC sample ID, production cross section, event filter efficiency, effective cross section, the available number of MC events, and the corresponding integrated luminosity.

Sample	ID	$\sigma$ [pb]	$\varepsilon_{\text{EF}}$	$\sigma_{\text{eff}}^{\text{NLO}}$ [pb]	$N_{\text{MC}}$	$L$ [ $\text{fb}^{-1}$ ]
$t\bar{t} \rightarrow l\nu l\nu$ or $l\nu qq$	5200	833	0.54	450	$600 \cdot 10^3$	1.33
$t\bar{t} \rightarrow qq qq$	5204	833	0.46	383	$100 \cdot 10^3$	0.26

that the ALPGEN samples were passed through the ATLFAST detector simulation, while the full detector simulation was employed for the fewer events of the MC@NLO samples. Reconstruction efficiencies of the ALPGEN samples have been corrected to match those of the full detector simulation samples.

The total  $t\bar{t}$  production cross section of 833 pb was determined by NLO calculations including a next-to-leading log (NLL) resummation [172]. For the LO ALPGEN samples, this implies a  $k$  factor of 2.02.

The MC@NLO production of  $t\bar{t}$  processes, listed in Table 8.5, is divided into a semi/full leptonic, and a full hadronic  $t\bar{t}$  decay sample. The division is performed with an event filter at generation level.

The ALPGEN production of  $t\bar{t}$  processes is listed in Table 8.6. It is divided into full hadronic ( $t\bar{t} \rightarrow qq qq$ ), semi leptonic ( $t\bar{t} \rightarrow l\nu qq$ ), and full leptonic ( $t\bar{t} \rightarrow l\nu l\nu$ ) decay channels. Additionally, due to the usage of ALPGEN, each decay channel is sub-divided by the (additional) parton multiplicity. Similarly to the ALPGEN  $W/Z$  boson production, the MLM technique is used to avoid double counting. All ALPGEN samples are exclusive with respect to each other.

An event filter at generation level was applied to the ALPGEN samples, requiring:

- at least four jets, out of which one has a transverse momentum above 40 GeV, OR at least two jets, out of which one has a transverse momentum above 80 GeV,
- and missing transverse energy above 50 GeV.

### Diboson production

The contributions of the diboson processes  $WW$ ,  $ZZ$  and  $WZ$  are almost negligible for multi-jet SUSY analyses as they are strongly suppressed by typical SUSY selections requiring a large number of jets with high transverse momenta and large missing transverse energy. The data samples were generated at leading order with the HERWIG MC generator, including the full off-shell structure for  $Z/\gamma$ . The cross sections were then normalised to the NLO cross sections calculated with the MCFM code [173].

An event filter at generation level was applied, requiring at least one electron or muon with transverse momentum above 10 GeV and within  $|\eta| < 2.8$ . Details of the diboson production are given in Table 8.7.

**Table 8.6:** ALPGEN production of  $t\bar{t}$  processes, additional matrix element parton multiplicity (N), production cross section, parton - jet MLM matching efficiency, event filter efficiency,  $k$  factor, recalculated effective cross section, the available MC number of events, and the corresponding integrated luminosity  $L$ .

Sample	N	$\sigma$ [pb]	$\varepsilon_{\text{MLM}}$	$\varepsilon_{\text{EF}}$	$k$ factor	$\sigma_{\text{eff}}^{\text{NLO}}$ [pb]	$N_{\text{MC}}$	$L$ [fb $^{-1}$ ]
$t\bar{t} \rightarrow l\nu l\nu$	0	49.41	0.504	0.1075	2.02	5.4	574272	106
	1	32.03	0.425	0.3189	2.02	8.8	444640	51
	2	13.15	0.365	0.5768	2.02	5.6	324100	58
	3	4.22	0.403	0.7512	2.02	2.6	152420	59
$t\bar{t} \rightarrow l\nu qq$	0	197.62	0.502	0.1713	2.02	34.4	1495869	43
	1	128.03	0.425	0.3831	2.02	42.1	1294400	31
	2	52.71	0.367	0.5419	2.02	21.2	762269	36
	3	17.01	0.404	0.6307	2.02	8.8	321559	37
$t\bar{t} \rightarrow qqqq$	0	197.63	0.502	0.0087	2.02	1.8	77604	43
	1	128.10	0.424	0.0169	2.02	1.9	56663	30
	2	52.72	0.366	0.0261	2.02	1.0	36690	37
	3	16.92	0.403	0.0378	2.02	0.5	19246	38

**Table 8.7:** HERWIG production of dibosons, ATLAS MC sample ID, production cross section, event filter efficiency,  $k$  factor, recalculated effective cross section, the available number of MC events, and the corresponding integrated luminosity.

Sample	ID	$\sigma$ [pb]	$\varepsilon_{\text{EF}}$	$k$ factor	$\sigma_{\text{eff}}^{\text{NLO}}$ [pb]	$N_{\text{MC}}$	$L$ [fb $^{-1}$ ]
$WW$	5985	70	0.35	1.594	39.05	$5 \cdot 10^4$	1.3
$ZZ$	5986	11	0.19	1.348	2.83	$5 \cdot 10^4$	17.7
$WZ$	5987	27	0.29	1.803	14.06	$5 \cdot 10^4$	3.6



## Chapter 9

# Reconstruction and Expected Performance

The raw ATLAS detector data consist of about 1.5 MB of nearly unprocessed signals from the inner detector, calorimeters, muon spectrometer, and the TDAQ system. In addition to the design and construction of the detector, the development of specialised software tools for the raw signal conversion, the calibration and alignment of the different systems, and the reconstruction and identification of physics objects has been a major challenge. The reconstruction stage can be described as a big data reduction process: millions of raw input signals are reduced to the few relevant physics quantities. In fact, the fully reconstructed event size is reduced from the initial 1.5 MB to about 100 kB [110]. All common off-line software has been made available in one framework, named Athena. This chapter is dedicated to the description of the physics reconstruction algorithms relevant to the SUSY studies which are described in Chapter 10. Note that most information which is presented in this chapter has been obtained from Ref. [26, 50].

In Section 9.1 the Athena framework with its basic concepts is briefly introduced. Sections 9.2–9.5 review the standard off-line reconstruction algorithms for electrons, muons, jets, and missing transverse energy. The basic design principles of the various reconstruction and identification algorithms are described, together with their expected performance.

### 9.1 Off-Line Reconstruction

The common ATLAS software framework, Athena, is used for various tasks, mainly in the off-line environment but also the high-level trigger makes use of some Athena components (cf. Chapter 4). The full task of extracting the physics quantities from the raw data is broken down into smaller tasks, to facilitate the use of common tools. Examples of such tools are: raw event data stream converters, transient–persistent converters, fitting tools, etc. Athena provides a common framework for all software, the event-loop (and possibly input file-loop), and a common way to exchange data-objects (known as StoreGate). It further defines three types of software components: algorithms, tools, and services. Algorithms are executed once per event. A typical algorithm example

is the reconstruction of electrons. The electron finder algorithm runs once per event to identify all electron candidates and to assign quality flags. Algorithms can use private or public (shared with other software components) tools to perform specific tasks. Tools are thus not executed from the Athena event-loop. A typical example of a tool is the software component that reads one sampling of the EM calorimeter and provides useful variables. It is used from within the electron algorithm, but also the muon and missing energy reconstruction algorithms utilise it. Services are designed to provide certain information to a wide range of algorithms and tools. Some typical services are dedicated to the detector geometry, the calibration constants, and the trigger configuration. A comprehensive description of the Athena software framework can be found in Ref. [110].

The following sections describe the algorithms which perform the reconstruction of physics quantities that are relevant for the SUSY analysis: electrons, muons, jets, and missing transverse energy. Other standard ATLAS algorithms, which are not used in the present work, include: jet b-tagging,  $\tau$ -lepton reconstruction, and photon reconstruction.

It is noteworthy that the reconstruction algorithms can produce overlapping objects, such as a jet and an electron both with the same calorimeter cluster. This issue is dealt with by a so-called *overlap removal* procedure, which is discussed in Chapter 10.

## 9.2 Electrons

Powerful and efficient electron identification is demanded by many physics studies, including the one-lepton SUSY analysis, as described later. The main challenge lies in the very low signal-to-background ratio: the ratio between the rate of isolated electrons and the rate of QCD jets with a  $p_T$  in the range of 20 – 50 GeV is expected to be of the order of  $10^{-5}$  at the LHC [26]. It is nearly two orders of magnitude higher ( $10^{-3}$ ) at the Tevatron. To retain the same electron identification and background rejection capabilities, the LHC experiments thus have to improve their corresponding performance by almost two orders of magnitude.

Two complementary electron reconstruction algorithms have been implemented in the ATLAS off-line framework. Both employ the same event data model. The ATLAS default algorithm starts from clusters in the EM calorimeters, and then provides identification variables based on information from the inner detector and the calorimeters.

The second ATLAS electron reconstruction algorithm is optimised for low energy electrons. It is seeded from inner detector tracks which are then matched to relatively isolated energy depositions in the EM calorimeters.

The first algorithm — calorimeter-seeded — is the one used in the SUSY studies presented in this work, and it is further discussed in the following.

### 9.2.1 Pre-selection of electron candidates

Potentially interesting electrons are pre-selected by the following procedure:

---

- Start from EM calorimeter clusters with a transverse energy above  $\sim 3$  GeV (seeds).
- Search for a matching track among all reconstructed inner detector tracks. Tracks are extrapolated to the EM calorimeter, and then required to match the cluster within a coarse  $\Delta\eta \times \Delta\phi$  window of  $0.05 \times 0.10$ .
- Finally, the  $E/p$  ratio (energy of the cluster over the momentum of the associated track) is required to be below 10.

All electrons that satisfy the above criteria are stored in the so-called electron container of the analysis data files. The efficiency of this pre-selection procedure was found to be around 93%, for simulated single electrons with  $E_T > 20$  GeV and  $|\eta| < 2.5$  [26].

The identification of electrons is performed using the combined information of the calorimeters and the inner detector, including the discriminating techniques of the TRT. The ATLAS default identification is based on simple box-cuts, as described below. More advanced multi-variate techniques have been studied and shown to improve the identification to a certain extent [26]. For initial data-taking, however, the recommended default is the cut-based method.

## 9.2.2 Electron identification with the cut-based method

The cut-based method for electron identification uses inner detector and calorimeter variables to distinguish electrons from background. Each input variable is treated independently, i.e. correlations are not considered. The cuts have been optimised in up to seven bins in  $\eta$  and up to six bins in  $p_T$ . All cut results are stored in a bit-pattern for each electron candidate in the electron container. To facilitate the combination of the different cuts, and ease comparison, three reference sets of cuts have been defined: loose, medium, and tight.

### Loose cuts

The set of loose cuts is based on limited information from the calorimeters alone. It provides very good identification efficiency but low background rejection. The list of variables used is given in Table 9.1.

These selection cuts, applied to the measurements in the hadronic calorimeter and the second sampling of the EM calorimeters, are designed to reject the overwhelming background of hadronic jets.

### Medium cuts

The set of medium cuts adds further requirements on variables of the EM calorimeter strips (first sampling/layer) and the tracking. The jet rejection increases by a factor of 3 to 4 while the electron efficiency drops by approximately 10%, all with respect to the loose cuts [26]. Table 9.2 lists the variables used for the medium set.

---

**Table 9.1:** Summary of the variables used in the set of loose electron cuts. Most cut values depend on  $\eta$  and  $p_T$  and are therefore not given.

Type	Description (loose cuts)	
Acceptance	L1	$ \eta  < 2.47$
Hadronic leakage	L2	Ratio of $E_T$ in the first sampling of the hadronic calorimeter to the $E_T$ of the EM cluster.
2 <sup>nd</sup> layer of EM cal.	L3	Lateral shower shape, given by ratio in $\eta$ of cell energies in $3 \times 7$ versus $7 \times 7$ cells.
	L4	Lateral width, given by ratio in $\phi$ of cell energies in $3 \times 3$ versus $3 \times 7$ cells.

**Table 9.2:** Summary of the variables used in the set of medium electron cuts. Most cut values depend on  $\eta$  and  $p_T$  and are therefore not given.

Type	Description (medium cuts)	
	L1 - L4 All loose cuts are included.	
1 <sup>st</sup> layer of EM cal.	M1	Difference in energy of second-highest maximum to the minimum: $\Delta E = E_{\max 2} - E_{\min}$ , in $\Delta\eta \times \Delta\phi = 0.125 \times 0.2$ around the cluster cell with the highest $E_T$ .
	M2	Second-highest energy maximum normalised to the cluster energy: $R_{\max 2} = E_{\max 2} / (1 + 9 \cdot 10^{-3} E_T)$ , where $E_T$ is the transverse energy of the cluster in the EM cal. in units of GeV, and $E_{\max 2}$ as above.
	M3	Total shower width: $\sqrt{\sum_i E_i (i - i_{\max})^2 / \sum_i E_i}$ , where $i$ is the strip number, and $i_{\max}$ the strip number of the first local maximum, determined in a $\Delta\eta \times \Delta\phi = 0.125 \times 0.2$ window.
	M4	Shower width for three strips around maximum strip.
	M5	Fraction of energy outside core of three central strips: $[E(\pm 3) - E(\pm 1)] / E(\pm 1)$ , where $E(\pm n)$ is the energy in $\pm n$ strips around the strip with the highest energy.
Track quality	M6	Number of hits in the pixel detector (at least one).
	M7	Number of hits in the pixel and SCT detectors (at least nine).
	M8	Transverse impact parameter ( $< 1$ mm).

**Table 9.3:** Summary of the variables used in the set of tight electron cuts. Most cut values depend on  $\eta$  and  $p_T$  and are therefore not given.

Type		Description (tight cuts)
	L1 - L4	All loose cuts are included.
	M1 - M8	All medium cuts are included.
Vertexing layer	T1	Number of hits in the vertexing-layer (at least one).
Track matching	T2	$\Delta\eta$ between the cluster and the track ( $< 0.005$ ).
	T3	$\Delta\phi$ between the cluster and the track ( $< 0.02$ ).
	T4	Tighter cut on $E/p$ ratio.
TRT	T5	Total number of hits in the TRT.
	T6	Ratio of the number of high-threshold hits to the total number of hits in the TRT.

The selection cuts applied in the first layer of the EM calorimeters (M1-M5) aim at further rejecting jets with a large EM component.

### Tight cuts

The set of tight cuts exploits all available information. In addition to the cuts applied in the loose and medium sets, it adds requirements on variables of the inner detector, and the track-cluster matching. The list of variables used is given in Table 9.3.

After the calorimeter cuts of the medium set have been applied, the contamination of the inclusive signal from charged hadrons is reduced. It can be further reduced by requiring the presence of a vertexing-layer hit, a good quality track pointing to an EM cluster, and a close energy-momentum match. The tight cuts increase the jet rejection by a factor of the order of  $\mathcal{O}(400)$  at the expense of reducing the electron efficiency by about 15%, all with respect to the medium cuts.

### Isolation

An isolation requirement can be used to further increase the jet rejection by reducing the rate of non-isolated electron candidates. Two approaches have been studied, based on:

- calorimeter isolation, requiring a limited energy in a cone around the electron cluster,
- tracking isolation, requiring a maximum (sum of) high- $p_T$  track(s) in the inner detector around the electron candidate.

The default calorimeter-based isolation variable collects all calorimeter energy not belonging to the electron cluster in a cone of size  $\Delta R < 0.2$  around the electron candidate. A typical cut value, used in these SUSY studies, is to require this isolation variable to be below 10 GeV.

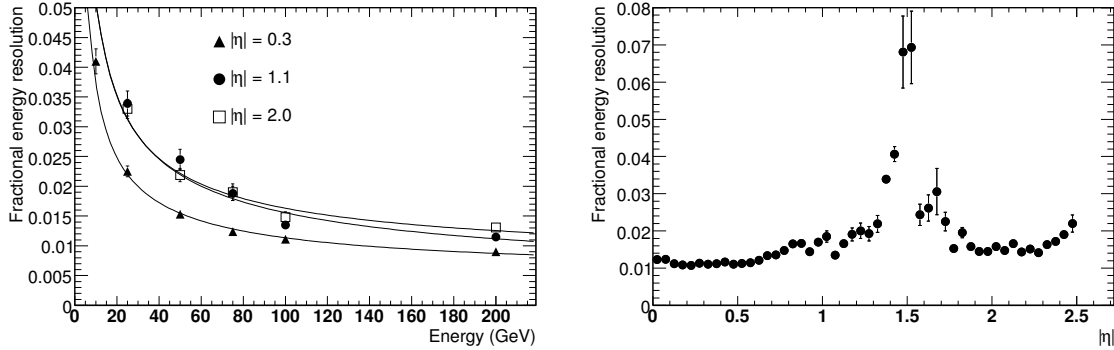


**Figure 9.1:** Expected electron fractional energy resolution as a function of energy (left) and  $|\eta|$  (right), taken from Ref. [50]. The results were obtained from: electrons with the indicated fixed  $\eta$  values (left plot) and with a fixed electron energy of 100 GeV (right plot). The solid lines (left) represent fits to a function containing a stochastic term, a constant term, and a noise term.

### 9.2.3 Performance

The electron reconstruction performance is studied mainly in terms of efficiency and (energy) resolution.

The electron energy resolution, as a function of the energy and  $|\eta|$ , is shown in Fig. 9.1. The results depending on the energy (left plot) were fitted with a function  $\sigma/E = a/\sqrt{E} \oplus b/E \oplus c$ , where the terms on the right-hand side are respectively: stochastic term ( $a$ ), noise term ( $b$ ), and constant term ( $c$ ). The stochastic term was found to be 10.0%, 15.1%, and 14.5% for electrons with three fixed  $\eta$  values of 0.3, 1.1, and 2.0 respectively. The significant increase observed in the stochastic term for increased  $\eta$ -values is due to the much larger amount of material in front of the EM calorimeter.

The energy resolution dependence on  $|\eta|$  (right plot) shows a clear degradation in the  $\eta$ -region between 1.37 and 1.52. This is the transition region between barrel and end-cap cryostats. Electrons from this region are excluded in the SUSY analysis, as described later.

The electron identification performance is summarised in Table 9.4 [26]. It can be seen that the set of tight cuts together with the isolation requirement yields the required jet rejection of the order of  $10^5$  while retaining about 64% of the isolated electrons in the  $E_T$  range above  $\approx 20$  GeV. The efficiency for non-isolated electrons, as obtained from  $b, c \rightarrow e$  processes, is significantly lower than for isolated electrons, as obtained from  $Z \rightarrow ee$ . As expected, this is particularly noticeable in combination with the isolation requirement, which is applied together with the set of tight cuts. Non-isolated electrons with significant overlap with nearby hadronic showers are strongly suppressed.

The electron efficiency in SUSY events, as shown in Fig. 9.2, is slightly lower than that of the single electron samples. This is expected because of the high level of hadronic activity generated in the long SUSY decay chains. The  $|\eta|$  dependency of the electron efficiency shows the typical detector geometry features: the efficiency in the end-caps is worse than in the barrel because of the larger amount of material, and the drop around  $|\eta| \sim 1.35$  corresponds to the barrel/end-cap

**Table 9.4:** Expected efficiencies for isolated ( $Z \rightarrow ee$ ) and non-isolated ( $b, c \rightarrow e$ ) electrons and corresponding jet background rejections for the three reference sets of electron identification cuts (see text), taken from Ref. [26]. The background rejection results were obtained from a simulated filtered dijet sample, with an  $E_T$ -thresholds of 17 GeV. The statistical errors are given together with the electron efficiencies. The tight cuts include the calorimeter-based isolation requirement (10 GeV).

Cuts	Electron identification efficiencies (%)		Jet rejection
	$Z \rightarrow ee$	$b, c \rightarrow e$	
Loose	$87.96 \pm 0.07$	$50.8 \pm 0.5$	$567 \pm 1$
Medium	$77.29 \pm 0.06$	$30.7 \pm 0.5$	$2184 \pm 13$
Tight (with isol.)	$64.22 \pm 0.07$	$17.3 \pm 0.4$	$(9.8 \pm 0.4) \cdot 10^4$

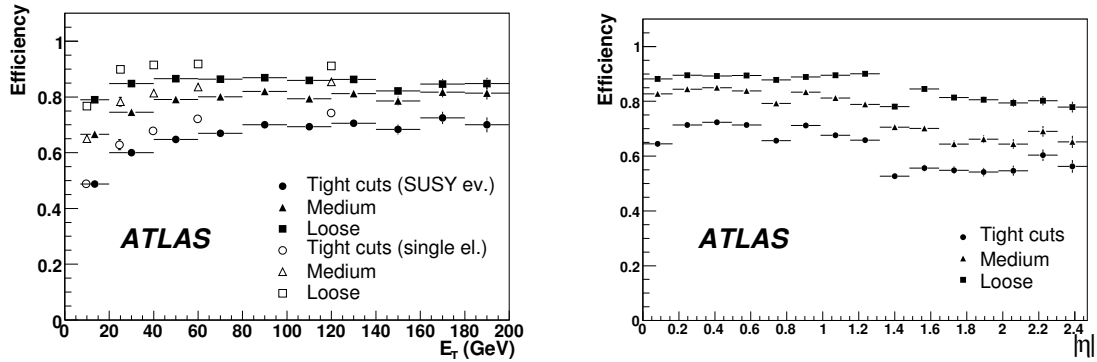


**Figure 9.2:** Electron identification efficiency as a function of  $E_T$  (left) and  $|\eta|$  (right), taken from Ref. [26]. The full symbols correspond to electrons produced in SUSY (SU3) events, while the open symbols correspond to single electrons with fixed  $E_T$ . The efficiencies as a function of  $|\eta|$  are shown for electrons with an  $E_T$  cut of 17 GeV. The set of tight cuts includes the calorimeter-based isolation requirement (10 GeV).

transition region.

The uncertainty on the knowledge of the electron efficiency is expected to be around 0.5% for an integrated luminosity of  $1 \text{ fb}^{-1}$  [26]. It will be derived from data by the so-called tag-and-probe method [174] from known resonance processes, like  $Z \rightarrow ee$ . The systematic uncertainties on the energy scale and energy resolution of electrons are expected to be 1% and 10% respectively, again for  $1 \text{ fb}^{-1}$  of integrated luminosity.

### 9.3 Muons

Akin to electrons, high- $p_T$  muons are very interesting objects to probe SM as well as beyond-SM physics processes. The ATLAS detector has been designed to provide precision measurements of muons with momenta ranging from approximately 3 GeV to 3 TeV. Muons are identified and measured in the muon spectrometer and inner detector. The calorimeters are exploited to improve the efficiency in regions poorly instrumented in the muon spectrometer ( $|\eta| \sim 0$ ) and to provide information about possible large energy losses in the calorimeter material. The inner detector

provides the best measurement at low to intermediate muon  $p_T$ , whereas the muon spectrometer dominates the measurement precision for  $p_T \gtrsim 30$  GeV.

### 9.3.1 Reconstruction

The strategies for the reconstruction and identification of muons are:

- *Stand-alone muons*: reconstruction of muons solely from data of the muon spectrometer.
- *Combined muons*: obtained from matching stand-alone muons to nearby inner detector tracks.
- *Tagged muons*: obtained from inner detector tracks where the extrapolated track to the muon spectrometers can be matched to hits/segments.

Each of these approaches is implemented by two competing algorithms in the ATLAS framework. The algorithms are grouped into two families, named after the algorithms for the combined muons: Staco (statistical combination) [175] and Muid [176]. Consequently, the analysis data files contain one muon container for each family. The Staco algorithm collection is the current ATLAS default for physics analyses. It has also been used for the SUSY analysis of this thesis.

#### Stand-alone muons

The two ATLAS algorithms that provide stand-alone muon reconstruction are named Muonboy [175] and Moore (muon object oriented reconstruction) [177]. Muonboy belongs to the Staco family, while Moore is part of the Muid group.

Both algorithms implement the following track reconstruction logic: pre-processing of raw data to form drift-circles in the MDTs or clusters in the CSCs and the trigger chambers (RPCs and TGCs); pattern-finding and segment-making; segment-combining; and finally track-fitting.

The track segments are defined as straight lines in a single muon station. The final track-fitting process takes into account the full geometrical description of the traversed material and the magnetic field inhomogeneities along the muon trajectory.

Successful muon spectrometer tracks are extrapolated back to the interaction point. This back-propagation process corrects for multiple scattering and energy loss in the calorimeters. The energy lost by  $dE/dX$  in the calorimeters is estimated using a parametrised method: the expected energy loss is obtained as a function of the amount of material traversed in the calorimeters. Additionally, it is possible to use the calorimeter energy measurements: the measured energy is used only if it significantly deviates from the most probable energy loss and if the muon track is isolated.

The stand-alone muon reconstruction covers the full muon spectrometer range over  $|\eta| < 2.7$ . This acceptance coverage, however, contains a hole around  $\eta = 0$  (inner detector cables, cryogenic lines) and is degraded in the  $1.1 < |\eta| < 1.7$  region. This issue is further discussed in the muon performance section.



### Combined muons

The combination of stand-alone muon tracks with inner detector tracks is performed in the range up to  $|\eta| < 2.5$ , which corresponds to the geometrical acceptance of the inner detector. It is expected to considerably improve the momentum resolution for muons with  $p_T < 100$  GeV. It further helps to suppress fake muon background arising from pion punch-through or pion and kaon decays in flight.

Both Staco, Muid use the same matching technique. A match  $\chi^2$  is defined by the two track vectors and weighted by their combined covariance matrix:

$$\chi_{\text{match}}^2 = (\mathbf{T}_{\text{MS}} - \mathbf{T}_{\text{ID}})^T (\mathbf{C}_{\text{MS}} + \mathbf{C}_{\text{ID}})^{-1} (\mathbf{T}_{\text{MS}} - \mathbf{T}_{\text{ID}}),$$

where  $\mathbf{T}$  denotes a vector of five track parameters,  $\mathbf{C}$  is the corresponding covariance matrix, and the subscripts ID and MS stand for inner detector and muon spectrometer, respectively. The used inner detector tracks are obtained from the default algorithm, see Ref. [178] for a comprehensive description.

A cut on the  $\chi_{\text{match}}^2$  quantity selects good track pairs. The value used in the SUSY studies of this work is  $\chi_{\text{match}}^2 < 100$ .

The method to obtain the combined track-vector is different for the two algorithms. Staco performs a statistical combination of the two tracks:

$$\mathbf{T}_{\text{comb}} = (\mathbf{C}_{\text{MS}}^{-1} + \mathbf{C}_{\text{ID}}^{-1})^{-1} (\mathbf{C}_{\text{MS}}^{-1} \mathbf{T}_{\text{MS}} + \mathbf{C}_{\text{ID}}^{-1} \mathbf{T}_{\text{ID}}).$$

Muid implements a partial re-fitting: the muon spectrometer hits are re-fitted starting from the existing inner detector track and covariance matrix. The fit accounts for the material and magnetic field.

### Tagged muons

Two algorithms implement the muon spectrometer tagging strategy: MuTag [175] (part of the Staco family) and MuGirl [179] (grouped with the Muid algorithms). The logic of both algorithms is: start from inner detector tracks with sufficient momentum; extrapolate the tracks to the inner muon stations; associate the extrapolated tracks to muon segments. The last step of the logic, the matching or tagging, is implemented differently by the two algorithms. MuTag defines a  $\chi^2$  using the extrapolated track prediction and nearby segments, whereas MuGirl employs a neural network to select muon segments.

The additional tagged muons significantly improve the overall muon reconstruction efficiency. The muon tag reconstruction can identify muons which have been missed by the stand-alone reconstruction, for the following reasons:

- low- $p_T$  muons (below typically 6 GeV) do not always reach the middle and outer muon stations;

- the middle muon stations are missing (staged) in the barrel/end-cap transition region of  $1.1 < |\eta| < 1.7$ ;
- the geometrical acceptance of the muon stations is reduced in the regions at  $\eta \approx 0$  and in the detector feet.

For successful tagged muons, both algorithms simply use the inner detector track measurements. A combination or re-fitting step is not expected to improve the momentum measurement for low- $p_T$  muons.

One important technical difference between the two algorithms is: MuTag considers only inner detector tracks and muon segments not used by the Staco algorithm, whereas MuGirl attempts to find all muons. Therefore, muons reconstructed by MuTag and Staco do not overlap, which is not the case for muons identified by MuGirl and Muid.

### 9.3.2 Performance

The muon performance which is shown here has been obtained using the default muon algorithms (Staco), without cavern background nor pile-up.

Fig. 9.3 shows the expected fractional momentum resolution of stand-alone and combined muons, as a function of  $|\eta|$ ,  $\phi$ , and  $p_T$ .

The resolution vs  $|\eta|$  plot (top left) features a large degradation for the stand-alone muons in the region  $1.1 < |\eta| < 1.7$ . This degradation is due to: the absence of the middle muon stations in the barrel/end-cap transition region for the initial data-taking period ( $1.1 < |\eta| < 1.3$ ); the lower bending power of the magnetic field in the transition region between the barrel and end-cap toroids; and the extra material of the coils of the end-cap toroids.

In the resolution vs  $\phi$  plot (top right), one can see a degradation in the  $\phi = 240$  and  $300$  degree regions, corresponding to the location of the detector feet.

The two lower resolution plots indicate where the resolution improves when combining the muon spectrometer and inner detector measurements, as a function of  $p_T$ . As expected, the gain is most pronounced in the low- $p_T$  regime.

Fig. 9.4 shows the single muon reconstruction efficiency, as a function of  $p_T$  (left) and  $|\eta|$  (right). The efficiency is defined as the fraction of reconstructed and matched muons to the simulated muons, where the matching requires a geometrical agreement within a cone of size  $\Delta R = 0.2$ . Basically no muons are reconstructed around  $|\eta| = 0$  due to the large gap in this region, mentioned earlier. As expected, the tagged muons increase the overall efficiency in the low- $p_T$  region, but contribute only to a limited extent in the remaining part.

The uncertainty of the muon efficiency is expected to be around 0.3% for an integrated luminosity of  $1 \text{ fb}^{-1}$  [26]. As for electrons, it will be derived from data studies in processes like  $Z \rightarrow \mu\mu$ . The energy scale and energy resolution of muons are expected to be understood and known to 0.3% and 4% respectively, again for  $1 \text{ fb}^{-1}$  of integrated luminosity.

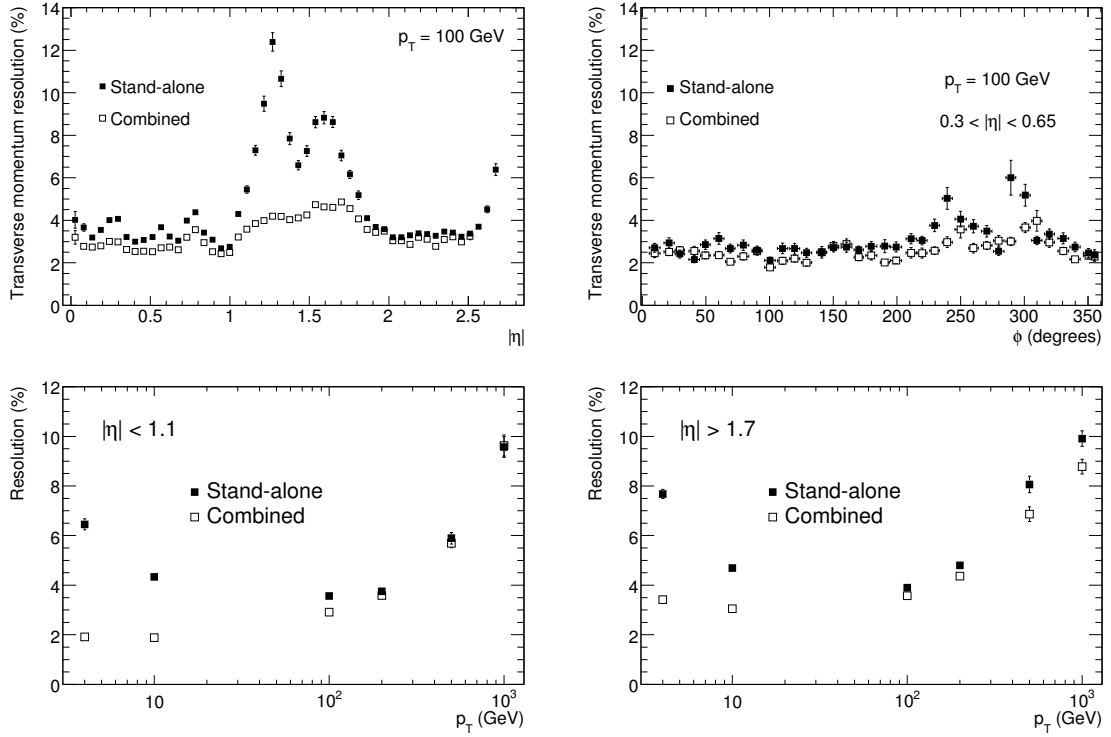


**Figure 9.3:** Expected muon stand-alone and combined fractional momentum resolution as a function of:  $|\eta|$  (top left) and  $\phi$  (top right), as well as  $p_T$  in the barrel with  $|\eta| < 1.1$  (bottom left) and end-cap with  $|\eta| > 1.7$  (bottom right), taken from Ref. [50]. The results were obtained from simulated single muons, with  $p_T = 100$  GeV for the two top plots.

## 9.4 Jets

The precise reconstruction of jets is the only way to obtain information about the strongly interacting partons (and similarly squarks and gluinos). It is thus of great importance for SUSY studies since high- $p_T$  squarks and gluinos are expected to commonly occur in the long decay chains.

The ATLAS jet reconstruction strategy follows the guidelines extracted from the CDF run II, as reported in Ref. [180]. Further jet concepts employed in ATLAS can be found in Ref. [181].

Several important theoretical and experimental considerations should be made when reconstructing jets:

- *Infrared safety*: jets should be invariant under the addition of soft particles, not coming from the fragmentation of a hard scattered parton.
- *Collinear safety*: the jet reconstruction should find the same jet irrespective of whether a contributing particle is split into two particles (sharing the same  $p_T$ ) or not.
- *Detector independence*: the reconstructed jets should be detector independent. This requires an elaborate calibration procedure.

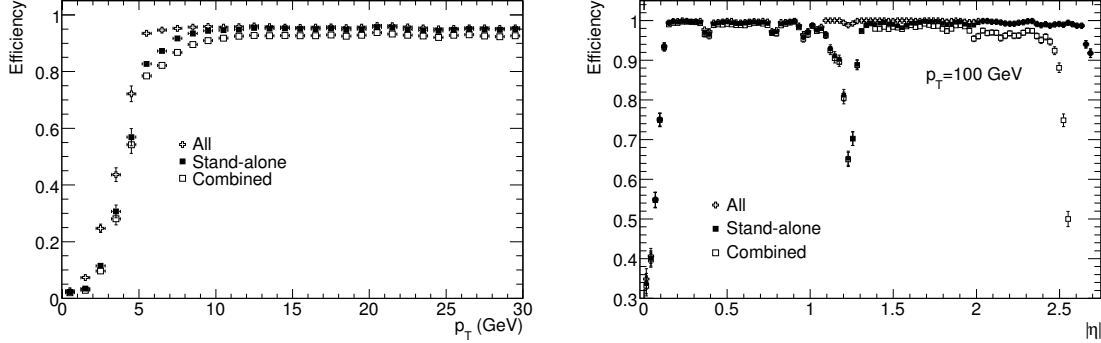


**Figure 9.4:** Muon reconstruction efficiency as a function of  $p_T$  (left) and  $|\eta|$  (right), taken from Ref. [50]. Muons with  $p_T = 100$  GeV were used for the  $|\eta|$  efficiency plot (right). The results are shown for stand-alone muons, combined muons, and combined plus the tagged muons (all).

The most commonly used jet finder programs in ATLAS are a seeded fixed cone algorithm with split-and-merge [182], and a  $k_T$  algorithm [183]. Both are further described in the following. It is however anticipated that all implementations from the FASTJET library [184] ( $k_T$ , anti- $k_T$ , Cambridge flavour  $k_T$  [185]) as well as the seedless and infrared-safe cone algorithm SIScone [186] will be available for initial data-taking.

### 9.4.1 Reconstruction

#### Calorimeter towers and clusters

The most important detector for jet reconstruction is the calorimeter system (see Section 3.2.3 for a brief overview). It comprises roughly 200 thousand input channels, one for each calorimeter cell. Cells have various sizes and geometries and different readout technologies. To facilitate jet finding, all calorimeter cells are combined into larger signal objects with physically meaningful four-momenta. Two different implementations are available in ATLAS: *calorimeter towers* and *topological cell clusters*:

- *Calorimeter towers*: all calorimeter cells are projected onto a fixed grid in pseudorapidity ( $\eta$ ) and azimuth ( $\phi$ ). The bins of this grid are the calorimeter towers, with size  $\Delta\eta \times \Delta\phi = 0.1 \times 0.1$  in the whole acceptance region of the calorimeters ( $|\eta| < 5$  and  $-\pi < \phi < \pi$ ). The total number of calorimeter towers is thus  $100 \times 64 = 6400$ . Cells that are not fully covered by one tower contribute a fraction of their signal corresponding to the geometrical overlap. The signal from the cells is taken at the basic EM energy scale. No further corrections or calibrations are applied at this stage.
- *Topological cell clusters*: they represent an attempt to reconstruct calorimeter showers by three-dimensional cell clusters. The clustering process begins with seed cells that exceed a signal significance threshold of  $|E_{\text{cell}}| > 4\sigma_{\text{cell}}$ , where  $\sigma_{\text{cell}}$  includes the noise from electronics and pile-up. All direct neighbours — in three dimensions — are collected into the cluster, independently of their signal values. A secondary signal significance threshold

(typically  $|E_{\text{cell}}| > 2\sigma_{\text{cell}}$ ) determines whether a neighbour cell is considered as a secondary seed. The process continues to collect all direct neighbours of the secondary seeds, similarly to the first round. Finally, all surrounding cells above a very low threshold (typically  $|E_{\text{cell}}| > 0\sigma_{\text{cell}}$ ) are added if no more secondary seeds are among the direct neighbours. After all initial clusters are identified, they are analysed for multiple local signal maxima. In case of more than one maximum in a given cluster, it is split into smaller clusters (again in three dimensions) along the signal valleys.

Both calorimeter towers and cell clusters are initially formed using the basic cell signals at the EM energy scale. Optionally, in a second step clusters can be calibrated to a local hadronic energy scale [26].

One important difference between towers and cell clusters is the number of calorimeter cells used. Towers include all cells of the calorimeters, while the clusters use considerably fewer cells. This is due to the signal significance cuts in the clustering procedure, which effectively leads to a noise suppression.

All jet finding algorithms (cone,  $k_T$ ,...) can run on both towers and clusters.

#### Fixed cone jet finder

The default ATLAS cone implementation is an iterative seeded fixed-size cone jet finder algorithm which can be outlined as follows.

First, all input objects (can be towers, clusters, or also partons, particles from simulated data) are ordered by their transverse energy ( $E_T$ ). If the highest  $E_T$  object is above a given seed threshold (typically 1 GeV) then all objects falling into a cone of radius  $\Delta R = \sqrt{\Delta\eta^2 + \Delta\phi^2}$  will be collected and combined with the seed. The combined four-momentum yields a new cone direction which is used to refine the centre of the cone. Objects around this new centre are re-collected, and again the direction is updated. This process continues until the direction (centre) of the cone does not change anymore. At this point, the cone is considered stable and is called a jet. The whole procedure is repeated for all input objects above the seed threshold.

The jets built in this way can share input objects. In order to resolve these overlaps, all jets are revised in a split-and-merge step. Overlapping jets with shared  $E_T$  above a given threshold (typically 50%) are merged. Conversely, if the common  $E_T$  is below the threshold then the jets will be split.

It should be noted that:

- parts of the input signals might not be used by any jet (resulting in so-called dark towers),
- this algorithm is not infrared safe (partly recovered by split-and-merge procedure).

Default parameters in ATLAS are  $\Delta R = 0.4$  for narrow and  $\Delta R = 0.7$  for wide cone jets. The narrow cone size is used for instance in  $W \rightarrow jj, t\bar{t}$ , and SUSY studies, where jets are close to each other or a high jet multiplicity is expected. The wide cone size, on the other hand, is used for

example in inclusive jet cross section measurements, where it is important to cover all calorimeter activities belonging to the hard scattered partons.

### Sequential recombination ( $k_T$ ) algorithms

The default ATLAS implementation of the sequential recombination jet finder is the  $k_T$  algorithm. The basic concept can be summarised as follows.

The list of all input objects (towers, clusters, partons, particles, etc.) is analysed. For this purpose a weighted distance between two objects ( $i, j$ ) is defined as

$$d_{ij} = \min(p_{T,i}^2, p_{T,j}^2) \frac{\Delta R_{ij}^2}{R^2},$$

where  $p_{T,i}^2$  and  $p_{T,j}^2$  are the transverse momenta of objects  $i$  and  $j$  respectively,  $\Delta R_{ij}^2 = \Delta\eta_{ij}^2 + \Delta\phi_{ij}^2$  is the distance between the two objects, and  $R$  is a free parameter of the algorithm. Additionally, a weighted distance to the beam is defined as  $d_i = p_{T,i}^2$  for object  $i$ .

Among all  $d_{ij}$  and  $d_i$  the algorithm finds the minimum  $d_{\min}$ . If  $d_{\min}$  belongs to the class of  $d_{ij}$  then the corresponding objects  $i$  and  $j$  will be combined into a new object  $k$  using four-momentum recombination. Subsequently, both objects  $i$  and  $j$  are removed from the list of input objects and the new object  $k$  is added to it. If the  $d_{\min}$  belongs to the class of  $d_i$  then object  $i$  will be considered a jet by itself and is removed from the list of input objects.

This procedure continues until all objects have been removed from the list of input objects. Thereby, all initial input objects end up being either part of a jet or a jet by themselves. By design, the constructed jets do not share any input objects. The method is infrared safe (no seeds are used), and also collinear safe.

The algorithm parameter  $R$  gives some control over the size of the jets. Default values in ATLAS are  $R = 0.4$  for narrow and  $R = 0.6$  for wide jets, with similar physics use-cases as for the cone algorithm.

A full description of the  $k_T$  implementation in ATLAS can be found in Ref. [187] (initial design) and Ref. [184] (current design).

### 9.4.2 Jet calibration

Reconstructed jets, which are at the EM energy scale, are calibrated using the so-called H1-style method [188] which is based on cell signal weighting. This approach can be applied to both tower and cluster jets. The basic idea behind it is that low signal densities in the calorimeter indicate a hadronic signal in a non-compensating calorimeter, while high signal densities are more likely to be generated by EM showers. To compensate for this, hadronic showers are weighted by a factor of the order of the electron/pion signal ratio. In practise the weight factor is a function depending on the cell location and the cell signal density. It is roughly 1 for high density signals and rises up to 1.5 with decreasing cell signal densities. Simulated QCD dijet events are used to determine the

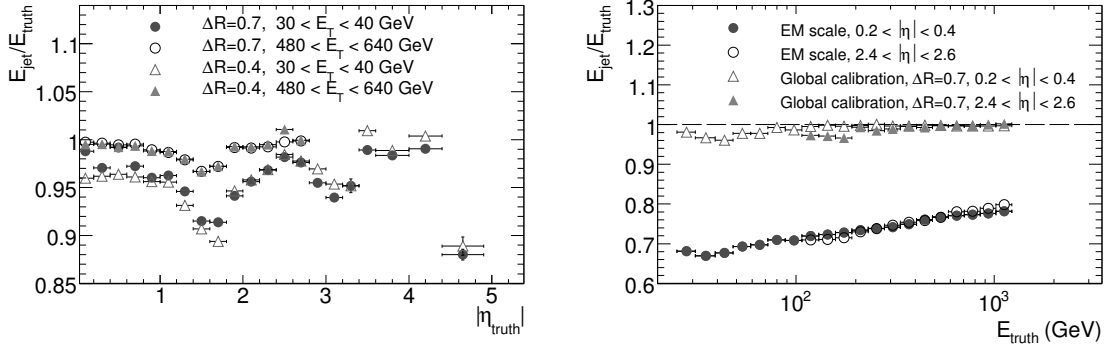


**Figure 9.5:** Expected jet signal linearity for cone-tower jets, taken from Ref. [50]. Left: fully (global) calibrated jets with cone size  $R = 0.7$  and  $0.4$ , in two energy ranges, as a function of  $|\eta|$ . Right: comparison of jets at the EM energy scale and after the global calibration, for a cone size of  $R = 0.7$ , in two different  $|\eta|$  ranges, as a function of the energy.

weight function in a global fit that compares reconstructed jets with jets reconstructed using the generated interacting particles.

### 9.4.3 Performance

The results shown here are only for the fixed cone jet finder algorithm, with a cone size of either  $R = 0.7$  or  $0.4$ . The cone jet algorithm with the above cone sizes is the current ATLAS default. It has also been used in the SUSY studies of this work, where the narrow cone size of  $R = 0.4$  has been chosen since a high jet multiplicity is expected.

Fig. 9.5 shows the jet signal linearity, defined by the ratio of reconstructed jet energy to the matching truth jet energy. The left plot of Fig. 9.5 shows the signal uniformity for jets with the global calibration, as a function of  $|\eta|$ . The dips correspond to detector transition regions and the limited coverage for high  $|\eta|$  values. The jets of the higher energy range are less affected by these detector imperfections.

The right plot indicates the expected deviations for jets reconstructed at the EM energy scale with respect to jets reconstructed with the global (H1-style) calibration. Jets reconstructed at the EM energy scale are off by  $\sim 30\%$  to  $\sim 20\%$ . This gives an idea of the expected jet energy scale for very early data, when the H1 calibration scheme will not have been validated.

The expected jet energy resolution is shown in Fig. 9.6. For central jets in the region  $0.2 < |\eta| < 0.4$  the stochastic term is about  $60\%$ , while the constant term is approximately  $3\%$ .

## 9.5 Missing Transverse Energy

Missing transverse energy ( $E_T^{\text{miss}}$ ) is the most important discriminating variable for nearly all SUSY searches, as well as for many other physics studies. Its reconstruction, however, poses a task of unprecedented difficulty. The challenge lies in measuring precisely  $E_T^{\text{miss}}$  in terms of

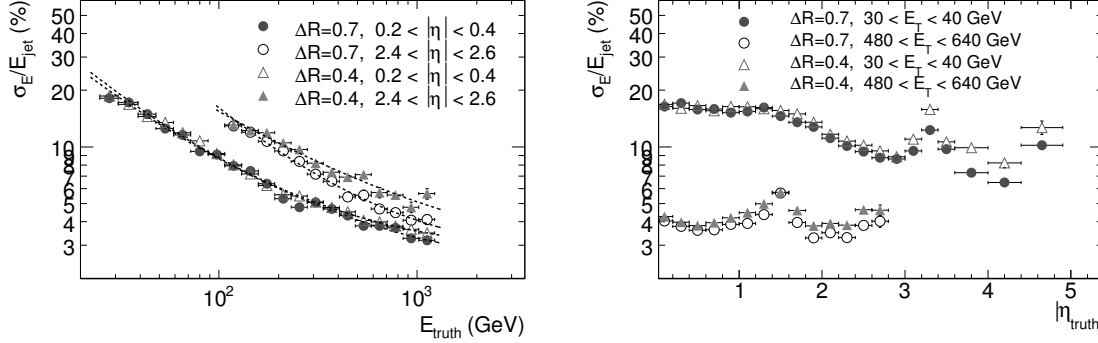


**Figure 9.6:** Expected jet fractional energy resolution as a function of energy (left) and  $|\eta|$  (right), taken from Ref. [50]. The results were obtained from calibrated cone-tower jets with a cone size of  $R = 0.7$  and  $0.4$ , in two different  $\eta$ -regions (left) and two different energy regions (right).

linearity and accuracy, and minimising the effects of fake  $E_T^{\text{miss}}$ . The imperfect detector coverage, e.g. in the transition regions of the calorimeters, unavoidably leads to tails. Furthermore, the smallest detector malfunction or mis-measurement — in particular hot/noisy or dead calorimeter cells — causes fake  $E_T^{\text{miss}}$ .

### 9.5.1 Reconstruction

For the reconstruction of missing and total transverse energy, ATLAS has implemented one baseline algorithm based on the calorimeter cells.

This cell-based  $E_T^{\text{miss}}$  algorithm starts from the transverse energy deposited in the calorimeters. It further corrects for energy losses in the cryostat, and accounts for the muon energy. The total missing energy reads

$$E_{x,y}^{\text{miss}} = (E_{x,y}^{\text{miss}})_{\text{calo}} + (E_{x,y}^{\text{miss}})_{\text{cryo}} + (E_{x,y}^{\text{miss}})_{\text{muon}}. \quad (9.1)$$

The calorimeter term is obtained from the sum over all cells which belong to a cluster:

$$(E_{x,y}^{\text{miss}})_{\text{calo}} = - \sum_{\text{cell} \in \text{cluster}} E_{x,y}.$$

Two slightly different approaches can be taken in order to suppress calorimeter noise. First, all calorimeter cells to be included in the  $E_T^{\text{miss}}$  calculation are required to significantly exceed a noise value, e.g.  $|E_{\text{cell}}| > 2\sigma_{\text{noise}}$ . The symmetric cut is important to avoid a bias towards one direction. The second approach consists of using the topological cell clusters (cf. Section 9.4) which include a noise cut already. By default, the topological cell clusters are used.

In either case, the calorimeter cells are calibrated, as outlined in Section 9.4, following the H1-style method.

In the final (optional) calorimeter refinement step, clusters are associated to reconstructed high- $p_T$  objects whose calibrated energy is then used instead. The identification of clusters with high- $p_T$



objects proceeds in a well defined order: electrons, photons, muons, hadronically decaying  $\tau$ -leptons, b-jets, and finally light jets. Subsequently, the energy of the matched calibrated high- $p_T$  objects substitutes the corresponding calorimeter cells. Clusters not matched to any high- $p_T$  object are kept, with the H1-calibrated energy.

Note that certain calibration/correction terms of the high- $p_T$  objects are excluded. For instance the out-of-cone energy of an electron must not be considered because it is already accounted for by the non-matched calorimeter clusters, and cells.

The reconstructed  $E_T^{\text{miss}}$  from this refinement step is referred to as refined  $E_T^{\text{miss}}$ , where typically the cryostat and muon correction terms are also included.

The second term in Eq. (9.1) recovers (partly) the loss of energy in the cryostat between LAr EM and hadronic tile calorimeters. The thickness of this dead material is about half an interaction length, in the barrel region. The basic principle is that the energy loss is correlated to the calorimeter energies of the last EM layer and the first hadronic compartment. The correction term is thus defined as

$$(E_{x,y}^{\text{miss}})_{\text{cryo}} = - \sum_{\text{reco. jets}} w_{\text{cryo}} \sqrt{E_{x,y}^{\text{EMB3}} \cdot E_{x,y}^{\text{TILE0}}},$$

where the sum is over all reconstructed jets,  $w_{\text{cryo}}$  is a constant weight factor,  $E_{x,y}^{\text{EMB3}}$  is the  $x$  or  $y$  component of the jet's energy in the last EM layer, and  $E_{x,y}^{\text{TILE0}}$  denotes the  $x$  or  $y$  component of the jet's energy in the first hadronic compartment.

The  $w_{\text{cryo}}$  parameter is assumed to be independent of energy and  $\eta$ . It is determined together with the calorimeter cell weights in the global fit of the H1-style calibration.

The third term in Eq. (9.1) collects the energy of muons:

$$(E_{x,y}^{\text{miss}})_{\text{muon}} = - \sum_{\text{reco. muon}} E_{x,y}.$$

The sum is over all reconstructed muons, where a matched inner detector track is required in the region  $|\eta| < 2.5$  in order to reduce contributions from fake muons. The muon momentum is obtained from the stand-alone muon spectrometer. Energy lost by the muons in the calorimeters is thus not double counted, since it is already taken into account in the calorimeter term.

### 9.5.2 Fake $E_T^{\text{miss}}$

Fake missing transverse energy is defined as the difference between reconstructed and true  $E_T^{\text{miss}}$ . It can induce significant backgrounds from many different source:

- beam-gas scattering and other machine backgrounds;
- a displaced interaction vertex;
- hot, noisy, or dead calorimeter cells/regions;
- mis-measurements in the detector itself, mainly due to: high- $p_T$  particles that escape detection outside the fiducial acceptance of the detector; undetected energy deposits in detector

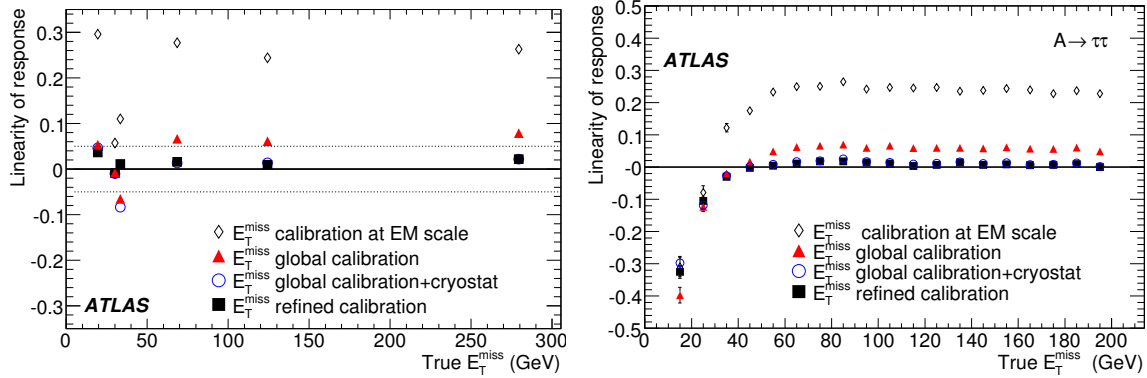


**Figure 9.7:** Linearity of the reconstructed  $E_T^{\text{miss}}$ , as a function of the average true  $E_T^{\text{miss}}$  for different physics processes, taken from Ref. [26]. In the left plot the results were obtained from:  $Z \rightarrow \tau\tau$  for the data point with average true  $E_T^{\text{miss}}$  of 20 GeV ;  $W \rightarrow e\nu$  and  $W \rightarrow \mu\nu$  for the data point at 35 GeV ; semi-leptonic  $t\bar{t}$  decays for the point at 68 GeV ;  $A \rightarrow \tau\tau$  with  $m_A = 800$  GeV for the point at 124 GeV ; and finally SUSY decays with a typical mass scale of 1 TeV for the average true  $E_T^{\text{miss}}$  of 280 GeV. All results shown in the right plot were obtained from the process  $A \rightarrow \tau\tau$  with  $m_A = 800$  GeV.

cracks or inactive material; or the limited detector resolution (in particular energy fluctuations of high- $p_T$  jets).

A detailed discussion of the strategies to remove sources of fake  $E_T^{\text{miss}}$  in early data and to measure the  $E_T^{\text{miss}}$  resolution and scale can be found in Ref. [26]. The main concepts considered for removing fake  $E_T^{\text{miss}}$  are: requiring a minimum azimuthal angular separation between the  $E_T^{\text{miss}}$  vector and all jets in the event; employ track-jets (reconstructed from inner detector tracks) as a complementary measure to the standard calorimeter-based jets. In the latter approach, one can for example impose the track-jet momentum to match (in a certain window) the corresponding standard jet energy. Another approach to clean fake  $E_T^{\text{miss}}$  is to mask certain detector regions which are known to malfunction, and or require the  $E_T^{\text{miss}}$  vector not to point toward these regions.

### 9.5.3 Performance

The performance results shown here are only for the cell-based  $E_T^{\text{miss}}$  algorithm, which is the current default in ATLAS. The cell-based  $E_T^{\text{miss}}$  algorithm together with the refined calibration has also been used for the SUSY studies of this thesis.

Fig. 9.7 shows the  $E_T^{\text{miss}}$  response linearity as a function of the true  $E_T^{\text{miss}}$ , as obtained by different physics processes. The linearity is defined as the difference of true to reconstructed  $E_T^{\text{miss}}$ , normalised to the true  $E_T^{\text{miss}}$ .

The use of uncalibrated calorimeter cells, i.e. at the EM energy scale, leads to a bias of about 30%. As expected, this bias is significantly smaller for  $W \rightarrow e\nu$  and  $W \rightarrow \mu\nu$  events (data point at 35 GeV) due to the reduced hadronic activity. The  $E_T^{\text{miss}}$  reconstructed from globally calibrated calorimeter cells, and including the muon correction term, shows a bias of about 5%. Further including the cryostat term reduces the bias to 1%, except for  $E_T^{\text{miss}}$  from the  $W \rightarrow e\nu$  process. Finally, the use of the refined calibration together with the muon and cryostat corrections terms

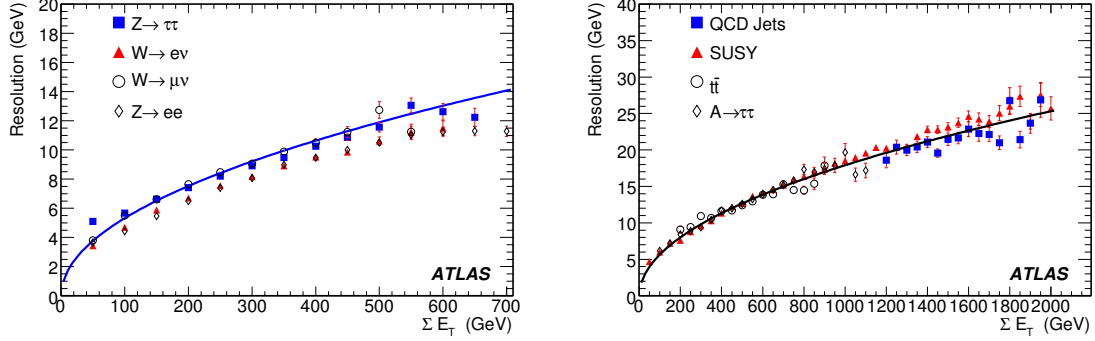


**Figure 9.8:** Resolution of  $E_T^{\text{miss}}$  in the range low to medium (left) and low to high (right) values of total transverse energy ( $\sum E_T$ ), taken from Ref. [26]. Both variables  $E_T^{\text{miss}}$  and  $\sum E_T$  were obtained from the cell-based  $E_T^{\text{miss}}$  algorithm with the refined calibration. The solid lines correspond to the fits  $\sigma = 0.53\sqrt{\sum E_T}$  through the points from  $Z \rightarrow \tau\tau$  events (left) and  $\sigma = 0.57\sqrt{\sum E_T}$  through the points from  $A \rightarrow \tau\tau$  events (right). The points of the  $A \rightarrow \tau\tau$  process were obtained with  $m_A$  ranging between 150 GeV and 800 GeV. The QCD jets correspond to a sample with a  $560 < p_T < 1120$  GeV range for the hard scattering.

leads to a  $E_T^{\text{miss}}$  linearity below 1%, including the  $W \rightarrow e\nu$  process.

The right plot of Fig. 9.7 shows the  $E_T^{\text{miss}}$  linearity as obtained alone from the  $A \rightarrow \tau\tau$  process with  $m_A = 800$  GeV. One observes a negative bias for small true  $E_T^{\text{miss}}$  values. Since  $E_T^{\text{miss}}$  is by design a positive quantity, small  $E_T^{\text{miss}}$  values cause a negative bias.

The  $E_T^{\text{miss}}$  resolution is shown as a function of the total transverse energy ( $\sum E_T$ ) in Fig. 9.8. The resolution is obtained from a Gaussian fit to the difference of reconstructed to true  $E_T^{\text{miss}}$ , in each  $\sum E_T$  bin. Solid lines represent fits to  $\sigma = a \cdot \sqrt{\sum E_T}$ , which describes the observed stochastic behaviour of the  $E_T^{\text{miss}}$  resolution. The fitted  $a$  parameter was found to be between 0.53 and 0.57, for the different physics processes and  $\sum E_T$  ranges. It is noteworthy that the  $E_T^{\text{miss}}$  reconstructed from SUSY events shows a similar resolution.

The performance of  $E_T^{\text{miss}}$  will be determined (and the simulations validated) with the first collision data. Several studies have been proposed:

- Minimum bias events can be used to monitor and diagnose  $E_T^{\text{miss}}$  reconstruction problems in the very beginning;
- $W \rightarrow e\nu$  and  $W \rightarrow \mu\nu$  decays accompanied by jets can be used to test the  $E_T^{\text{miss}}$  reconstruction and determine the  $E_T^{\text{miss}}$  scale in-situ in the 20 – 150 GeV range;
- $Z \rightarrow \tau\tau$  can be used in conjunction with the  $Z$  mass constrain to determine the  $E_T^{\text{miss}}$  scale in-situ;
- $Z \rightarrow ee$  and  $Z \rightarrow \mu\mu$  processes can be used to test for  $E_T^{\text{miss}}$  biases, and the resolution;
- Finally, semi-leptonic  $t\bar{t}$  decays can be used to test the  $E_T^{\text{miss}}$  reconstruction in a busy environment, which is relevant for SUSY studies.



## Chapter 10

# Search for Supersymmetry in the Inclusive One-Lepton Channel

The one-lepton inclusive channel is among the most prominent modes for SUSY searches with early LHC data. The one-lepton requirement reduces background from QCD jets, leaving  $t\bar{t}$  (91%) and  $W$ +jets (8%) processes as the dominant and subdominant SM backgrounds, respectively.

This chapter is devoted to the detailed description of the one-lepton SUSY search channel. This analysis along with the simulated datasets (described in Chapter 8) was part of the so-called computing system commissioning (CSC) programme [26].<sup>1</sup> The author significantly contributed to the SUSY note of the CSC-book, namely to the one-lepton search mode, the scan and optimisation section, and to a lesser extent also to the zero-lepton channel.

Section 10.1 explains the objects and variable definitions. The one-lepton event selection cuts are discussed in Section 10.2, where also the corresponding event flow is given for the SM background processes, and the SUSY benchmark points. The trigger efficiencies for the signal are described in Section 10.3.

In Section 10.4 the statistical procedure to derive a signal significance, and systematic background uncertainties are discussed. The estimated discovery potential is then presented for several mSUGRA models, including a parameter scan. The expected number of background events is obtained directly from MC simulation, and systematic uncertainties are assigned per process type ( $t\bar{t}$ ,  $W$  + jets, etc.). Finally, Section 10.6 considers a multivariate analysis technique which is compared to the baseline one-lepton analysis.

---

<sup>1</sup>As mentioned in Chapter 8: note that the results differ slightly from those in the SUSY CSC chapter “Prospects for Supersymmetry Discovery Based on Inclusive Searches”, because high statistics Alpgen  $t\bar{t}$  samples are used here, whereas the CSC plots have been obtained with the MC@NLO top samples.

## 10.1 Object and Variable Definition

The signature of the inclusive one-lepton SUSY channel is based on one isolated electron or muon, multiple hard jets, and large missing transverse energy. The corresponding reconstruction algorithms are described in Chapter 9. This section details the employed reconstruction parameters, the quality and identification cuts, as well as the isolation requirements imposed on the various objects.

Electrons are “only” required to satisfy the medium purity cuts since the background from the production of QCD multijets is expected to be already significantly reduced by the event selection of four hard jets and large  $E_T^{\text{miss}}$ , as described later. A strong jet rejection is therefore not needed in the electron identification cuts, leading to a considerable gain in signal efficiency.

Muons are obtained from combined inner detector tracks and muon spectrometer tracks. Tagged muons are discarded since they improve the muon performance only in the low- $p_T$  region.

The expected high jet multiplicity in typical SUSY decays favours the use of a jet algorithm with a narrow cone size. The tower-cone jet algorithm was chosen, despite its known shortcomings (infrared and collinear unsafe), to conform to the current ATLAS default.

The objects used are fully defined as follows:

- *Electrons* are reconstructed with the default  $e/\gamma$  algorithm. They must satisfy the set of medium cuts (cf. Section 9.2), and the quality cuts:  $|\eta| < 2.5$  and  $p_T > 10$  GeV. Furthermore, the calorimeter-based isolation requirement is imposed: less than 10 GeV of energy in a cone of size  $\Delta R = 0.2$  around the electron (excluding the electron energy).
- *Muons* are reconstructed using the default Staco algorithm. They are required to be combined muons with a matching  $\chi^2$  below 100. If more than one inner detector track matched the stand-alone muon track, then only the one with the smallest distance in  $\Delta R$  is kept (best-match flag). The same quality cuts and isolation criteria as for electrons are applied:  $|\eta| < 2.5$ ,  $p_T > 10$  GeV, and  $E_T^{\text{cone}} < 10$  GeV with cone size  $\Delta R = 0.2$ .
- *Jets* are reconstructed as cone-tower jets with a cone size of  $R = 0.4$ , and are required to satisfy:  $|\eta| < 2.5$ , and  $p_T > 20$  GeV. They are calibrated using the H1-style method.
- *Missing transverse energy* ( $E_T^{\text{miss}}$ ) is reconstructed using the default calorimeter-based algorithm with the refined calibration and including the cryostat and muon terms.
- *Taus* and *photons* are not considered separately, but treated as jets.

In the remainder of this analysis the word “lepton” is used to denote isolated electrons and muons.

### 10.1.1 Electron-crack veto

In the present simulated datasets, the calorimeter-based isolation variable ( $E_T^{\text{cone}}$ ) was incorrectly calculated. However, this bug introduces a significant bias only in the calorimeter crack region,

**Table 10.1:** Definition of global event variables.

Variable	Definition
$M_{\text{eff}}$	Scalar sum of $E_T^{\text{miss}}$ and the $p_T$ of the four hardest jets and the lepton: $M_{\text{eff}} = E_T^{\text{miss}} + \sum_{i=1}^4 p_T^{\text{jet } i} + p_T^{\text{lep}}$
$M_T$	Transverse (invariant) mass of lepton and $E_T^{\text{miss}}$ : $M_T^2 = 2p_T^{\text{lep}} E_T^{\text{miss}} (1 - \cos(\Delta\phi))$ , where $\Delta\phi$ is the azimuthal angle between $E_T^{\text{miss}}$ and the lepton
$S_T$	Transverse sphericity: $S_T = 2\lambda_2/(\lambda_1 + \lambda_2)$ , where $\lambda_1$ and $\lambda_2$ are the eigenvalues of the $2 \times 2$ sphericity tensor $S_{ij} = \sum_k p_{ki} p_{kj}$ , where the sum runs over all jets and the lepton, and $i$ and $j$ are $x$ or $y$

defined by  $1.37 < |\eta| < 1.52$ . In this region the electron measurement is also degraded because of the large amount of material in front of the calorimeters and the crack (transition) between the barrel and extended barrel of the calorimeters (cf. Section 9.2).

Events with an electron reconstructed in this region (before the isolation requirement and before overlap removal) are therefore rejected.

### 10.1.2 Overlap removal

Jets reconstructed within a cone of  $\Delta R = 0.2$  around an identified electron (as defined above) are discarded from the jet list. This procedure prevents the same object being reconstructed both as a jet and as an electron.

Conversely, an electron is removed from the list of identified electrons if it is found within a distance  $0.2 < \Delta R < 0.4$  of a remaining jet. Such electron candidates are likely to be associated with the decay of a particle within that jet.

Similarly, muons found within a distance  $\Delta R < 0.4$  of a jet are discarded. Effectively, the last two selections constitute a second electron/muon isolation requirement.

### 10.1.3 Global event variables

In addition to the physics objects defined above, the SUSY search mode relies on three event variables: effective mass ( $M_{\text{eff}}$ ), transverse mass ( $M_T$ ), and transverse sphericity ( $S_T$ ). Their definition is given in Table 10.1.

The first variable ( $M_{\text{eff}}$ ) reflects the total (visible and invisible) activity of an event in terms of momentum. It is therefore expected to be a sensitive variable for the detection of SUSY, which presumably has high-mass states that generate many high- $p_T$  objects in its long decay chains. The  $M_{\text{eff}}$  variable is also strongly correlated to the SUSY mass scale [56, 189]. The peak of the SUSY  $M_{\text{eff}}$  distribution indicates the minimum sparticle mass, cf. Fig. 10.1 for some mSUGRA models.

The transverse mass ( $M_T$ ) is obtained from the lepton and  $E_T^{\text{miss}}$  of an event. For SM  $W$  boson

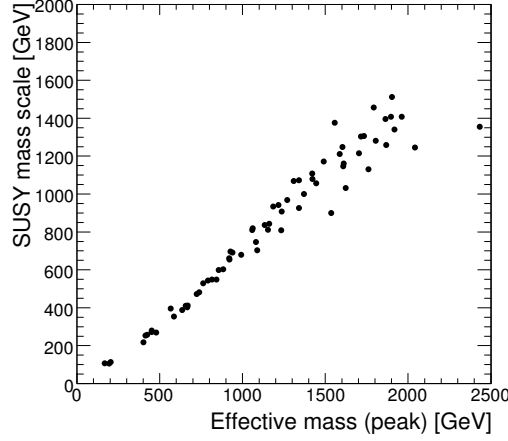


**Figure 10.1:** SUSY mass scale versus the peak of the  $M_{\text{eff}}$  distribution for various mSUGRA models. The SUSY mass scale is defined as the minimum of all squark masses and the gluino mass.

processes, i.e. the  $E_T^{\text{miss}}$  is due to one neutrino and the neutrino and lepton stem from the  $W$  boson decay, the transverse mass distribution shows a characteristic edge structure at around 90 – 100 GeV. Thereby, the transverse mass is a powerful variable to discriminate  $W + \text{jets}$  and semi-leptonic  $t\bar{t}$  processes.

The transverse sphericity ( $S_T$ ) is a measure of the event sphericity in terms of momentum, in the  $(x, y)$ -plane. It can take a value between 0 and 1, where 0 is obtained for instance from two perfectly aligned back-to-back momentum vectors, and 1 corresponds to a perfectly spherical event, e.g. four momentum-vectors that are pairwise perpendicular and all have the same magnitude. The  $S_T$  variable is used to further suppress the abundance of QCD dijets. Events with SUSY particles are expected to be relatively spherical ( $S_T \lesssim 1$ ): heavy SUSY particles are usually produced nearly at rest in the detector and subsequently emit many lighter particles in a wide range of directions.

## 10.2 Event Selection

The event selection cuts are similar to those used in the ATLAS Physics TDR [56] except for one additional requirement on the  $M_T$  variable. They are summarised in Table 10.2, where also the corresponding sequential selection efficiencies for the benchmark point SU3 are given.

The event selection cuts C1 and C2 define the one-lepton analysis. They further ensure that all events are disjoint with respect to the other inclusive SUSY search modes, in particular the zero-lepton and two-lepton channels. This facilitates the simple combination of results obtained from the different SUSY search modes. The requirement of one isolated electron or muon strongly suppresses events from QCD jet production. The combined C1 and C2 efficiency for the filtered QCD samples is  $(2.5 \pm 0.2) \cdot 10^{-3}$ , where the error is due to MC statistics.<sup>2</sup>

<sup>2</sup>The different jet sample weights are taken into account (cf. Ref. [190]). Possible correlations with the generator filter (jet multiplicity, jet  $p_T$ , and  $E_T^{\text{miss}}$ ), however, are neglected here.



**Table 10.2:** Event selection for the one-lepton search channel and corresponding sequential signal selection efficiencies for the SUSY benchmark point SU3.

Selection Requirement	cut #	Definition	$\varepsilon_{\text{SU3}}$
Lepton selection	C1	One isolated electron or muon with $p_T > 20$ GeV	0.160
Veto on additional lepton	C2	No additional isolated leptons with $p_T > 10$ GeV	0.144
Jet selection	C3	At least four jets with $p_T > 50$ GeV, and, out of the four jets, one must have $p_T > 100$ GeV	0.054
Missing transverse energy	C4	$E_T^{\text{miss}} > 100$ GeV and $E_T^{\text{miss}} > 0.2 M_{\text{eff}}$	0.036
Transverse sphericity	C5	$S_T > 0.2$	0.028
Transverse mass	C6	$M_T > 100$ GeV	0.016

The jet and  $E_T^{\text{miss}}$  selection cuts C3 and C4 are intended to reduce the SM background. Most simulated SM samples were produced with jet and  $E_T^{\text{miss}}$  filters at generator level in order to enrich the MC statistics after the corresponding cuts C3 and C4. Consequently, SM distributions without these cuts are not meaningful and hence will not be shown. After cuts C1 to C4, about two-thirds of the total SM background originates from semi-leptonic  $t\bar{t}$  processes, and the remaining one-third mainly arises in equal shares from full-leptonic  $t\bar{t}$  and  $W$ +jets processes. The  $Z$ +jets production contributes at the  $\mathcal{O}(1\%)$  level, while QCD multijets have been suppressed to zero within the limited available MC statistics.<sup>3</sup> The full cut flow table for the various SUSY benchmark points and the SM background processes (after cuts C1 to C4) is shown in Table 10.3.

The transverse sphericity cut C5 is designed to further reduce contributions from QCD multijets with a fake lepton and with large fake  $E_T^{\text{miss}}$ . Its efficiency for the SUSY benchmark points and the SM processes can be inferred from Table 10.3. For the QCD jet samples the C5 stand-alone efficiency (without applying the cuts C1 to C4) is  $0.297 \pm 0.002$  (error due to statistics).

Finally, the transverse mass cut C6 removes a significant fraction of events where the  $E_T^{\text{miss}}$  comes from a  $W$  boson decay. It is noteworthy that after the application of C6, full-leptonic  $t\bar{t}$  decays constitute the dominant SM background. The second lepton of these processes escapes identification mainly due to hadronic  $\tau$ -lepton decays.

Additionally, a cut on  $M_{\text{eff}}$  is applied to study the discovery potential. This is further discussed in Section 10.5.

The sequential event selection efficiencies for the cuts C1 to C6 on the mSUGRA signal grid are shown in Fig. 10.2. The total selection efficiency is in the range of a few percent for the bulk part of the sampled mSUGRA parameter space. One can observe that the  $E_T^{\text{miss}}$  requirement (C4) drastically reduces the top/left region of the mSUGRA grid. This is because the LSP is charged in this region ( $\tilde{\tau}_1$ ), and hence no  $E_T^{\text{miss}}$  is generated by the LSPs. Of course a charged LSP is experimentally excluded, this region is therefore marked as not viable (cf. dashed region in Fig. 8.1).

Figure 10.3 shows the selected  $E_T^{\text{miss}}$ ,  $M_{\text{eff}}$ ,  $M_T$  and lepton  $p_T$  distributions for the SU3 model

<sup>3</sup>The QCD jet samples are very limited in MC statistics, see Table 8.3. A larger and highly pre-filtered sample is clearly desirable for future studies.

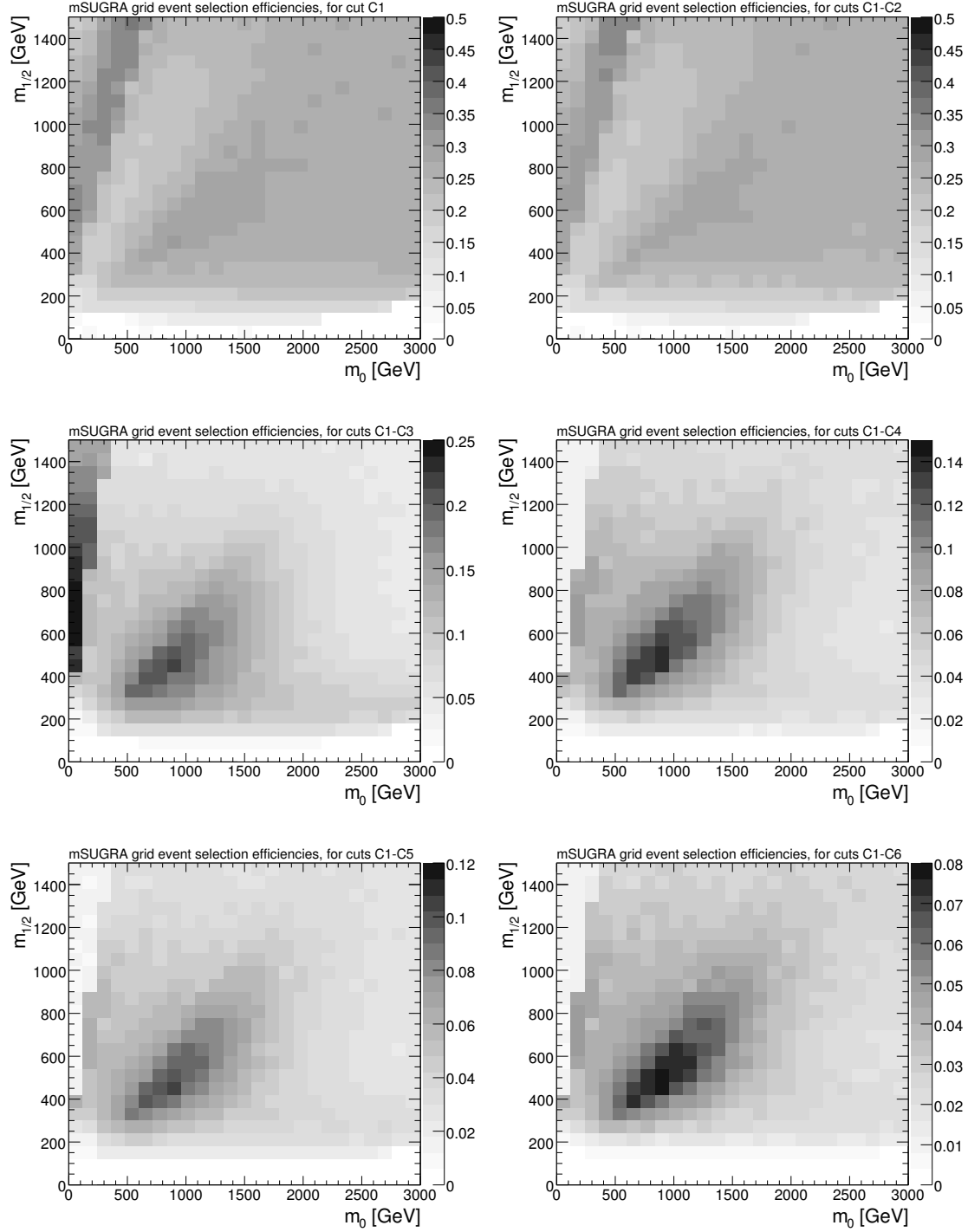


**Figure 10.2:** Sequential event selection efficiencies for the cuts C1 to C6 (defined in Table 10.2) on the mSUGRA signal grid. Note that the efficiency ( $z$ ) scale is different for the six plots.

**Table 10.3:** Expected number of events after the selection cuts for the SUSY benchmark points and the relevant SM background processes. The results are normalised to  $1 \text{ fb}^{-1}$  of integrated data. Note that the SM background samples were generated with event filters (cf. Section 8.3.1). Therefore, SM event numbers are only given after the selection cuts C1 to C4.

Sample	Before cuts	C1	C2	C3	C4	C5	C6
SU1	10,860	2,534	2,294	767	572	423	260
SU2	7,180	1,035	940	193	87	75	46
SU3	27,680	4,441	3,998	1,492	996	768	450
SU4	402,190	74,120	67,094	18,451	7,524	6,260	2,974
SU6	6,070	1,102	986	463	342	251	162
SU8	8,700	1,136	1,065	414	296	214	151
$t\bar{t} \rightarrow qq\bar{q}\bar{q}$					0.3	0.1	0.1
$t\bar{t} \rightarrow l\nu q\bar{q}$					2,040.8	1,275.4	33.9
$t\bar{t} \rightarrow l\nu l\nu$					429.3	256.3	131.6
$W + \text{jets}$					507.5	316.1	13.8
$Z + \text{jets}$					26.5	15.9	1.3
Di-bosons					7.5	4.6	0.8
QCD jets					0.0	0.0	0.0
Combined SM background					3,012.0	1,868.5	181.4

and the SM background processes.

### 10.3 Trigger

The trigger efficiency with respect to the off-line event selection (defined in Table 10.2) has been studied for the SUSY benchmark points. For this purpose, the trigger menu has been adapted to the trigger thresholds defined for  $L = 2 \times 10^{33} \text{ cm}^{-2} \text{ s}^{-1}$  in the high-level trigger TDR [75]. The naming convention is explained in Chapter 5.

Table 10.4 lists the obtained trigger efficiencies for a selection of simple triggers which are not pre-scaled. The shown triggers select (from top to bottom) one or multiple high- $p_T$  jets; significant  $E_T^{\text{miss}}$ ; one jet +  $E_T^{\text{miss}}$ ; and an electron or muon. The  $E_T$  thresholds, which are part of the trigger names, are indicative. This is because the thorough (energy) correction and calibration of the off-line reconstruction cannot be used on-line by trigger algorithms due to the tight time constraints.

In Table 10.4, the j70\_xe70 trigger (requiring a jet with  $p_T$  above 70 GeV and missing transverse energy exceeding 70 GeV) has generally a high signal selection efficiency. The efficiency of the lepton trigger, defined as the logical OR of the mu20 and e22i triggers, is approximately 80% for all studied models. Note that the electron trigger threshold is above the off-line electron requirement, which is undesirable.

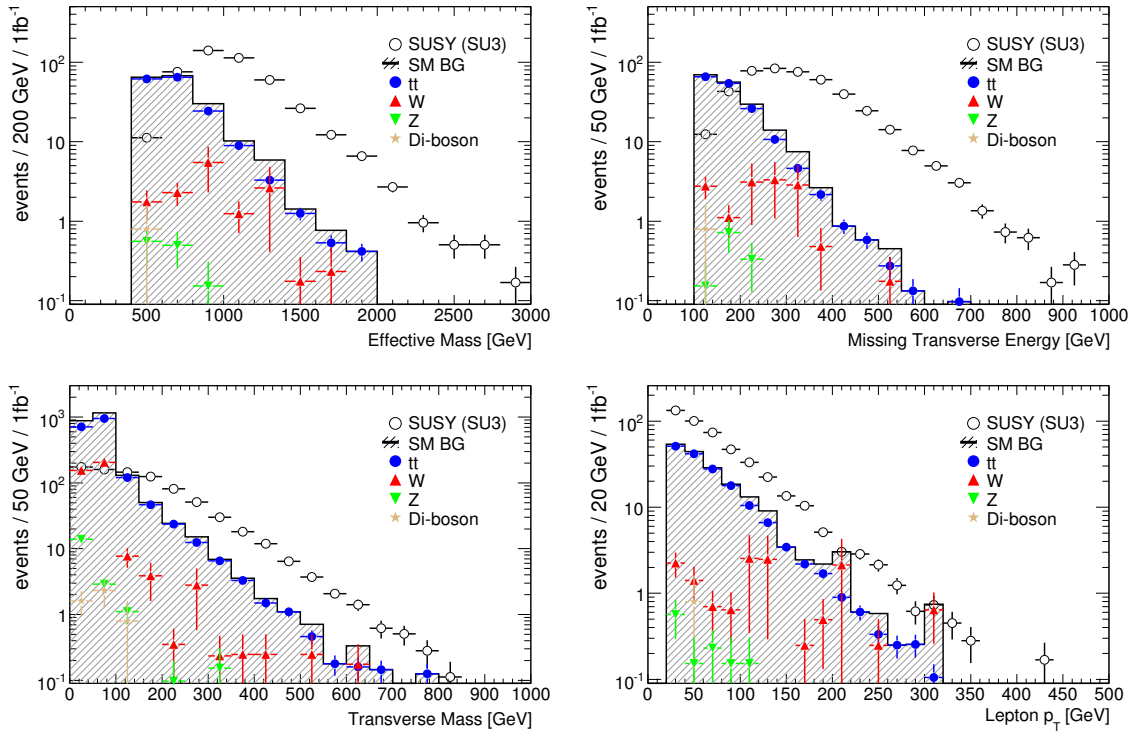


**Figure 10.3:** SUSY (SU3) and SM background distributions of events selected according to the cuts described in Table 10.2. From top left to bottom right:  $M_{\text{eff}}$ ,  $E_T^{\text{miss}}$ ,  $M_T$ , lepton  $p_T$ . The cut  $M_T > 100$  GeV was dropped for the  $M_T$  distribution. The apparent cut on  $M_{\text{eff}}$  is indirectly caused:  $M_{\text{eff}} = E_T^{\text{miss}} + \sum_{i=1}^4 p_T^{\text{jet } i} + p_T^{\text{lep}} \geq 100 \text{ GeV} + 250 \text{ GeV} + 20 \text{ GeV} = 370 \text{ GeV}$

**Table 10.4:** Trigger efficiency [%] for events passing the one-lepton event selection cuts C1 to C6 (see Table 10.2).

Trigger	SU1	SU2	SU3	SU4	SU6	SU8
j400	17.8	11.7	9.7	1.4	21.0	14.0
3j165	21.5	25.1	15.0	2.4	24.5	23.7
4j110	26.0	44.4	22.1	6.3	32.5	31.2
xe120	96.6	91.1	93.0	69.5	95.2	96.5
j70_xe70	99.6	99.0	98.9	95.6	98.9	99.1
mu20 OR e22i	81.2	81.0	79.9	80.3	80.4	79.5

The basic performance of the leptonic and j70\_xe70 triggers will be determined from data using SM events such as  $Z$  bosons and  $t\bar{t}$ .

It is noteworthy that the triggers shown here have not been specifically designed for the SUSY one-lepton analysis (or any other analysis part of the CSC programme). The coordination between the trigger and physics groups is clearly a very important task. Corresponding efforts have started recently, e.g. triggers in the menu must now be requested and justified by physics and or performance groups.

## 10.4 Systematic Uncertainties and Statistical Significance

In order to assess the discovery potential in a somewhat realistic way, systematic uncertainties of the SM background must be taken into account. The expected background and its uncertainties will have to be obtained from an interplay between thorough data-driven background estimation studies, and iteratively improving simulations of the physics processes and the detector. Background estimation techniques are systematically discussed in Chapter 11, while in this chapter the background is directly taken from simulation.

Anticipating the results of background estimation methods and following the CSC SUSY notes [26], the background systematic uncertainties are assumed to be:

- 20% for the  $t\bar{t}$ ,  $W$  + jets,  $Z$  + jets, and diboson samples; and
- 50% for the QCD jets.

The uncertainties are taken to be uncorrelated and independent of any variable (flat). However, several systematic effects, such as the jet energy scale, are common and should lead to correlated errors. The above numbers should be taken as indicative uncertainties. They are included in the significance calculation, as described below, and also contribute to the error bars of all shown histograms. In the latter case, the statistical MC error, scaled according to the luminosity, and the above systematic uncertainties are added in quadrature.

The statistical significance is obtained from a profile likelihood including nuisance parameters due

to uncertainties in the background expectations, which are assumed to have Gaussian likelihood components. The expected number of SM events  $\bar{N}^{\text{SM}}$  is an incoherent sum of  $n^{\text{SM}}$  background contributions with  $\bar{N}_i^{\text{SM}}$  expected events for SM background type  $i$ , where  $i = 1, \dots, n^{\text{SM}}$ . Each background contribution  $i$  has an associated uncertainty  $\sigma_i^{\text{SM}}$ , composed of a statistical and a systematic component, which is assumed to be the width of a Gaussian distribution. Moreover, the various background uncertainties  $\sigma_i^{\text{SM}}$  can be correlated. All this is contained in the covariance matrix  $C$ . The  $-\ln(\text{likelihood})$  estimator for these conditions, and for  $N$  observed events, is given by

$$\begin{aligned}
 -\ln\mathcal{L} = & N'^{\text{SM}} - N \ln N'^{\text{SM}} + \ln N! + \frac{n^{\text{SM}}}{2} \ln(2\pi) + \frac{1}{2} \ln |C| \\
 & + \frac{1}{2} \sum_{i,j=1}^{n^{\text{SM}}} \left( N'_i{}^{\text{SM}} - \bar{N}_i^{\text{SM}} \right) C_{ij}^{-1} \left( N'_j{}^{\text{SM}} - \bar{N}_j^{\text{SM}} \right), \quad (10.1)
 \end{aligned}$$

where  $N'^{\text{SM}} = \sum_i N'_i{}^{\text{SM}}$ . The  $N'_i{}^{\text{SM}}$  ( $i = 1, \dots, n^{\text{SM}}$ ) are the varying parameters that can be used to minimise  $-\ln\mathcal{L}$ , and  $|C|$  is the determinant of  $C$ .

Minimising Eq. (10.1) yields the test statistics, which can be transformed into a p-value to observe data with equal or lesser compatibility with the null hypothesis<sup>4</sup> relative to the measured data ( $N$ ). The calculation of the p-value under these conditions can be performed analytically, and has been implemented in the package *StatTools*, see Appendix C. More general descriptions of this topic can also be found in Ref. [191, 192] and references therein.

## 10.5 Expected Discovery Potential

The discovery potential is determined using the expected total number of background and signal events. In addition to the event selection defined in Table 10.2, four final  $M_{\text{eff}}$  cuts are studied:  $M_{\text{eff}} > 0.4, 0.8, 1.2$ , and  $1.6$  TeV. The  $M_{\text{eff}}$  cut increases the sensitivity to high-mass final states, and the four cuts have been found to yield a good coverage of the studied SUSY parameter space. Fig. 10.4 shows the  $M_{\text{eff}}$  distribution for the SUSY benchmark models and the combined SM background (before the  $M_{\text{eff}}$  cut is applied).

The signal significance is obtained from the remaining background and signal events after one of the four  $M_{\text{eff}}$  cuts, using the statistical method and including the systematic background uncertainties, as discussed in Section 10.4.

This is the current ATLAS baseline method to assess the signal significance of the inclusive SUSY search channels. Typically, the highest significance out of the four (one for each  $M_{\text{eff}}$  cut) is stated as the expected discovery potential.<sup>5</sup>

<sup>4</sup>The null hypothesis is: data are described by the SM alone.

<sup>5</sup>The p-value has to be corrected for the four trials (so-called look-elsewhere-effect). The fact that events are shared between the four trials ( $M_{\text{eff}}$  cuts are inclusive) leads to a correlation which weakens the correction factor: a 100% correlation is equivalent to one analysis and thus no p-value correction. Under the conservative assumption of no correlations, the p-value increases by a factor 4 (number of trials), which turns a significance of  $5\sigma$  into  $4.7\sigma$ . In our case of the four inclusive  $M_{\text{eff}}$  cuts (0.4, 0.8, 1.2, 1.6 TeV) with the corresponding expected SM events for  $L = 1 \text{ fb}^{-1}$  (181, 49, 9, 1), the p-value correction factor is approximately 3.9.

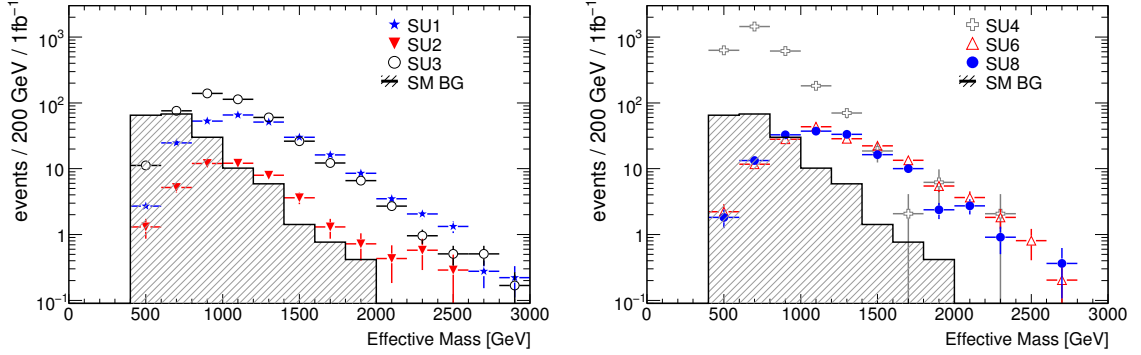


**Figure 10.4:** Distribution of  $M_{\text{eff}}$  for SUSY benchmark models and combined SM background events selected according to the cuts described in Table 10.2.

**Table 10.5:** Number of expected events for the SUSY benchmark points and the SM background ( $L = 1\text{fb}^{-1}$ ) for the various  $M_{\text{eff}}$  cuts considered, and the statistical significance numbers  $Z_n$  from the *StatTools* package including systematic uncertainties (see text).

Sample	$M_{\text{eff}} > 0.4 \text{ TeV}$		$M_{\text{eff}} > 0.8 \text{ TeV}$		$M_{\text{eff}} > 1.2 \text{ TeV}$		$M_{\text{eff}} > 1.6 \text{ TeV}$	
	$N^{\text{exp}}$	$Z_n$	$N^{\text{exp}}$	$Z_n$	$N^{\text{exp}}$	$Z_n$	$N^{\text{exp}}$	$Z_n$
SM background	181		49		9		1	
SU1	260	6.7	232	15.3	114	17.8	33	11.6
SU2	46	1.3	39	3.3	15	3.8	3	2.1
SU3	450	11.1	363	21.7	110	17.4	24	9.3
SU4	2974	32.1	896	31.3	99	16.2	10	5.2
SU6	162	4.3	148	10.7	76	13.4	26	9.8
SU8	151	4.0	136	10.0	66	12.1	17	7.3

Table 10.5 gives the number of expected signal and SM background events as a function of the four  $M_{\text{eff}}$  cuts, for  $L = 1\text{fb}^{-1}$ . Also shown are the statistical significance numbers (in units of the standard deviation  $\sigma$ ) obtained using the *StatTools* package, including the above systematic uncertainties. It can be seen that all considered SUSY models except SU2 could be discovered with good significance in the one-lepton channel. For SU2, the production cross section is dominated by gaugino pair production, so a different analysis is required [26]. The significances obtained from  $Z_n$  are well below the simplistic  $S/\sqrt{B}$  values, e.g. for SU1 and the lowest  $M_{\text{eff}}$  cut  $Z_n$  is 6.7 while  $S/\sqrt{B}$  is 19.3. This is expected because  $S/\sqrt{B}$  neglects the systematic uncertainties.

The results for the benchmark models described above use signal and background cross sections normalised to next-to-leading-order (NLO) calculations (cf. Section 8.3). Such NLO calculations were not performed for the mSUGRA parameter scan, because of the large number of grid points.<sup>6</sup> The cross sections of the mSUGRA grid points are therefore normalised to the leading-order values, as obtained from the HERWIG generator. The resulting mSUGRA reach estimates are

<sup>6</sup>Every SUSY model (grid point or benchmark point) involves many production processes. The NLO calculation must be performed for each of these processes.

thus conservative, since the background processes use the NLO corrections, and all  $k$  factors used here increase the cross section.

The mSUGRA grid is used in order to:

- verify that the analysis performs well on a wider range of possibly SUSY signatures;
- study the possible discovery/exclusion reach of the analysis.

Fig. 10.5 shows the signal significance (in units of the standard deviation  $\sigma$ ) of the one-lepton channel on the mSUGRA grid, again for an integrated luminosity of  $1 \text{ fb}^{-1}$ . The four plots correspond to the four  $M_{\text{eff}}$  cuts, as indicated in the plots. The significance calculations include the same systematic uncertainties as in Table 10.5. The significance scale ( $z$ -axis) is set to a maximum of 7 in the plots.

The shown mSUGRA discovery reach is to a first approximation the result of the production cross sections (cf. Section 8.1) and the selection efficiencies (cf. Section 10.3). Additionally, the four  $M_{\text{eff}}$  cuts have to be considered. It can be seen that the  $M_{\text{eff}} > 0.4 \text{ TeV}$  and  $M_{\text{eff}} > 0.8 \text{ TeV}$  cuts provide a good coverage over the region  $m_{1/2} \lesssim 250 \text{ GeV}$ , while the  $M_{\text{eff}} > 1.2 \text{ TeV}$  and  $M_{\text{eff}} > 1.6 \text{ TeV}$  cuts yield  $5\sigma$  signal significances in the  $m_0 \lesssim 1.5 \text{ TeV}$  and  $m_{1/2} \lesssim 0.5 \text{ TeV}$  parameter space region. High  $M_{\text{eff}}$  cuts select high-mass final states, and the mass of the final states is closely linked to the gluino and squark masses (cf. grey/dashed lines in the plots).

Following the procedure of taking the “best cut result” (highest significance) leads to the overall discovery reach shown in Fig. 10.6. This indicates a good performance on the studied SUSY parameter space. ATLAS could discover/exclude signals from R-parity conserving mSUGRA models with gluino and squark masses less than  $\mathcal{O}(1 \text{ TeV})$  after having accumulated and understood an integrated luminosity of  $1 \text{ fb}^{-1}$ . This also assumes that the SM background processes are understood to the level of systematic uncertainties considered here: 50% for QCD jets, and 20% for  $t\bar{t}$ ,  $W + \text{jets}$ ,  $Z + \text{jets}$ , and diboson processes.

The discovery reaches of the zero- and one-lepton analyses have been shown to be approximately equivalent at the LHC [26]. Compared with the multiple lepton SUSY channels, the one-lepton mode yields a better performance for most of the studied models. This together with the high robustness against background from QCD jets, makes the one-lepton analysis a prominent SUSY search mode for early LHC data.

## 10.6 Comparison of a Multivariate Technique

In this section, an optimisation of the one-lepton analysis using a multivariate technique based on boosted decision trees (BDT) is considered.<sup>7</sup> The employed BDT is provided by the TMVA (toolkit for multivariate data analysis) package [193].

The goal of this multivariate analysis (MVA) optimisation is to study potential improvements over the traditional cut-based analysis, presented in the previous sections. As opposed to box-cut

<sup>7</sup>Neural networks have also been studied. BDTs, however, proved to be more robust with respect to weakly discriminating input variables.



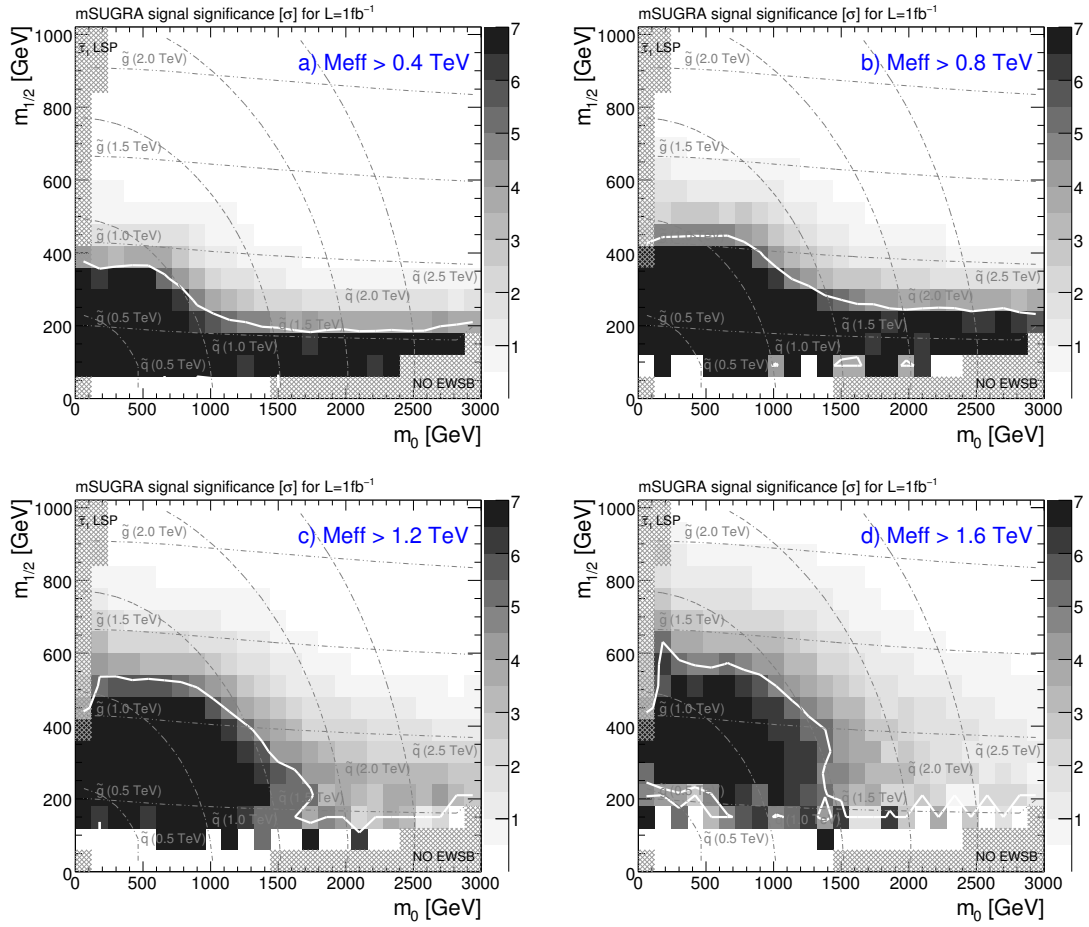


**Figure 10.5:** Expected signal significance (in units of the standard deviation  $\sigma$ ) on the mSUGRA grid for an integrated luminosity of  $1 \text{ fb}^{-1}$ , as obtained from the one-lepton channel with the four  $M_{\text{eff}}$  cuts indicated in the plots. Systematic uncertainties on the background are included (see text). The thick solid white lines indicate the  $5\sigma$ -reach, and contour lines of equal gluino and squark masses in steps of 500 GeV are shown in grey/dashed. The dashed region is theoretically not viable in the models.

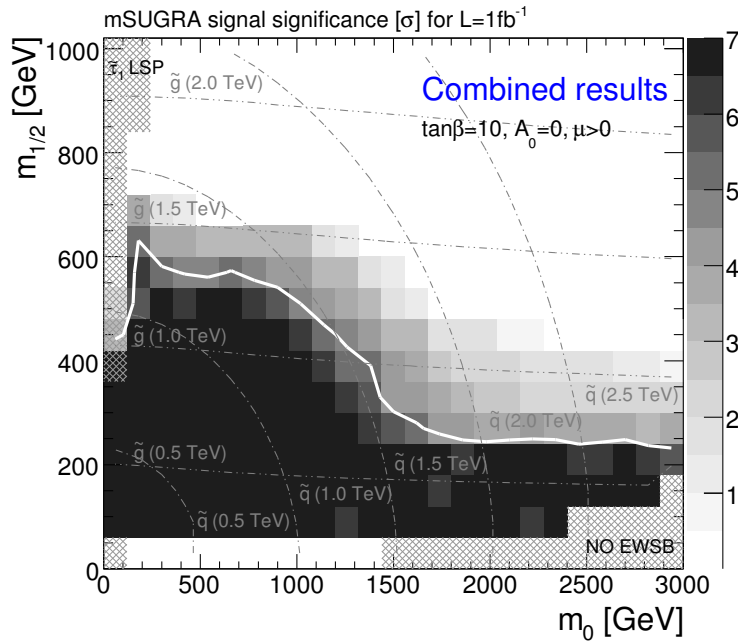


**Figure 10.6:** Expected signal significance (in units of the standard deviation  $\sigma$ ) on the mSUGRA grid for an integrated luminosity of  $1 \text{ fb}^{-1}$ , as obtained from the one-lepton channel. All four  $M_{\text{eff}}$  cuts ( $M_{\text{eff}} > 0.4, 0.8, 1.2, 1.6 \text{ TeV}$ ) were used, and the highest significance number is displayed for each grid point. The significance calculation includes systematic uncertainties on the background (see text), and more than five SUSY events are required (otherwise the significance is set to 0). The thick solid white line indicates the  $5\sigma$ -reach, and contour lines of equal gluino and squark masses in steps of 500 GeV are shown in grey/dashed. The dashed region is theoretically not viable in the models.

**Table 10.6:** Event pre-selection for the MVA one-lepton analysis.

Selection Requirement	cut #	Definition	$\varepsilon_{\text{SU3}}$
Lepton selection	K1	One isolated electron or muon with $p_T > 20$ GeV	0.160
Veto on additional lepton	K2	No additional isolated leptons with $p_T > 10$ GeV	0.144
Jet selection	K3	At least four jets with $p_T > 40$ GeV, and, out of the four jets, one must have $p_T > 100$ GeV	0.067
Missing transverse energy	K4	$E_T^{\text{miss}} > 100$ GeV	0.060

analyses, an MVA can exploit the correlations of input variables. Therefore, several new input variables — such as  $\Delta\phi$  between the jet and  $E_T^{\text{miss}}$  vectors — have been considered.

### 10.6.1 Pre-selection of events

The same datasets, object, and variable definitions as in the previous sections are used. Events are pre-selected according to the cuts given in Table 10.6. This pre-selection represents a relaxed version of the standard one-lepton event selection (cf. Table 10.2), with the following modifications:

- the jet  $p_T$  cut is lowered from 50 GeV to 40 GeV,
- the  $E_T^{\text{miss}} > 0.2 M_{\text{eff}}$  cut is not used,
- the transverse sphericity cut ( $S_T > 0.2$ ) is dropped, and
- the transverse mass cut ( $M_T > 100$  GeV) is dropped.

The remaining cuts (K1 to K4) select the one-lepton channel, and ensure that all event filters at generator level are met. The MC events surviving this pre-selection are divided into training and evaluation samples, where the training events are not used in the subsequent analysis steps.

The use of these relaxed cuts (instead of the standard event selection) serves mainly two purposes. Firstly, the limited MC statistics surviving the standard event selection cuts poses a serious problem in an MVA analysis, where adequate statistics are required for not only the training but also the evaluation. Therefore, most of the standard cuts have been dropped. Secondly, a more relaxed pre-selection of the events provides more flexibility to the MVA in combining the correlated input variables (although a better MVA performance is often obtained by applying obvious box-cuts before).

### 10.6.2 Input variables

The variables considered as input for the BDT are as follows, ordered by their separation power  $\langle S^2 \rangle$  between the SU3 benchmark point and the combined SM background<sup>8</sup> (for events that passed

<sup>8</sup>The separation power  $\langle S^2 \rangle$  is defined as  $(1/2) \int dx (\hat{S}(x) - \hat{B}(x))^2 / (\hat{S}(x) + \hat{B}(x))$ , where  $x$  is the variable of interest, and  $\hat{S}/\hat{B}(x)$  are the signal/background PDFs.

the pre-selection):

Input variable	Description	$\langle S^2 \rangle$
$E_T^{\text{miss}}$	Missing transverse energy	$3.5 \cdot 10^{-1}$
$M_{\text{eff}}$	Effective mass	$3.0 \cdot 10^{-1}$
$M_T$	Transverse mass	$2.5 \cdot 10^{-1}$
$m_{\text{top}}$	Invariant top mass	$1.7 \cdot 10^{-1}$
$p_T^{\text{jet1}}$	Transverse momentum of the hardest jet	$1.4 \cdot 10^{-1}$
$p_T^{\text{jet2}}$	Transverse momentum of the second hardest jet	$1.3 \cdot 10^{-1}$
$E_T^{\text{miss}}/M_{\text{eff}}$	Ratio of missing transverse energy to effective mass	$1.1 \cdot 10^{-1}$
$\Delta\phi(E_T^{\text{miss}}, \text{lep})$	Azimuthal angle between $E_T^{\text{miss}}$ and the lepton	$1.0 \cdot 10^{-1}$
$p_T^{\text{jet3}}$	Transverse momentum of third hardest jet	$8.8 \cdot 10^{-2}$
$p_T^{\text{jet4}}$	Transverse momentum of fourth hardest jet	$6.5 \cdot 10^{-2}$
$\Delta\phi(\text{jet1}, \text{lep})$	Azimuthal angle between the hardest jet and the lepton	$4.3 \cdot 10^{-2}$
$\Delta\phi(E_T^{\text{miss}}, \text{jet2})$	Azimuthal angle between $E_T^{\text{miss}}$ and the second hardest jet	$2.5 \cdot 10^{-2}$
$\Delta\phi(E_T^{\text{miss}}, \text{jet1})$	Azimuthal angle between $E_T^{\text{miss}}$ and the hardest jet	$2.1 \cdot 10^{-2}$
$\Delta\phi(\text{jet1}, \text{jet2})$	Azimuthal angle between the hardest and second hardest jets	$1.1 \cdot 10^{-2}$
$\Delta\phi(\text{jet2}, \text{jet3})$	Azimuthal angle between the second and third hardest jets	$7.6 \cdot 10^{-3}$
$S_T$	Transverse sphericity	$6.2 \cdot 10^{-3}$
$\Delta\phi(\text{jet1}, \text{jet3})$	Azimuthal angle between the hardest and third hardest jets	$6.1 \cdot 10^{-3}$
$\Delta\phi(E_T^{\text{miss}}, \text{jet3})$	Azimuthal angle between $E_T^{\text{miss}}$ and the third hardest jet	$5.0 \cdot 10^{-3}$
$\Delta\phi(\text{jet2}, \text{lep})$	Azimuthal angle between the second hardest jet and the lepton	$2.8 \cdot 10^{-3}$

The global event variables  $M_{\text{eff}}$ ,  $M_T$ , and  $S_T$  are defined as before (cf. Table 10.1). The invariant top mass ( $m_{\text{top}}$ ) is based on simple kinematics. Assuming a semi-leptonic  $t\bar{t}$  decay,  $m_{\text{top}}$  is calculated from the lepton, neutrino ( $E_T^{\text{miss}}$ ), and one out of the four hardest jets: the  $W$  boson mass constraint is used to obtain the  $z$ -component of the neutrino momentum; and each of the four hardest jets is combined with the lepton and neutrino; the combination yielding an invariant mass closest to the top mass (set to 175 GeV) is kept.

Figs. 10.7 and 10.8 show the SU3 and combined SM background distributions of events pre-selected according to cuts defined in Table 10.6 for all variables used as input for the BDT-based analysis.

### 10.6.3 MVA results

#### Optimisation of SU3

The BDT training was carried out on  $100 \times 10^3$  SM background MC events — taking into account the different sample weights — and  $15 \times 10^3$  SU3 MC signal events, leaving around  $131 \times 10^3$  SM background and  $\sim 15 \times 10^3$  SU3 MC events in the evaluation samples.

Fig. 10.9 shows the resulting BDT background rejection as a function of the signal efficiency (left plot) and the BDT response to signal and background (right plot). Also shown are the rejection/efficiencies of the standard cut-based method, for all four  $M_{\text{eff}}$  cuts. All efficiencies are

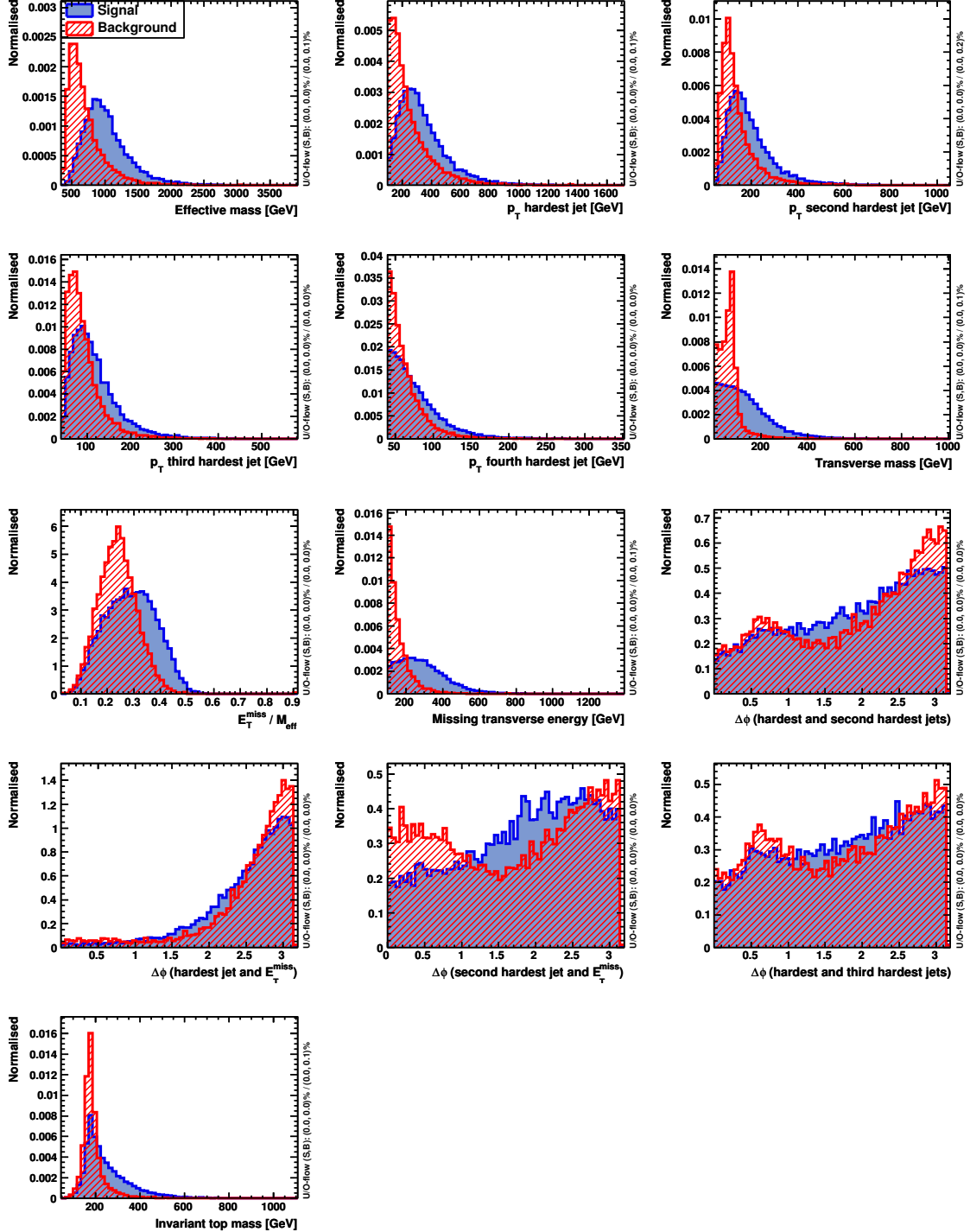


**Figure 10.7:** SU3 (blue/solid histograms) and SM background (red/dashed histograms) distributions of events pre-selected according to the cuts defined in Table 10.6. The shown variables are used as input to the BDT-based analysis (from top left to bottom right):  $M_{\text{eff}}$ ,  $p_T^{\text{jet1}}$ ,  $p_T^{\text{jet2}}$ ,  $p_T^{\text{jet3}}$ ,  $p_T^{\text{jet4}}$ ,  $M_T$ ,  $E_T^{\text{miss}}/M_{\text{eff}}$ ,  $E_T^{\text{miss}}$ ,  $\Delta\phi(\text{jet1}, \text{jet2})$ ,  $\Delta\phi(E_T^{\text{miss}}, \text{jet1})$ ,  $\Delta\phi(E_T^{\text{miss}}, \text{jet2})$ ,  $\Delta\phi(\text{jet1}, \text{jet3})$ , and  $m_{\text{top}}$ . The remaining BDT input variables are shown in Fig. 10.8.

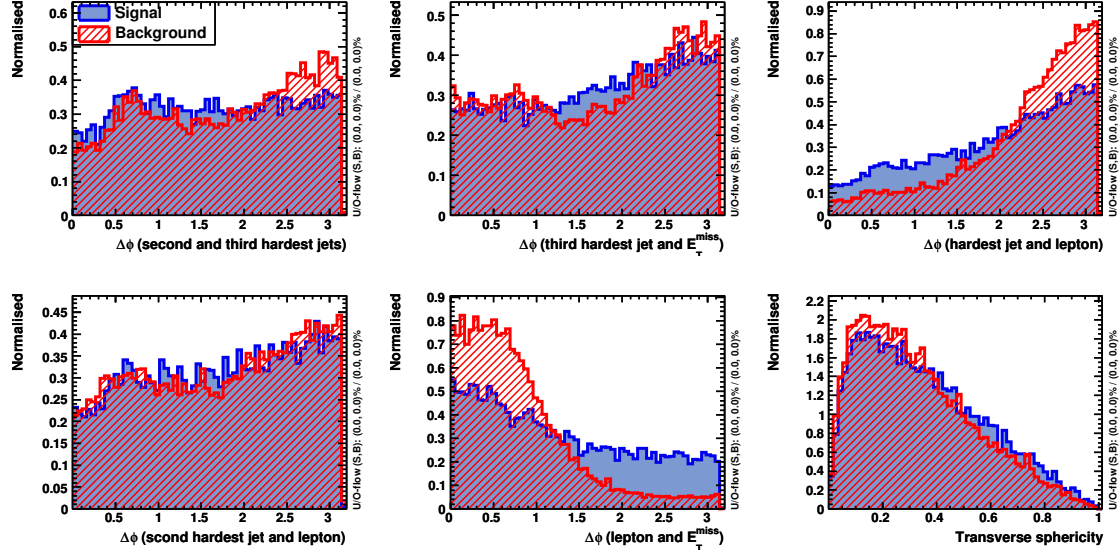


**Figure 10.8:** SU3 (blue/solid histograms) and SM background (red/dashed histograms) distributions of events pre-selected according to the cuts defined in Table 10.6. The shown variables are used as input to the BDT-based analysis (from top left to bottom right):  $\Delta\phi(\text{jet2, jet3})$ ,  $\Delta\phi(E_T^{\text{miss}}, \text{jet3})$ ,  $\Delta\phi(\text{jet1, lep})$ ,  $\Delta\phi(\text{jet2, lep})$ ,  $\Delta\phi(E_T^{\text{miss}}, \text{lep})$ , and  $S_T$ .

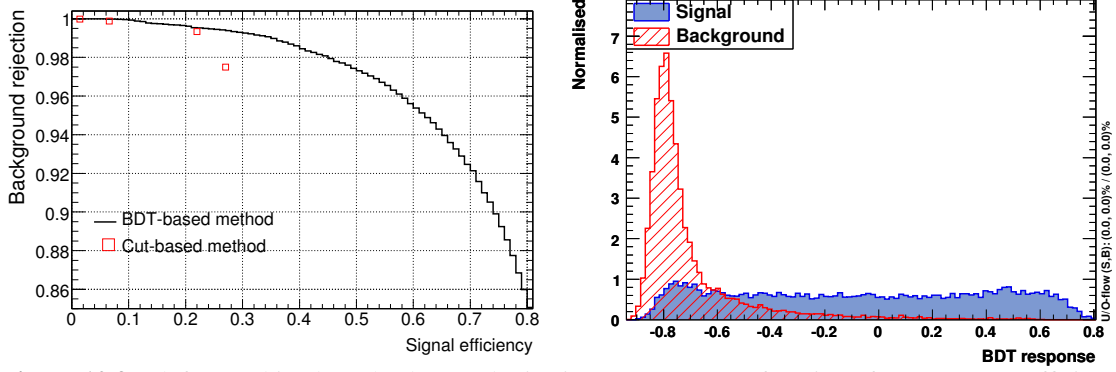
normalised to the pre-selection cuts. The BDT results are obtained from the independent evaluation samples.

Table 10.7 quantifies the signal/background efficiencies for both the BDT and cut-based methods. As expected, the BDT performs better than all of the four  $M_{\text{eff}}$  cuts.

The mSUGRA signal grid is used to study the performance of this SU3-trained BDT analysis for a wider range of SUSY models. Again, all (training) events are pre-selected according to Table 10.6. A final cut on the BDT response variable then selects the events which are considered for the significance calculation. Four different BDT cuts are applied, and the highest significance is taken, similarly to the “best cut result” of the four  $M_{\text{eff}}$  cuts. The significance calculation includes the same systematic uncertainties as for the cut-based method.

**Table 10.7:** Expected SUSY (SU3) and SM background efficiencies for the four  $M_{\text{eff}}$  cuts, normalised to the pre-selection cuts (cf. Table 10.6). The efficiencies for the BDT-based method are given for a fixed SU3 or SM background efficiency. The quoted errors are statistical.

Cuts	Cut-based method		BDT-based method	
	$\epsilon_{\text{SU3}}$	$\epsilon_{\text{SM}}$	$\epsilon_{\text{SU3}} @ \text{fixed } \epsilon_{\text{SM}}$	$\epsilon_{\text{SM}} @ \text{fixed } \epsilon_{\text{SU3}}$
$M_{\text{eff}} > 0.4 \text{ TeV}$	$(2.7 \pm 0.1) \cdot 10^{-1}$	$(2.5 \pm 0.2) \cdot 10^{-2}$	$4.9 \cdot 10^{-1}$	$6.0 \cdot 10^{-3}$
$M_{\text{eff}} > 0.8 \text{ TeV}$	$(2.2 \pm 0.1) \cdot 10^{-1}$	$(6.7 \pm 1.0) \cdot 10^{-3}$	$2.8 \cdot 10^{-1}$	$4.7 \cdot 10^{-3}$
$M_{\text{eff}} > 1.2 \text{ TeV}$	$(6.6 \pm 0.6) \cdot 10^{-2}$	$(1.2 \pm 0.4) \cdot 10^{-3}$	$1.2 \cdot 10^{-1}$	$\sim 10^{-4}$
$M_{\text{eff}} > 1.6 \text{ TeV}$	$(1.4 \pm 0.3) \cdot 10^{-2}$	$(1.9 \pm 1.6) \cdot 10^{-4}$	$8.0 \cdot 10^{-2}$	$\sim 10^{-5}$



**Figure 10.9:** (left) Combined SM background rejection ( $1 - \varepsilon_{\text{SM}}$ ) as a function of SUSY (SU3) efficiency, for the BDT and cut-based analyses. All efficiencies are with respect to the pre-selection cuts. (right) BDT response for signal (SU3) and combined SM background.

The resulting signal significance on the mSUGRA grid is shown in Fig. 10.10. The (projected) position of the SU3 benchmark point, which has been used for the BDT training, is indicated on the grid by the white “X”. In the left plot, the  $5\sigma$  reach lines are given for the BDT-based method (solid/white) and the cut-based analysis (dotted/red). It can be seen that the BDT method slightly improves the discovery reach. The right plot shows the relative significance of the two methods, and the white contour line indicates where both methods yield a similar significance. As can be seen, a gain in some region of parameter space (in particular close to the SU3 point) is obtained, while it is also evident that the BDT-based method performs worse than the standard cut-based method in other regions of the parameter space.

Using the SU3-trained MVA on other signal models (here the mSUGRA grid) is not biased, but it is sub-optimal. We will therefore next consider a combination of BDTs trained on different signal models.

### Optimisation of mSUGRA grid points

The BDT-based method is further studied by splitting the analysis into four distinct BDTs, each trained for one specific SUSY model (and the combined SM background as before). The four signal points chosen for training are all on the mSUGRA grid plane ( $A_0 = 0$ ,  $\tan\beta = 10$ , and  $\mu > 0$ ), and were arbitrarily selected to cover the discovery region of the cut-based method:

- point 1 (P1)  $m_0 = 1500$  GeV and  $m_{1/2} = 390$  GeV,
- point 2 (P2)  $m_0 = 2460$  GeV and  $m_{1/2} = 210$  GeV,
- point 3 (P3)  $m_0 = 420$  GeV and  $m_{1/2} = 210$  GeV, and
- point 4 (P4)  $m_0 = 660$  GeV and  $m_{1/2} = 570$  GeV.

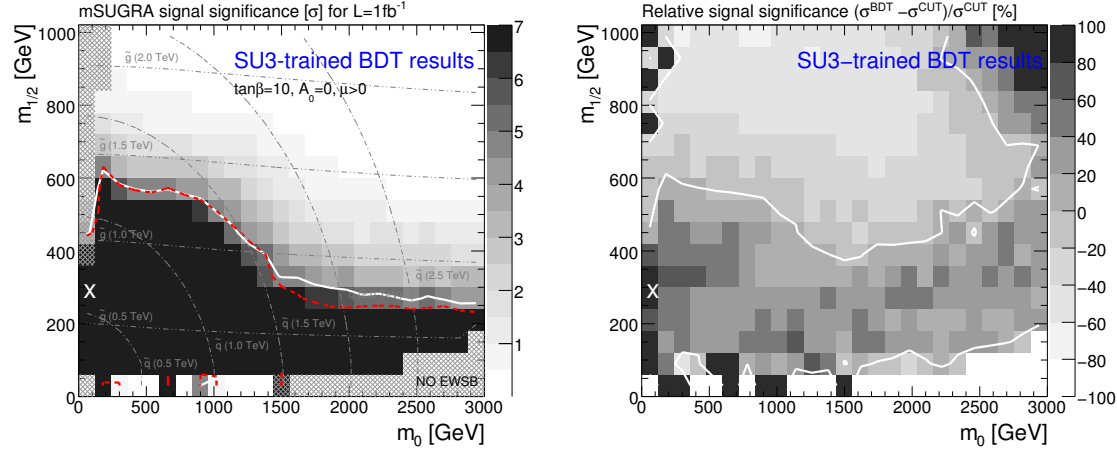


**Figure 10.10:** Expected signal significance on the mSUGRA grid, as obtained from the SU3-trained BDT analysis, for  $L = 1 \text{ fb}^{-1}$ , and including all systematic uncertainties. Left plot: the BDT signal significance is shown in the grey colour coding, and the  $5\sigma$  reach of the BDT-based (cut-based) method is indicated by the thick solid/white (dotted/red) line. Right plot: relative signal significance  $(\sigma^{\text{BDT}} - \sigma^{\text{cut}})/\sigma^{\text{cut}}$  in percent, the thick white contour line indicates where both methods perform equally well. The white 'X' indicates in both plots the  $(m_0, m_{1/2})$  position of SU3 on the mSUGRA grid. The SU3 parameter values of  $\tan\beta = 6$  and  $A_0 = -300 \text{ GeV}$  are different from those of the mSUGRA grid.

The training and analysis of the four BDTs was performed similarly to the SU3-trained BDT analysis.<sup>9</sup> Fig. 10.11 shows for each of the BDTs the relative signal significance with respect to the cut-based method. We can see that the four BDT analyses improve the signal significance with respect to the cut-based method over different, but also overlapping regions in parameter space.

Fig. 10.12 shows the signal significance results of the combined BDT analysis. All four trained BDTs have been used to determine the highest significance.<sup>10</sup> A considerable gain in the  $5\sigma$  discovery reach can be observed with respect to the cut-based method (cf. dotted/red with solid/white contour lines).

## 10.7 Conclusions

The inclusive one-lepton search mode is one of the primary discovery channels for SUSY with early LHC data. Its requirement of one isolated lepton in addition to multiple high- $p_T$  jets and large  $E_T^{\text{miss}}$  significantly reduces the abundant QCD multijet background. Thereby the one-lepton channel is more robust than the zero-lepton SUSY search mode. The remaining SM background stems dominantly from  $t\bar{t}$  and subdominantly from  $W + \text{jets}$  processes, which are expected to be under better control than QCD jet production.

The discovery reach for R-parity conserving mSUGRA models has been studied for an integrated

<sup>9</sup>The use of the SUn benchmark points instead of mSUGRA grid points could be beneficial for the training, since the mSUGRA grid points were generated with only  $20 \times 10^3$  events.

<sup>10</sup>The look-elsewhere-effect of the combined BDT analysis has been conservatively corrected: the obtained best significance is scaled down by a factor of 0.94.



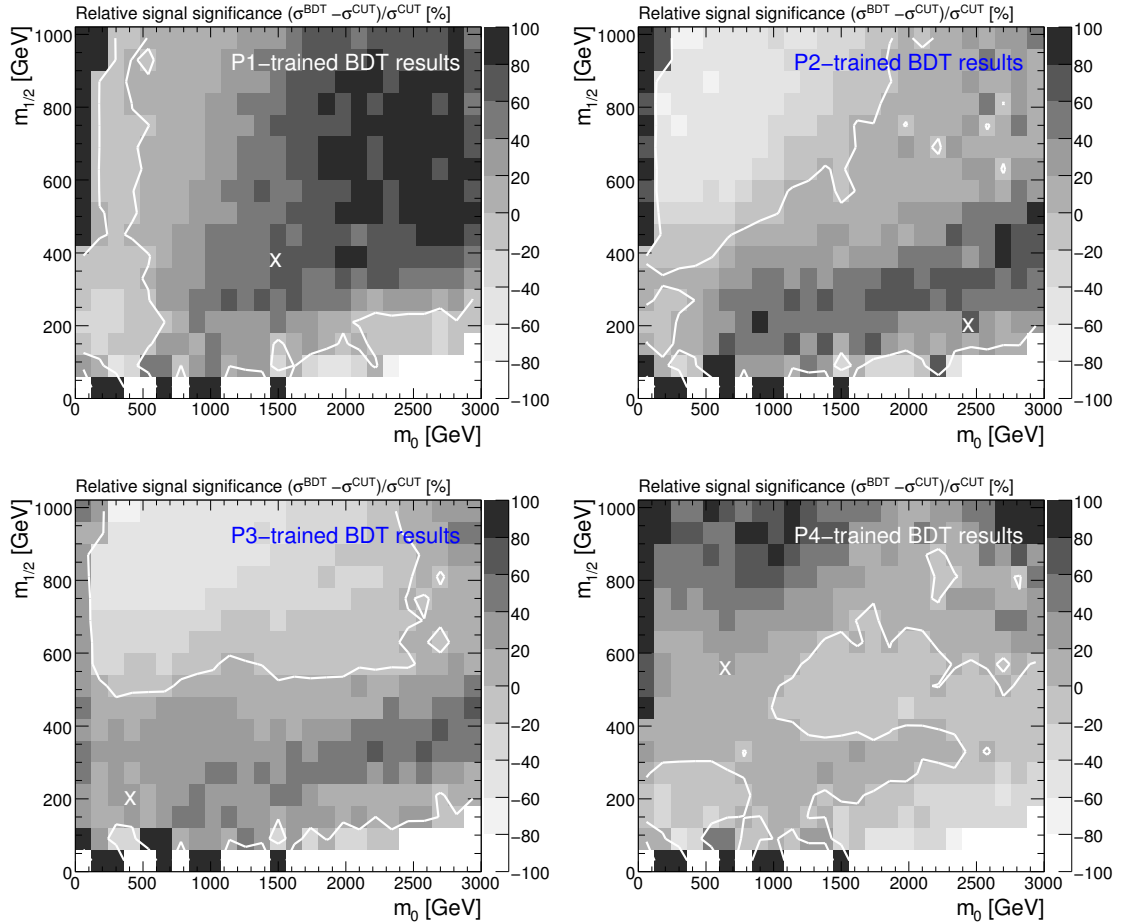


**Figure 10.11:** Relative expected signal significances of the P1 to P4 trained BDT analyses, with respect to the cut-bases method, for  $L = 1 \text{ fb}^{-1}$ , and including all systematic uncertainties. The white 'X' indicates the position of the signal models used for training, and the white contour lines show where the BDT and cut-based methods yield the same significances.

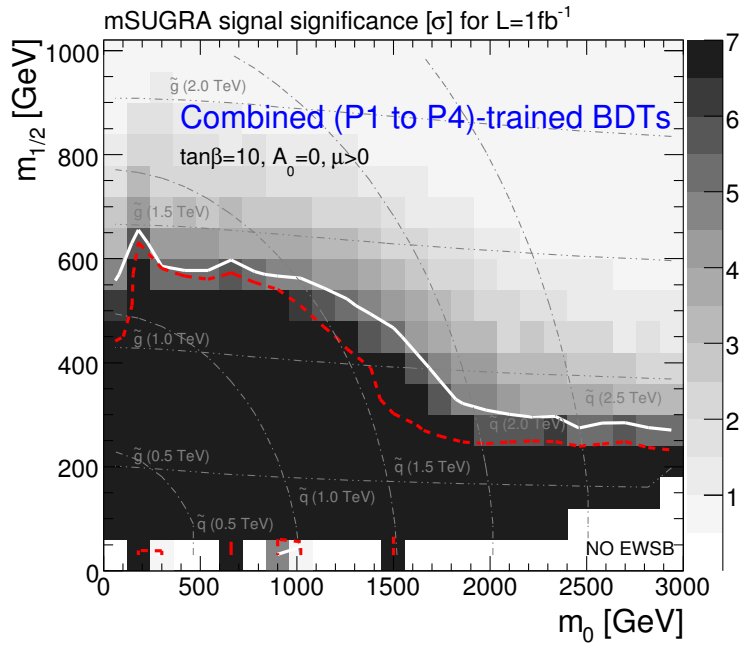


**Figure 10.12:** Expected signal significance (in units of the standard deviation  $\sigma$ ) on the mSUGRA grid for an integrated luminosity of  $1 \text{ fb}^{-1}$ , as obtained from the combined BDT analysis (four trained BDTs) in the one-lepton channel. The significance calculation includes the standard systematic uncertainties on the background. The shown significance of the combined BDT analysis has been conservatively corrected for the look-elsewhere-effect. The solid white (dotted red) line indicates the  $5\sigma$ -reach of the BDT-based (cut-based) analysis. The contour lines of equal gluino and squark masses in steps of 500 GeV are shown in grey/dashed. The dashed region is theoretically not viable in the models.

---

luminosity of  $1 \text{ fb}^{-1}$ . Models with squark and gluino masses of less than  $\mathcal{O}(1 \text{ TeV})$  have been found to be within the  $5\sigma$  discovery reach.

A multivariate analysis technique has been used to show the potential improvements of the one-lepton analysis. A considerable gain in discovery reach was achieved, at the expense of increased complexity. The priority for early data analyses, however, is a robust method with emphasis on the background estimation from data. This is the subject of the next chapter.

---



## Chapter 11

# Background Estimation

The reliable determination of the SM background is of upmost importance for beyond-SM searches. This chapter is devoted to the description of background estimation methods. The author significantly contributed to all of the presented work, which is also separately available in Ref. [194].

This chapter is organised as follows. Section 11.1 gives a general introduction to background estimation in SUSY searches. It further briefly discusses and compares different methods developed within ATLAS. In Section 11.2 the traditional background determination method is reviewed. Its shortcomings are pointed out and improvements are suggested. In Section 11.3 the *Tiles* Method for  $2 \times 2$  Tiles and general  $n \times n$  Tiles is derived, remedying most of the problems of the  $M_T$ -method. Systematic uncertainties arising from the residual MC dependence are quantified and the SUSY discovery potential using this method is evaluated.

### 11.1 Introduction

In  $R$ -parity conserving Supersymmetry (SUSY), the hard-scattering interaction of two protons can only produce an even number of Supersymmetric particles, which decay incoherently in cascades to ever lighter particles, conserving the initial negative  $R$  parity in each decay. Consequently, the lightest SUSY particle, denoted LSP, is stable and, because it is weakly interacting only, escapes detection. The resulting characteristic missing transverse energy ( $E_T^{\text{miss}}$ ) signature drives the search strategy for such events. Due to the production of two LSPs in the event, its kinematic reconstruction is under-determined (transverse balance of the event provides only one two-dimensional constraint), thus not allowing one to reconstruct the masses of the involved SUSY particles in the cascades on an event-by-event basis. One is hence left with searching for a statistical excess in events with large  $E_T^{\text{miss}}$ , rather than mass peaks over broader background. This significantly complicates the analysis. While background under a peak can be empirically determined from the observed data using simultaneous fits together with the signal without relying on Monte Carlo (MC) simulation, use of simulation is required when comparing event abundances only, without extracting shape information from the data. However, for experiments operating at the high energy frontier it is not possible to rely solely on MC simulation. They are inaccurate due to various uncertainties, including parton density distributions for protons at 14 TeV CM energy,

cross sections of the involved Standard Model (SM) processes, and the details of the detector response. It is thus mandatory to develop strategies to determine the expected SM background (and, simultaneously, the observed signal abundance) in an as model-independent manner as possible.

Throughout this chapter it is assumed that the overall numbers of SM background and beyond-SM signal events<sup>1</sup> in the observed data sample are unknown. Some prior information from MC simulation and/or “calibration” measurements on the shapes of the discriminating variables must therefore be inserted, since otherwise the problem would be underdetermined. A convenient approach, often called the  *$M_T$ -method* [26], has been to define an area of *low* transverse mass<sup>2</sup>  $M_T$  and  $E_T^{\text{miss}}$  values, which is assumed to be background dominated, and a corresponding *high*  $M_T$ ,  $E_T^{\text{miss}}$  area, sensitive to the SUSY signal. The number of signal events can then be approximated by  $N^{\text{signal}}[\text{high}] = N^{\text{observed}}[\text{high}] - f^{\text{SM}}[\text{high}]/f^{\text{SM}}[\text{low}] \cdot N^{\text{observed}}[\text{low}]$ , where  $f^{\text{SM}}$  denotes a relative fraction of events. However, in presence of signal contamination in the low region, the number of signal events in the high region is in general underestimated, which – depending on the SUSY model – can be a gross effect. To remedy this bias, iterative procedures have been developed (so called *New  $M_T$ -method* [26]), reinserting the estimated number of signal events in the low region and repeating the  $N^{\text{signal}}[\text{high}]$  estimate. However, such methods do not converge if no additional prior information is inserted. For the case that additional prior information is used, the iterative methods may still not be well-behaved, and it may be difficult to define an unambiguous stop criterion. Another problem with this method is that it relies on vanishing correlations between the two variables ( $M_T$ ,  $E_T^{\text{miss}}$ ) both for signal and SM background. This conjecture however is inaccurate, leading to biases in the determined SM background in the high region. In particular, positive (negative) correlations in the SM background sample lead to an underestimation (overestimation) of the SM abundance in the high region.

This chapter systematically revisits the formalism to determine background estimates from data after insertion of prior information on the distributions of the discriminating variables for the SM background. The regions in the (generally, but not necessarily) two-dimensional variable space are denoted *Tiles*. It is shown that for at least  $2 \times 2$  Tiles the resulting system of linear equations can be solved without requiring zero-signal contamination in the background dominated area, and without the assumption of vanishing correlations between the variables for background events, albeit maintaining this assumption for signal. While for  $2 \times 2$  Tiles the solution can be analytically derived, a fit must be performed for a larger number of Tiles because the system is overconstrained. In all these cases, a unique best solution is found, and there is no need to recur to iterations.

Other background estimation techniques have been developed and are fully described in [26]. These include estimating the individual background contributions from full reconstruction or MC “redecay”, using extrapolation from sidebands, as well as carrying out a combined fit to the signal and control regions. To have confidence in the background estimate it is important to be able to cross check these methods against each other. The Tiles method should give similar results to a combined fit method, and these results should be compatible with summing up estimates of the individual background components from other methods. If this is not the case this indicates that the backgrounds are not well understood. The main difference between the Tiles method and the

---

<sup>1</sup>While all studies involving signal MC throughout this work employ SUSY (mSUGRA) models, the proposed background estimation method is largely independent of it. It only requires at least two variables capable of discriminating signal from background, and can hence be applied to almost any analysis searching for unknown beyond-SM signals.

<sup>2</sup> $M_T$  is defined in Table 10.1.

---

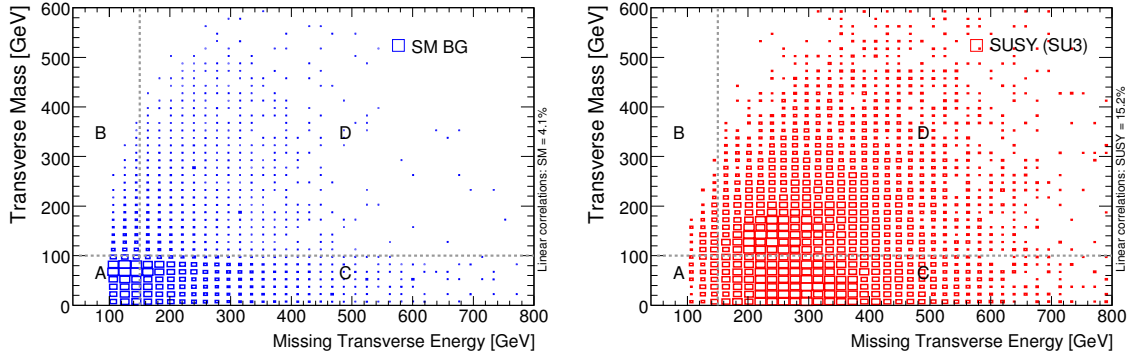


**Figure 11.1:** Distributions of SM background events (left) and SUSY SU3 events (right) in the plane  $(E_T^{\text{miss}}, M_T)$ . The plane is divided into four areas A, B, C, D, which form the control (A+C), signal (B+D), and normalisation (B) regions.

combined fit method is that the Tiles method does not require to model the signal PDF – beyond the stated assumption.

Throughout this chapter, the standard (i.e. cut-based) one-lepton SUSY search channel is used, as described in Chapter 10, including the datasets, object and variable definitions, and the event selection cuts. The only difference is that the  $M_T < 100$  GeV cut is dropped.

## 11.2 Two-Dimensional Sideband Background Estimation

The so-called  $M_T$ -method is a data-driven background estimation approach for the one-lepton search channel [26]. The combined SM background in the signal region is estimated from sidebands in  $M_T$  and in a second variable, which is assumed to be uncorrelated with  $M_T$ . In the following discussion,  $E_T^{\text{miss}}$  is used as the second variable; another typical choice would be  $M_{\text{eff}}$ . The impact of signal contamination and variable correlations is investigated and the resulting bias is studied for several SUSY scenarios.

### 11.2.1 The $M_T$ Sideband Method

A full description of the  $M_T$ -method can be found in the SUSY CSC notes [26] (Section 2.3.1 of the chapter “Data-Driven Determinations of W, Z and Top Backgrounds to Supersymmetry”). A brief overview is given in the following.

Figure 11.1 shows the distribution of SU3 and SM background events in the two-dimensional plane  $(E_T^{\text{miss}}, M_T)$ . The plane is divided into four regions A, B, C, D, corresponding to the requirements  $M_T < 100$  GeV,  $E_T^{\text{miss}} < 150$  GeV (region A),  $M_T \geq 100$  GeV,  $E_T^{\text{miss}} < 150$  GeV (B),  $M_T < 100$  GeV,  $E_T^{\text{miss}} \geq 150$  GeV (C), and  $M_T \geq 100$  GeV,  $E_T^{\text{miss}} \geq 150$  GeV (D).

The control region is the low transverse mass space (regions A and C) in which only little SUSY signal is found according to MC models (cf. also the  $M_T$  distribution in Fig. 10.3). The  $M_T$ -method predicts the SM event distribution as a function of  $E_T^{\text{miss}}$  in the signal region (B and D) as

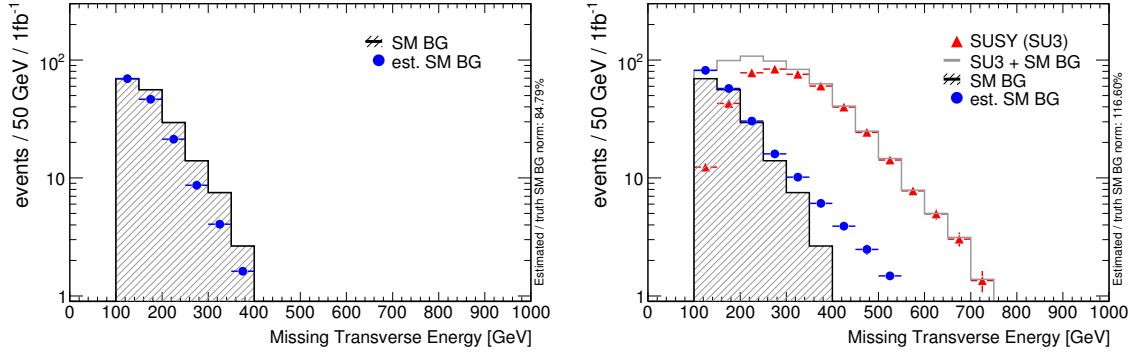


**Figure 11.2:**  $E_T^{\text{miss}}$  event distributions in the absence of SUSY (left) and for the mSUGRA point SU3 (right). Shown as circles is the SM distribution estimated with the  $M_T$ -method. The hatched histogram represents the SM MC and triangles indicate the SU3 SUSY MC. The open histogram in the right plot is the sum of SM and SUSY MC.

follows:

- the shape is determined by the observed events in the control region;
- the distribution is normalised in the normalisation region B to the total number of observed events in that region.

The  $M_T$ -method is based on two main assumptions:

- the SM background shape is equal in the control and signal regions, which in general requires that the two variables  $M_T$  and  $E_T^{\text{miss}}$  are uncorrelated;<sup>3</sup>
- no SUSY signal contaminates the normalisation region or the control region.

These assumptions are analysed in the following.

### 11.2.2 Impact of Variable Correlations and SUSY Contamination

The estimated  $E_T^{\text{miss}}$  background distribution in the signal region in the absence of SUSY signal is shown in the left plot of Fig. 11.2. The estimated SM background is normalised correctly in the first bin because no SUSY events contaminate this bin or the control sample. However, the shapes of the true MC SM background and the estimated background are different because of correlations, leading to underestimation of background by 15% for  $E_T^{\text{miss}} > 100$  GeV and by 32% for  $E_T^{\text{miss}} > 200$  GeV.

Figure 11.3 compares the normalised SM distributions versus  $E_T^{\text{miss}}$  and  $M_{\text{eff}}$  in the control and signal regions, respectively. As clearly visible from the ratio plots, the shapes of both variables

<sup>3</sup>Equality of shapes may also occur in presence of correlations by virtue of fortuitous cancellations. This however is difficult to control systematically.



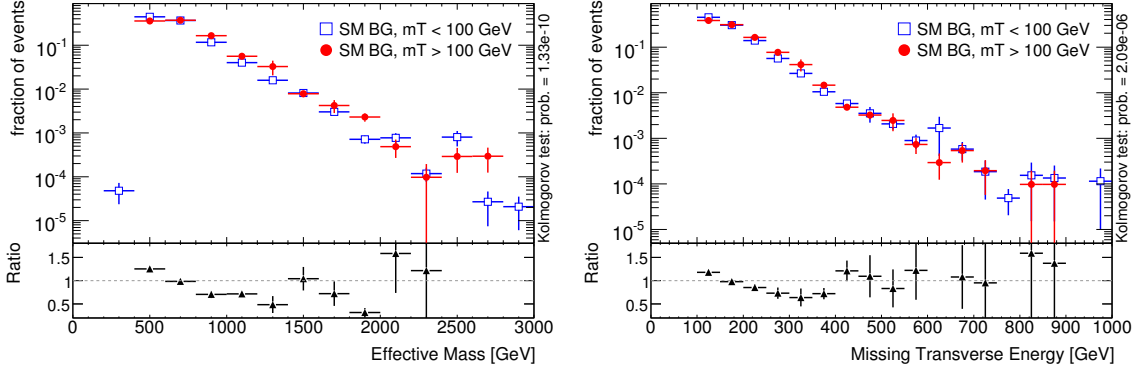


**Figure 11.3:** Comparison of the SM background shape in the control region ( $M_T < 100$  GeV) with that in the signal region ( $M_T > 100$  GeV) for the variables  $M_{\text{eff}}$  (left) and  $E_T^{\text{miss}}$  (right). The probability for the shapes to be compatible within statistical uncertainties (Kolmogorov test) is also shown.

differ significantly between the two regions.<sup>4</sup> For the purpose of illustration, the linear correlation coefficients<sup>5</sup> are quoted below. Even for vanishing linear correlations one can still have problems from non-linear correlations, but the linear correlation gives an idea of how big the effects from correlations may be. between the variables  $M_T$  and  $M_{\text{eff}}$ , and between  $M_T$  and  $E_T^{\text{miss}}$  for SM background and the two SUSY benchmark points SU3 and SU4:

Correlation factor	SM	SU3	SU4
$M_T$ and $M_{\text{eff}}$	0.07	0.11	0.22
$M_T$ and $E_T^{\text{miss}}$	0.04	0.15	0.28

Figure 11.4 shows the correlation factor for the variable pair  $(M_{\text{eff}}, M_T)$  on the mSUGRA grid.

The estimated  $E_T^{\text{miss}}$  background distribution for SU3 is shown in the right plot of Fig. 11.2. Here, the true MC SM background is overestimated because of SUSY contamination of the normalisation region and, as visible in the tail by comparison with the left plot of Fig. 11.2, of the control region.

For the variable pairs  $(M_T, M_{\text{eff}})$  and  $(M_T, E_T^{\text{miss}})$ , the correlation and contamination effects affect the predicted integrated background abundance in opposite ways and the net effect depends on the manifestation of the SUSY signal.

### 11.2.3 Performance on the mSUGRA Grid

The performance of the  $M_T$ -method is evaluated on the mSUGRA  $(m_0, m_{1/2})$  grid against a wide variety of SUSY cross sections and shapes. The SM background is estimated using the  $M_T$ -method as described in Section 11.2.1. The grid scan is performed for four different cuts on  $M_{\text{eff}}$  ( $M_{\text{eff}} > 0.4, 0.8, 1.2$  or  $1.6$  TeV).

<sup>4</sup>A Kolmogorov-Smirnov test yields minuscule probabilities for the shapes to be compatible within the expected size of statistical fluctuations.

<sup>5</sup>a

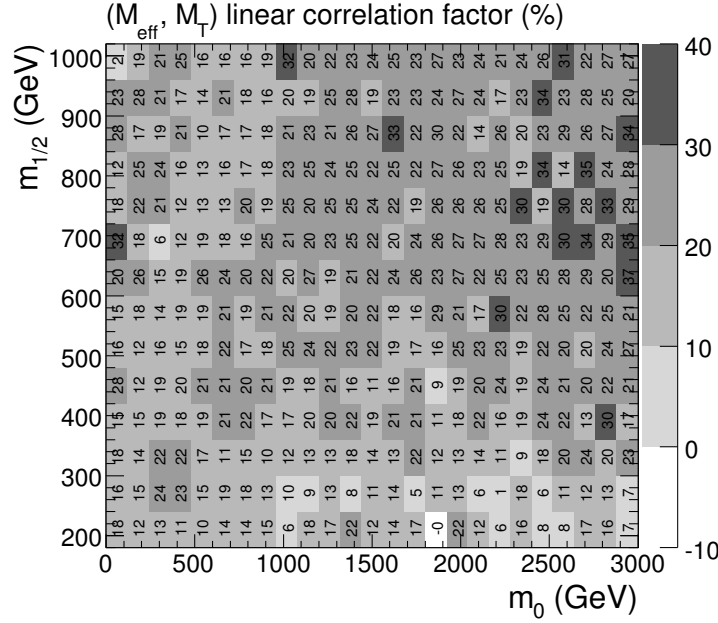


**Figure 11.4:** Linear correlation coefficients (in percent) for the variable pair  $(M_{\text{eff}}, M_T)$  throughout the mSUGRA grid ( $A_0 = 0$ ,  $\tan\beta = 10$ , and  $\mu > 0$ ), after applying all selection cuts (except  $M_T$ ) for the one-lepton search mode (cf. Section 10.2).

The results are shown in Fig. 11.5 where the four plots correspond to the four different  $M_{\text{eff}}$  cuts. For every point on the grid, the colour coding expresses the ratio of estimated to true MC background events. The SM background is overestimated for  $m_{1/2} < 200\text{--}500$  GeV (depending on  $m_0$  and the  $M_{\text{eff}}$  cut) and is underestimated for higher  $m_{1/2}$ . This is because the SUSY cross section drops quickly with increasing  $m_{1/2}$ . For low  $m_{1/2}$  the background is overestimated because of SUSY contamination in the normalisation region. At high  $m_{1/2}$  the contamination is negligible but correlations between  $M_T$  and  $E_T^{\text{miss}}$  lead to an underestimation of the background. The white contour line indicates where the two effects cancel and the estimated background reproduces the true SM background.

The plots for  $M_{\text{eff}} > 0.4, 0.8$ , and 1.2 TeV also show that, for high masses, the background is stronger underestimated at high  $M_{\text{eff}}$ . This is readily understood by the observation that  $M_{\text{eff}}$  is strongly correlated with  $E_T^{\text{miss}}$  ( $M_{\text{eff}} = E_T^{\text{miss}} + \text{lepton and jet } p_T$ ), and because the background is underestimated at high  $E_T^{\text{miss}}$  in the absence of SUSY contamination (left plot of Fig. 11.2). For  $M_{\text{eff}} > 1.6$  TeV this trend is hidden by statistical fluctuations (only 1.4 SM MC events).

The discovery potential with estimated background is evaluated by applying the ‘best-of- $M_{\text{eff}}$ ’ strategy that was employed in the CSC notes: for each mSUGRA point, the SUSY signal significance is calculated for all four  $M_{\text{eff}}$  cuts and the maximal significance is taken. The significance is calculated only if more than five SUSY signal events are found.<sup>6</sup>

The significance  $Z_n$  is shown in Fig. 11.6 in units of standard deviations ( $\sigma$ ). In the left plot, the SM background is estimated with the  $M_T$ -method and the true background from MC is used in

<sup>6</sup>The significance should be corrected for the “look elsewhere effect” although this has not been done here.

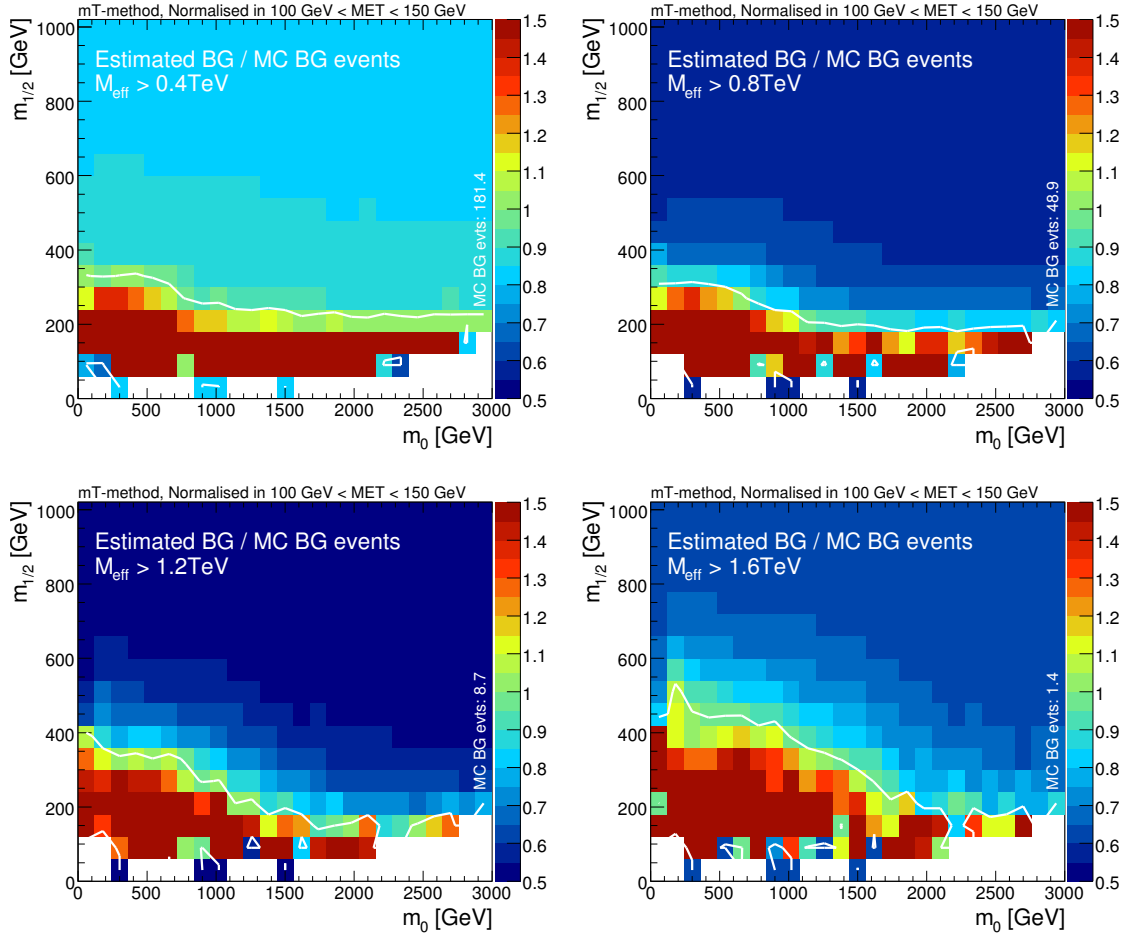


**Figure 11.5:** Ratio of estimated to true (MC) SM background events for different mSUGRA masses  $m_0$  and  $m_{1/2}$ . The white contour line indicates where the estimate agrees with MC. The four plots correspond to four different  $M_{\text{eff}}$  cuts.

the right plot. The white contour line indicates the  $5\sigma$  discovery reach. Also shown are lines of constant gluino and squark masses for which the squark masses are taken as the mass of the lightest squark except for stop and sbottom squarks. In all significance calculations the SM background events were given a systematic uncertainty of 20%.

The discovery reach is larger for the estimated background because the background is underestimated. The application of the ‘best of  $M_{\text{eff}}$ ’ strategy enhances this effect as described above.

#### 11.2.4 The $M_T$ -Method with Decorrelated Variables

In the  $M_T$ -method the number of background events in the signal region (B+D) is estimated by

$$N_{\text{est}}^{\text{SM}} = (N(A) + N(C)) \cdot \frac{N(B)}{N(A)}, \quad (11.1)$$

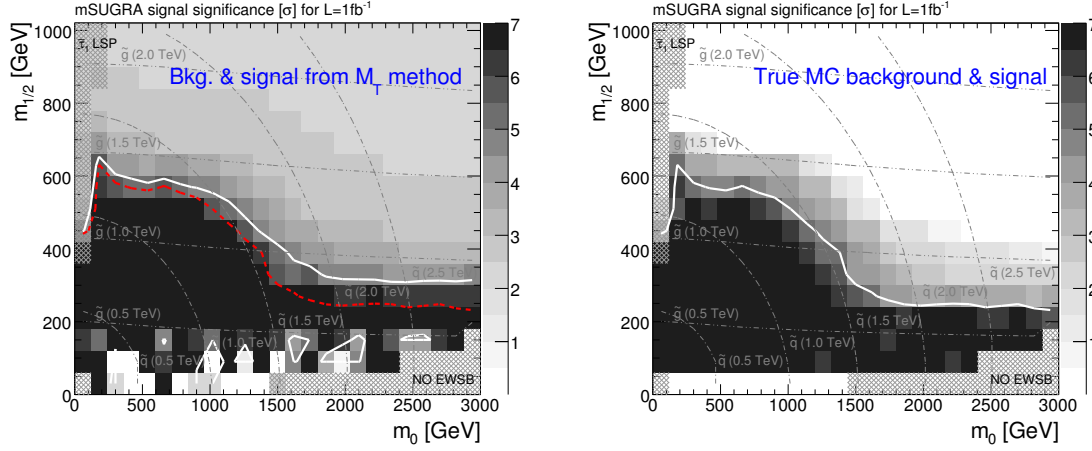


**Figure 11.6:** Significance of SUSY signal in units of standard deviations ( $\sigma$ ). In the left plot, the SM background abundance is estimated using the  $M_T$ -method; in the right plot the true MC background is used (similar to Fig. 10.6). The white contour lines indicate the  $5\sigma$  discovery reach. In the left plot the dotted/red line shows for comparison the  $5\sigma$  reach as obtained from the MC-based method (white line in the right plot). Also shown are lines of constant gluino and squark masses. The hatched regions are theoretically excluded due to lack of electroweak symmetry breaking, tachyon particles, or a charged LSP.

where  $N(i)$  is the number of data events observed in region  $i$ . In the present study,  $N(i) = N_{\text{MC}}^{\text{SM}}(i) + N^{\text{SUSY}}(i)$ . If no SUSY events contribute, one has  $N_{\text{est}}^{\text{SM}} = N_{\text{MC}}^{\text{SM}}(B + D)$ , if

$$\frac{N_{\text{MC}}^{\text{SM}}(A)}{N_{\text{MC}}^{\text{SM}}(C)} = \frac{N_{\text{MC}}^{\text{SM}}(B)}{N_{\text{MC}}^{\text{SM}}(D)}. \quad (11.2)$$

In presence of SUSY,  $N_{\text{est}}^{\text{SM}}$  is still a good estimate if, in addition, the numbers of SUSY events in regions A and B are small. Condition (11.2) is fulfilled if the two variables that are used to define the regions are uncorrelated. It was shown in Section 11.2.2 that this is not the case and that, as a consequence, the background is underestimated, leading to fake SUSY signal.

To improve the background estimation TMVA [193] has been used to decorrelate  $M_{\text{eff}}$  and  $M_T$  for the SM background events. It lead to the transformed variables  $M_{\text{eff}} - 0.107M_T$  and  $M_T - 0.031M_{\text{eff}}$ . Here,  $M_{\text{eff}}$  and  $M_T$  have been chosen because the four standard  $M_{\text{eff}}$  cuts can then be applied in a straightforward manner. If instead one wants to use  $E_T^{\text{miss}}$  and  $M_T$ , all three variables  $E_T^{\text{miss}}$ ,  $M_T$ , and  $M_{\text{eff}}$  must be decorrelated.

In the transformed space of the decorrelated variables, new control, signal and normalisation regions are selected, improving the compliance with condition (11.2) over the original (untransformed) case. Figure 11.7 shows the distribution of SM events in the  $(M_{\text{eff}}, M_T)$  plane. Indicated with dashed lines are the original cuts dividing the plane into the A, B, C, and D regions. The SM distribution in the plane of the decorrelated variables is shown in Fig. 11.8 together with the chosen cuts in the new variables. These cuts are not a transformation of the cuts in the original variables. Only the contact point of the regions A, B, C, D is transformed and new cuts are defined from this point by keeping either one of the transformed variables constant. The edges in the distributions of the untransformed variables introduce correlations at low values of the transformed variables. These correlations are removed with two additional cuts. The new cuts are shown as solid lines in

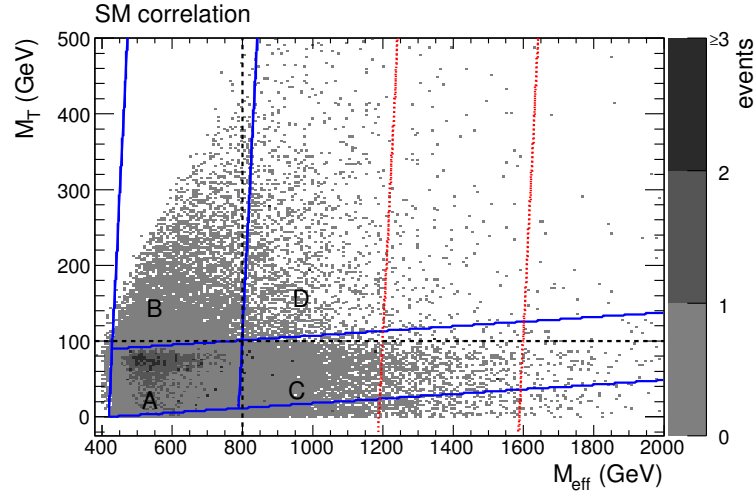


**Figure 11.7:** Distribution of SM events in the  $(M_{\text{eff}}, M_T)$  plane. Also shown are cuts which segment the plane into control, signal, and normalisation regions. The dashed lines are the original cuts; the solid lines are the new cuts found in the plane of the decorrelated variable (Fig. 11.8). The dotted lines indicate the new cuts corresponding to  $M_{\text{eff}} > 1200$  GeV and  $M_{\text{eff}} > 1600$  GeV at fixed  $M_T = 100$  GeV.

the plane of the original variables in Fig. 11.7. The cuts on  $M_{\text{eff}}$  are translated to the new variable  $M_{\text{eff}} - 0.107 M_T$  by transforming the point  $(M_{\text{eff}}^{\text{cut}}, M_T = 100 \text{ GeV})$ . The equivalents of the cuts  $M_{\text{eff}} > 1200$  GeV and  $M_{\text{eff}} > 1600$  GeV are illustrated as dotted lines in Figs. 11.7 and 11.8.

### Results with Decorrelation

The results obtained with the cuts found in the decorrelated plane are shown in Figs. 11.9 and 11.10. Fig. 11.9a shows the signal distribution of estimated and true SM events as a function of the decorrelated variable  $M_{\text{eff}} - 0.107 M_T$  in the absence of SUSY. The description of the true background is greatly improved with respect to the original  $M_T$ -method (left plot of Fig. 11.2). Fig. 11.9b shows the same distribution in presence of SUSY SU3 events. Here the background is overestimated because of significant SUSY contributions in the normalisation region. This leads to a reduced discovery potential. For the standard  $M_T$ -method (right plot of Fig. 11.2) this effect is partially cancelled by the correlations.

The performance of the original and the decorrelated  $M_T$ -method on the mSUGRA  $(m_0, m_{1/2})$  grid is shown in Fig. 11.10 in terms of the difference between estimated and true significance. Positive differences correspond to fake signal and negative differences correspond to reduced discovery potential. The following requirements have been imposed (for both the original and the decorrelated method) to protect the method against insufficient statistics:  $N(B + D) - N_{\text{est}}^{\text{SM}} > 5$  (more than five observed SUSY events in the signal region) and  $N(j) > 9$  for  $j = A, B$  (more than nine measured events in each of the normalisation regions A and B). The decorrelation reduces the fake signal at high masses by two standard deviations. At low masses the SUSY contribution in the normalisation region is large such that the background normalisation is overestimated leading to a reduced sensitivity to new physics. In the original  $M_T$ -method this effect is partly compensated by the SM background correlations.

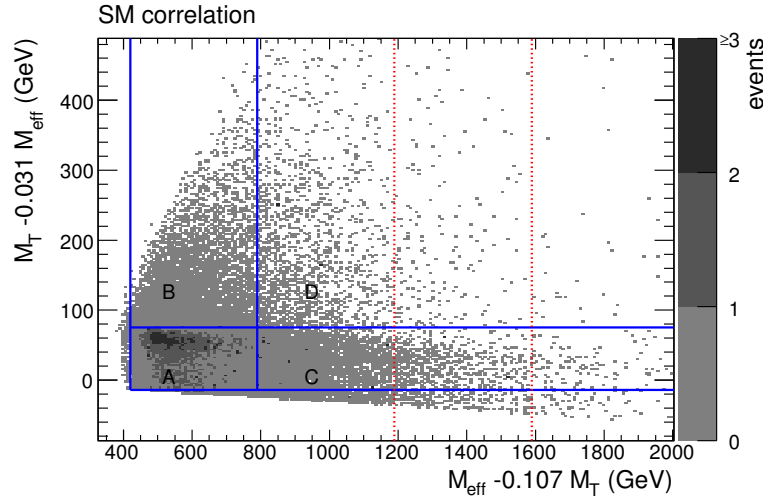


**Figure 11.8:** Distribution of SM events in the decorrelated variable plane. The solid lines indicate the new cuts which segment the plane into control, signal, and normalisation regions. The dotted lines indicate the new cuts corresponding to  $M_{\text{eff}} > 1200$  GeV and  $M_{\text{eff}} > 1600$  GeV at fixed  $M_T = 100$  GeV.

### Systematic Uncertainties Affecting the Decorrelation

The proposed improvement of the  $M_T$ -method relies on an accurate simulation of the correlations between  $M_T$  and  $M_{\text{eff}}$  for SM events. It is sensitive to systematic effects due to uncertainties in the relative cross sections of the contributing SM processes, and due to inaccuracies in the simulation of the detector response.

Varying the SM MC composition by scaling the  $t\bar{t}$  contribution by a factor of 2 and at the same time scaling the  $W + \text{jet}$  events by 0.5 (and vice versa) alters the significance throughout the mSUGRA grid by generally only  $0.3\text{--}0.5\sigma$ , and by up to  $1\sigma$  at most for small masses.

Variations of the jet energy scale by  $\pm 10\%$  and subsequent recalculation of all affected reconstructed quantities, including  $E_T^{\text{miss}}$ ,  $M_T$ , and  $M_{\text{eff}}$ , change the significance by  $0.3\sigma$  on average, by up to  $0.5\sigma$  at small masses.

Worsening the  $E_T^{\text{miss}}$  resolution by a factor of 2 has a negligible effect ( $0.1\sigma$ ) on the signal significance throughout the entire studied mSUGRA grid.

Furthermore, it was studied if the decorrelation transformation could be obtained from data alone, without having to rely on SM MC, by decorrelating the sum of SUSY MC and SM MC events. This approach yields worse results because the correlation of SM events is in general different from that of SUSY events. Even when restricting the determination of the transformation to region A, where only few SUSY events contribute, the performance is worsened significantly by the introduction of  $2\sigma$  fake signal at high masses and up to  $5\sigma$  at small masses.

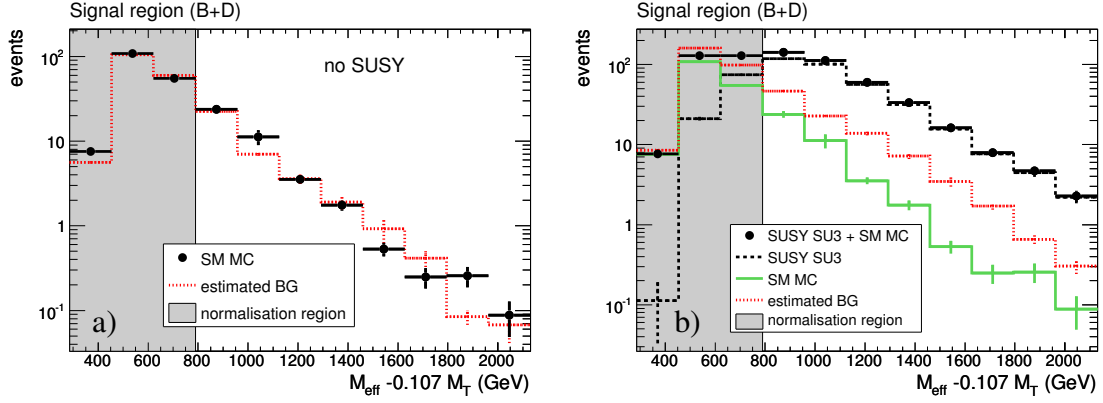


**Figure 11.9:** Event distributions in the signal region (B+D) as a function of the decorrelated variable  $M_{\text{eff}} - 0.107 M_T$  in the absence of SUSY signal (a) and in the case of SU3 (b).

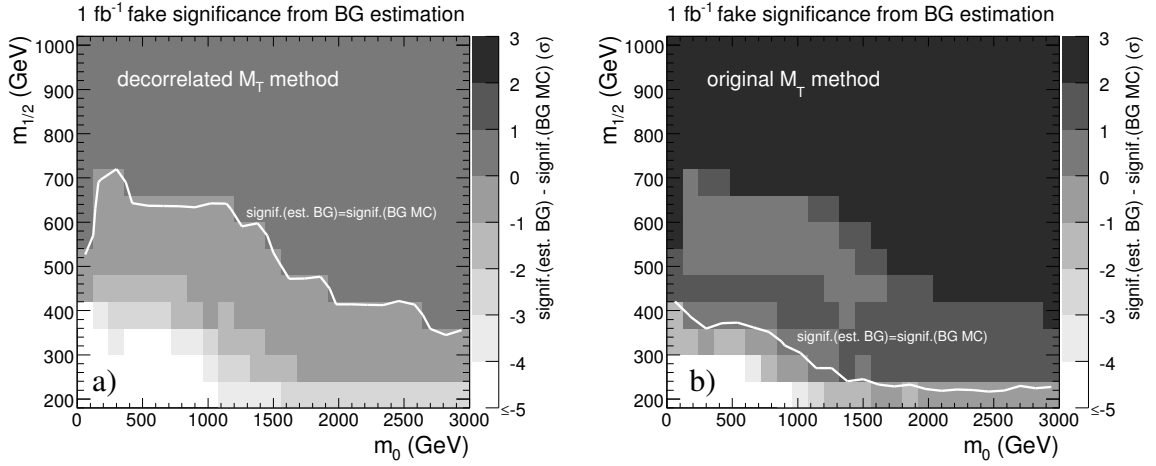


**Figure 11.10:** Difference between the significance from estimated background and the true significance for the decorrelated  $M_T$ -method (a) and the original  $M_T$ -method (b). The white contour lines indicate where the estimated significance corresponds to the true significance.

## Discussion

Decorrelating the variables reduces the fake signal introduced by the  $M_T$  sideband method by up to two standard deviations at high mSUGRA masses  $m_0$  and  $m_{1/2}$ . While the decorrelation remedies to some extent a dangerous shortcoming of the  $M_T$ -method leading to false discovery signal, the problem of SUSY contamination of the normalisation and control regions remains. At low mSUGRA masses, the discovery potential is reduced because SUSY events contribute significantly in the normalisation region, leading to overestimated background. The performance of the decorrelated  $M_T$ -method is only weakly affected by uncertainties in the MC description of SM processes.

### 11.3 The Tiles Method

The *Tiles method* is an approach to derive the number of SM background and beyond-SM signal events from data, using varying degrees of MC dependency. It addresses some of the problems present in the  $M_T$ -method, namely the biases caused by signal contamination in the background region and by variable correlations (cf. Section 11.2). Akin to the  $M_T$ -method, the Tiles method exploits two discriminating variables with good separation power to segment the data into several quadrants (tiles). Figure 11.11 shows the most basic setup of  $2 \times 2$  tiles in the variables  $M_T$  and  $M_{\text{eff}}$ . Generalisation to another set of variables, or to more than two variables is straightforward, but not discussed here.

The Tiles method in its most basic form requires the following assumptions.

1. The relative inclusive fractions of SM background events in each tile are predicted by MC simulation. In the limit of an infinite number of infinitesimal tiles it is required that the full two-dimensional probability density function of the chosen variables is known.
2. The discriminating variables are mutually independent for signal events. (This condition can be alleviated as discussed in Section 11.3.6.)
3. In presence of signal, the distributions of events among the tiles need to be different for signal and background.

Assumptions 1. and 2. can be only approximately realised in an analysis, and violations must be thoroughly studied. The accurateness of assumption 3. is not known *a priori*. In presence of signal it will be empirically ascertained by the Tiles method: if a significant signal yield is found such that the zero-signal hypothesis is excluded, the signal events must be distributed differently from the SM background, otherwise their discrimination from background would not be possible. On the other hand, if no *significant* signal is present, a distribution of signal events among the tiles cannot be determined so that also the signal abundance itself is undetermined. The no-signal case is therefore not detected by a vanishing signal yield (which can be anything), but by a solution of the Tiles method (either analytical, or via a fit) that is approximately independent of the signal yield that is assumed.<sup>7</sup> The no-signal case is effectively equal to the case where signal and background distributions are indistinguishable. Both cases would exhibit anticorrelations close to unity between the signal and background yields returned by the method, whose sum must be equal to the number of observed events.

With the above assumptions, the Tiles method has remarkable features as outlined below.

- The overall SM background event yields for one or several inclusive background components, and the tile-by-tile inclusive beyond-SM event yield are fully derived by the method.
- No assumption is made about the distribution of signal events among the tiles, thereby excluding any prejudice about background domination in particular tiles.

---

<sup>7</sup>In other words, the  $\Delta \ln \mathcal{L}$  difference between free signal yield and signal yield fixed to zero is insignificant (cf. Section 11.3.3).



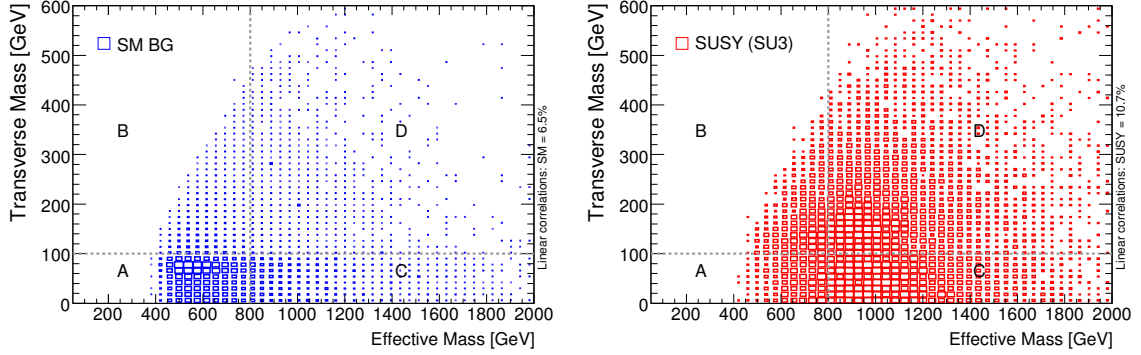


**Figure 11.11:** Transverse mass ( $M_T$ ) versus effective mass ( $M_{\text{eff}}$ ) distributions for simulated SM background events (left) and SUSY SU3 events (right). Indicated by the capital letters are the  $2 \times 2$  tiles determined by the cross borders along  $M_{\text{eff}} = 800$  GeV and  $M_T = 100$  GeV.

- The Tiles method also determines the signal event fraction in each tile, thus providing a signal shape estimate within the chosen granularity of the tiles.
- If the model consists of more than  $2 \times 2$  tiles, the unknowns are overconstrained and the assumptions can be tested via a log-likelihood test statistics.
- If the model consists of more than  $2 \times 2$  tiles, parts of the model assumptions can be relaxed to improve the goodness of the model.

First, the minimum  $2 \times 2$  tiles setup is discussed, before generalising the approach to  $n \times n$  tiles. Various configurations are studied using toy experiments. Systematic uncertainties are evaluated by varying the MC composition and shape. Within this context, we limit ourselves to the one-lepton search channel and, for continuity, choose the event variables  $M_T$  and  $M_{\text{eff}}$  to segment the data into tiles. The Tiles method is applied to preselected data samples including a minimum  $E_T^{\text{miss}}$  requirement (cf. Section 10.2 without the  $M_T$  requirement).

### 11.3.1 $2 \times 2$ Tiles Method

Following Fig. 11.11 we denote the four tiles  $(M_{\text{eff}}^{\text{low}}, M_T^{\text{low}})$ ,  $(M_{\text{eff}}^{\text{low}}, M_T^{\text{high}})$ ,  $(M_{\text{eff}}^{\text{high}}, M_T^{\text{low}})$ , and  $(M_{\text{eff}}^{\text{high}}, M_T^{\text{high}})$  by the letters *A*, *B*, *C*, and *D*, respectively, where the low and high areas are segmented along the values  $M_{\text{eff}} = 800$  GeV and  $M_T = 100$  GeV. The expected total number of events in each tile is given by

$$\begin{aligned} \bar{N}_A &= f_A^{\text{SM}} \bar{N}^{\text{SM}} + f_A^{\text{S}} \bar{N}^{\text{S}}, & \bar{N}_B &= f_B^{\text{SM}} \bar{N}^{\text{SM}} + f_B^{\text{S}} \bar{N}^{\text{S}}, \\ \bar{N}_C &= f_C^{\text{SM}} \bar{N}^{\text{SM}} + f_C^{\text{S}} \bar{N}^{\text{S}}, & \bar{N}_D &= f_D^{\text{SM}} \bar{N}^{\text{SM}} + f_D^{\text{S}} \bar{N}^{\text{S}}, \end{aligned} \quad (11.3)$$

where the first and second terms on the r.h.s. denote the expected SM background and beyond-SM signal contribution, respectively, determined by the expected number of events passing the preselection requirements, and by the corresponding fractions of events in the tiles. Unitarity implies  $\bar{N}_A + \bar{N}_B + \bar{N}_C + \bar{N}_D = \bar{N}^{\text{SM}} + \bar{N}^{\text{S}}$ .

Equation (11.3) forms a system of four independent linear equations which, once confronted with the observations  $\bar{N}_A = N_A, \dots, \bar{N}_D = N_D$ , contains 10 unknowns. Taking the SM tile fractions  $f_A^{\text{SM}}, \dots, f_D^{\text{SM}}$  from MC (condition 1) reduces the number of unknowns to 6. Requiring further that the signal variables be independent (condition 2), one can write

$$\begin{aligned} f_A^{\text{S}} &= (1 - f_{M_{\text{eff}}}^{\text{S}})(1 - f_{M_T}^{\text{S}}), & f_B^{\text{S}} &= (1 - f_{M_{\text{eff}}}^{\text{S}})f_{M_T}^{\text{S}}, \\ f_C^{\text{S}} &= f_{M_{\text{eff}}}^{\text{S}}(1 - f_{M_T}^{\text{S}}), & f_D^{\text{S}} &= f_{M_{\text{eff}}}^{\text{S}}f_{M_T}^{\text{S}}, \end{aligned} \quad (11.4)$$

leaving 4 unknowns that can be eliminated by solving the system (11.3). For example, for the expected number of SM background events one finds<sup>8</sup>

$$\begin{aligned} N^{\text{SM}} &= \frac{1}{2(f_A f_D - f_B f_C)} \left\{ f_D N_A - f_C N_B - f_B N_C + f_A N_D \right. \\ &\quad - \left[ \left( - (f_C N_B) - f_D (N_A + 2N_B) + f_B N_C + f_A N_D + 2f_B N_D \right)^2 \right. \\ &\quad \left. \left. - 4(f_D N_B - f_B N_D) \left( (f_C + f_D)(N_A + N_B) - (f_A + f_B)(N_C + N_D) \right) \right]^{1/2} \right\}, \end{aligned} \quad (11.5)$$

where we used the shorthand notation  $f = f^{\text{SM}}$ . The number of signal events is then given by

$$N^{\text{S}} = N_A + N_B + N_C + N_D - N^{\text{SM}}. \quad (11.6)$$

The relations (11.4) lead to sum rules of which only one is independent (allowing to eliminate two out of three unknown signal tile fractions – the fourth fraction being constrained from unitarity):

$$\frac{f_B^{\text{S}}}{f_A^{\text{S}} + f_B^{\text{S}}} = \frac{f_D^{\text{S}}}{f_C^{\text{S}} + f_D^{\text{S}}}. \quad (11.7)$$

This sum rule can be verified in a model-dependent way using SUSY signal MC, and allows to test whether the conditions that went into Eq. (11.5) are fulfilled. For example, for SU3 events the difference between the left and right-hand sides of Eq. (11.7) is  $-0.026 \pm 0.006$  (the error is due to MC statistics), while for the corresponding events with correlations removed<sup>9</sup> one finds

<sup>8</sup>The signal tile fractions are given by

$$\begin{aligned} f_{M_{\text{eff}}}^{\text{S}} &= 1 + \frac{1}{2(f_A + f_B)(N_C + N_D) - 2(f_C + f_D)(N_A + N_B)} \left( f_D N_A + f_C(2N_A + N_B) - f_B N_C \right. \\ &\quad - f_A(2N_C + N_D) + \left[ f_D^2 N_A^2 + f_C^2 N_B^2 + (f_B N_C - f_A N_D)^2 - 2f_D(f_C N_A N_B + f_B N_A N_C \right. \\ &\quad \left. \left. - 2f_A N_B N_C + f_A N_A N_D) - 2f_C(f_B N_B N_C - 2f_B N_A N_D + f_A N_B N_D) \right]^{1/2} \right), \\ f_{M_T}^{\text{S}} &= 1 + \frac{1}{2(f_A + f_C)(N_B + N_D) - 2(f_B + f_D)(N_A + N_C)} \left( f_D N_A - f_C N_B + f_B(2N_A + N_C) \right. \\ &\quad - f_A(2N_B + N_D) + \left[ f_D^2 N_A^2 + f_C^2 N_B^2 + (f_B N_C - f_A N_D)^2 - 2f_D(f_C N_A N_B + f_B N_A N_C \right. \\ &\quad \left. \left. - 2f_A N_B N_C + f_A N_A N_D) - 2f_C(f_B N_B N_C - 2f_B N_A N_D + f_A N_B N_D) \right]^{1/2} \right). \end{aligned}$$

<sup>9</sup>Turning off the correlation between variables is obtained by event mixing (without replacement), i.e.,  $M_T$  is taken from event  $n$  and  $M_{\text{eff}}$  from event  $n + 1$ .

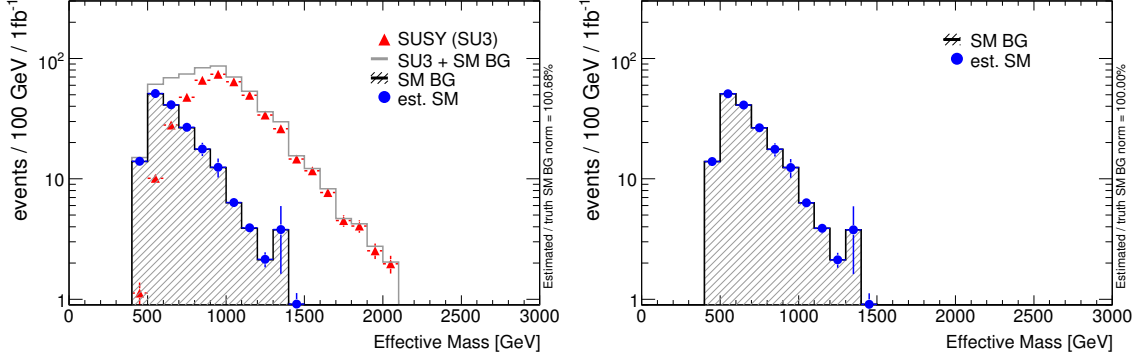


**Figure 11.12:** Illustration of the 2×2 Tiles method to estimate the SM background yield in presence of SUSY signal corresponding to the benchmark points SU3 (left), and with no SUSY signal (right). The hatched area is the true SM background, and the full/blue dots represent the estimate. Note that the SM tile fractions have been obtained with the same MC samples as used for the distributions, so that statistical fluctuations in the estimated number of SM background events are suppressed. Any remaining difference between true and estimated numbers of SM events is due to the neglect of signal correlations in Eq. (11.5).

$0.005 \pm 0.006$ , as expected. The presence of signal correlations violates the sum rule (and hence the underlying assumption for the Tiles method) at the 3% level for this particular SUSY point.<sup>10</sup>

In case of sufficient event counts in the four tiles, we may estimate the statistical error of Eqs. (11.5) and (11.6) by assuming square-root errors for the number of observed events in each tile, and ignoring uncertainties in the SM background tile fractions.<sup>11</sup> The square-root errors are propagated to the estimated  $N^Y$  ( $Y = \text{SM}, \text{S}$ ) and, by virtue of the statistical independence of the tiles, the respective deviations can be added in quadrature

$$\sigma_{N^Y}^2 \simeq \sum_{X \in (A, B, C, D)} \left[ N^Y - N^Y \left( N_X \rightarrow N_X \pm \sqrt{N_X} \right) \right]^2. \quad (11.8)$$

<sup>10</sup>Replacing  $M_{\text{eff}}$  by the variable  $\text{HT2} = \sum_{i=2}^4 p_T^{\text{jet}i} + p_T^{\text{lep}}$  (where the hardest jet is excluded from the sum) in the tiles plane has insignificant effect on the signal correlation, while exhibiting reduced separation power  $\langle S^2 \rangle$  (defined in two dimensions by  $\langle S^2 \rangle = (1/2) \iint dx dy (\hat{S}(x, y) - \hat{B}(x, y))^2 / (\hat{S}(x, y) + \hat{B}(x, y))$ , where  $x, y$  are the variables of the tiles plane, and  $\hat{S}/\hat{B}(x, y)$  are the signal/background PDFs). A more promising definition seems to be the variable  $\text{HT2}' = \sum_{i=2}^4 p_T^{\text{jet}i}$ , with significantly reduced correlation with  $M_T$ , and better separation power in conjunction with  $M_T$  than HT2 :

Tile plane	SU1		SU2		SU3		SU4		SU6		SU8	
	$\rho$	$\langle S^2 \rangle$	$\rho$	$\langle S^2 \rangle$	$\rho$	$\langle S^2 \rangle$	$\rho$	$\langle S^2 \rangle$	$\rho$	$\langle S^2 \rangle$	$\rho$	$\langle S^2 \rangle$
$(M_T, M_{\text{eff}})$	0.11	0.64	0.15	0.69	0.11	0.54	0.22	0.21	0.12	0.72	0.13	0.73
$(M_T, \text{HT2})$	0.15	0.49	0.17	0.58	0.14	0.41	0.20	0.18	0.19	0.58	0.15	0.58
$(M_T, \text{HT2}')$	0.01	0.53	0.04	0.62	-0.03	0.45	0.04	0.18	0.01	0.61	-0.03	0.60
$(E_T^{\text{miss}}, \text{HT2})$	0.45	0.63	0.57	0.55	0.47	0.50	0.48	0.10	0.48	0.65	0.44	0.65
$(E_T^{\text{miss}}, \text{HT2}')$	0.47	0.63	0.56	0.55	0.48	0.51	0.47	0.10	0.48	0.65	0.44	0.64

An assessment of the pros and cons of these or other alternative tile planes requires a full statistical and systematic analysis, which is beyond the scope of this chapter.

<sup>11</sup>As discussed later, the full error analysis – not using the approximation (11.8) – includes penalty functions to include the uncertainties in the predictions of the SM tile fractions.

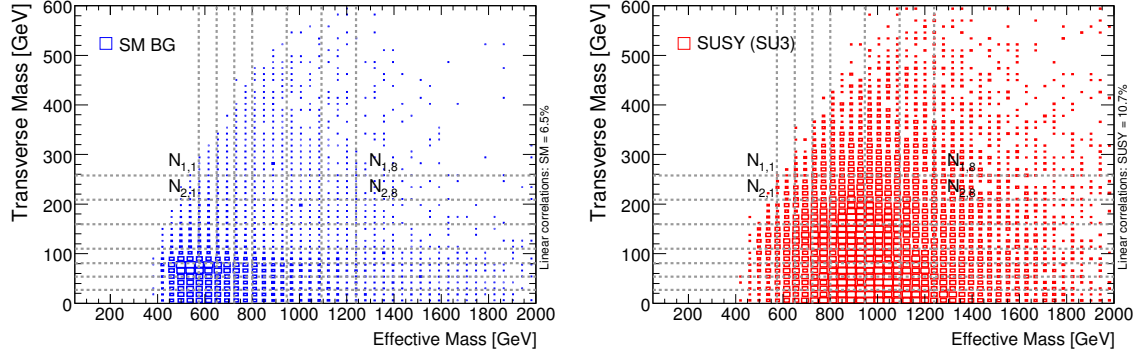


**Figure 11.13:** Demonstration of  $8 \times 8$  tiles setup. Transverse mass ( $M_T$ ) versus effective mass ( $M_{\text{eff}}$ ) distributions for simulated SM background events (left) and SUSY SU3 events (right). Each tile is denoted by a tuple  $(i, j)$ , e.g., the number of observed events in the top left tile is called  $N_{1,1}$ .

As an exercise, we apply the  $2 \times 2$  Tiles method to determine the total (inclusive) number of SM background events in presence of SUSY SU3 signal and in absence of SUSY. We use the variables  $M_T$  and  $M_{\text{eff}}$  and the aforementioned tile boundaries at 100 GeV and 800 GeV, respectively. With a true number of 1868 SM events and 768 SU3 events, we estimate from Eqs. (11.5) and (11.8)  $1881 \pm 61$  SM events. Without SUSY,  $1868 \pm 60$  SM events are estimated. Note that the SM tile fractions used in this estimate have been obtained with the same MC samples hence suppressing statistical fluctuations. The deviation from the truth observed in the SU3 case is thus due to the neglect of signal correlations (see Section 11.3.5).

Figure 11.12 shows the true (hatched area) and estimated (full/blue dots) number of SM background events versus  $M_{\text{eff}}$  in presence of SU3 (left plot) and no (right plot) signal. In both plots, red triangles represent the SUSY signal and the grey histograms give the sum of all events. Recall that only the overall normalisation is estimated from the data, while the shape of the SM distribution is taken from MC such that shape agreement is achieved by construction here. As expected, signal contamination and SM background correlations have no effect on the results from the Tiles method.

### 11.3.2 $n \times n$ Tiles Method

We can generalise the  $2 \times 2$  Tiles method, with a single boundary in each dimension, to  $n \times n$  tiles with  $(n - 1)$  boundaries per variable. Again all  $n^2$  tiles are statistically independent hence forming a system of independent linear equations.<sup>12</sup> Figure 11.13 shows a configuration of  $8 \times 8$  tiles, and also introduces the notation used for the tiles.

In the generalised  $n \times n$  mode, the division lines are set by the following procedure. The initial boundaries at  $M_{\text{eff}} = 800$  GeV and  $M_T = 100$  GeV are kept and  $n/2$  tiles are arranged below and above these lines (if  $n$  is odd,  $(n - 1)/2$  go below and  $(n + 1)/2$  above). The very first and very last tile boundary is chosen (in both variables) such that the corresponding tiles contain a minimum of  $1/n$  of the total events in the projected variable. In this step, SM background and

<sup>12</sup>Further generalisation may introduce  $m \times n$  tiles, which does however not significantly alter the proposal, so that it is not considered any further here.

SU3 signal events are used to populate the variable space. The variable space between the fixed initial boundaries and the first (last) boundaries is equidistantly distributed among the remaining tiles.

Ignoring signal correlations, the method provides  $n^2$  equations determining  $2n$  unknowns:  $2(n-1)$  unknowns for the projected signal fractions and 2 unknowns for the overall signal and SM background event yields. The problem is hence overconstrained for  $n > 2$ , and a unique solution can be found only via minimisation of an estimator which allows to optimise the agreement between model and observed data, thereby adjusting the unknown model parameters. We hence define the following extended negative log-likelihood estimator

$$-\ln\mathcal{L} = \sum_{i,j=1}^n (\bar{N}_{ij} - N_{ij} \ln \bar{N}_{ij}) , \quad (11.9)$$

where  $N_{ij}$  denotes the number of observed events in tile  $(i, j)$ , and where  $\bar{N}_{ij} = f_{ij}^{\text{SM}} \bar{N}^{\text{SM}} + f_{M_T, i}^{\text{S}} f_{M_{\text{eff}}, j}^{\text{S}} \bar{N}^{\text{S}}$  is the corresponding expected number of events in tile  $(i, j)$  ( $f_{ij}^{\text{SM}}$  is the shorthand notation of  $f_{M_T, i; M_{\text{eff}}, j}^{\text{SM}}$ ). Owing to the unitarity condition  $\sum_{i,j} f_{ij}^{\text{SM}, \text{S}} = 1$ , their sum obeys  $\bar{N} = \sum_{i,j} \bar{N}_{ij} = \bar{N}^{\text{SM}} + \bar{N}^{\text{S}}$ . Minimising  $-\ln\mathcal{L}$  is equivalent to solving an unbinned maximum-likelihood (ML) fit, where the background and signal probability density functions (PDF) are one two-dimensional and two one-dimensional binned histograms, respectively, with the bin boundaries equal to the tile divisions. Both fit versions have been implemented for this analysis, namely, a TMinuit minimisation of Eq. (11.9), and an unbinned ML fit using RooFit [195], both giving identical results. Minimising Eq. (11.9) for  $2 \times 2$  tiles reproduces the results from the analytical solution, with a minimum estimator value  $\ln\mathcal{L}_{\text{min}}$  at its theoretical minimum because there is no degree of freedom.

The generalisation to  $n \times n$  ( $n > 2$ ) tiles has advantages and drawbacks.

- It improves the information content of the fit and thus should in most cases (except for very small sample sizes) lead to a more precise determination of the overall SM and signal yields. There exists however an optimum choice: a too large number of tiles dilutes the information and increases the statistical errors on the fit parameters.
- It probes the signal shape in the two-dimensional variable space.
- The use of many tiles increases the dependence on a correct description of the two-dimensional background shape.
- The  $\ln\mathcal{L}_{\text{min}}$  value returned by the fit can be used to estimate the goodness of the fit by comparison with toy MC experiments.
- Bad goodness-of-fit values may be improved by relaxing the model assumptions, e.g., by adding free parameters correcting deficiencies in the prediction of the background PDFs, or by including a limited amount of signal correlations that are determined by the fit (see below).

### 11.3.3 Signal Significance

The significance of a signal observed with the Tiles method for any number of tiles  $n \geq 2$  can be derived in a straightforward manner using the  $\ln\mathcal{L}$  estimator defined in Eq. (11.9). Two fits are performed for this purpose, one with free varying  $N^S$ , and another where  $N^S = 0$  is fixed (null hypothesis). The difference ( $\Delta\ln\mathcal{L}$ ) between the  $\ln\mathcal{L}$  values found in these fits is compared to the expectation from toy experiments generated for the null hypothesis. One hence obtains the p-value to observe a given difference in presence of SM events only (cf. Section 10.4). Note that this method is practical only up to a significance level of 4–5 sigma due to the large amount of toys needed to go higher.

If all tiles contain a sufficiently large number of events, one could be tempted to compute the p-value of  $\Delta\ln\mathcal{L}$  via  $\text{Prob}(-2\Delta\ln\mathcal{L}, 1)$ . This fails however because the number of degrees of freedom for  $\ln\mathcal{L}$  is not the same in the signal and no-signal fits as the signal tile fractions are not measurable in the background only fit, so that the number of degrees of freedom of  $\Delta\ln\mathcal{L}$  is larger than one.<sup>13</sup>

### 11.3.4 Uncertainties in the SM Tile Fractions

Systematic errors such as the jet energy scale (JES),  $E_T^{\text{miss}}$  resolution etc. generically change the distributions in the two variables. Hence, each systematic error yields a new set of SM background fractions for the tiles  $f_{ij}^{\text{SM}}$ . One can use the new tile fractions, repeat the fit and use the difference to the nominal fit as a measure of the systematic uncertainty. Several systematic errors can thus be added in quadrature to the extent that they are uncorrelated.

Alternatively, the systematic uncertainties can be introduced in the likelihood fit itself in the form of penalty functions. We assume that the systematic effects can be described by Gaussian likelihoods and widths given by  $f_{ij}^{\text{SM}} - f_{ij}^{\text{SM}}$ . As all tile fractions belonging to one systematic error are fully correlated among each other, we allow them to vary in a coherent way

$$f_{ij}^{\text{SM}} \rightarrow f_{ij}^{\text{SM}} + \sum_{k=1}^m \left( f_{ij}^{(k)\text{SM}} - f_{ij}^{\text{SM}} \right) s_k, \quad (11.10)$$

where  $m$  is the number of considered systematic errors,  $s_k$  denotes a free scale parameter that parametrises the effect of systematic error  $k$ , and  $f_{ij}^{(k)\text{SM}}$  are the SM background fractions for tile  $(i, j)$  obtained including the systematic error  $k$ .

The different systematic errors are assumed to be uncorrelated and thus the fit parameters  $s_k$  are constrained by adding the penalty

$$\frac{1}{2} \sum_{k=1}^m (s_k^2) \quad (11.11)$$

to the  $-\ln\mathcal{L}$  given in Eq. (11.9).

---

<sup>13</sup>In the simplest  $2 \times 2$  tiles configuration, one may want to use the number of background events estimated in the most sensitive tile  $D$ ,  $f_D^{\text{SM}} N^{\text{SM}}$ , and compute the probability to observe  $N_D$  events under null hypothesis according to the method discussed in Section 10.4. However, since  $N_D$  and  $N^{\text{SM}}$  are not independent, a careful evaluation requires the generation of toy MC experiments.

**Table 11.1:** Summary of results obtained for various SUSY benchmark models (see Section 8.3.1 for a definition of the models) using the tile configurations  $2 \times 2$ ,  $8 \times 8$ , and  $12 \times 12$ . For all SUx points, the statistical error ( $\sigma^S$ ) and bias ( $\Delta N^S$ ) relative to the true number of signal events are given. Mean and  $\sigma$  are obtained from Gaussian fits to the toy distributions (cf. Fig. 11.14).

	SU1	SU2	SU3	SU4	SU6	SU8
Correlation coefficient ( $M_{\text{eff}}$ , $M_T$ )	12%	21%	11%	29%	16%	17%
$N_{\text{MC}}^S$ [events]	423	75	768	6260	251	214
$2 \times 2$ tiles: $\sigma_{\text{stat}}^S / N_{\text{MC}}^S$	11%	64%	7%	4%	15%	17%
$2 \times 2$ tiles: $\Delta N^S / N_{\text{MC}}^S$	-1%	3%	-1%	-28%	-2%	-2%
$8 \times 8$ tiles: $\sigma_{\text{stat}}^S / N_{\text{MC}}^S$	8%	60%	6%	3%	12%	13%
$8 \times 8$ tiles: $\Delta N^S / N_{\text{MC}}^S$	-6%	-19%	-7%	-32%	-9%	-8%
$12 \times 12$ tiles: $\sigma_{\text{stat}}^S / N_{\text{MC}}^S$	9%	98%	6%	3%	15%	17%
$12 \times 12$ tiles: $\Delta N^S / N_{\text{MC}}^S$	-7%	-14%	-7%	-30%	-14%	-12%

### 11.3.5 Validation With Toy Experiments

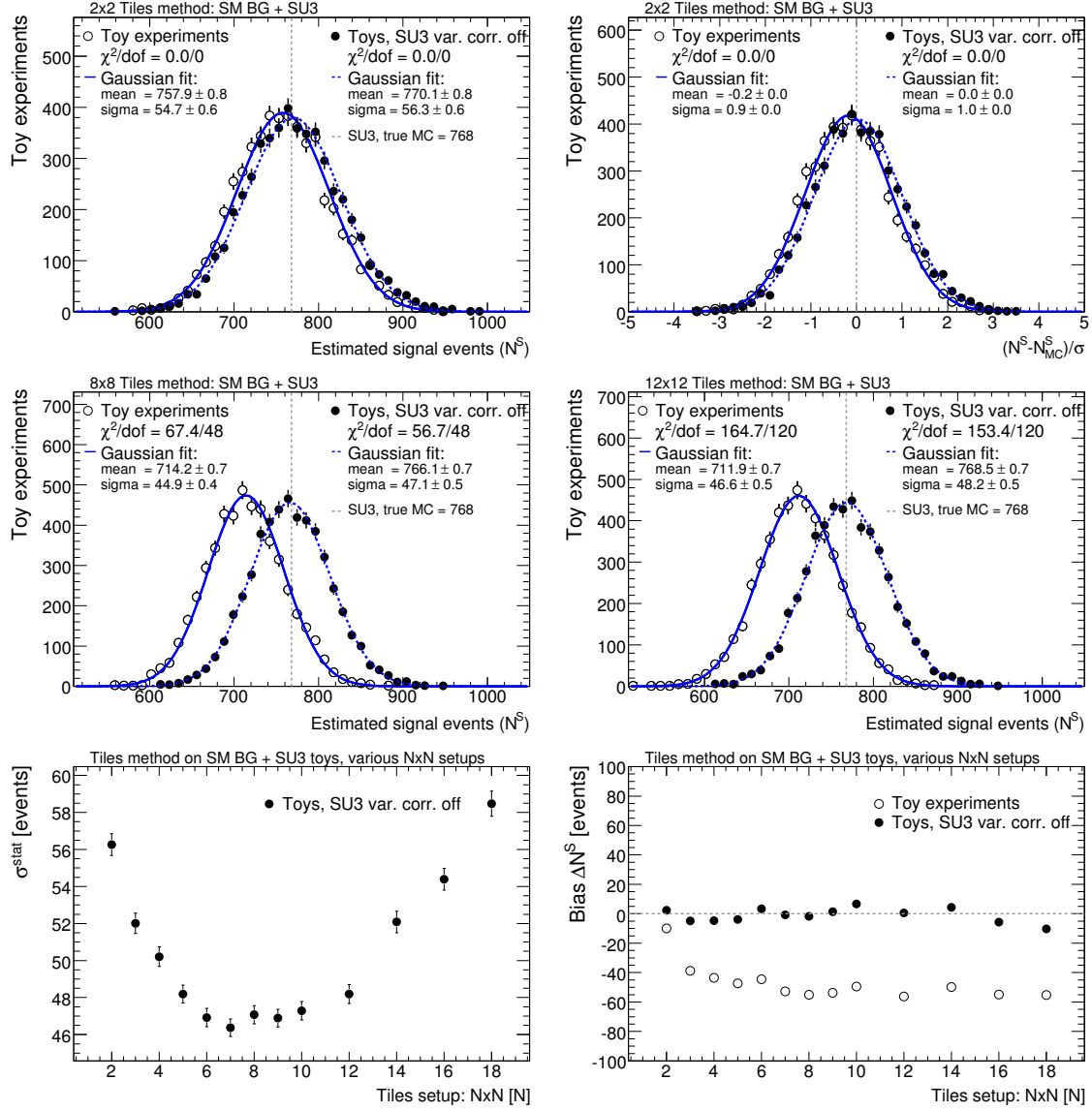
Toy experiments are used to study the statistical and systematic properties of the Tiles method. First, the preselected  $M_T$  and  $M_{\text{eff}}$  data samples – after the one-lepton event selection (cf. Section 10.2 without the  $M_T$  requirement) – are fitted using a two-dimensional, unbinned kernel estimation method implemented in RooFit [195]. This yields PDFs for the combined SM background and the SUSY benchmark points, which fully model the variable correlations, and which are used to generate toy MC samples corresponding each to an integrated luminosity of  $L = 1 \text{ fb}^{-1}$ . The Tiles method is applied on each toy experiment, where for the SM tile fractions the true values are used. Systematic effects are not considered here. They will be discussed in detail in the following sections.

Figure 11.14 shows fit results for various tile configurations obtained with 5000 toy experiments, using SU3 as signal model (each toy MC experiment consists on average of 1868 SM background and 768 SU3 events). Bias in the fitted signal yields are observed, which are caused by signal correlations being ignored in the likelihood model. Test fits where the signal correlations are turned off via event mixing accurately return the true values on average.

The lower left-hand plot in Fig. 11.14 gives the error on the fitted signal yield versus the tile configuration. As expected an increased number of tiles first improves the statistical precision of the fit owing to the refined shape information exploited by fit. However, for a too large number of tiles, the precision deteriorates because large statistical fluctuations within the tiles obstruct an accurate determination of the tile fractions.

Table 11.1 lists the statistical errors and biases due to signal correlations for all SUSY benchmark points for a setup of  $2 \times 2$ ,  $8 \times 8$ , and  $12 \times 12$  tiles. Signal correlations are further discussed in Section 11.3.6, where Fig. 11.15 shows toy experiment results for the SUSY benchmark point SU4.





**Figure 11.14:** In 5000 toy experiments, each representing  $1 \text{ fb}^{-1}$  of SM background and SU3 signal, the signal yield is fitted using the Tiles method for different tile configurations:  $2 \times 2$  (top left, top right shows the corresponding pull distributions),  $8 \times 8$  (middle left), and  $12 \times 12$  (middle right). Open/black circles and the solid/blue lines represent results from the toy experiment and Gaussian fits, respectively. Filled/black circles and the dashed/blue lines represent the same, but for experiments with variable correlations turned off for signal. The mean  $\chi^2$  provides a measure for the goodness-of-fit. The bottom two plots show the evolution of the Gaussian  $\sigma$  (left) and absolute bias w.r.t. true MC (right) versus the tile configuration.



### 11.3.6 Signal Correlations

Signal correlations do not need to be neglected. With more than  $2 \times 2$  tiles the fit has degrees of freedom allowing one to introduce additional parameters in the signal description. One may use these to alleviate condition 2 (the independence of Tiles variables for signal) by dynamically determining the linear signal correlation as part of the fit, and correcting the tile-by-tile signal estimate for it.

The procedure is as follows. At each fit step we have a background estimate, which we use to do a background subtraction in each tile. From this binned, background subtracted distribution we calculate the correlation coefficient,  $\rho$ , plus the mean and RMS of both  $M_T$  and  $M_{\text{eff}}$ .<sup>14</sup> The correlation is used to calculate a correction factor  $w_{ij} = f_{ij}(\rho)/f_{ij}(0)$  for each tile. As an approximation,  $f(\rho)$  is chosen to be a correlated two-dimensional Gaussian with the means and widths estimated, akin to in Eq. (11.12), from the signal distribution among the tiles, and evaluated at the centre of each tile. The signal estimate used to calculate the likelihood is then  $cw_{ij}f_{M_T,i}^S f_{M_{\text{eff}},j}^S \bar{N}^S$ , where  $c$  is set to ensure the unitarity  $\sum_{i,j} cw_{ij}f_{M_T,i}^S f_{M_{\text{eff}},j}^S = 1$ .

Tests have shown that the proposed correlation correction properly removes biases in the fitted signal and background yields for academic toy examples with two linearly correlated and Gaussian distributed signal variables. Due to the additional correlations between parameters the errors on the fitted SM and signal yields are increased. For the (more realistic) case of nonlinear correlations, and non-Gaussian variables, the correction  $w_{ij}$  is incomplete. Nevertheless, it improves the accuracy of the signal yield over the uncorrected result.

Figure 11.15 shows results from toy experiments for the most difficult SUSY benchmark model SU4, obtained using the Tiles method without and with the corrective treatment for signal correlations. The observed bias of 32% (30%) for  $8 \times 8$  ( $12 \times 12$ ) tiles is reduced to 22% (20%) with the correction, albeit not removed. The calculated correlation of  $\rho = 0.12$  undershoots the true value (0.15).

### 11.3.7 Splitting SM Contributions

Generalisation to  $n \geq 3$  tile configurations allows to extend the number of fitted event yields and to thus determine individual background components. For example, a  $3 \times 3$  tiles fit provides  $9 - 6 = 3$  degrees of freedom such that up to 4 background contributions may be determined. It

<sup>14</sup>The covariance at tile granularity level reads

$$C_{x_a, x_b} = \frac{1}{\bar{N}^S} \sum_{i,j=1}^n \bar{N}_{ij}^S x_{a,i} x_{b,j} - \left( \frac{1}{\bar{N}^S} \sum_{i,j=1}^n \bar{N}_{ij}^S x_{a,i} \right) \cdot (x_{a,i} \leftrightarrow x_{b,j}), \quad (11.12)$$

where  $a, b = 1, 2$ , and  $x_1 = M_T$ ,  $x_2 = M_{\text{eff}}$ . The additional subscript  $i$  in  $x_{a,i}$  denotes the value of  $x_a$  corresponding to the projection of all tiles  $ij$  upon the  $x_a$  axis. It is taken to be the tile centre. The total number of expected signal events ( $\bar{N}^S$ ), and their distribution among the tiles ( $\bar{N}_{ij}^S$ ) occurring in Eq. (11.12) are obtained via  $\bar{N}^S = N - N^{\text{SM}}$  and  $\bar{N}_{ij}^S = N_{ij} - f_{ij}^{\text{SM}} N^{\text{SM}}$ , respectively. The correlation coefficient  $\rho(M_T, M_{\text{eff}})$  is derived from Eq. (11.12) in the usual manner, and must be updated at every fit step as it depends on the fit parameters.

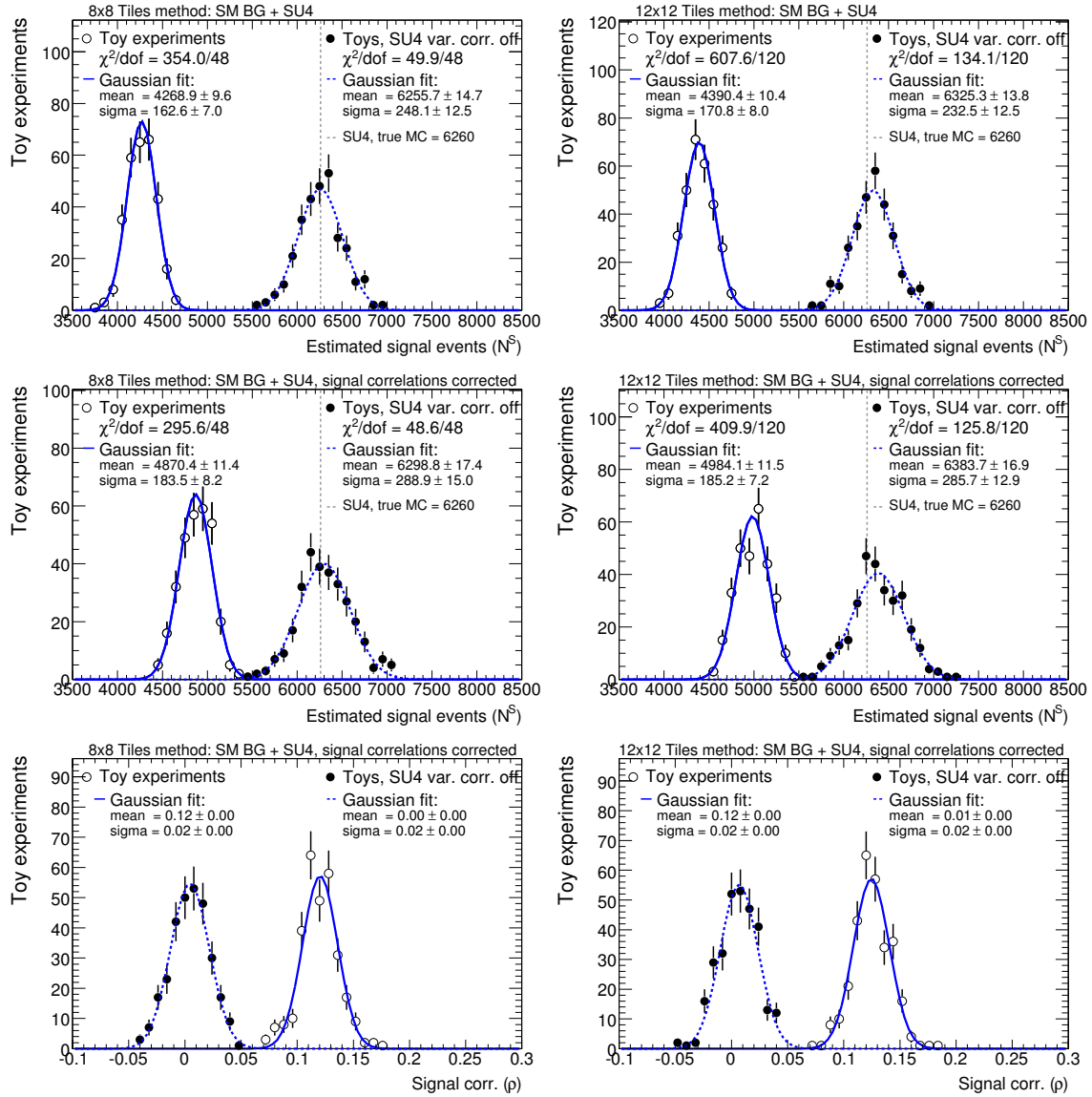


**Figure 11.15:** Fitted number of SU4 signal events in 300 toy experiments, each corresponding to  $L = 1 \text{ fb}^{-1}$ , for  $8 \times 8$  (left) and  $12 \times 12$  tiles (right). Top row: signal correlations are ignored in fits (nominal Tile method), middle row: signal correlations are corrected in fits; bottom row: values of calculated signal correlation (true value:  $\rho = 0.15$ ).

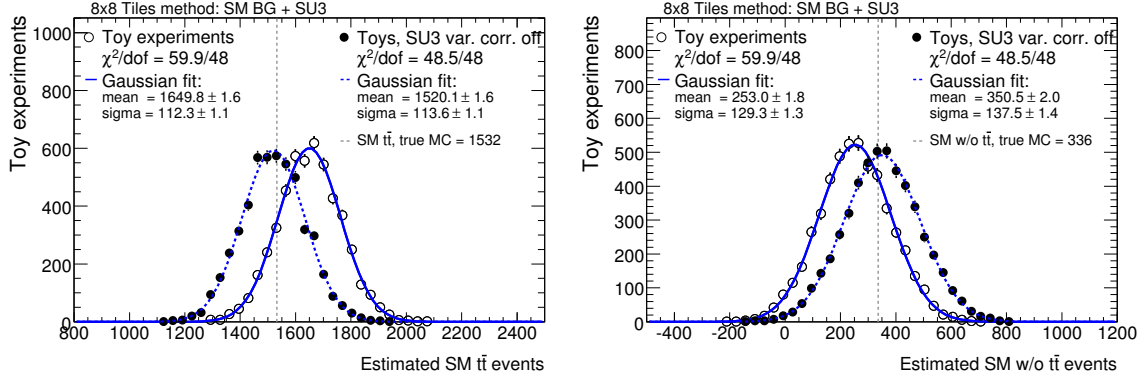


**Figure 11.16:** Fitted number of SM  $t\bar{t}$  events (left) and remaining SM events (right) for the  $8 \times 8$  tile configuration in 5000 toy experiments, each corresponding to an integrated luminosity of  $L = 1 \text{ fb}^{-1}$ .

allows to improve the finesse of the background estimate, which reduces systematic errors.<sup>15</sup> For  $K$  individual SM background contributions, the expected number of events for tile  $ij$  is given by

$$\bar{N}_{ij} = \sum_{k=1}^K f_{ij,k}^{\text{SM}} \bar{N}_k^{\text{SM}} + f_{M_T,i}^S f_{M_{\text{eff}},j}^S \bar{N}^S, \quad (11.13)$$

where  $\sum_{ij} f_{ij,k}^{\text{SM}} = 1$  for all  $k = 1, \dots, K$ , and where all  $f_{ij,k}^{\text{SM}}$  are taken from MC simulation. Only background components with sufficiently different shapes (and hence different fractions  $f_{ij,k}^{\text{SM}}$ ) can be constrained by the fit (cf. Fig. 10.3 in Section 10.2). Shape similarity will lead to anticorrelations between the fitted  $\bar{N}_k^{\text{SM}}$ .

As an example, we have decomposed the inclusive SM background contribution into  $t\bar{t}$  (1532 events) and the remaining part (316  $W$ +jets, 15  $Z$ +jets, 5 dibosons events) in the fit. Figure 11.16 shows the two fitted SM yields obtained in 5000 toy experiments using  $8 \times 8$  tiles. When signal correlations are absent, the true SM event yields are correctly reproduced by the fit. They exhibit a strong anticorrelation (on average we find a coefficient of  $-0.9$ ), and the statistical error on the signal yield increases with respect to the nominal fit from 45 to 53 events. With signal correlations, the fit results are biased.

We point out that splitting the SM background into more than one components, with their yields determined by the fit, is equivalent to the treatment for “uncertainties in the tile fractions” discussed in Section 11.3.4 when using Eq. (11.10) without adding the penalty (11.11). In most cases prior information on the expected yields from MC simulation is available and should be used via adding a penalty function to the fit.

### 11.3.8 Systematic Studies

The Tiles method depends on the SM MC fractions for each tile and we cannot expect the simulation to fully reproduce the data. We have thus studied the effects of systematic uncertainties in

<sup>15</sup>More precisely: parameters that suffer from systematic uncertainties are determined from data; hence systematic errors are transformed into statistical ones.

the SM fractions on the fitted signal event yield and tile fractions, to assess the sensitivity of the method to its inherent assumptions.

Where necessary, systematic variations have been propagated throughout the entire analysis chain to properly include all effects. This applies to the uncertainties in the JES and  $E_T^{\text{miss}}$  resolution. Elsewhere, we simply rescale cross sections of certain processes. Examples here are uncertainties in the relative background composition and in the lepton ID and jet reconstruction efficiencies. Common to all systematic effects is that they affect the distributions of the discriminating variables and thereby modify the SM tile fractions.

Various systematic effects are discussed in the following, the deviations in the SM tile fractions of which are explicitly given for the simplest  $2 \times 2$  tiles configuration. Moreover, systematic effects on the signal yields are quantified for different tile configurations for the SUSY benchmark point SU3.

*Note that the central  $M_T$  tile boundary has been moved from 100 GeV to 110 GeV in this study, that is, away from the sharp edge in its distribution, which drastically reduces the sensitivity to systematic effects in that variable.*

### Jet Energy Scale (JES)

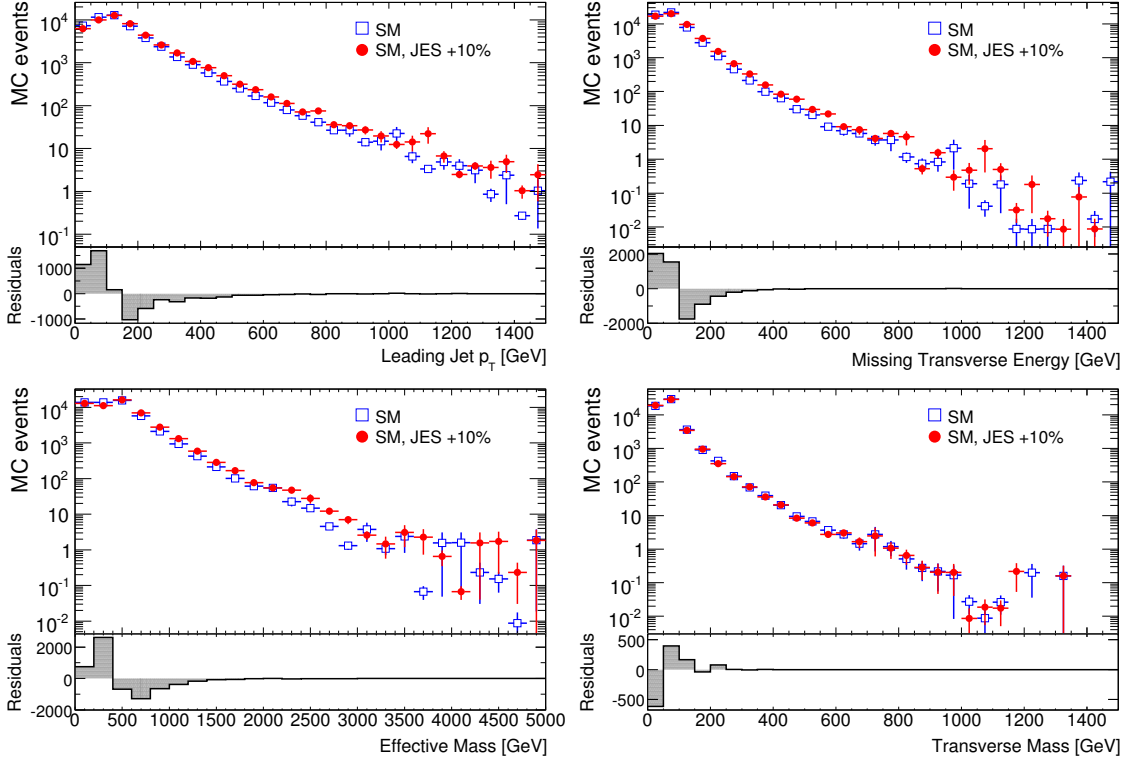
Assuming a 10% systematic uncertainty in the JES, the energies and momenta of all jets are correspondingly scaled up and down. The rescaling is subsequently propagated into the transverse components of the  $E_T^{\text{miss}}$  vector. All derived variables including  $E_T^{\text{miss}}$ ,  $M_{\text{eff}}$ , and  $M_T$  and the corresponding tile fractions are then recomputed.

Figure 11.17 shows the SM MC distributions for the hardest jet  $p_T$  (top left),  $E_T^{\text{miss}}$  (top right),  $M_{\text{eff}}$  (bottom left), and  $M_T$  (bottom right), before and after applying a +10% JES shift. Table 11.2 gives the corresponding impact on the SM tile fractions for the  $2 \times 2$  tiles configuration. The systematic effects on the fitted number of signal events ( $N^S$ ) for SU3 versus the tile configuration are shown in Fig. 11.18 (left plot). A bias of order 30 (60) events is found for  $2 \times 2$  ( $8 \times 8$ ) tiles, corresponding to a systematic error of 4% (8%).

### $E_T^{\text{miss}}$ Resolution

The effect of a systematic uncertainty in the  $E_T^{\text{miss}}$  resolution is studied by independently smearing the transverse components of the  $E_T^{\text{miss}}$  vector via addition of a Gaussian noise term of width in units of the  $E_T^{\text{miss}}$  resolution,  $0.64 \cdot \sum E_T [\text{GeV}]$ , cf. top left of Fig. 11.19. We have studied the impact of a degradation of the nominal  $E_T^{\text{miss}}$  resolution by 20% and 100%.

Figure 11.19 shows the results of a 100% smearing on  $E_T^{\text{miss}}$  (top right),  $M_{\text{eff}}$  (bottom left), and  $M_T$  (bottom right). The independent smearing of the transverse components strongly affects  $M_T$ . Table 11.2 gives the corresponding systematic errors in the SM tile fractions for the  $2 \times 2$  tiles configuration. The systematic errors in  $N^S$  for SU3 are given in the right plot of Fig. 11.18 versus the tiles setup. A bias of 10 (4) events for  $2 \times 2$  ( $8 \times 8$ ) tiles is observed for a 100% smearing, corresponding to a systematic error of 1% (< 1%).



**Figure 11.17:** SM background distributions before (open/blue squares) and after a JES rescaling by +10% (filled/red circles) for the hardest jet  $p_T$  (top left),  $E_T^{\text{miss}}$  (top right),  $M_{\text{eff}}$  (bottom left), and  $M_T$  (bottom right). All distributions are before applying the one-lepton selection requirements.

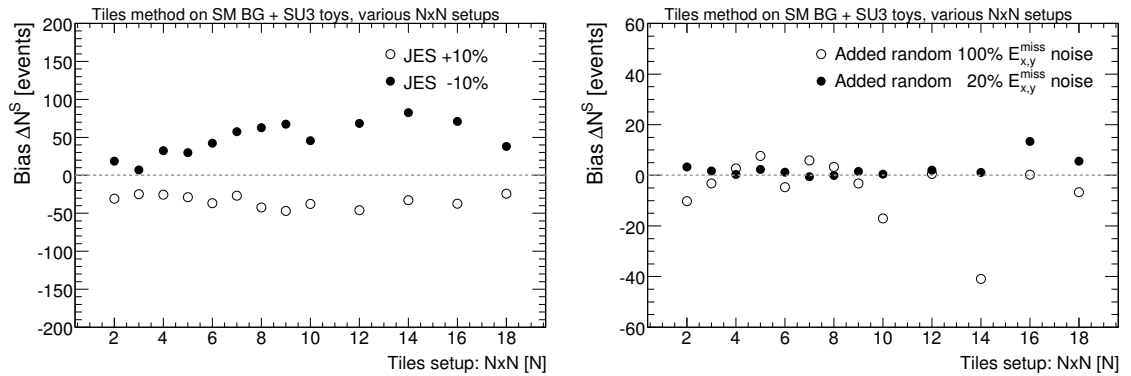


**Figure 11.18:** Biases in the fitted signal yields introduced by the JES (left plot) and  $E_{x,y}^{\text{miss}}$  systematic effects (right plot) as a function of the tile configuration. All results are obtained with the Tiles method running on SU3 signal and SM background.

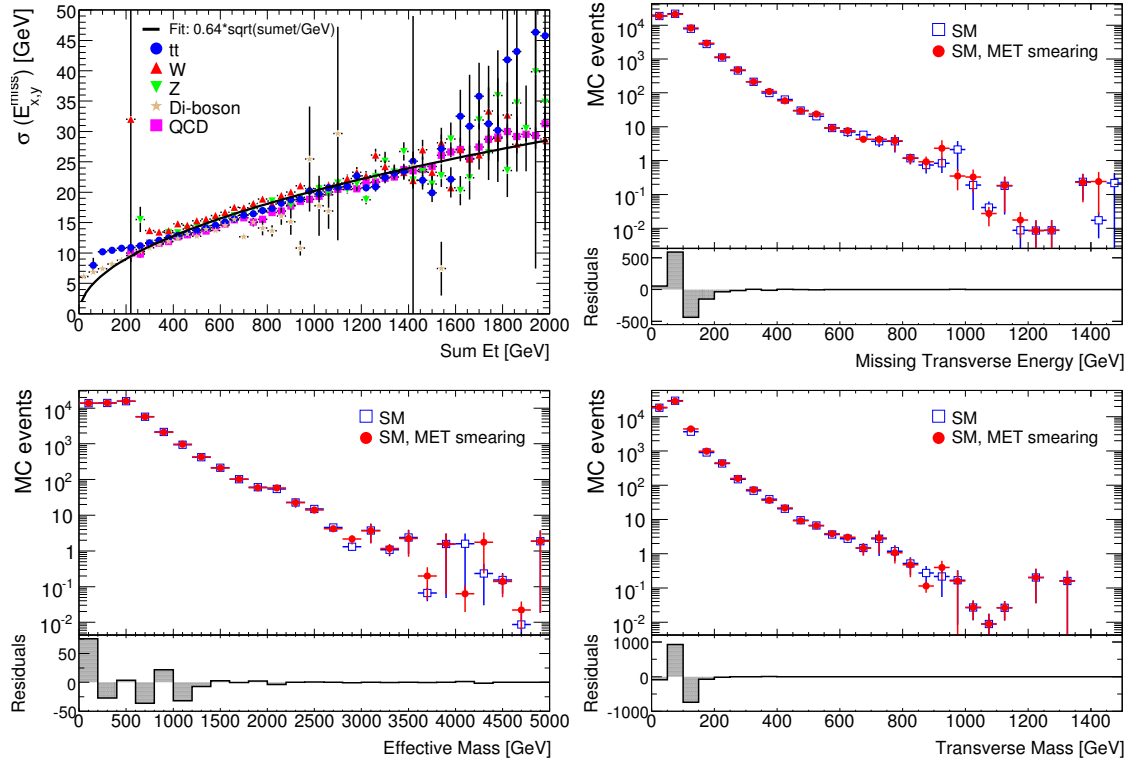


**Figure 11.19:** Top left: MC resolution of the transverse components of the  $E_T^{\text{miss}}$  vector. Other plots: SM background before (open blue squares) and after  $E_T^{\text{miss}}$  smearing (filled red circles) in the variables:  $E_T^{\text{miss}}$  (top right),  $M_{\text{eff}}$  (bottom left), and  $M_T$  (bottom right). All plots are before the one-lepton SUSY event selection.

## SM Cross Sections

The SM background comprises several processes whose cross sections have uncertainties. Since the tile fractions differ in general among these processes, the cross section uncertainties create systematic effects.<sup>16</sup> Here only the dominant  $t\bar{t}$  (92%) and  $W$ +jets (7%) contributions are considered, to each of which is assigned a 50% cross section uncertainty, that are conservatively scaled in opposite directions. (The shapes of the  $M_T$  and  $M_{\text{eff}}$  distributions for  $t\bar{t}$  and  $W$ +jets are shown in Fig. 11.21.)

The resulting systematic errors in the  $2 \times 2$  tile fractions are given in Table 11.2. The systematic errors on  $N^S$  for SU3 versus the tile configuration are shown in Fig. 11.20 (left plot). We find a bias of the order of 90 events (12%) for both  $2 \times 2$  and  $8 \times 8$  configurations.

## Top Sample Composition

The composition of the  $t\bar{t}$  background is affected by systematic uncertainties in the simulation of the lepton identification and jet reconstruction efficiencies. It is studied in an approximative

<sup>16</sup>Unless the SM background components are fitted separately, as described in Section 11.3.7.

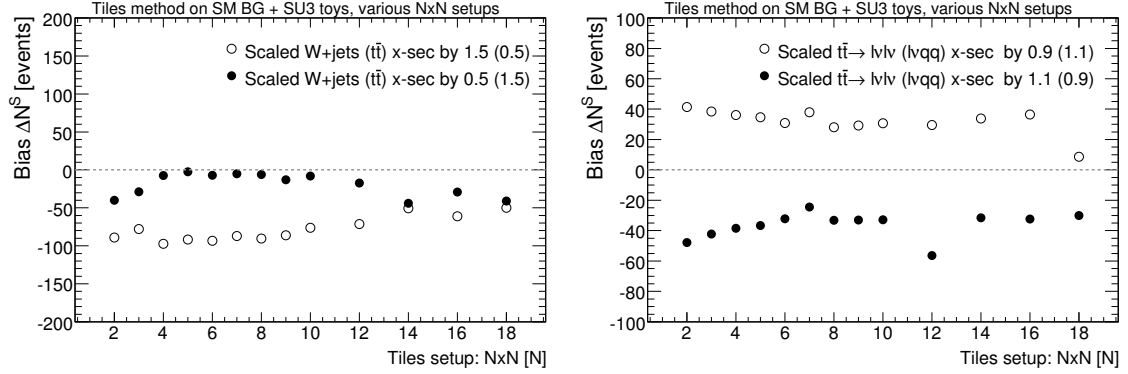


**Figure 11.20:** Biases in the fitted signal yields introduced by the systematic uncertainties in the  $t\bar{t}$ ,  $W$ +jets cross sections (left) and the  $t\bar{t}$  background composition (right). All results are obtained with the Tiles method running on SU3 signal and SM background.

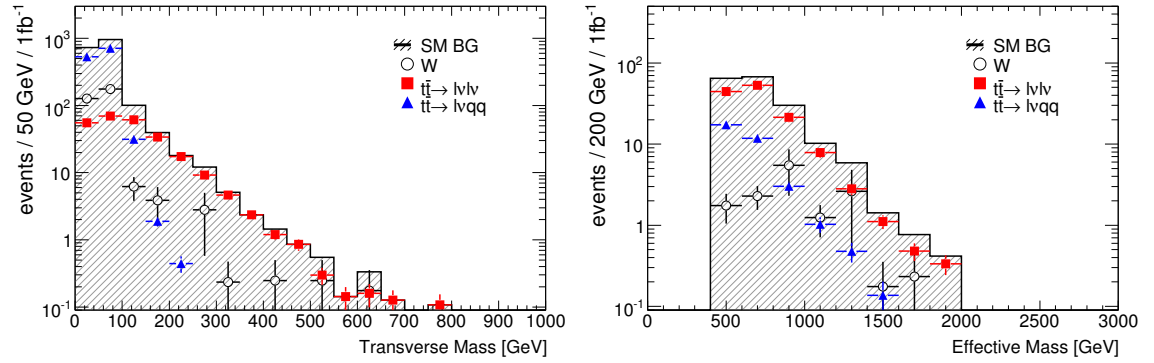


**Figure 11.21:** Distributions of  $M_{\text{eff}}$  (left) and  $M_T$  (right) for SM background decomposed into  $W$ +jets (open/black circles),  $tt \rightarrow l\nu l\nu$  (filled/red squares), and  $tt \rightarrow l\nu qq$  (filled/blue triangles) contributions. Both plots are after the one-lepton event selection (the  $M_T$  requirement has been dropped in the  $M_T$  plot).

way, by varying the cross sections of the  $tt \rightarrow l\nu l\nu$  and  $tt \rightarrow l\nu qq$  processes in analogy to Section 11.3.8, because these two processes exhibit different shapes – in particular for  $M_T$  (see Fig. 11.21). We have applied relative cross section shifts of  $\pm 10\%$  to both processes in opposite directions.

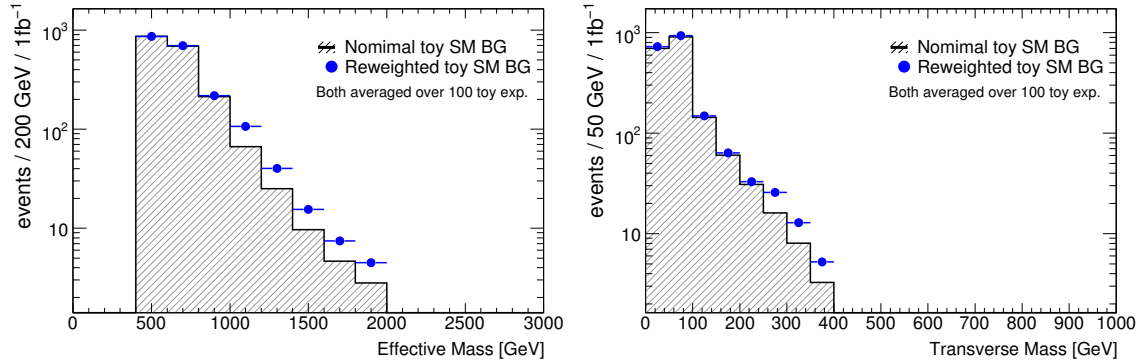
Table 11.2 quotes the resulting systematic errors in the SM tile fractions for  $2 \times 2$  tiles. The systematic errors on  $N^S$  for SU3 versus the tile configuration is shown in the right plot of Fig. 11.20. A bias of 48 (33) events is observed for  $2 \times 2$  ( $8 \times 8$ ) tiles, corresponding to a systematic error of 6% (4%).

### Monte Carlo Generator

Uncertainties in the generation of the physics processes have been studied by replacing Alpgen  $t\bar{t}$  samples by MC@NLO ones. However, since the Alpgen sample is an efficiency corrected fast simulation of the ATLAS detector whereas the MC@NLO events passed through full GEANT

**Table 11.2:** Systematic errors in the SM tile fractions ( $2 \times 2$  tiles configuration).

	$f_A^{\text{SM}}$	$f_B^{\text{SM}}$	$f_C^{\text{SM}}$	$f_D^{\text{SM}}$
No systematics	0.750	0.056	0.172	0.022
JES +10%	-0.010	-0.004	+0.016	-0.001
JES -10%	+0.008	+0.007	-0.018	+0.003
$E_{x,y}^{\text{miss}}$ smeared by 100%	0.000	+0.006	-0.007	+0.001
$E_{x,y}^{\text{miss}}$ smeared by 20%	+0.001	0.000	-0.001	0.000
Scaled $\sigma_{t\bar{t}}$ ( $\sigma_W$ ) by factor 1.5 (0.5)	+0.014	+0.006	-0.020	0.000
Scaled $\sigma_{t\bar{t}}$ ( $\sigma_W$ ) by factor 0.5 (1.5)	-0.027	-0.011	+0.039	-0.001
Scaled $\sigma_{t\bar{t} \rightarrow \ell\nu\ell\nu}$ ( $\sigma_{t\bar{t} \rightarrow \ell\nu q\bar{q}}$ ) by 1.1 (0.9)	-0.011	+0.007	+0.001	+0.003
Scaled $\sigma_{t\bar{t} \rightarrow \ell\nu\ell\nu}$ ( $\sigma_{t\bar{t} \rightarrow \ell\nu q\bar{q}}$ ) by 0.9 (1.1)	+0.010	-0.007	-0.001	-0.003
MC generator	+0.022	-0.012	-0.010	0.000

**Figure 11.22:** Distributions of  $M_{\text{eff}}$  (left) and  $M_T$  (right) before (histogram) and after (dots) reweighting the SM events that fall into a tail region defined by  $M_{\text{eff}} > 1000$  GeV or  $M_T > 250$  GeV. All events have passed the one-lepton event selection (without the  $M_T$  cut).

simulation, the direct comparison of the two includes MC more effects than the generator difference alone. In addition, the MC statistics available for the MC@NLO sample (around  $1 \text{ fb}^{-1}$ ) is much smaller than the one for the Alpgen samples. The results of the study are therefore to be seen as an upper limit of the systematic effects that can be expected from the physics simulation. A bias of 95 (85) events is observed for  $2 \times 2$  ( $8 \times 8$ ) tiles, corresponding to a systematic error of 12% (11%).

### Uncertainties in the Tails of the SM Distributions

We have case-studied the effects of systematic uncertainties in the tails of the simulated SM distributions, where the tail region is defined by  $M_{\text{eff}} > 1000$  GeV and or  $M_T > 250$  GeV, corresponding to approximately 131 expected SM events (about 7% of the total selected SM sample) at given luminosity. The SM events falling into this region are reweighted by an (arbitrary) factor



of 1.6, to quantify the impact of the tails on the fitted signal yield. This study does *not* aim at a realistic estimate of the corresponding systematic error, which is impossible at present. Figure 11.22 shows the  $M_{\text{eff}}$  (left) and  $M_T$  (right) distributions of the SM events before and after the reweighting.

For SM-only toy MC experiments we find average fake signal significances of  $2.9\sigma$  ( $2\times 2$  tiles) and  $3.4\sigma$  ( $8\times 8$ ). These values are obtained from the mean  $\Delta\ln\mathcal{L}$  value found in these toy experiments, compared to the expected  $\Delta\ln\mathcal{L}$  distribution for toy MC experiments not containing signal (cf. Section 11.3.3). In toys that include SU3 signal, the signal yields are shifted by respectively  $+13.6\%$  ( $2\times 2$ ) and  $+13.9\%$  ( $8\times 8$ ), *exceeding* the increased number of SM events due to the tail systematic by one third. Because the signal can only model uncorrelated data and the additional SM events in the tail region exhibit an intrinsic correlation due to the shape of the tail region, extra SM events in the non-tail region are absorbed by the signal component of the fit.

### Summary of Systematic Uncertainties

Summaries of the sources of systematic errors considered (not including here the MC generator systematic whose evaluation was incomplete) and their effects on the fitted signal yields for the various SUSY benchmark models (cf. Section 8.3.1) and for the tile configurations  $2\times 2$  and  $8\times 8$  are given in Table 11.3. For the total systematic error per configuration we have assumed no correlations between the sources. Separately listed (and not included in the total systematic errors) are the biases due to signal correlations, which are model dependent. It is noticeable that for all SUSY models studied signal correlations lead to an underestimate of the signal yield.

The total error on the signal yield, including statistical fluctuations and systematic effects, can be computed by adding in quadrature all errors, or by repeating the fit with the systematic uncertainties added in form of penalty functions (cf. Section 11.3.4). We have compared both methods for the SUSY benchmark model SU3 and the  $2\times 2$  tiles configuration. We find errors of 120 events for the quadratic sum and 105 events for the penalty approach. A decrease in error is expected since the fit will to some extent constrain the scale parameters for important systematic errors. The fitted values for  $N^S$  remain constant in average ( $751.36 \rightarrow 751.43$ ) in the fit with penalty functions.

It is noteworthy that the dominant systematic uncertainties arising from the SM cross sections and the relative top contributions can be included in the fit by splitting the SM components (cf. Section 11.3.7). However, such a fit requires more than  $2\times 2$  tiles.

### 11.3.9 Stability Test

The stability of the Tiles method can be studied by varying the  $M_{\text{eff}}$  and  $M_T$  tile boundaries. Apart from statistical fluctuations, the results obtained should be independent of the positions of the boundaries. Inaccurate SM tile fractions and presence of signal correlations (if not corrected) break this invariance. We have studied variations in the  $M_{\text{eff}}$  tile boundary for  $2\times 2$  tiles with a single inclusive background component and without correcting for signal correlations. Figure 11.23 shows the number of estimated SM background events in presence of SU3 (top plot) and SU4 signal (bottom plots) versus the  $M_{\text{eff}}$  tile boundary. While SU3 exhibits a fairly uniform distribution

**Table 11.3:** Relative systematic errors on the signal yield for  $2 \times 2$  (top) and  $8 \times 8$  (bottom) tiles and various SUSY benchmark models. Also given are the statistical errors and the biases due to signal correlations obtained from toy experiments.

$2 \times 2$	SU1	SU2	SU3	SU4	SU6	SU8
$N_{MC}^S$ [events]	423	75	768	6260	251	214
Statistical error	11%	64%	7%	4%	15%	17%
JES	6%	48%	4%	8%	11%	13%
$E_T^{\text{miss}}$ resolution	3%	21%	1%	2%	4%	4%
SM cross sections	18%	52%	12%	26%	33%	42%
$t\bar{t}$ sample comp.	11%	55%	6%	2%	16%	18%
Total systematics error	22%	92%	14%	27%	38%	48%
Total error	25%	112%	16%	28%	41%	51%
Bias due to signal corr	1%	3%	1%	28%	2%	2%
$8 \times 8$	SU1	SU2	SU3	SU4	SU6	SU8
$N_{MC}^S$ [events]	423	75	768	6260	251	214
Statistical error	8%	61%	6%	3%	12%	13%
JES	8%	22%	8%	8%	10%	17%
$E_T^{\text{miss}}$ resolution	3%	16%	< 1%	2%	8%	2%
SM cross sections	15%	45%	12%	5%	18%	23%
$t\bar{t}$ sample comp.	9%	34%	4%	3%	12%	5%
Total systematics error	19%	63%	15%	10%	25%	29%
Total error	21%	87%	16%	11%	28%	32%
Bias due to signal corr	6%	21%	7%	32%	9%	8%

reproducing the true result, significant deviations occur for SU4 (bottom left plot). After removing signal correlations a fair stability of the result is recovered (bottom right plot).

## 11.4 Conclusions

This chapter discusses a new method for a data-driven determination of the Standard Model (SM) background in the inclusive one-lepton SUSY search analysis. A popular background-determination approach, the so called  $M_T$  Method, has been reviewed. It is shown to suffer from two critical problems: signal contamination in the background region, and correlations between the variables - both of which can lead to an incorrect determination of the background. The method is improved by decorrelating the SM background events using input from Monte Carlo (MC) simulation, which significantly reduces the biases introduced by the correlations. However, effects from residual, non-linear correlations remain, and also the problem due to the neglected

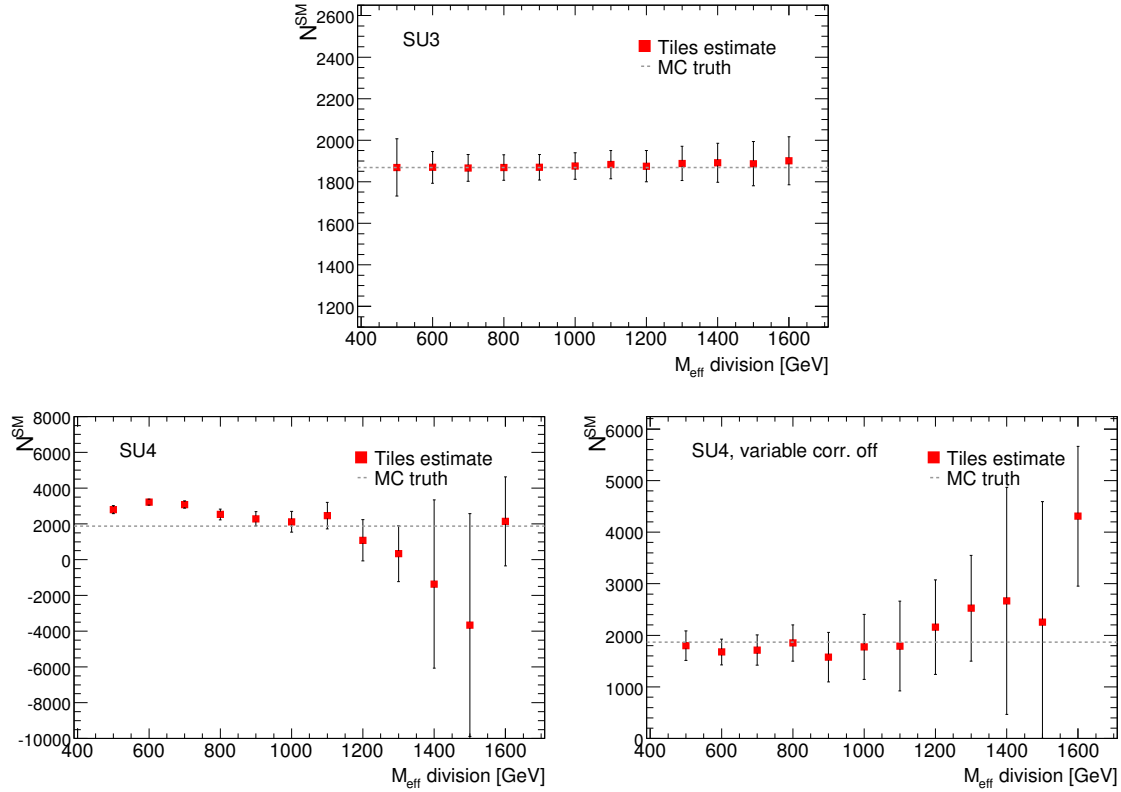


**Figure 11.23:** Stability test for the Tiles method using  $2 \times 2$  tiles. The estimated number of SM background events (filled/red squares) is plotted versus the  $M_{\text{eff}}$  tile boundary for SU3 (top) and SU4 signal (bottom plots). The true value is indicated by the dotted line. The signal correlations are turned off for SU4 in the bottom right plot.

signal contamination in the background (control) region is unsolved.

A novel approach, denoted *Tiles Method*, has been developed. It takes into account correlations between the discriminating variables for the SM background (while assuming them to vanish for SUSY signal), and omits assumptions about the distribution of signal events, in particular no regions with signal or background dominance are assumed. It does however require input on the relative fractions of background events in the tiles from simulation (but not their overall normalisation).

In the Tiles Method the data are split up into  $n \times n$  tiles in the two-dimensional space spanned by the discriminating variables ( $M_T$ ,  $M_{\text{eff}}$  for the studies here). For  $2 \times 2$  tiles there is an exact solution for the number of signal events, for  $n > 2$  the system is over-constrained and a maximum-likelihood fit is performed. In this case the quality of the fit provides information about how well the data is described by the model (for example large signal correlations would show up as a poor fit quality – as the model ignores signal correlation). Different tile configurations have been studied, and  $8 \times 8$  was found to give the best statistical power for an analysis of  $1 \text{ fb}^{-1}$  of LHC data, and a typical mSUGRA model point.

This chapter targets mostly the presentation of the new method. Some of the details (number of tiles, best binning, inclusion of signal correlations, etc.) need to be studied further. Since the method relies on input from MC simulation, systematic effects that arise from differences between the simulation and the data have been case studied. The study gives a qualitative impression of how sensitive the method is to these effects, whereas a full quantitative study requires calibration of simulation with real data via control samples. Only after these studies have been done (once data are available) will we be able to define the best tile configuration to be used in the analysis.

The studies show that presence of correlations among the signal variables biases the fitted event yields obtained from the Tiles method – and this bias worsens with increasing tile granularity. An extension of the Tiles method has been investigated, allowing linear signal correlations in the fit to be absorbed – which can partly correct the bias observed for some SUSY benchmark scenarios.

For  $n > 2$  the Tiles method also allows to separately determine different SM background components using or not prior information on the relative cross sections from MC simulation. It reduces the systematic error from uncertainties on the background composition, which is currently the dominant systematic effect.

The Tiles method is a promising way to determine the background in a one-lepton SUSY analysis. It solves many of the problems seen with the  $M_T$  method – at the expense of an increased simulation dependence when more than  $2 \times 2$  Tiles are used to increase the statistical yield. Initial studies indicate that the systematics associated with this simulation dependence are under control – but further studies on this will be needed.

---

# Chapter 12

## Outlook

With the imminent start of LHC data-taking, the operational phase of ATLAS is about to commence. Thereby the focus of the collaboration will move to understanding the detector and its performance, and finally to data analysis. This last chapter briefly discusses the data strategy and the necessary steps towards early physics. It is important, however, to point out that many details of the forthcoming studies depend on the data itself as well as the detector performance, i.e. we will to some extent be guided by the physics and the machine-specific needs.

Section 12.1 describes the expected start-up of the LHC. In Section 12.2 the strategy for an early SUSY analysis is discussed. Finally, Section 12.3 briefly compares the potential of the LHC and a next-generation linear collider in terms of SUSY measurements.

### 12.1 Expected LHC start-up

In a nutshell, the ATLAS start-up roadmap, from a SUSY point of view, can be summarised as follows.

1. *Before data-taking*: utilise test-beam, and cosmic-ray data for pre-alignment, calibration, and detector/trigger timing; exercise the data processing.
2.  $\mathcal{O}(10 \text{ pb}^{-1})$ : initial detector and trigger synchronisation (timing) and commissioning, calibration and alignment, material mapping, etc.; search for extraordinary new physics signatures.
3.  $\mathcal{O}(100 \text{ pb}^{-1})$ : accurate in-situ detector alignment and physics performance calibration, understand SUSY backgrounds from Standard Model (SM) processes, perform initial SUSY searches.
4.  $\mathcal{O}(1 \text{ fb}^{-1})$ : explore SUSY and other new resonances up to masses of  $\mathcal{O}(1 \text{ TeV})$ .

As can be seen, this roadmap essentially depends on the performance of the LHC. The ATLAS experiment has conducted extensive cosmic ray runs in autumn 2008 (cf. Section 3.3 for a brief

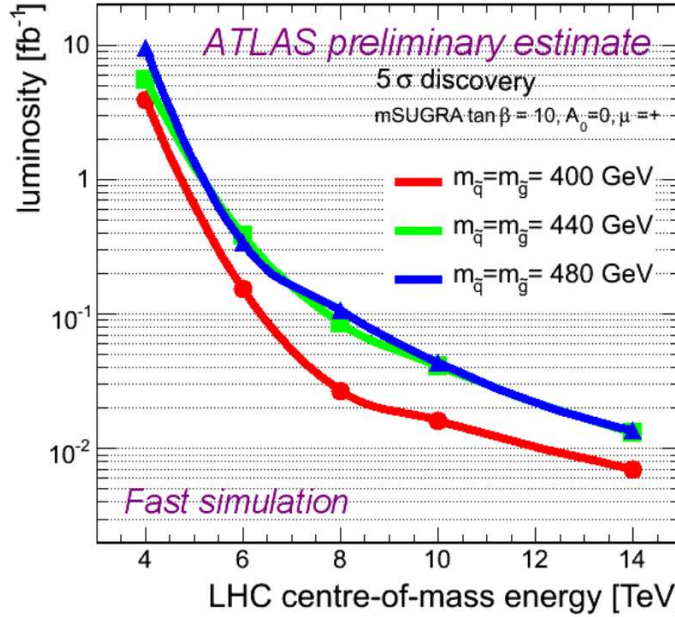


**Figure 12.1:** SUSY observation depending on luminosity and CM energy, taken from Ref. [196].

description), and carried out initial alignment, calibration and timing studies. Combined and stand-alone test-beam runs were conducted up till 2004, see Ref. [50] for detailed results.

Following the LHC Chamonix workshop 2009 [77], the LHC schedule has been re-organised to allow for a long physics run period between end of 2009 and end of 2010. After a short period of initial 900 GeV centre-of-mass (CM) collisions, the bulk data is planned to be collected with 10 TeV CM energy. Running also at a reduced machine luminosity (starting with  $10^{31}$  then ramping up to  $10^{32} \text{ cm}^{-2} \text{ s}^{-1}$ ), a total integrated luminosity of approximately  $200 \text{ pb}^{-1}$  is expected by the end of 2010.

As an input to the LHC Chamonix workshop, ATLAS (as well as the other LHC experiments) studied the physics prospects depending on the reduced CM energy [196]. Note however that these studies are based on simpler techniques and approximations than is usual for ATLAS results, in order to quickly give input to the LHC operating strategy. Fig. 12.1 compares the SUSY discovery sensitivity ( $5\sigma$  observation) for three mSUGRA models with equal mass squarks and gluinos, as a function of CM energy and integrated luminosity. All results have been obtained from fast simulation, and using the baseline one-lepton search mode (cf. Chapter 10).

One can see that at 10 TeV CM energy the current Tevatron exclusion limits (around 400 GeV squark masses in mSUGRA models) are met with a few tens of  $\text{pb}^{-1}$  of understood LHC data. The sensitivity drops away rather quickly below a CM energy of  $\sim 8 \text{ TeV}$ . It is also noteworthy that typical SUSY distributions, such as  $M_{\text{eff}}$  or  $E_T^{\text{miss}}$ , are not much affected in shape when going to somewhat lower CM energies. This is because the heavy SUSY particles are presumably produced nearly at rest.

Definite predictions concerning the LHC CM energy and luminosity beyond this 10 TeV CM energy,  $L \simeq 200 \text{ pb}^{-1}$  run period are very difficult to make at this point. Only after operational

experience from the 2009/2010 run period can we expect reasonably reliable predictions.

## 12.2 First SUSY data analysis

The first SUSY data analysis at ATLAS will most likely be the baseline one-lepton analysis (one isolated electron or muon + high- $p_T$  jets + significant  $E_T^{\text{miss}}$ ), as described in Chapter 10. It will search for squark and or gluino production at a mass scale just above the Tevatron limits (around 400 GeV). The requirement of an isolated lepton greatly suppresses background contributions from QCD processes, which will have significant uncertainties in early LHC data. Furthermore, initial analyses will put much emphasis on data-driven background estimation methods.

Before any LHC experiment could possibly claim a SUSY discovery, or a stricter exclusion, detailed and thorough studies of the detector, the trigger system, the reconstruction performance, as well as the SM processes will have to be carried out. Once the LHC machine delivers colliding beams, the required steps for early physics are:

- commission the trigger system (timing, efficiency, stability, etc.);
- understand, align, and calibrate the detector systems;
- understand the performance of physics objects, in particular  $e$ ,  $\mu$ , jets, and  $E_T^{\text{miss}}$  ;
- establish signals for, and measure rates of well-known Standard Model signatures.

Only then, we can expect any observation of, or limits on, new physics!

The one-lepton analysis can be based on a multijet trigger or on a single lepton trigger (combination of an electron or a muon trigger). Triggers selecting  $E_T^{\text{miss}}$  will probably take more time until they are under control.

In many search studies the most critical variable to detect new physics (in particular SUSY) is  $E_T^{\text{miss}}$ . This variable, however, is also very sensitive to nearly all detector and reconstruction issues (cf. Section 9.5 for a brief description of fake- $E_T^{\text{miss}}$ ). Therefore, its understanding will be top priority. A reasonable calibration of the  $E_T^{\text{miss}}$  scale and resolution will be required. This requires various control data samples, such as  $W/Z$  + jets, balanced and imbalanced QCD dijet events.

Secondly, it will be very important to understand the performance of isolated electrons and muons (leptons), in particular the fake rate of a jet being wrongly reconstructed as an electron. For both leptons the identification efficiency in busy events is needed, as a function of the number of jets, or distance to the closest jet. Furthermore, the isolation criteria and their efficiencies have to be understood. A reasonable momentum scale and energy resolution are also needed, but the ultimate precision is not required for early analyses searching for an excess (opposed to dilepton mass measurements). Samples of non-isolated leptons can be useful to study backgrounds: semileptonic heavy quark decays can lead to leptons which are mis-identified as isolated leptons, and to  $E_T^{\text{miss}}$ .

For jets, a high reconstruction efficiency for energetic partons is very desirable. Furthermore, a good calibration of the jet energy scale and energy resolution are important. Both have a strong impact on their  $E_T^{\text{miss}}$  counterparts. However, the ultimate precision is not required for initial SUSY search studies.

The various backgrounds in the one-lepton SUSY analysis can be classified as originating from non-physics and physics sources. The first group comprises, for example, cosmic ray muons, and beam-related backgrounds. Special clean-up cuts are expected to suppress non-physics backgrounds to a large extent.

Simulation studies have shown that the main sources of physics backgrounds are:  $t\bar{t}$  production and  $W$ +jets processes. A smaller contribution is expected to arise from QCD processes, and  $Z$ +jets production, cf. Chapter 10 for a detailed discussion.

The determination of all SM background processes will be a crucial task. It is foreseen to heavily rely on data-driven methods, while also requiring consistency with Monte Carlo simulations. The initial simulations will have large uncertainties, in particular in the very important tails of the variable distributions. Much effort will be spent on comparing simulation with data. Several data-driven background determination methods have been proposed and studied (cf. Chapter 11). Again, consistency among the different estimates will be required.

Individual components of the backgrounds can be estimated using dedicated control samples. A full kinematic top reconstruction, for example, can be used in order to obtain and study a clean sample of  $t\bar{t}$  production. This will be augmented by combined fits, such as the Tiles Method, where the abundances of SM and beyond-SM events are determined in signal and sideband regions using different fitting techniques.

To some extent, the required performance and SM physics studies will overlap with other, non-SUSY early physics studies. Within ATLAS several performance and physics groups have been established to organise and steer the overall strategies. The cross section measurements of  $t\bar{t}$ ,  $W$ +jets, and  $Z$ +jets production, for example, will be high priority tasks of the Top and SM physics groups. These measurements would also be very important for SUSY studies, albeit the kinematic phase-space of the SUSY analysis significantly increases the uncertainties and will make further studies inevitable.

### 12.3 Measuring SUSY with the LHC and ILC

If “light” SUSY exists in nature, then it should be seen by the LHC. Once a signature consistent with SUSY has been established, the experimental focus will be to measure and understand it. Some of the urgent questions would be: Are the heavy particle signals really the superpartners, i.e. are the couplings and spins as predicted by SUSY? Furthermore, the manifestation of SUSY needs to be understood: What is the breaking mechanism? What is the relation to grand unification? What is the relation to the Higgs mechanism? What is the role of SUSY in the early universe?

These issues can only be partly tackled by the LHC, see Section 7.4.1 for some simple examples of SUSY measurements at the LHC. Precise measurements of the whole SUSY mass spectrum, the couplings, and spins will require an interplay between the LHC, and a next-generation linear col-



lider (NLC). Prominent candidates for the NLC are the International Linear Collider (ILC) [197], and the Compact Linear Collider (CLIC) [198]. Both are being designed to provide electron–positron collisions at a CM energy in the range between  $\sim 500$  GeV and a few TeV.

The LHC and NLC would be complementary for SUSY measurements in the following sense. The LHC characteristics are:

- reach a mass scale up to a few TeV ;
- squarks would be strongly produced, with “huge” cross sections;
- sleptons and gauginos would be produced weakly or in cascades (maybe difficult to see);
- the LSP cannot be fully reconstructed due to missing information, mainly sensitive to mass differences.

The NLC characteristics are:

- all SUSY processes within mass reach would have similar cross sections, all particles can be cleanly reconstructed;
- the LSP could be reconstructed from kinematic quantities, all absolute masses could be measured;
- all particles would be produced in electroweak processes that can be calculated accurately, particle couplings could be measured;
- depending on the maximum NLC CM energy, squarks and gluinos could be too heavy to be produced.

In the second stage of the SUSY roadmap, a NLC would be required to precisely map out the couplings, and also for accurate mass measurements.

---



# **Appendices**

## Appendix A

# HLT Steering terminology

- *LVL1*: First-level trigger (hardware based).
- *LVL2*: Second-level trigger (software based).
- *Event filter* (EF): Third-level trigger (software based).
- *HLT*: High-level trigger, consists of LVL2 and EF.
- *Region of interest* (ROI): a geometric detector region which contains a high- $p_T$  object (muon, electron, jet, etc.). ROIs are identified by LVL1 and are sent, together with some additional information, to LVL2 to initiate further processing around the detector regions.
- *Trigger item*: one out of 256 LVL1 triggers. The overall LVL1 decision is the logical OR combination of all trigger items.
- *Trigger chain*: a trigger in LVL2 or EF. The word “chain” is used because LVL2/EF triggers consist of several steps. The overall LVL2 (EF) decision is the logical OR combination of all LVL2 (EF) trigger chains.
- *Trigger element* (TE): a successor of an ROI. TEs represent the processing (refinement) status of a given ROI.
- *Feature*: an HLT trigger data object, e.g. a cluster or a track.
- *FEX*: a feature extraction (trigger) algorithm. FEX algorithms perform time consuming operations such as data unpacking, or the calculation of physics quantities.
- *HYP0*: a hypothesis (trigger) algorithm. HYP0 algorithms perform quick selection cuts ( $p_T$ , isolation, etc.) based on existing features.
- *Pre-scale* (PS): a PS factor  $N$  causes the item/chain to be rejected in  $(1 - N)$  out of  $N$  cases.
- *Pass-through* (PT): a PT factor  $N$  causes the chain to be accepted (passed-through) in 1 out of  $N$  cases independent of the chain decision. The other  $(N - 1)$  cases are passed subject to the result of the chain decision.

- *Streaming tag*: an event-classification name, based on which trigger(s) fired. The streaming tag is used to write accepted events to different output files.
  - *Trigger sequence*: a bundle of FEX and HYPO algorithms together with the configured input TE type(s) and the output type.
  - *Trigger (chain) signature*: defines a requirement to fulfill one step of a trigger chain.
-

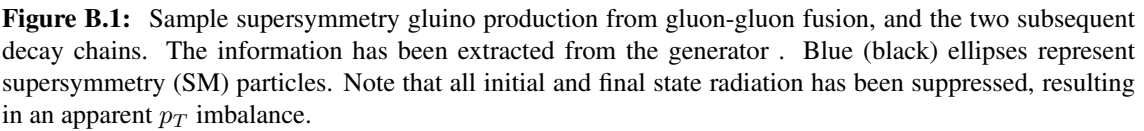
## Appendix B

# Sample SUSY production and cascade decays

The production of supersymmetric particles and the subsequent cascade decays are illustrated using one mSUGRA model (the benchmark point SU3, which is defined in Chapter 8). Fig. B.1 shows the first example of a strong gluino production. The same generated event was also passed through the full ATLAS detector simulation. The resulting detector event display, which is based on the reconstructed objects, is shown in Fig. B.2.

Fig. B.3 shows the second example of strong squark production. The corresponding detector event display is given in Fig. B.4, again using the full ATLAS simulation.

The two shown examples were selected because they represent good candidate events for the one-lepton analysis: they both result in several high- $p_T$  jets and leptons, plus a significant amount of missing transverse energy ( $E_T^{\text{miss}}$ ). Also shown are the sparticle masses for the used mSUGRA model (cf. Table 8.2 for the complete mass spectrum).



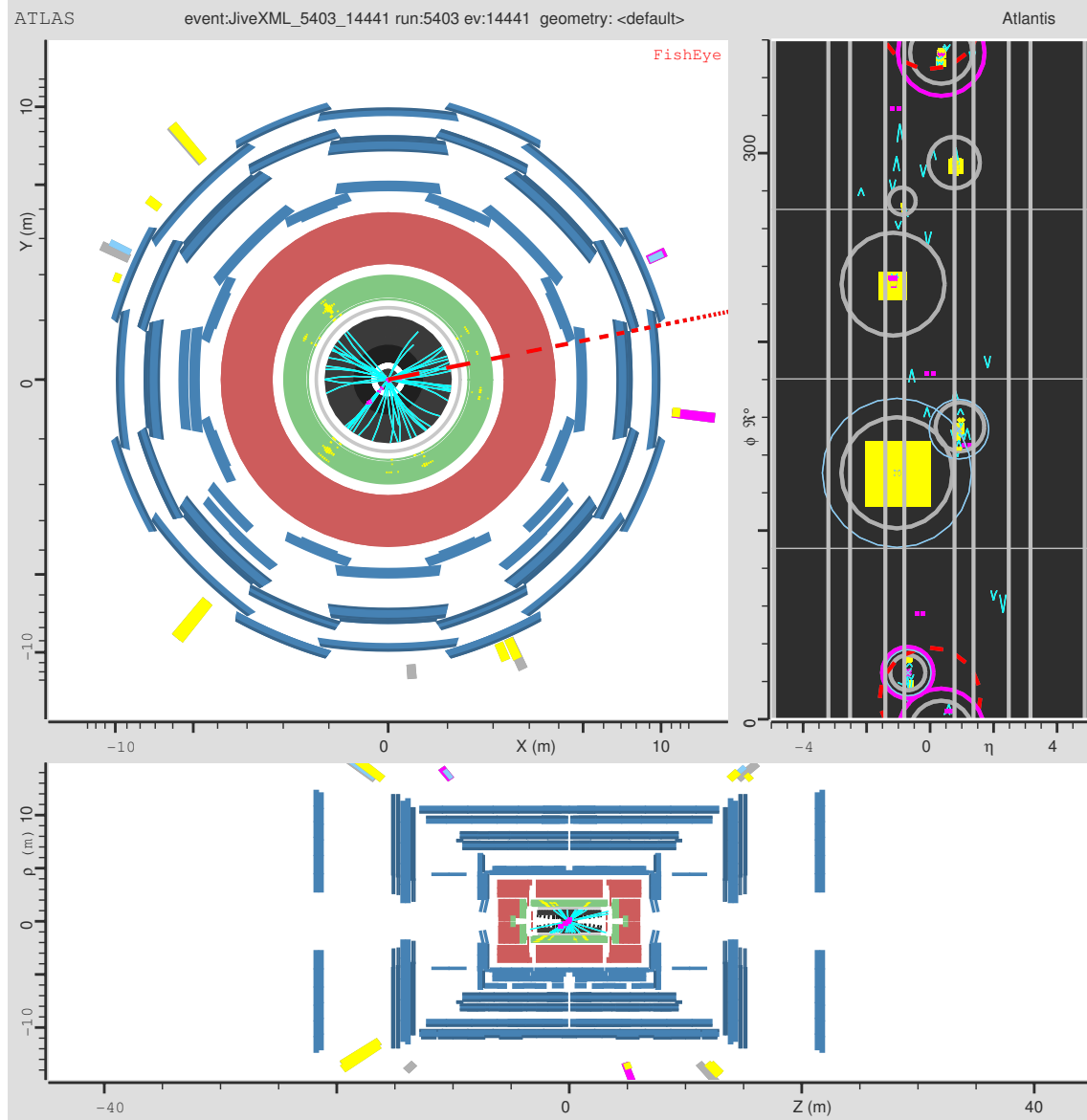


**Figure B.2:** Sample ATLAS event display showing the reconstructed objects resulting from the supersymmetry decay shown in Fig. B.1. The red/dotted line represents the reconstructed  $E_T^{\text{miss}}$  (219.2 GeV), electrons are shown in yellow, and jets in grey, or pink for b-tagged jets, or light blue for tau-tagged jets. Clearly visible, the high- $p_T$  electron (at  $\eta = -1.0, \phi = 2.3$ ) which is reconstructed with  $p_T = 251.7$  GeV. No information from the hadronic calorimeters could be displayed (for technical reasons).



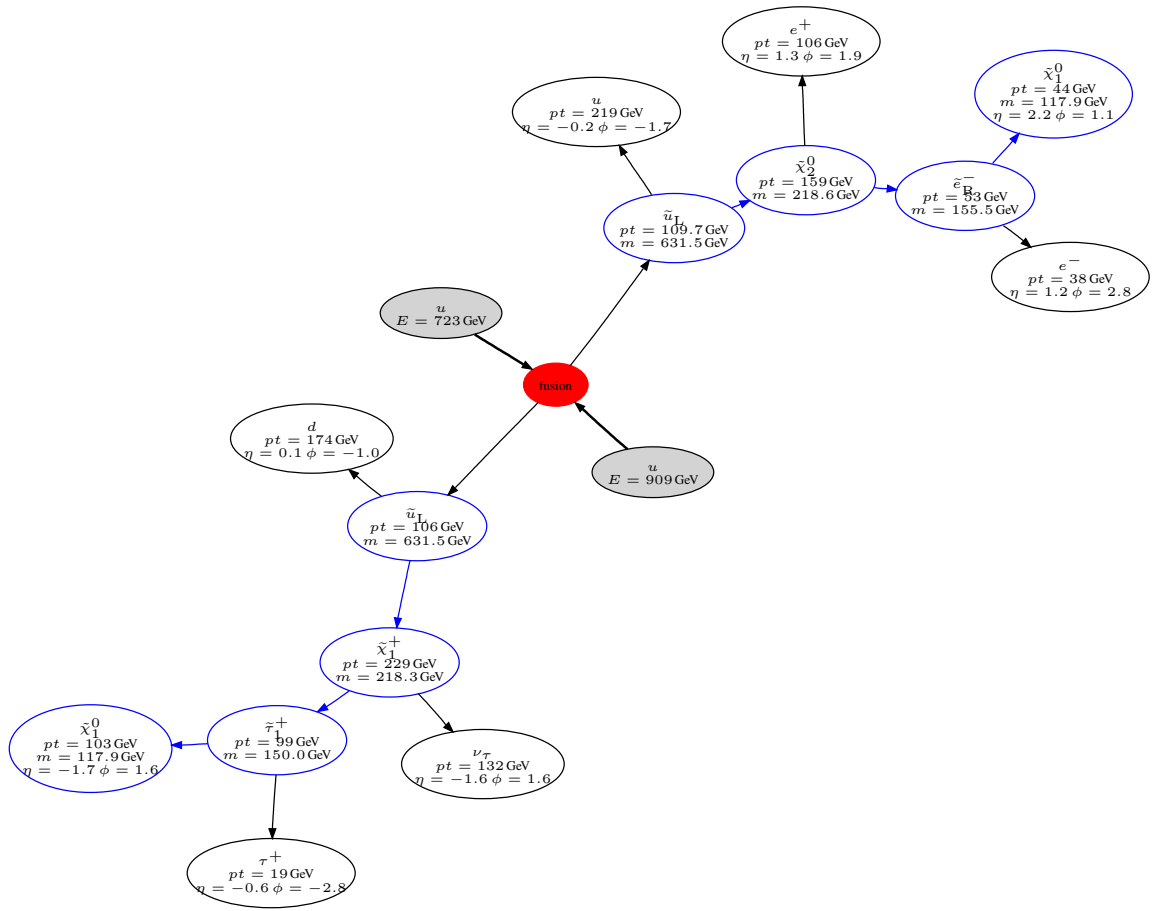


**Figure B.3:** Sample supersymmetry squark production from quark-quark scattering ( $t$ -channel), and the two subsequent decay chains. The information has been extracted from the generator. Blue (black) ellipses represent supersymmetry (SM) particles. Note that all initial and final state radiation has been suppressed, resulting in an apparent  $p_T$  imbalance.

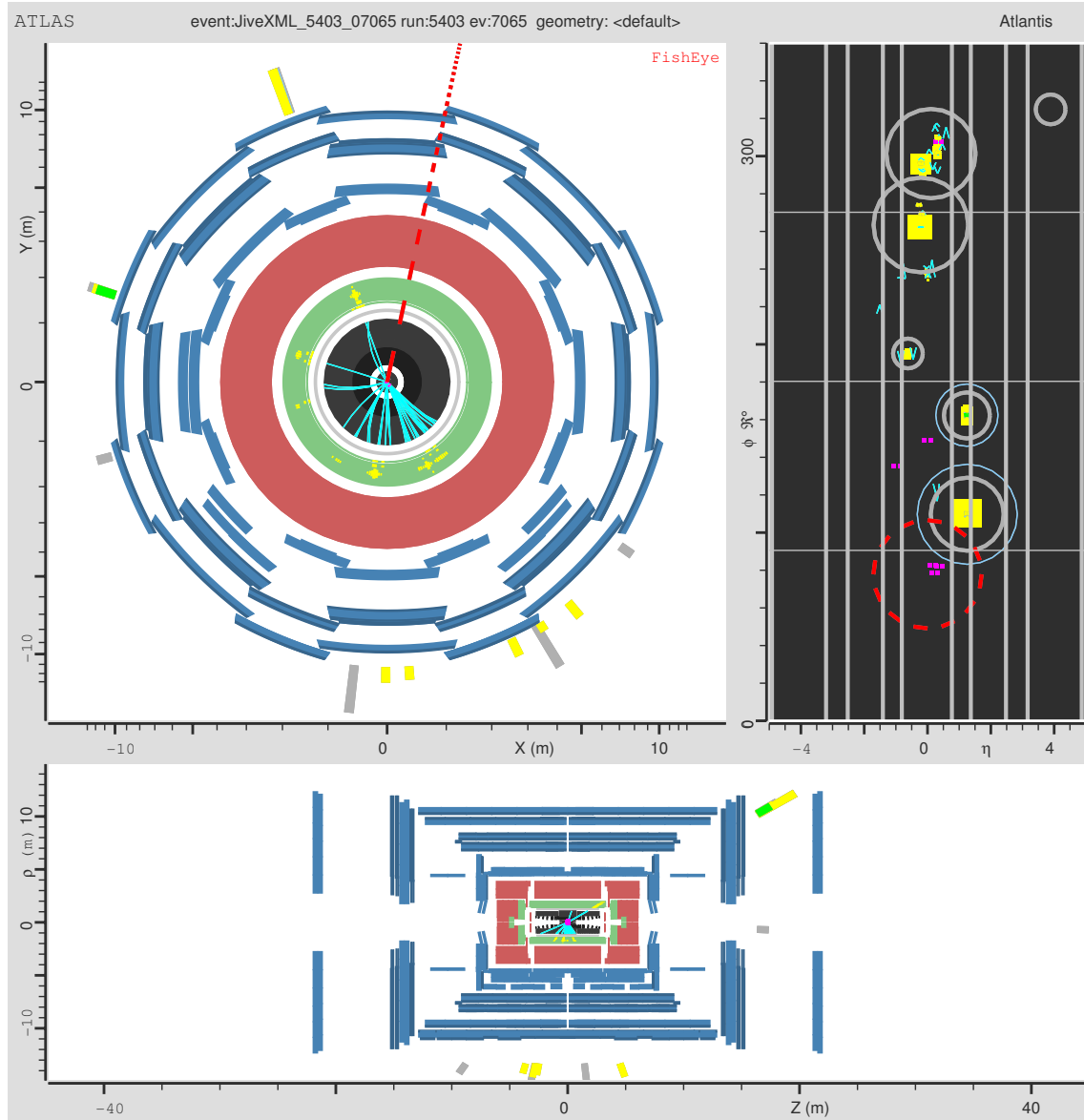


**Figure B.4:** Sample ATLAS event display showing the reconstructed objects resulting from the supersymmetry decay shown in Fig. B.3. Similar colours coding as in Fig. B.2 are used. The reconstructed  $E_T^{\text{miss}}$  is 252 GeV.

## Appendix C

# StatTools - Calculation of Significances in Search Analyses

For an ensemble of cut requirements, a search analysis observes  $N$  Poisson-distributed events. The expected number of Standard Model (SM) events  $\bar{N}$ , passing the requirements, is an incoherent sum of  $n_{\text{bkg}}$  background contributions with  $\bar{N}_{B,i}$  expected events for background type  $i$  ( $i = 1, \dots, n_{\text{bkg}}$ ). Each background contribution  $i$  has an associated uncertainty  $\sigma_{B,i}$ , which has statistical and systematic components, and which is assumed to be the width of a Gaussian distribution. (Theoretical systematic uncertainties that cannot be approximated by the width of a Gaussian can also be treated, but will not be discussed here). The uncertainties among different backgrounds can be correlated, and the associated covariance matrix is denoted  $C$ . The  $-\ln(\text{likelihood})$  estimator for these conditions is given by

$$\begin{aligned} -\ln \mathcal{L}_{\text{SM}} &= N'^{\text{SM}} - N \ln N'^{\text{SM}} + \ln N! + \frac{n_{\text{bkg}}}{2} \ln(2\pi) + \frac{1}{2} \ln |C| \\ &\quad + \frac{1}{2} \sum_{i,j=1}^{n_{\text{bkg}}} (N_{B,i} - \bar{N}_{B,i}) C_{ij}^{-1} (N_{B,j} - \bar{N}_{B,j}) , \end{aligned} \quad (\text{C.1})$$

where  $N'^{\text{SM}} = \sum_i N_{B,i}$ , the  $N_{B,i}$ ,  $i = 1, \dots, n_{\text{bkg}}$ , are varying *nuisance parameters* that can be used to minimize  $-\ln \mathcal{L}_{\text{SM}}$ , and  $|C|$  is the determinant of  $C$ . To simplify the minimisation, the multivariate background function can be reduced to a single inclusive background  $N_B$ , which has a Gaussian distribution with  $\bar{N} \pm \sigma_{\bar{N}}$  expected events, where  $\sigma_{\bar{N}}^2 = \sum_{ij} C_{ij}$ .

### C.1 Hypothesis testing

The probability value (p-value) of a statistical hypothesis test is the probability, under assumption of the null hypothesis (H), to observe data with equal or lesser compatibility with H relative to the measured data ( $N$ ), where compatibility with H is described by the test statistic, here  $-\ln \mathcal{L}_{\text{SM}}$ .

Note, the p-value is not the probability that H is true.<sup>1</sup> Statistical hypothesis tests need to define beforehand what observed event numbers can lead to an exclusion of the null hypothesis. Here, the SM is excluded if (and only if) significantly *more* events than predicted in the SM are observed. This corresponds to a one-sided hypothesis test (as opposed to a two-sided hypothesis test).

In the following, we derive approximate and accurate p-values for the minimisation problem at hand, thereby always assuming that the nuisance parameters can be described by Gaussian probability density distributions (which may turn out to be an inaccurate assumption for certain problems, in particular if the systematic errors are due to model or theory uncertainties). We consider six different approaches.

### C.1.1 Gauss approximation

In this and the following section, we consider the maximum *profile likelihood* with respect to the nuisance parameters, to derive null hypothesis p-value estimates. The profile likelihood is suggested to have good coverage properties. For a single convolved background species, the solution of the minimization problem  $-d \ln \mathcal{L}_{\text{SM}}(N_B)/dN_B|_{N_B=N_B^{\min}} = 0$  is readily obtained. For large  $N$ , the Poisson term in (C.1) may be approximated by a Gaussian,<sup>2</sup> so that one finds at the minimum  $N_B = N_B^{\min}$

$$-\ln \mathcal{L}_{\text{SM}}^{\min} = \frac{(N - \bar{N})^2}{N + \sigma_{\bar{N}}^2}. \quad (\text{C.2})$$

In case of multiple, non-convolved background species for which a  $n_{\text{bkg}}$ -dimensional system of linear equations must be solved, the numerical solution of the minimisation problem obtained with MINUIT/MIGRAD will be a handy replacement of the analytical one. If we continue the parallel with standard HEP fitting techniques, we can obtain an estimate for the p-value in units of standard deviations by identifying the  $-\ln \mathcal{L}_{\text{SM}}$  in its minimum with a  $\chi^2$ -like function, so that

$$\chi^2 = -2 \ln \mathcal{L}_{\text{SM}}. \quad (\text{C.3})$$

A one-sigma error estimate would then correspond to  $\chi^2 = 1$ . This is the way MINOS estimates the error of a parameter (here  $N$ ) in presence of nuisance parameters: it determines for freely varying nuisance parameters the maximum intervals  $N \pm \Delta_{\pm}$  for which  $\chi^2 = 1$  (or any other range). The  $\chi^2$  for the null hypothesis is obtained similarly. The one-sided p-value for wrongly rejecting the Standard Model is estimated by

$$p = \frac{1}{2} \text{erfc} \left( \sqrt{-\ln \mathcal{L}_{\text{SM}}^{\min}} \right), \quad (\text{C.4})$$

where  $\text{erfc}$  is the complementary error function. The p-value expressed in units of standard deviations is found by inverting Eq. (C.4).

---

<sup>1</sup>Terminology: the *significance level* of a statistical hypothesis test is the fixed probability of wrongly rejecting the null hypothesis, if it is true. It is the probability for a *Type-I error* to occur. The p-value is compared with the significance level and, if it is smaller, the result is significant.

<sup>2</sup>The statement “for large  $N$ ” is not quite accurate: also required for a valid replacement of the Poisson by a Gauss distribution is the condition  $|N - \bar{N}| \ell^+ \ell^- N$  to hold. In that case, the approximations  $\ln N! \approx (N + 1/2) \ln N + \ln \sqrt{2\pi} - N$ , for  $N \gg 1$  (Stirling’s formula), and  $N \ln(\bar{N}/N) + N - \bar{N} \approx -(N - \bar{N})^2/(2N)$ , for  $\bar{N}/N \rightarrow 1$ , allow to identify the two distributions.

---

### C.1.2 Poisson approximation

If the event counts do not allow the replacement of the Poisson distribution by a Gaussian, it is still straightforward to solve the minimisation problem analytically if all background contributions are convolved into a single one. Instead of only minimising  $-\ln \mathcal{L}_{\text{SM}}(N_B)$ , one may determine the offset-corrected profile likelihood

$$-\Delta \ln \mathcal{L}(N_B) = -\ln \mathcal{L}_{\text{SM}}(N_B) + N(\ln N - 1), \quad (\text{C.5})$$

for which one finds the physical minimum at  $N_B = N_B^{\min}$

$$-\Delta \ln \mathcal{L}^{\min} = \frac{1}{2} \left( \bar{N} - A + \frac{1}{4\sigma_{\bar{N}}^2} (\bar{N} + A)^2 \right) + N (\ln N - 1 - \ln (\bar{N} - A) + \ln 2), \quad (\text{C.6})$$

with

$$A = \sigma_{\bar{N}}^2 - \left( \bar{N}^2 + 4N\sigma_{\bar{N}}^2 - 2\bar{N}\sigma_{\bar{N}}^2 + \sigma_{\bar{N}}^4 \right)^{1/2}. \quad (\text{C.7})$$

The p-value is then estimated with Eq. (C.4).

Equation (C.2) is obviously an approximation, which fails when the number of expected background events is zero with negligible uncertainty. In that case any observed event dismisses the null hypothesis, and  $-\ln \mathcal{L}_{\text{SM}}^{\min}$  should diverge giving a zero p-value. Instead one finds  $-\ln \mathcal{L}_{\text{SM}}^{\min} = N$ . In contrast, the Poisson approximation (C.6) does exhibit the expected property.

### C.1.3 Exact Poisson solution

To compute the exact p-value one needs to evaluate the convolved Poisson distribution

$$\begin{aligned} P_c(N, \bar{N}) &= \int_0^\infty \dots \int_0^\infty P\left(N, \sum_{i=1}^{n_{\text{bkg}}} N_{B,i}\right) \frac{1}{(2\pi)^{n_{\text{bkg}}/2} \sqrt{|C|}} e^{-\frac{1}{2} \sum_{i,j=1}^{n_{\text{bkg}}} (N_{B,i} - \bar{N}_{B,i}) C_{ij}^{-1} (N_{B,j} - \bar{N}_{B,j})} \\ &\quad \times \delta\left(\bar{N} - \sum_{i=1}^{n_{\text{bkg}}} N_{B,i}\right) dN_{B,1} \dots dN_{B,n_{\text{bkg}}}, \end{aligned} \quad (\text{C.8})$$

with  $P(N, \bar{N}) = \bar{N}^N e^{-\bar{N}} / N!$ , and  $\bar{N} = \sum_i \bar{N}_{B,i}$ . Reducing in the usual manner the correlated Gaussian background contributions to a single inclusive term with  $\bar{N} \pm \sigma_{\bar{N}}$  events, where  $\sigma_{\bar{N}}^2 = \sum_{ij} C_{ij}$ , the convolved Poisson simplifies to

$$P_c(N, \bar{N}) = \int_0^\infty P(N, \bar{N}') \frac{1}{\sqrt{2\pi}\sigma_{\bar{N}}} e^{-\frac{1}{2} \left( \frac{\bar{N}' - \bar{N}}{\sigma_{\bar{N}}} \right)^2} d\bar{N}', \quad (\text{C.9})$$

The convolution can be solved analytically and, for  $\sigma_{\bar{N}}^2 < \bar{N}$ , is given by

$$P_c(N, \bar{N}) = 2^{(N-1)/2} \sigma_{\bar{N}}^{N+1} e^{-\bar{N}^2/2\sigma_{\bar{N}}^2} \left( A_1 + \sqrt{2} \frac{\bar{N} - \sigma_{\bar{N}}^2}{\sigma_{\bar{N}}} A_2 \right), \quad (\text{C.10})$$

where

$$A_k = \Gamma\left(\frac{N+k}{2}\right) {}_1F_1\left(\frac{N+k}{2}, k - \frac{1}{2}, \frac{(\bar{N} - \sigma_{\bar{N}}^2)^2}{2\sigma_{\bar{N}}^2}\right). \quad (\text{C.11})$$

The confluent hypergeometric function of the first kind,  ${}_1F_1$ , has the series

$${}_1F_1(a, b, z) = \sum_{n=0}^{\infty} (a)_n z^n / (b)_n n!,$$

where  $(a)_n = a(a+1)\dots(a+n)$ .  ${}_1F_1(a, b, z)$  also has an integral representation,<sup>3</sup> which is useful for numerical applications. A simpler and not much slower solution is the direct numerical integration of (C.9).

The one-sided p-value is obtained by the sum

$$p = \sum_{n=N}^{\infty} P_c(n, \bar{N}). \quad (\text{C.12})$$

Alternatively,<sup>4</sup> we can combine Eqs. (C.12) and (C.9), and first perform the summation using

$$\sum_{n=N}^{\infty} P(n, \bar{N}') = 1 - \frac{\Gamma(N, \bar{N}')}{\Gamma(N)}, \quad (\text{C.13})$$

where  $\Gamma(N) = (N-1)!$ , and  $\Gamma(a, x)$  is the incomplete gamma function.<sup>5</sup> The remaining integral over the product of the incomplete gamma function and the Gaussian resolution function must be solved numerically. In spite that it represents the most efficient way of deriving the exact Poisson p-value.

### C.1.4 Monte Carlo sampling

Another way of evaluating the exact p-value is to throw toy Monte Carlo experiments with null hypothesis, and determine the fraction of toy experiments that finds a number of observed events (distributed according to a Poisson distribution) that is equal or larger than  $N$  (the number of observed events found in the dataset to be tested). The expected number of events in these toy experiments fluctuates according to a Gaussian distribution with mean  $\bar{N}$  and width  $\sigma_{\bar{N}}$ .

By definition, the Monte Carlo approach has good coverage, because it represents itself a test for coverage. Moreover, since the exact Poisson solution discussed above corresponds to the (quasi-)analytical description of the Monte Carlo sampling, it also has good coverage.

<sup>3</sup> ${}_1F_1(a, b, z) = \frac{\Gamma(b)}{\Gamma(a)\Gamma(b-a)} \int_0^1 e^{zt} x^{a-1} (1-x)^{b-a-1} dx$ .

<sup>4</sup>Solution suggested by Sascha Caron, Universität Freiburg, Germany.

<sup>5</sup>The incomplete gamma function is given by the integral  $\Gamma(a, x) = \int_x^{\infty} t^{a-1} e^{-t} dt$ . If  $a \in \mathbb{Z}$ , it can be expressed as  $\Gamma(a, x) = (a-1)! e^{-x} \sum_{k=0}^{a-1} x^k / k!$ .

## C.2 A numerical example

Figure C.1 shows p-value curves obtained with the four approaches (Gauss approximation, Poisson approximation, exact Poisson solution and toy sampling) for an example of  $N = 50$  observed events and a varying number of expected events,  $\bar{N}$ , according to the labels given on the abscissa. The toy solution has been obtained with 500k experiments in each scan point (50 points for each plot – the resulting curves have been smoothed). For the upper plots the  $\bar{N}$  values have no uncertainty, whereas  $\sigma_B = 10$  is used for each scan point in the lower plots. The following observations can be made:

- as expected, the Gauss approximation fails to converge towards the exact solution for small numbers of expected events (upper plots in Fig. C.1);
- this failure is less pronounced once significant Gaussian uncertainties on  $\bar{N}$  come into play (lower plots);
- as it should, the toy and the exact solutions agree everywhere (within the statistical fluctuations of the toy), but the toy fails to probe p-values smaller than  $2 \times 10^{-6}$  in average;
- the Poisson approximation is excellent for small  $\bar{N}$  (small p-values), but becomes Gaussian-like for large  $\bar{N}$  (large p-values);
- all differences diminish with rising uncertainties on the background (lower plots).

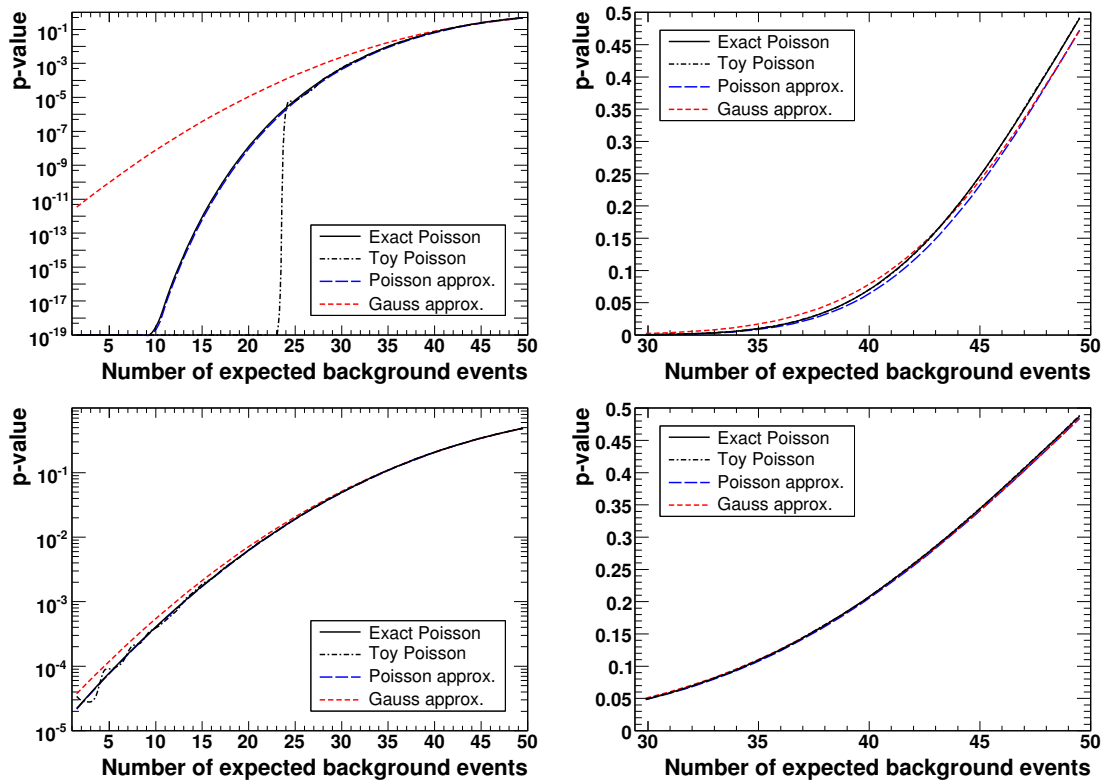


**Figure C.1:** Example for p-values obtained with the four discussed approaches. In all cases the observed number of events is  $N = 50$ , and the expected number of events is given by the abscissa. Left and right plots show the same curves in logarithmic and zoomed linear scales, respectively. Upper plots: the number of expected events has no associated uncertainty. Lower plots: the number of expected events has a constant uncertainty of  $\sigma_B = 10$  events in each scan point.



# Bibliography

- [1] A. Einstein. The foundation of the general theory of relativity. *Annalen Phys.*, 49:769–822, 1916.
- [2] C. Amsler et al. Review of particle physics. *Phys. Lett.*, B667:1, 2008.
- [3] S. L. Glashow. Partial Symmetries of Weak Interactions. *Nucl. Phys.*, 22:579–588, 1961.
- [4] Steven Weinberg. A Model of Leptons. *Phys. Rev. Lett.*, 19:1264–1266, 1967.
- [5] Abdus Salam. Gauge Unification of Fundamental Forces. *Rev. Mod. Phys.*, 52:525–538, 1980.
- [6] R. P. Feynman. Space-time approach to nonrelativistic quantum mechanics. *Rev. Mod. Phys.*, 20:367–387, 1948.
- [7] R. P. Feynman. Mathematical formulation of the quantum theory of electromagnetic interaction. *Phys. Rev.*, 80:440–457, 1950.
- [8] Chen-Ning Yang and Robert L. Mills. Conservation of isotopic spin and isotopic gauge invariance. *Phys. Rev.*, 96:191–195, 1954.
- [9] E. Noether. Invariante Variationsprobleme. *Nachr. d. König. Gesellsch. d. Wiss. zu Göttingen*, pages 235–257, 1918.
- [10] H. Weyl. *Raum, Zeit, Materie*. Verlag von Julius Springer, 1919.
- [11] Peter W. Higgs. Broken Symmetries, Massless Particles and Gauge Fields. *Phys. Lett.*, 12:132–133, 1964.
- [12] Peter W. Higgs. Broken Symmetries and the Masses of Gauge Bosons. *Phys. Rev. Lett.*, 13:508–509, 1964.
- [13] F. Englert and R. Brout. Broken Symmetry and the Mass of Gauge Vector Mesons. *Phys. Rev. Lett.*, 13:321–322, 1964.
- [14] G.S. Guralnik, C.R. Hagen, and T.W.B. Kibble. Global Conservation Laws and Massless Particles. *Phys. Rev. Lett.*, 13:585–587, 1964.
- [15] R. Barate et al. Search for the standard model Higgs boson at LEP. *Phys. Lett.*, B565:61–75, 2003. arXiv:hep-ex/0306033.

- 
- [16] The Tevatron New-Phenomena and Higgs working group (TEVNPH). Combined CDF and DØ Upper Limits on Standard Model Higgs-Boson Production with up to 4.2 fb<sup>-1</sup> of Data. FERMILAB-PUB-09-060-E, more information can be found at <http://tevnpwhg.fnal.gov>.
- [17] The LEP Electroweak Working Group (LEPEWWG) combines results from the ALEPH, DELPHI, L3, and OPAL detector collaborations. <http://lepewwg.web.cern.ch/LEPEWWG/>.
- [18] Y.A. Simonov. The Confinement. *Phys. Usp.*, 39:313–336, 1996. arXiv:hep-ph/9709344.
- [19] D. J. Gross and Frank Wilczek. Asymptotically Free Gauge Theories. 1. *Phys. Rev.*, D8:3633–3652, 1973.
- [20] H. David Politzer. Reliable perturbative results for strong interactions? *Phys. Rev. Lett.*, 30:1346–1349, 1973.
- [21] Murray Gell-Mann. A Schematic Model of Baryons and Mesons. *Phys. Lett.*, 8:214–215, 1964.
- [22] M. Kobayashi and T. Maskawa. CP Violation in the Renormalizable Theory of Weak Interaction. *Prog. Theor. Phys.*, 49:652–657, 1973.
- [23] N. Cabibbo. Unitary Symmetry and Leptonic Decays. *Phys. Rev. Lett.*, 10:531–533, 1963.
- [24] M. Ciuchini et al. 2000 CKM triangle analysis: A Critical review with updated experimental inputs and theoretical parameters. *JHEP*, 07:013, 2001. arXiv:hep-ph/0012308.
- [25] J.M. Campbell, J.W. Huston, and W.J. Stirling. Hard interactions of quarks and gluons: A primer for LHC physics. *Rept. Prog. Phys.*, 70:89, 2007. arXiv:hep-ph/0611148.
- [26] ATLAS Collaboration (G. Aad *et al.*). Expected Performance of the ATLAS Experiment, Detector, Trigger and Physics (“CSC book”). *CERN-OPEN-2008-020*, 2008.
- [27] D. Kaplan. Physics beyond the standard model. HCP CERN Summer School, CERN 2007. Web page <http://hcpss.web.cern.ch/hcpss/2007>.
- [28] G. ’t Hooft (ed. ) et al. Recent Developments in Gauge Theories. Proceedings, Nato Advanced Study Institute, Cargese, France, August 26 - September 8, 1979. New York, USA: Plenum (1980) 438 P. (Nato Advanced Study Institutes Series: Series B, Physics, 59).
- [29] C.F. Kolda and H. Murayama. The Higgs mass and new physics scales in the minimal standard model. *JHEP*, 07:035, 2000. arXiv:hep-ph/0003170.
- [30] T. Hambye and K. Riessellmann. Matching conditions and Higgs mass upper bounds revisited. *Phys. Rev.*, D55:7255–7262, 1997. arXiv:hep-ph/9610272.
- [31] J.R. Ellis, S. Kelley, and D. V. Nanopoulos. Probing the desert using gauge coupling unification. *Phys. Lett.*, B260:131–137, 1991.
- [32] A. D. Sakharov. Violation of CP Invariance, c Asymmetry, and Baryon Asymmetry of the Universe. *Pisma Zh. Eksp. Teor. Fiz.*, 5:32–35, 1967.
-

- 
- [33] A. Riotto and M. Trodden. Recent progress in baryogenesis. *Ann. Rev. Nucl. Part. Sci.*, 49:35–75, 1999. arXiv:hep-ph/9901362.
- [34] F. Zwicky. Spectral displacement of extra galactic nebulae. *Helv. Phys. Acta*, 6:110–127, 1933.
- [35] K. G. Begeman, A. H. Broeils, and R. H. Sanders. Extended rotation curves of spiral galaxies: Dark haloes and modified dynamics. *Mon. Not. Roy. Astron. Soc.*, 249:523, 1991.
- [36] J. Dunkley et al. Five-Year Wilkinson Microwave Anisotropy Probe (WMAP) Observations: Likelihoods and Parameters from the WMAP data. *Astrophys. J. Suppl.*, 180:306–329, 2009. arXiv:astro-ph/0803.0586.
- [37] G. Bertone, D. Hooper, and J. Silk. Particle dark matter: Evidence, candidates and constraints. *Phys. Rept.*, 405:279–390, 2005. arXiv:hep-ph/0404175.
- [38] J. Ellis. Physics Beyond the Standard Model. 2009. arXiv:hep-ph/0902.0357.
- [39] S.P. Martin. A supersymmetry primer, 1997. arXiv:hep-ph/9709356.
- [40] J.R. Ellis, K.A. Olive, and Y. Santoso. Constraining supersymmetry. *New J. Phys.*, 4:32, 2002. arXiv:hep-ph/0202110.
- [41] H. Goldberg. Constraint on the photino mass from cosmology. *Phys. Rev. Lett.*, 50:1419, 1983.
- [42] J.R. Ellis, J.S. Hagelin, D.V. Nanopoulos, K.A. Olive, and M. Srednicki. Supersymmetric relics from the big bang. *Nucl. Phys.*, B238:453–476, 1984.
- [43] G. Jungman, M. Kamionkowski, and K. Griest. Supersymmetric dark matter. *Phys. Rept.*, 267:195–373, 1996. arXiv:hep-ph/9506380.
- [44] S. Dimopoulos. LHC, SSC and the universe. *Phys. Lett.*, B246:347–352, 1990.
- [45] P. Langacker and M. Luo. Implications of precision electroweak experiments for  $M_t$ ,  $\rho_0$ ,  $\sin^2 \theta_W$  and grand unification. *Phys. Rev.*, D44:817–822, 1991.
- [46] L. Evans, and P. Bryant, editors. LHC Machine. *JINST*, 3:S08001, 2008.
- [47] O. S. Brüning, P. Collier, P. Lebrun, S. Myers, R. Ostojic, J. Poole, and P. Proudlock, editors. *LHC Design Report*, volume 1 : The LHC Main Ring. CERN, Geneva, 2004. CERN-2004-003-V-1.
- [48] O. S. Brüning, P. Collier, P. Lebrun, S. Myers, R. Ostojic, J. Poole, and P. Proudlock, editors. *LHC Design Report*, volume 2 : The LHC Infrastructure and General Services. CERN, Geneva, 2004. CERN-2004-003-V-2.
- [49] M. Benedikt, P. Collier, V. Mertens, J. Poole, and K. Schindl, editors. *LHC Design Report*, volume 3 : The LHC Injector Chain. CERN, Geneva, 2004. CERN-2004-003-V-3.
- [50] ATLAS Collaboration (G. Aad *et al.*). The ATLAS Experiment at the CERN Large Hadron Collider. *JINST*, 3:S08003, 2008.
-

- 
- [51] CMS Collaboration (R. Adolphi *et al.*). The CMS experiment at the CERN LHC. *JINST*, 3:S08004, 2008.
  - [52] LHCb Collaboration (A. Alves *et al.*). The LHCb Detector at the LHC. *JINST*, 3:S08005, 2008.
  - [53] ALICE Collaboration (L. Aamodt *et al.*). The ALICE experiment at the CERN LHC. *JINST*, 3:S08002, 2008.
  - [54] LHCf Collaboration (O. Adriani *et al.*). The LHCf detector at the CERN Large Hadron Collider. *JINST*, 3:S08006, 2008.
  - [55] TOTEM Collaboration (G. Anelli *et al.*). The TOTEM experiment at the CERN Large Hadron Collider. *JINST*, 3:S08007, 2008.
  - [56] ATLAS Collaboration. *ATLAS Detector and Physics Performance: Technical Design Report*, volume 2. CERN, Geneva, 1999. CERN-TDR-015, CERN-LHCC-99-15.
  - [57] R. D. Field. The underlying event in hard scattering processes, 2002. FERMILAB-CONF-02-009-E, hep-ph/0201192, arXiv:0201192 [hep-ph].
  - [58] A. Moraes, C. Buttar, and I. Dawson. Prediction for minimum bias and the underlying event at LHC energies. *Eur. Phys. J.*, C50:435–466, 2007.
  - [59] ATLAS Collaboration. *ATLAS Detector and Physics Performance: Technical Design Report*, volume 1 of *Technical Design Report ATLAS*. CERN, Geneva, 1999. CERN-TDR-014, CERN-LHCC-99-14.
  - [60] ATLAS Collaboration. *ATLAS Magnet System Technical Design Report*. CERN, 1997. CERN-LHCC-97-18.
  - [61] ATLAS Collaboration. *ATLAS Central Solenoid Technical Design Report*. CERN, 1997. CERN-LHCC-97-21.
  - [62] ATLAS Collaboration. *ATLAS Barrel Toroid Technical Design Report*. CERN, 1997. CERN-LHCC-97-19.
  - [63] ATLAS Collaboration. *ATLAS End-Cap Toroids Technical Design Report*. CERN, 1997. CERN-LHCC-97-20.
  - [64] Aad, G. and others. ATLAS Pixel Detector Electronics and Sensors. *JINST*, 3:P07007, 2008.
  - [65] ATLAS Collaboration. *ATLAS Inner Detector Technical Design Report*, volume 1. CERN, 1997. CERN-LHCC-97-16.
  - [66] ATLAS Collaboration. *ATLAS Inner Detector Technical Design Report*, volume 2. CERN, 1997. CERN-LHCC-97-17.
  - [67] ATLAS Collaboration. *ATLAS Pixel Detector Technical Design Report*. CERN, 1998. CERN-LHCC-98-13.
-

- 
- [68] A. Ahmad et al. The Silicon microstrip sensors of the ATLAS semiconductor tracker. *Nucl. Instrum. Meth.*, A578:98–118, 2007.
- [69] E. Abat et al. The ATLAS Transition Radiation Tracker (TRT) proportional drift tube: Design and performance. *JINST*, 3:P02013, 2008.
- [70] ATLAS Collaboration. *ATLAS Liquid Argon Calorimeter Technical Design Report*. CERN, 1996. CERN-LHCC-96-41.
- [71] ATLAS Collaboration. *ATLAS Tile Calorimeter Technical Design Report*. CERN, 1996. CERN-LHCC-96-42.
- [72] ATLAS Collaboration. *ATLAS Calorimeter Performance Technical Design Report*. CERN, 1996. CERN-LHCC-96-40.
- [73] ATLAS Collaboration. *ATLAS Muon Spectrometer Technical Design Report*. CERN, 1997. CERN-LHCC-97-22.
- [74] ATLAS Collaboration. *ATLAS First-Level Trigger Technical Design Report*. CERN, 1998. CERN-LHCC-98-14.
- [75] ATLAS Collaboration. *ATLAS High-Level Trigger, Data Acquisition and Controls Technical Design Report*. CERN, 2003. CERN-LHCC-2003-022.
- [76] A. Barriuso Poy et al. The detector control system of the ATLAS experiment. *JINST*, 3:P05006, 2008.
- [77] C. Carli. Proceedings of the 2009 Chamonix workshop on LHC performance. Technical Report CERN-ATS-2009-001, CERN, Geneva, Apr 2009.
- [78] M.J. Costa. Commissioning of the ATLAS detector with cosmic rays and first LHC beams. Technical Report ATL-GEN-PROC-2009-004. ATL-COM-GEN-2009-005, CERN, Geneva, Jan 2009.
- [79] P. Jenni. The ATLAS Experiment Entering Operation: Overview, Motivation and Status. Technical Report ATL-GEN-PROC-2009-003. ATL-COM-GEN-2009-003. 2, CERN, Geneva, Nov 2008.
- [80] R. Achenbach *et al.*. The ATLAS level-1 calorimeter trigger. *JINST*, 3:P03001, 2008.
- [81] Barrel Muon Trigger Groups. The Barrel Muon Trigger system of the ATLAS First Level Trigger. 2008. to be submitted to JINST.
- [82] Endcap Muon Trigger Groups. The Endcap Muon Trigger system of the ATLAS First Level Trigger. 2008. to be submitted to JINST.
- [83] Central Trigger Groups. The Central Trigger system of the ATLAS First Level Trigger. 2008. to be submitted to JINST.
- [84] S. Ask et al. The ATLAS central level-1 trigger logic and TTC system. *JINST*, 3:P08002, 2008.
-

- 
- [85] M. Abolins *et al.*. Specification of the lvl1 / lvl2 trigger interface, version 2.0. Technical Report ATL-DAQ-99-015, CERN, Geneva, Oct 1999.
- [86] M. L. Ferrer, H. P. Beck, S. Gadomski, and K. Kordas. Performance of the final Event Builder for the ATLAS Experiment. *IEEE Trans. Nucl. Sci.*, 55:176–181, 2008.
- [87] A. Negri. Infrastructure of the ATLAS event filter. Prepared for IFAC 2006 (in Italian), Pavia, Italy, 19-21 Apr 2006.
- [88] A. Negri. ATLAS TDAQ System Integration and Commissioning. Technical Report ATL-DAQ-PROC-2009-009. ATL-COM-DAQ-2009-030, CERN, Geneva, Apr 2009.
- [89] I. Riu *et al.* Integration of the Trigger and Data Acquisition Systems in ATLAS. *IEEE Trans. Nucl. Sci.*, 55:106–112, 2008.
- [90] M. Abolins *et al.*. Integration of the trigger and data acquisition systems in ATLAS. *J. Phys. Conf. Ser.*, 119:022001, 2008.
- [91] G. Comune *et al.*. Steering the ATLAS High Level Trigger. *199 Proceedings of CHEP06, Feb 2006, Mumbai, India*, 2006.
- [92] M. Grothe *et al.*. Architecture of the ATLAS high level trigger event selection software. *ECONF*, C0303241:WEPT004, 2003. arXiv:physics/0306097.
- [93] S. Armstrong *et al.*. Design, deployment and functional tests of the online event filter for the ATLAS experiment at LHC. *IEEE Trans. Nucl. Sci.*, 52:2846–2852, 2005.
- [94] C. Santamarina *et al.*. Implementation and performance of the seeded reconstruction for the ATLAS event filter. *IEEE Trans. Nucl. Sci.*, 53:864–869, 2006.
- [95] H. von der Schmitt *et al.*. A configuration system for the ATLAS trigger. *JINST*, 1:P05004, 2006. arXiv:physics/0602180.
- [96] D. Berge *et al.*. The configuration system of the ATLAS Trigger. *IEEE Trans. Nucl. Sci.*, 55:392–398, 2008.
- [97] A. Hocker *et al.*. Overview of the High Level Trigger Steering and Selection for the ATLAS experiment at the LHC. *IEEE Trans. Nucl. Sci.*, 55:165–171, 2008.
- [98] T. Fonseca-Martin *et al.*. Event reconstruction algorithms for the ATLAS trigger. *J. Phys. Conf. Ser.*, 119:022022, 2008.
- [99] P. Conde Muino *et al.*. Implementation and performance of the ATLAS second level jet trigger. *J. Phys. Conf. Ser.*, 119:022029, 2008.
- [100] D. Emeliyanov *et al.*. Trigger selection software for beauty physics in ATLAS. *J. Phys. Conf. Ser.*, 119:022020, 2008.
- [101] D. Torretta. Using Feedback to Control Deadtime in the CDF Trigger System. Presented at 15th IEEE Real Time Conference 2007 (RT 07), Batavia, Illinois, 29 Apr - 4 May 2007.
-

- 
- [102] R. Brun and F. Rademakers. ROOT: An object oriented data analysis framework. *Nucl. Instrum. Meth.*, A389:81–86, 1997. See also <http://root.cern.ch/>.
- [103] M. Barczyk et al. Online monitoring software framework in the ATLAS experiment. 2003. arXiv:0305096 [hep-ex].
- [104] M. Abolins *et al.*. The ATLAS trigger: Commissioning with cosmic rays. *J. Phys. Conf. Ser.*, 119:022014, 2008.
- [105] T. Pauly *et al.*. Commissioning of the ATLAS Level-1 Trigger with Cosmic Rays. *J. Phys. Conf. Ser.*, 110:092023, 2008. arXiv:0711.0938.
- [106] N. Berger *et al.*. The ATLAS high level trigger steering. *J. Phys. Conf. Ser.*, 119:022013, 2008.
- [107] T. Eifert *et al.*. The User Interface for the ATLAS Trigger and Its Use in Physics Studies. (ATL-DAQ-CONF-2008-001. ATL-COM-DAQ-2008-001), Oct 2007. Proceedings of NSS/MIC 2007, Honolulu, US.
- [108] J. Haller *et al.*. Access to Trigger Decision and Configuration Data in Offline Analysis. Technical Report ATL-COM-DAQ-2006-044, CERN, Geneva, Dec 2006.
- [109] J. Stelzer *et al.*. The Configuration System of the ATLAS Trigger. (ATL-COM-DAQ-2007-027), Jun 2007. Proceedings of RT 2007, Fermilab, US.
- [110] ATLAS Collaboration. *ATLAS Computing Technical Design Report*. CERN, 2005. CERN-LHCC-2005-022.
- [111] T. Sjostrand, S. Mrenna, and P. Skands. PYTHIA 6.4 physics and manual. *JHEP*, 05:026, 2006. arXiv:hep-ph/0603175.
- [112] H.P. Nilles. Supersymmetry, Supergravity and Particle Physics. *Phys. Rept.*, 110:1, 1984.
- [113] H.E. Haber and G.L. Kane. The Search for Supersymmetry: Probing Physics Beyond the Standard Model. *Phys. Rept.*, 117:75–263, 1985.
- [114] J. Wess and J. Bagger. Supersymmetry and supergravity. Princeton, USA: Univ. Pr. (1992) 259 p.
- [115] S. Weinberg. Implications of Dynamical Symmetry Breaking. *Phys. Rev.*, D13:974–996, 1976.
- [116] P. Nath and R.L. Arnowitt. Generalized Supergauge Symmetry as a New Framework for Unified Gauge Theories. *Phys. Lett.*, B56:177, 1975.
- [117] R.M. Godbole, P. Roy, and X. Tata. Tau signals of R-parity breaking at LEP-200. *Nucl. Phys.*, B401:67–92, 1993. arXiv:hep-ph/9209251.
- [118] G. Bhattacharyya and D. Choudhury. D and tau decays: Placing new bounds on R-parity violating supersymmetric coupling. *Mod. Phys. Lett.*, A10:1699–1704, 1995. arXiv:hep-ph/9503263.
-

- 
- [119] L. Girardello and Marcus T. Grisaru. Soft Breaking of Supersymmetry. *Nucl. Phys.*, B194:65, 1982.
- [120] S. Dimopoulos and D.W. Sutter. The Supersymmetric flavor problem. *Nucl. Phys.*, B452:496–512, 1995. arXiv:hep-ph/9504415.
- [121] M. L. Brooks et al. New Limit for the Family-Number Non-conserving Decay  $\mu^+ \rightarrow e^+ \gamma$ . *Phys. Rev. Lett.*, 83:1521–1524, 1999. arXiv:hep-ex/9905013.
- [122] E. Barberio et al. Averages of b-hadron properties at the end of 2006. arXiv:0704.3575 [hep-ex].
- [123] W. Buchmuller and D. Wyler. CP Violation and R Invariance in Supersymmetric Models of Strong and Electroweak Interactions. *Phys. Lett.*, B121:321, 1983.
- [124] G.W. Bennett et al. Measurement of the negative muon anomalous magnetic moment to 0.7-ppm. *Phys. Rev. Lett.*, 92:161802, 2004. arXiv:hep-ex/0401008.
- [125] L. Alvarez-Gaume, J. Polchinski, and M.B. Wise. Minimal low-energy supergravity. *Nucl. Phys.*, B221:495, 1983.
- [126] L.E. Ibanez. Locally Supersymmetric SU(5) Grand Unification. *Phys. Lett.*, B118:73, 1982.
- [127] J.R. Ellis, D.V. Nanopoulos, and K. Tamvakis. Grand unification in simple supergravity. *Phys. Lett.*, B121:123, 1983.
- [128] H. Komatsu K. Inoue, A. Kakuto and S. Takeshita. Aspects of grand unified models with softly broken supersymmetry. *Prog. Theor. Phys.*, 68:927, 1982.
- [129] A.H. Chamseddine, R. Arnowitt, and P. Nath. Locally supersymmetric grand unification. *Phys. Rev. Lett.*, 49:970, 1982.
- [130] F. Paige, S. Protopopescu, H. Baer, and X. Tata. *ISAJET 7.69: A Monte Carlo event generator for p p, anti-p p, and e+ e- reactions* hep-ph/0312045, 2003. arXiv:0312045 [hep-ph].
- [131] H.E. Haber and R. Hempfling. Can the mass of the lightest Higgs boson of the minimal supersymmetric model be larger than  $m(Z)$ ? *Phys. Rev. Lett.*, 66:1815–1818, 1991.
- [132] Y. Okada, M. Yamaguchi, and T. Yanagida. Upper bound of the lightest Higgs boson mass in the minimal supersymmetric standard model. *Prog. Theor. Phys.*, 85:1–6, 1991.
- [133] Y. Okada, M. Yamaguchi, and T. Yanagida. Renormalization group analysis on the Higgs mass in the softly broken supersymmetric standard model. *Phys. Lett.*, B262:54–58, 1991.
- [134] D.N. Spergel et al. Wilkinson Microwave Anisotropy Probe (WMAP) three year results: Implications for cosmology. *Astrophys. J. Suppl.*, 170:377, 2007. arXiv:astro-ph/0603449.
- [135] T. Falk, K.A. Olive, and M. Srednicki. Heavy Sneutrinos as Dark Matter. *Phys. Lett.*, B339:248–251, 1994.
- [136] J.R. Ellis, K.A. Olive, Y. Santoso, and V.C. Spanos. Supersymmetric Dark Matter in Light of WMAP. *Phys. Lett.*, B565:176–182, 2003. arXiv:hep-ph/0303043.
-



- 
- [137] The LEP SUSY Working Group (LEPSUSYWG) combines results from the ALEPH, DELPHI, L3, and OPAL detector collaborations. <http://www.cern.ch/lepsusy>.
- [138] V. M. Abazov et al. Search for squarks and gluinos in events with jets and missing transverse energy using  $2.1\text{ fb}^{-1}$  of  $p\bar{p}$  collision data at  $\sqrt{s} = 1.96\text{ TeV}$ . *Phys. Lett.*, B660:449–457, 2008. arXiv:0712.3805 [hep-ex].
- [139] T. Aaltonen et al. Inclusive Search for Squark and Gluino Production in  $p\bar{p}$  Collisions at  $\sqrt{s} = 1.96\text{ TeV}$ . 2008. arXiv:0811.2512 [hep-ex].
- [140] M.M. Nojiri and Y. Yamada. Neutralino decays at the LHC. *Phys. Rev.*, D60:015006, 1999. arXiv:hep-ph/9902201.
- [141] U. De Sanctis et al. Perspectives for the detection and measurement of Supersymmetry in the focus point region of mSUGRA models with the ATLAS detector at LHC. *Eur. Phys. J.*, C52:743–758, 2007. arXiv:0704.2515 [hep-ex].
- [142] G. Polesello and D.R. Tovey. Constraining SUSY dark matter with the ATLAS detector at the LHC. *JHEP*, 05:071, 2004. arXiv:hep-ph/0403047.
- [143] G. Belanger et al. micrOMEGAs: A program for calculating the relic density in the MSSM. *Comput. Phys. Commun.*, 149:103–120, 2002. arXiv:hep-ph/0112278.
- [144] M. M. Nojiri et al. Constraining dark matter in the MSSM at the LHC. *JHEP*, 03:063, 2006. arXiv:hep-ph/0512204.
- [145] A. J. Barr. Using lepton charge asymmetry to investigate the spin of supersymmetric particles at the LHC. *Phys. Lett.*, B596:205–212, 2004. arXiv:hep-ph/0405052.
- [146] G. Corcella et al. HERWIG 6: An event generator for hadron emission reactions with interfering gluons (including supersymmetric processes). *JHEP*, 01:010, 2001. arXiv:hep-ph/0011363.
- [147] T. Gleisberg et al. SHERPA 1.alpha, a proof-of-concept version. *JHEP*, 02:056, 2004. arXiv:hep-ph/0311263.
- [148] B.P. Kersevan and E. Richter-Was. The Monte Carlo event generator AcerMC version 1.0 with interfaces to PYTHIA 6.2 and HERWIG 6.3. *Comput. Phys. Commun.*, 149:142–194, 2003. arXiv:hep-ph/0201302.
- [149] M. Mangano et al. ALPGEN, a generator for hard multiparton processes in hadronic collisions. *JHEP*, 07:001, 2003. arXiv:hep-ph/0206293.
- [150] J. Alwall et al. MadGraph/MadEvent v4: The New Web Generation. *JHEP*, 09:028, 2007. arXiv:0706.2334.
- [151] S. Frixione and B.R. Webber. Matching NLO QCD computations and parton shower simulations. *JHEP*, 06:029, 2002.
- [152] S. Frixione, P. Naso, and B.R. Webber. Matching NLO QCD and parton showers in heavy flavour production. *JHEP*, 08:007, 2003. arXiv:hep-ph/0305252.
-

- 
- [153] J. Butterworth, J. Forshaw, and M. Seymour. Multiparton interactions in photoproduction at hera. *Z. Phys.*, C72:637–646, 1996. arXiv:hep-ph/9601371.
- [154] S. Jadach, Z. Was, R. Decker, and J.H. Kuhn. The tau decay library TAUOLA: Version 2.4. *Comput. Phys. Commun.*, 76:361–380, 1993.
- [155] E. Barberio and Z. Was. PHOTOS: A Universal Monte Carlo for QED radiative corrections. Version 2.0. *Comput. Phys. Commun.*, 79:291–308, 1994.
- [156] M.R. Whalley, D. Bourilkov, and R.C. Group. The Les Houches Accord PDFs (LHAPDF) and Lhaglu. 2005. hep-ph/0508110.
- [157] D. Stump et al. Inclusive jet production, parton distributions, and the search for new physics. *JHEP*, 10:046, 2003. arXiv:hep-ph/0303013.
- [158] J. Pumplin et al. New generation of parton distributions with uncertainties from global QCD analysis. *JHEP*, 07:012, 2002. arXiv:hep-ph/0201195.
- [159] J. Pumplin, A. Belyaev, J. Huston, D. Stump, and W.K. Tung. Parton distributions and the strong coupling strength  $\alpha(s)$ . *JHEP*, 02:032, 2006. arXiv:hep-ph/0512167.
- [160] G. Corcella et al. *HERWIG 6.5* hep-ph/0210213, 2002. arXiv:hep-ph/0210213.
- [161] J. Alwall *et al.* Comparative study of various algorithms for the merging of parton showers and matrix elements in hadronic collisions. *Eur. Phys. J.*, C53:473–500, 2008. arXiv:0706.2569.
- [162] E. Richter-Was, D. Froidevaux, and L. Poggioli. ATLFAST 2.0 a fast simulation package for ATLAS Atlas Note ATL-PHYS-98-131.
- [163] D. Cavalli *et al.* Performance of the ATLAS fast simulation ATLFAST. Technical Report ATL-PHYS-INT-2007-005. ATL-COM-PHYS-2007-012, CERN, Geneva, Jan 2007.
- [164] S. Agostinelli *et al.* GEANT4: A simulation toolkit. *Nucl. Instrum. Meth.*, A506:250–303, 2003.
- [165] D. Costanzo *et al.* ATLAS detector simulation: status and outlook. Technical Report ATL-SOFT-PUB-2005-004. CERN-ATL-SOFT-PUB-2005-004. ATL-COM-SOFT-2005-008, CERN, Geneva, Dec 2005.
- [166] K. Assamagan et al. The atlas monte carlo project. Technical Report ATL-COM-SOFT-2008-024, CERN, Geneva, Dec 2008. To be submitted to JINST.
- [167] W. Beenakker, R. Hopker, M. Spira, and P.M. Zerwas. Squark and gluino production at hadron colliders. *Nucl. Phys.*, B492:51–103, 1997. arXiv:9610490 [hep-ph], see also: <http://www.ph.ed.ac.uk/~tplehn/prospino>.
- [168] W. Beenakker et al. The production of charginos/neutralinos and sleptons at hadron colliders. *Phys. Rev. Lett.*, 83:3780–3783, 1999. arXiv:hep-ph/9906298.
- [169] Z. Nagy. Three-jet cross sections in hadron hadron collisions at next-to-leading order. *Phys. Rev. Lett.*, 88:122003, 2002. arXiv:hep-ph/0110315.
-

- 
- [170] Z. Nagy. Next-to-leading order calculation of three-jet observables in hadron-hadron collision. *Phys. Rev.*, D68:094002, 2003. arXiv:hep-ph/0307268.
- [171] K. Melnikov and F. Petriello. Electroweak gauge boson production at hadron colliders through  $O(\alpha(s)^2)$ . *Phys. Rev.*, D74:114017, 2006. arXiv:hep-ph/0609070.
- [172] R. Bonciani, S. Catani, M. L. Mangano, and P. Nason. NLL resummation of the heavy-quark hadroproduction cross-section. *Nucl. Phys.*, B529:424–450, 1998. arXiv:hep-ph/9801375.
- [173] J. Campbell, J. Ellis, and R. Keith. An update on vector boson pair production at hadron colliders. *Phys. Rev.*, D60:113006, 1999. arXiv:hep-ph/9905386.
- [174] D.E. Acosta et al. First measurements of inclusive  $W$  and  $Z$  cross sections from Run II of the Tevatron collider. *Phys. Rev. Lett.*, 94:091803, 2005. arXiv:0406078[hep-ex].
- [175] S. Hassani et al. A muon identification and combined reconstruction procedure for the ATLAS detector at the LHC using the (MUONBOY, STACO, MuTag) reconstruction packages. *Nucl. Instrum. Meth.*, A572:77–79, 2007.
- [176] T. Lagouri et al. A muon identification and combined reconstruction procedure for the ATLAS detector at the LHC at CERN. *IEEE Trans. Nucl. Sci.*, 51:3030–3033, 2004.
- [177] D Adams et al. Track reconstruction in the ATLAS Muon Spectrometer with MOORE 007. Technical Report ATL-SOFT-2003-007, CERN, Geneva, May 2003. revised version number 1 submitted on 2003-10-13 13:51:39.
- [178] T. Cornelissen et al. Concepts, Design and Implementation of the ATLAS New Tracking (NEWT). Technical Report ATL-SOFT-PUB-2007-007. ATL-COM-SOFT-2007-002, CERN, Geneva, Mar 2007.
- [179] S. Tarem and N. Panikashvili. Low momentum muon identification in the ATLAS detector at the LHC. *IEEE Trans. Nucl. Sci.*, 53:1304–1309, 2006.
- [180] G.C. Blazey et al. Run II jet physics. 2000. hep-ex/0005012.
- [181] C. Buttar et al. Standard Model Handles and Candles Working Group: Tools and Jets Summary Report. 2008. arXiv:0803.0678 [hep-ph].
- [182] S.D. Ellis and D.E. Soper. Successive combination jet algorithm for hadron collisions. *Phys. Rev.*, D48:3160–3166, 1993. arXiv:hep-ph/9305266.
- [183] S. Catani, Y.L. Dokshitzer, and B.R. Webber. The  $K$ -perpendicular clustering algorithm for jets in deep inelastic scattering and hadron collisions. *Phys. Lett.*, B285:291–299, 1992.
- [184] M. Cacciari and G.P. Salam. Dispelling the  $N^3$  myth for the  $k(t)$  jet-finder. *Phys. Lett.*, B641:57–61, 2006. arXiv:hep-ph/0512210.
- [185] Y.L. Dokshitzer et al. Better Jet Clustering Algorithms. *JHEP*, 08:001, 1997. arXiv:hep-ph/9707323.
-

- 
- [186] G.P. Salam and G. Soyez. A practical Seedless Infrared-Safe Cone jet algorithm. *JHEP*, 05:086, 2007. arXiv:0704.0292.
- [187] J.M. Butterworth et al. KtJet: A C++ implementation of the K(T) clustering algorithm. *Comput. Phys. Commun.*, 153:85–96, 2003.
- [188] I. Abt et al. The H1 detector at HERA. *Nucl. Instrum. Meth.*, A386:310–347, 1997.
- [189] D.R. Tovey. Inclusive SUSY searches and measurements at ATLAS. *Eur. Phys. J. direct*, C4:N4, 2002.
- [190] B. List. Statistical Error of efficiency Determination from Weighted Events, 1999. <https://www.desy.de/~blist/notes/effic.ps.gz>.
- [191] R.D. Cousins and V.L. Highland. Incorporating systematic uncertainties into an upper limit. *Nucl. Instrum. Meth.*, A320:331–335, 1992.
- [192] J.T. Linnemann. Measures of significance in HEP and astrophysics, 2003. arXiv:physics/0312059.
- [193] A. Hocker *et al.*. TMVA: Toolkit for multivariate data analysis. *PoS*, ACAT:040, 2007. arXiv:physics/0703039.
- [194] M. Backes, J. Boyd, T. Eifert, A. Hoecker, B.A. Petersen, and S. Schaetzel. The Tiles Method: Background Estimation for SUSY Searches. Technical Report ATL-PHYS-INT-2009-010. ATL-PHYS-PUB-2009-077, CERN, Geneva, Jan 2009.
- [195] W. Verkerke and D. Kirkby. The RooFit toolkit for data modeling. *arXiv:physics/0306116*, 2003.
- [196] ATLAS Collaboration, D. Charlton, and T. LeCompte. ATLAS Plots on Ecm Dependence of Physics Reach. Technical Report ATL-COM-PHYS-2009-069, CERN, Geneva, Feb 2009. See also: <https://twiki.cern.ch/twiki/bin/view/Atlas/AtlasResultsEcmDependence>.
- [197] G. Aarons et al. International Linear Collider Reference Design Report Volume 2: Physics at the ILC. 2007. arXiv:hep-ph/0709.1893.
- [198] M. Battaglia, A. de Roeck, J.R. Ellis, and D. Schulte. *Physics at the CLIC Multi-TeV Linear Collider : report of the CLIC Physics Working Group*. CERN, Geneva, 2004.
-

# Acknowledgments

When I came to Geneva/CERN to start as a fresh PhD student with UniGe, I was sure, as about every new student, to be just right in time for the first LHC collisions. Even though this thrilling time is yet to come, I consider the past three years enormously important in my life. I have had the chance to work together with brilliant people, in a highly challenging environment. I am very thankful and deeply indebted to all the following people for what I learnt scientifically; for their guidance, encouragement, and assistance; as well as for the good time in general.

Foremost, I am forever grateful to Maria. Your support and your love has been amazingly important for me. Mille grazie mio dolce amore! Auch meinen Eltern Christiane und Franz habe ich sehr viel zu verdanken: Ihr habt die Grundsteine meines Charakters gelegt, meine Neugier erweckt, meine Interessen gefördert und mir Vertrauen in meine eigenen Fähigkeiten gegeben. Vielen Dank!

At the Humboldt-University, Thomas Lohse and Christian Stegmann, who introduced me to research in experimental (astro) particle physics, had great influence on my career. Thanks to their key contributions I entered this field and learnt how much fun it is.

At the University of Geneva, I sincerely thank Allan Clark for giving me the opportunity to work on the ATLAS experiment, and for his constant support and guidance. My gratitude also goes to Xin Wu for his co-supervision, and the good advice throughout the whole period, as well as for introducing me to the ATLAS high-level trigger community.

At CERN, I have been guided and influenced by many great people. Above all, I am thankful to Andreas Höcker who has been an excellent supervisor with all his inspiring ideas and his endless enthusiasm. I am also very thankful to the other members of the high-level trigger core-software group: Tomasz Bold, Nicolas Berger, Johannes Haller, and Simon George. I learnt an enormous amount about triggers, software design, and the detector in general in the numerous and fruitful discussions. I further received assistance and guidance from many other people in the trigger community, for which I am thankful, most notably: Kyle Cranmer (who inspired the LVL2- $E_T^{\text{miss}}$  trigger project), John Baines (for helpful discussions), and Ricardo Goncalo (for the good discussions around the trigger user-interface).

I am deeply grateful to Andreas Höcker and Jamie Boyd for all their guidance and support in the SUSY group. It has been a pleasure and privilege to be part of this group. I am also very thankful to all the other members of this group, in particular: Amir Farbin (who taught me many details about analysis techniques), Jörg Stelzer (for solving all my TMVA issues), Brian Petersen (for introducing me to the details of log-likelihood fitting), Sebastian Schätzel (for being critical in a

very constructive way) Henning Flächer (for supporting the CSC studies), and David Berge (for all his insight).

A big thank-you goes to the whole Geneva group. In particular, I received support from: Alison and Andrée (who always bailed me out when it comes to French), Andrew (for running so fast, and good discussions including the best controversial lunch discussions), Arno (for all the excellent physics discussions, and the impressive mountain tours), Chiara (for the most cheerful nature, the support, and the climbing), Clemencia (who taught me everything I know about tennis), Mauro (for the Polenta, the help, and much more), Moritz (for crazy sailing trips), Olivier (for introducing me to the French lifestyle and the haute cuisine), Tica and Peggy (for solving all possible administrative issues), Will (who always knows the right book to find an answer), and Yann (for accepting my wish for an English keyboard).

A hello to all of you who have made my time here such a pleasant experience. “The duck” with the idea to express all of the phd physics content in form of a wild dance when presenting it during the viva (oral examination): I hope to see it! Monika, who has been assimilated for the 12 o’clock lunch. The vikings and princesses for the good moments. And all the others who I forgot ...

---